UNIVERSITY OF THESSALY
DEPARTMENT OF MECHANICAL ENGINEERING

Computational Study of Transport Phenomena in Flake Filled Composite Materials

by

Andreas Tsiantis

Diploma in Mechanical & Industrial Engineering, University of Thessaly, 1998
M.Sc. in Mechanical Engineering, University of Thessaly, 2016

Submitted in partial fulfillment of the requirements for the degree of Doctor of Philosophy in Mechanical Engineering at the University of Thessaly

January 2020

Approved by the Committee on Final Examination:

Advisor	Athanasios Papathanasiou Professor, Department of Mechanical Engineering University of Thessaly
Member	Panagiotis Tsiakaras Professor, Department of Mechanical Engineering University of Thessaly
Member	Anastasios Stamatellos Professor, Department of Mechanical Engineering University of Thessaly
Member	Vasilis Bontozoglou Professor, Department of Mechanical Engineering University of Thessaly
Member	Nikolaos Aravas Professor, Department of Mechanical Engineering University of Thessaly
Member	Nikolaos Andritsos Professor, Department of Mechanical Engineering University of Thessaly
Member	Georgios Georgiou Professor, Department of Mathematics and Statistics University of Cyprus
Date of approval	18-3-2020

Acknowledgements

I would like to express my gratitude to my supervisor Professor Athanasios Papathanasiou for his mentorship, guidance, criticism and continuous support during my research in University of Thessaly. The boundless freedom and the limitless advice he gave me for this thesis is tremendously appreciated, enriching my knowledge in both practical and theoretical sense and will have a profound influence to my career.

I am also grateful to my Phd committee members, Professor Panagiotis Tsiakaras and Professor Anastasios Stamatellos for their valuable advice and fruitful discussions during the research for this thesis.

Very special thanks to Dr. Ioannis Sarris for his significant help in understanding the power of computational fluid mechanics and for our collaboration.

I am also grateful for the financial support from the Department of Mechanical Engineering.

Last but not the least, I would like to thank my family: my wife and my son for their endless patience and help. Also my mother and my sister for supporting me spiritually throughout writing this thesis. Without their support this work would not have been completed.

Dedication

Dedicated to my family

Abstract

The aim of this thesis is to investigate how the effective diffusivity of flake filled polymeric membranes is altered by the presence and properties of flakes, such as their aspect ratio (α), volume fraction (ϕ), orientation (θ) and alignment relative to the direction of diffusion ($\theta + \epsilon$). We show that as a result of the dispersion of flakes in the polymeric matrix, materials with improved barrier properties are produced since the flake existence causes an increase in the distance travelled by the diffuse species through the membrane. This degree of difficulty is described by the Barrier Improvement Factor (BIF) and this coefficient is used to quantify the effect of the flake presence on the membrane barrier properties.

Besides the technological importance of this topic, an additional motivation for this investigation was the fact that the already proposed models have shown a small range of applicability and in general have limited success in providing a unifying framework for the description of the barrier properties of said materials. To address this issue we have carried out a comprehensive computational study and proposed and tested new theoretical models able to describe BIF for a range of flake concentrations and orientations.

The present thesis used 2D & 3D RVEs with periodic geometries and periodic boundary conditions that were created using a variety of computational tools including applications and algorithms that were written from scratch for the needs of this study. Subsequently with the created geometries we run simulations using the OpenFOAM toolbox in our laboratory cluster which was set up in the beginning of this thesis. With this combination of existing and new computational tools we managed to create a toolchain that enabled us to run thousands of simulations covering all the studied parameters in their full range and - in to our knowledge - the most comprehensive study in the literature so far. Also contrary to most earlier studies the simulations were carried out in RVEs of realistic complexity, containing 1000s of individual flakes. We also check our results against the existing models described in the literature and we examine some common misconceptions and problems that exist in the field.

Keywords: Composite materials, Flakes, Diffusion, Transport Phenomena, Barrier Properties, 2D & 3D modelling, Simulation, Barrier Improvement Factor (BIF).

Περίληψη

Σκοπός αυτής της εργασίας είναι η διερεύνηση του τρόπου με τον οποίο μεταβάλλεται ο συντελεστής διαπερατότητας ενός σύνθετου υλικού, ενισχυμένου με φυλλίδια, με έμφαση στις πολυμερικές μεμβράνες. Οι ιδιότητες των υλικών αυτών μεταβάλλονται από την παρουσία και τις ιδιότητες των φυλλιδίων, όπως η αναλογία διαστάσεων (α), το κλάσμα όγκου (φ), ο προσανατολισμός (ϑ) και η διακύμανση του προσανατολισμού (ϑ+ε). Δείχνουμε ότι ως αποτέλεσμα της διασποράς των φυλλιδίων στο υλικό, παράγονται υλικά με βελτιωμένες ιδιότητες φραγμού αφού η ύπαρξη των φυλλιδίων προκαλεί αύξηση στην διαδρομή που πρέπει να ακολουθηθεί από τα μόρια, ιόντα κλπ, διαμέσου του υλικού. Αυτός ο βαθμός δυσκολίας περιγράφεται από τον συντελεστή Barrier Improvement Factor (BIF), ο οποίος χρησιμοποιείται για την ποσοτικοποίηση της επίδρασης της παρουσίας φυλλιδίων στις ιδιότητες φραγμού.

Εκτός από την τεχνολογική σημασία αυτού του θέματος, πρόσθετο κίνητρο για την έρευνα αυτή ήταν το γεγονός ότι τα ήδη προτεινόμενα μοντέλα έχουν δείξει ένα μικρό εύρος εφαρμογής και γενικά έχουν περιορισμένη επιτυχία στην παροχή ενός ενοποιητικού πλαισίου για την περιγραφή των ιδιοτήτων φραγμού των εν λόγω υλικών. Για να αντιμετωπίσουμε αυτό το ζήτημα, πραγματοποιήσαμε μια ολοκληρωμένη υπολογιστική μελέτη και προτείνουμε νέα θεωρητικά μοντέλα ικανά να περιγράψουν το BIF για μια σειρά μεγεθών, συγκεντρώσεων και προσανατολισμών φυλλιδίων.

Στην παρούσα διατριβή χρησιμοποιήσαμε 2D & 3D RVEs με περιοδικές γεωμετρίες και περιοδικές οριακές συνθήκες που δημιουργήθηκαν χρησιμοποιώντας μια ποικιλία υπολογιστικών εργαλείων που περιλαμβάνουν εφαρμογές και αλγορίθμους που γράφτηκαν και υλοποιήθηκαν για τις ανάγκες αυτής της μελέτης. Στη συνέχεια δημιουργήθηκαν γεωμετρίες και εκτελέστηκαν προσομοιώσεις χρησιμοποιώντας την εργαλειοθήκη του OpenFOAM στο εργαστηριακό μας cluster το οποίο στήθηκε στην αρχή αυτής της διατριβής. Με αυτόν τον συνδυασμό υφιστάμενων και νέων υπολογιστικών εργαλείων καταφέραμε να δημιουργήσουμε μια ακολουθία ενεργειών που μας επέτρεψε να τρέχουμε χιλιάδες προσομοιώσεις και οι οποίες καλύψανε όλες τις παραμέτρους που μελετήθηκαν στο πλήρες εύρος τους και αποτελούν - όσο γνωρίζουμε - την πιο ολοκληρωμένη μελέτη στη βιβλιογραφία μέχρι στιγμής.

Επίσης αντίθετα με προηγούμενες μελέτες οι προσομοιώσεις πραγματοποιήθηκαν σε RVEs με ρεαλιστική πολυπλοκότητα, που περιείχαν περισσότερα από 1000 φυλλίδια. Ελέγξαμε επίσης τα αποτελέσματά μας σε σχέση με υπάρχοντα μοντέλα που περιγράφονται στη βιβλιογραφία και εξετάσαμε μερικές κοινές παρανοήσεις και προβλήματα που υπάρχουν στον τομέα.

Λέξεις κλειδιά: Σύνθετα υλικά, Φυλλίδια, Διάχυση, Φαινόμενα μεταφοράς, Ιδιότητες φραγμού, 2D & 3D μοντελοποίηση, προσομείωση, Συντελεστής βελτίωσης ιδιοτήτων φραγμού

Summary

After the introduction in Chapter 1 where we discuss the characteristics of composite materials and the theoretical background of diffusion, a new algorithm is introduced in Chapter 2 (FastRSA), with which we can create periodic 2D geometries that approach the packing limit at every value of (α). This has enabled us to calculate more accurately the statistical properties of such geometries especially at high (α) contrary to the classic RSA algorithm which shows a weakness in approaching the maximum packing limit in these cases.

From Chapter 3 to Chapter 6 we examine 2D systems that simulate composites with ribbon-like flakes. In Chapter 3 we examine the effect that deviations from perfect alignment have on barrier properties. The transition in the behavior of *BIF* between the dilute and concentrated regime is clearly shown in our computational results. Using these results we propose a model that is a function of ($\alpha\phi$) and (ϵ). In Chapter 4 we study unidirectional misaligned systems and uncover the combined effect of (θ) and ($\alpha\phi$) on *BIF*. This is expressed in the form of a model that, contrary to earlier published studies, respects the rotational invariance of the diffusivity tensor. With the use of this model we get excellent agreement with the computational results in all misalignment angles and for a wide range of ($\alpha\phi$) up to 40. At Chapter 5 a comparison is made between our model and existing models in the field. By comparing the existing models with our model and with the computational results we see how the existing models deviate in the semi-dilute and concentrated regime and how this deviation renders them unusable in these cases. The effect of geometrical formulation and boundary conditions is examined in detail and we show the problems that arise from poorly formulated simulations. At Chapter 6 we present a closed form solution for the effective diffusivity coefficient in cases where the flakes are randomly oriented inside the RVE. This solution predicts with accuracy the behavior of *BIF* even at large (θ) and ($\alpha\phi$).

Finally in Chapter 7 we extend successfully the 2D models to 3D geometries and we introduce a new metric (M) for the description of the *BIF* of 3D systems with flakes of various shapes that cover the most frequently flake geometries. For misaligned flakes they show that as (M) increases the evolution of *BIF* is no longer monotonic but it approaches a plateau value which is determined by (θ).

Contents

List of Tables

List of Figures

Chapter 1

Introduction

Polymeric membranes of various materials with remarkable properties that serve a wide range of applications have been developed and emerged by the polymer industry in recent decades. Approaching lower orders of magnitude, we notice that nanocomposite polymeric membranes belong to a new class of composites that promise many as materials with improved properties for almost all industrial applications and especially in medicine, food packaging, power generation. photovoltaic systems, fuel cells coatings, various chemical separations of elements such as water desalination as well as numerous other applications. In many applications and if required, the permeability of the membranes or otherwise their selective permeability can be controlled.

In particular, we refer to applications in the field of medicine or nano-medicine (referring to the nanometer-nm scale - 10^{-9}m), where nanotechnology achievements have already appeared recently in semi-permeable membrane filters. High-permeability polysulfone membranes, in which the porous texture of the inner layer is controlled at the nanoscale level, and pores with selective permeability have also been developed and tested. Also it is possible to construct "smart" membranes and integrate them into a continuous-mode, portable or implantable biological systems such as artificial kidneys. We also have applications in electronics where production of almost chemically pure deionized water, necessary for the production of computer boards and microchips, became possible after applying appropriate reverse osmosis systems by using new composite polymeric membranes. Nanocomposite polymeric membranes are also used in applications such as municipal waste treatment for the filtration and reuse of water, in modern food technology, enhancing consumer safety and maintaining food quality as of course in many other separation applications. Finally the use of membranes helps address the very important problem of lack of drinking water by methods of separation processes by membranes such as reverse osmosis and reverse electrodialysis, or even desalination with thermal methods. This gives access to 97% of the total ground water, which is in the seas and oceans with high dissolved salt content (about 35gr per liter), where the most energy-efficient solution today is desalination using reverse osmosis membranes using desalination modules as shown in Figure 1.1.

In recent years there has been a remarkable interest in composite membranes which use inorganic reinforcing agents in the form of flakes with high values of aspect ratio. These reinforcement cases include flakes with micron-size dimensions, from inorganic materials such as mica and more recently to nanoscale dimensions, using clay minerals such as Hectorite, Saponite and Montmorillonite [1]. Such enhancers have been shown to be highly effective since they have the potential to significantly increase the distance traveled by the diffusion molecules across the membrane. In addition a very important factor is that the desired insulation properties can be achieved by using a small amount of reinforcement means and therefore a low overall cost. Although membrane reinforcement is a well-known category of research, its dependence on microstructural factors such as spatial distribution, size distribution and orientation of the reinforcing agents in the polymer matrix is not well understood. A number of researches have been carried out in this field and in order to further understand the part of the dependence of

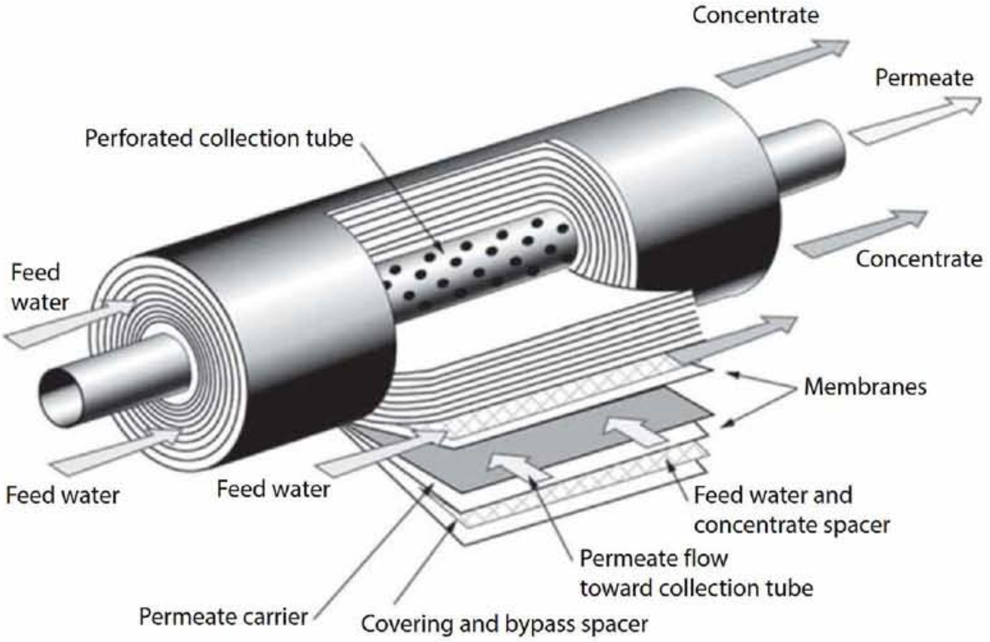

Figure 1.1: Representation of seawater desalination system using a spiral wound membrane module [2].

the membrane transport phenomena on factors of the microstructure of the reinforcing media, various results have been obtained and will be analyzed.

The study of such systems (of great geometrical complexity) requires the acceptance of certain assumptions in order to be implemented. For example, for a solution comprising of flakes with an aspect ratio (ratio of the length to the width of the flake to which the letter α will refer to) equal to 100, should have a charge rate of less than 0.01% to be considered diluted and therefore to accessed by analytical methods. For a non-dilute solution the concentration of the diffuser around each flake is disturbed by the presence of adjacent flakes, which makes the experimental verification difficult to impossible and their numerical approximation one-way. More specifically the product ($\alpha\phi$) (the aspect ratio (α) times the volume fraction (ϕ)) is an important factor to consider when analyzing such systems [1].

The present thesis presents an immediate numerical approach for predicting insulation properties and transport phenomena through flake-filled polymeric materials. In particular, we study the variation of their diffusion coefficient as a function of parameters such as the volume fraction, dimensions and orientation of the flakes. The numerical calculations are performed in two and three dimensions (2D & 3D) for composite membranes comprising of oriented and random orientated flakes using the OpenFOAM toolbox. In addition to reviewing the literature and studying some of the theoretical models of existing literature we attempt to predict the diffusion coefficient of composite polymeric membranes with a newly developed model that gives accurate results for both 2D and 3D geometries as well in a range that extends from the dilute well in to the concentrated regime. Also an attempt is made to evaluate the results and comment on their predictions.

1.1 Polymers

Polymers are materials consisting of large molecules (macromolecules) that are created by the repetition of building blocks (monomers) that are interconnected by covalent bonds. Polymers cover a wide range of applications and come from petroleum-based organic raw materials. In this class of materials belongs bakelite, neoprene, nylon, PVC, polystyrene, polyacrylonitrile etc. Etymologically, the word polymers comes from the Greek words very + part, which is a definition that appropriately describes the enormous number of molecules that make up the macromolecule. Polymers are prepared by joining many of the same molecules, that is, the monomers, by the following procedures:

1. The polymerization method
2. The method of polycondensation

Polymerization : This method produces polymers having the same composition as the original monomers such as the polymerization of ethylene to form polyethylene (Figure 1.2). During polymerization, products of double, triple and generally multiple molecular weight can be formed. Polymerization is effected by the influence of heat (thermal), free radicals (radical), catalysts (catalytic), radiation (radioactive) etc. The pure monomer and its solutions or emulsions under the presence of the above factors is polymerized. The quality and properties of the polymers prepared by polymerization are influenced by various physical and chemical factors, the most important of which are: the properties of the monomer, temperature, pressure the nature of the polymerization environment and the presence of impurities, excipients or stabilizers. Depending on the additions and process conditions polymers of different molecular weight are produced whose properties vary [3].

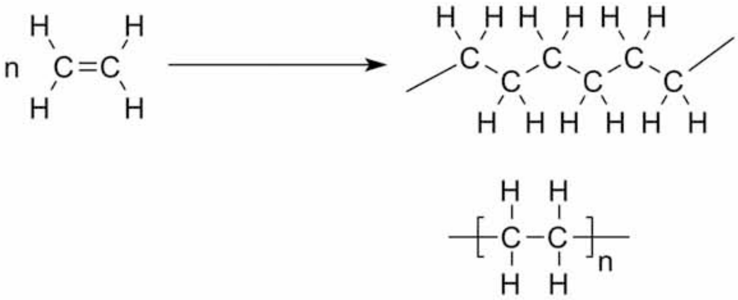

Figure 1.2: Polymerization of ethylene

Polycondensation : In this method, along with the formation of a megalomolecule, small molecular products such as water, hydrogen chloride, alcohol etc. are separated. There are two types of polycondensation reactions. Homopolymerization, which is a process between the same monomers e.g. amino acids and the heteropolyscubation in which two different monomers usually take part e.g. dicarbonic acid and diamine. The main factors that influence the course of the polycondensation and determine the properties of the products that are produced are the reaction temperature the structure of the original monomer and the types and amounts of catalysts. Synthetic resins, polyamides, polyesters, etc. are manufactured in the polycondensation industry [4].

1.2 Classification of polymers

The classification of polymers based on their mechanical response to high temperatures is shown in Figure 1.3. Another distinction of polymers can be made by the criterion of whether the molecular chain monomer is the same or different. This is how we distinguish between homopolymer and copolymer if we have the same or different monomer, respectively. Figure 1.4 shows this classification: In the same figure we can see that copolymers are divided into random, graft, and block groups depending on how the structural elements are rotated on the polymer chain. In Figure 1.5 we can see various cases of the molecular chain structure for a copolymer.

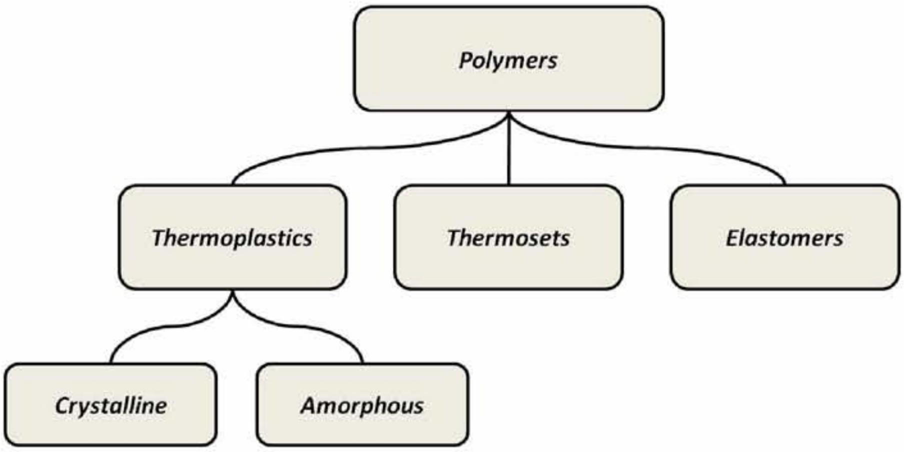

Figure 1.3: Classification of polymers based on their mechanical properties at high temperatures

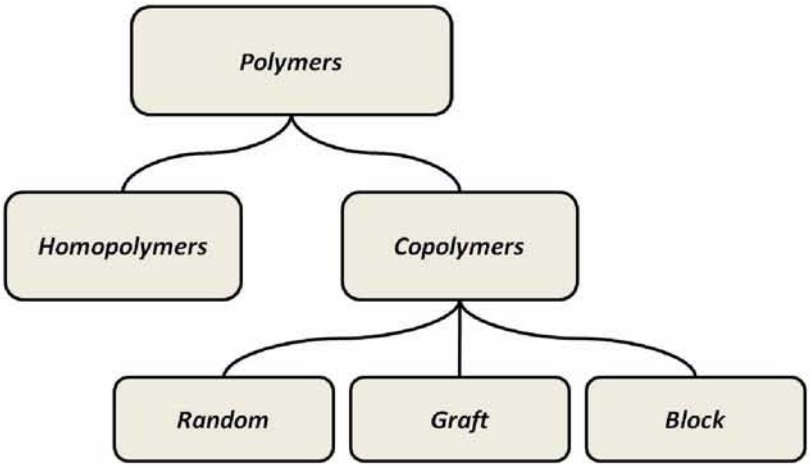

Figure 1.4: Classification of polymers by their structural units (monomers)

Figure 1.5: Structure of copolymers [5].

1.2.1 Composite materials

Composite materials are defined as the combination of two or more materials, each having different properties. In these cases we get an excellent combination of properties by mixing two or more materials. This improved behaviour is referred to as the principle of combined action. The modern term "composites" refers to materials that are made of artificial rather than natural. In addition, the two phases of the composite must be chemically dissimilar and separated by a distinct interface.

Composites are classified into three general categories (Figure 1.6): (a) particle-reinforced, (b) fiber-reinforced, and (c) structural composites. Each category has at least two subdivisions. In the first case, the dispersed phase has approximately the same dimensions in all directions. In the second case, the dispersed phase has the flake geometry (i.e. a large ratio of length/thickness). In the third case there is a combination of composite and homogeneous materials (This classification follows the presentation of materials found in [6]). Most composites consist of two phases: the matrix, which is continuous and surrounds the other phase, and the dispersed phase. The matrix of composites is a vital part of their composition and its role is to keep the flakes together and the choice of an appropriate matrix depends on the temperature and the environment that the material is to be used [7]. The good affinity between the dispersed phase and the matrix is very important for the proper functioning of the composite. The interface is defined as the contact area between the two constituent materials at the border of their surface.

On the other hand, the reinforcement phase is the phase that gives the composite material its improved properties compared to the properties of the matrix. However, in addition to the

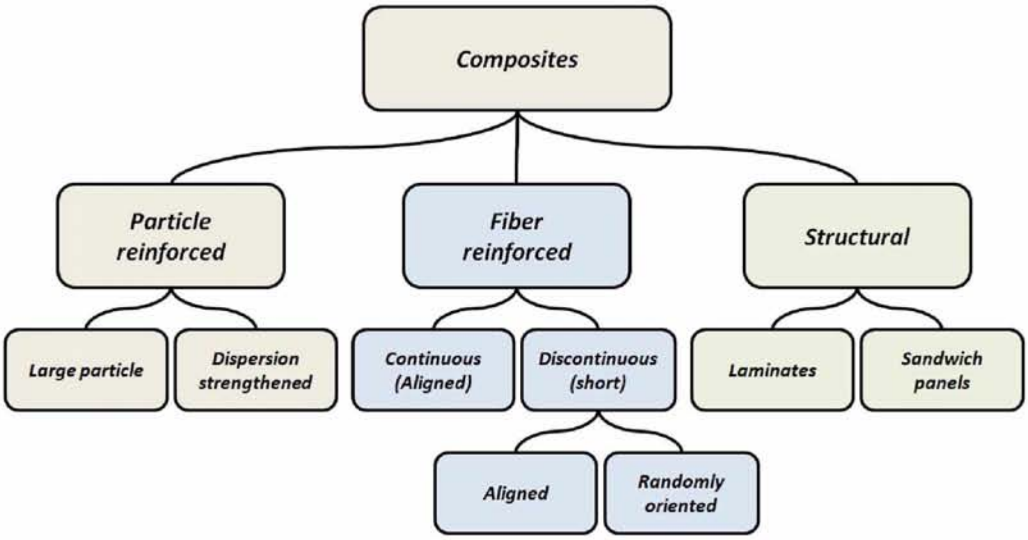

Figure 1.6: Classification of polymers.

structure and surface morphology of composite materials with reinforcing agents, there are also microscopic factors affecting these reinforcing agents and which influence the final properties of composites such as concentration, size, shape, distribution, alignment and also their orientation and length. The properties of the composite material are a function of the properties of the two phases, their relative proportion rates and the geometry of the dispersed phase. The latter means the shape and size of the dispersed particles, their distribution, and their orientation. These features are shown in Figure 1.7. In the present work as already mentioned, we will focus on how the diffusion coefficient varies with respect to the orientation of the flakes (θ), the degree of filling of the material (ϕ) and the ratio of the length/width of the flake (α for 2D problems and r for 3D problems).

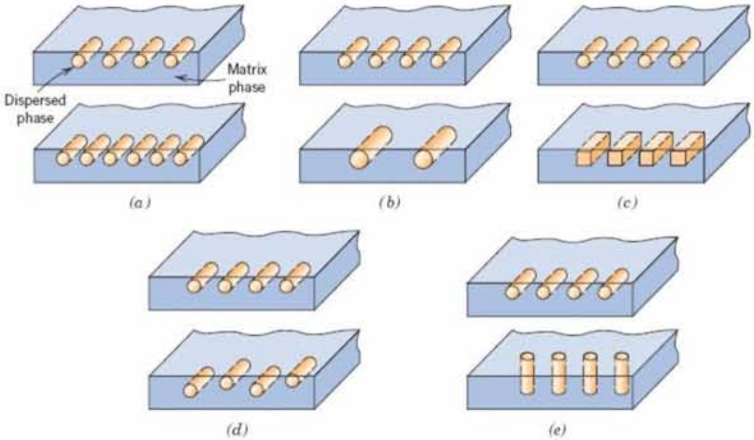

Figure 1.7: Schematic representations of the various geometrical and spatial characteristics of particles of the dispersed phase that may influence the properties of composites: (a) concentration, (b) size, (c) shape, (d) distribution, and (e) orientation [8].

1.2.2 Composite polymers

The term composite polymers is used to describe particle-reinforced polymers that occur in various forms, such as spheres, fibers and flakes. In the present work, we will deal with flake type reinforcement in polymeric membranes. The orientation of the amplification can be specific or random, so we have respectively aligned or random systems. Figure 1.8 shows the various cases of composite polymers [9]. In advanced composite materials, reinforcing agents are made of either inorganic materials (glass, carbon, metals, ceramics) or organic materials (polymers). The total worldwide market for composites was estimated at \$25x10^9 in 1998 and is estimated to grow by approximately 5% each year. The market for composites is dominated by glass-reinforced polyester and thermosetting resins which account for almost 90% of total production.

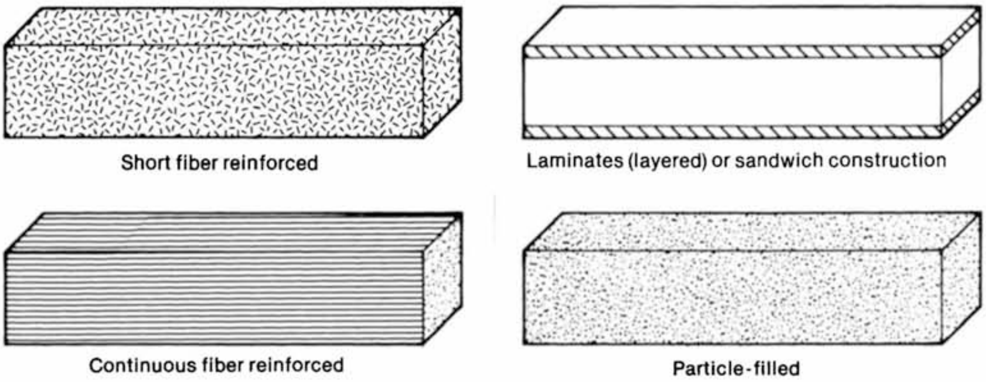

Figure 1.8: Reinforcement material distributions [9].

1.3 Membrane Technology

The membrane is a permeable or semi-permeable phase, which often consists of a thin polymer or other material, which restricts the movement of certain components. According to the IUPAC definition, it is a structure with very large lateral dimensions in relation to its thickness and through which, under the influence of various driving forces, the mass transfer effect may occur [10]. A more general definition is: "A membrane is called a phase or group of phases lying between two different phases, which is physically and/or chemically distinct from them and which, due to its properties and the applied field strength, can control the mass transfer between these two phases" [11]. More practical, therefore, is a material formed as a thin layer, which is inserted between two fluid phases (mixtures or solutions) and which is permeable to the components of these two phases. However, because each component has a different membrane crossing capability, we can, with the help of a suitable driving force (eg pressure, chemical potential, concentration) move material from one phase to another and as a result have different compositions on the side to which the movement is made relative to the other side. That is, this additional phase constitutes a barrier-insulation between a feed stream to be separated and a stream of products. The membrane controls the relative rate of transfer of the components through it and divides the supply into a stream enriched in specific components and into a stream of low concentration therein. Therefore, the membranes are characterized by a selectivity in the passage of molecules and can serve as separation processes for mixtures or solutions in their constituents. The driving force for the separation of gases and vapours is the partial pressure difference across the membrane, while for liquids the difference is the concentration. The membranes, depending on the material from which they are made, are divided into inorganic and polymeric. The former usually consist of ceramic materials or zeolites (solids with very specific pores, often referred to as “molecular sieves”) although there are also cases of appropriately prepared metal membranes. Inorganic membranes are microporous, i.e. their selectivity is due to the existence of pores with very small dimensions that allow passage only on particles below a certain size (micromoles, macromolecules, colloidal particles, depending on the pore size of each membrane).

An example of polymeric membranes is that of non-conductive polymeric membranes. Inorganic membranes can be used mainly in gas mixture separation, and in particular for low molecular weight components, because there are higher diffusion rates, which makes the process more efficient. These membranes are advantageous in terms of heat resistance and chemical stability but are disadvantaged in cost and mechanical strength. Polymeric membranes have an advantage where inorganic ones are disadvantaged - and vice versa. They are suitable for processes that occur in milder conditions, especially with respect to temperatures that cannot rise to very high levels without decomposing the polymeric material. Although it is possible to form membranes with pores of various dimensions, so-called asymmetric non-porous, dense membranes are of particular interest. Their characterization as asymmetric is due to their peculiar structure of two layers with different characteristics. In general, dense non-porous membranes have a much lower permeability coefficient than microporous but, due to their very small thickness, the rate of diffusion per unit cross-sectional area can be very high.

In addition to asymmetric and elastomeric membranes, there are also membranes consisting of amorphous polymers whose glass transition temperature (Tg) is above ambient temperature.

In them, the permeability plays a primary role, while in elastomeric materials, the solubility is equally, if not more important. The relative stiffness that characterizes the structure of these amorphous polymers makes them similar in this respect to inorganic membranes, although in terms of static characteristics they resemble elastomeric membranes because they are amorphous materials. Thus amorphous polymeric membranes are more applicable to gas mixtures, mainly of low molecular weight such as e.g. for the separation of atmospheric air into oxygen and nitrogen. Elastomeric materials will serve in cases of heavier components or liquids. However, the distinction is not absolute and the chemical similarity between polymer and passing constituents plays an important role [12].

1.4 Transport phenomena through membranes

There are many historical references to the birth of membrane science, but all acknowledge that Thomas Graham in 1829 was the first person to observe gas transport phenomena. Thomas Graham observed that a deflated pig bladder could swell to a point until it burst if exposed to CO_2. He then suggested that CO_2 dissolves on the wet surface of the bladder and then enter its interior through capillary phenomena [13]. After 37 years, in 1866, and after experiments involving the enrichment of oxygen using natural rubber, Thomas Graham proposed a three-stage diffusion mechanism called “Colloidal diffusion”. This model is now known as the “solution-diffusion model”. Very generally this mechanism involves the adsorption of the diffusible molecule to the membrane followed by its diffusion into the membrane and desorption on the other side. During the diffusion step, Thomas Graham suggested that the diffused component behaves as if it were liquid. All this has led to the development of the solution-diffusion model, which is the basis for modelling molecular transport phenomena through many materials [14], [15].

The transfer of gases through materials by the effect of a pressure gradient on the two ends of the material can take place through two basic mechanisms:

1. Diffusion and flow of gas to the bulk material through the solution-diffusion model
2. Flow through material imperfections (heterogeneous, pinholes, porous, micro-channels, small fractures and grain boundaries)

In conclusion, the mechanisms for transfer of gases through polymeric membranes require complete characterization of the microstructure and knowledge of the permeability properties of the matrix. Before discussing the mechanisms in more detail, some basic concepts are outlined below. The properties of a membrane with respect to its gas permeability are usually characterized by: a) the transmission rate of the gas, defined as the volume of gas at standard conditions of pressure and temperature, passing through a region of the membrane per second divided by the pressure difference on both sides of the membrane and b) the permeability of the gas to steady state.

Therefore the mean permeability through a material is the steady state flow (J) divided by the pressure difference at both ends. In the case of homogeneous polymeric membranes, such as polymeric films, and for gases that do not interact strongly with the polymer, such as oxygen, permeability is an essential property of the membrane independent of polymer thickness and is called intrinsic permeability [14].

In general, the process of transferring gases and vapour through membranes or films is called permeation. The driving force is a diversification in chemical potential. In many cases it is simpler and just as appropriate to use a variation in concentration or pressure. This is very useful in permeability measurements, which represent reality, by applying a difference in partial pressures on both sides of the membrane. In various technological applications there is often interest in calculating the diffusion coefficient of an element (e.g. a gas) through a polymeric membrane under equilibrium conditions. The size used practically to quantify the mass transfer phenomena of a polymeric membrane is the Permeation P defined as:

$$P = \frac{(\text{Gas Quntity}) \cdot (\text{Membrane Thickness})}{(\text{Surface}) \cdot (\text{Time}) \cdot (\text{Pressure Drop})} \tag{1.1}$$

where the above relationship applies to the case of a gas permeator located under different partial pressures on both sides of the membrane. The process of transfer (sorption-diffusion-desorption) of a gas to a polymeric membrane is shown in Figure 1.9. The gas transport consists of the following steps:

1. Adsorption of the gas to the surface of the membrane
2. Diffusion of gas into the polymeric membrane
3. Desorption from the surface of the opposite side of the membrane

To simulate, atomically, the overall phenomenon of gas flow in a polymeric membrane, is

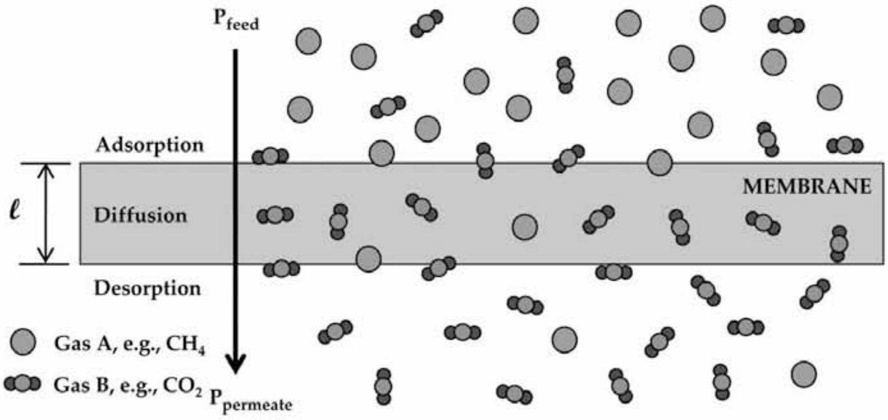

Figure 1.9: Sorption-diffusion-desorption process [16].

impossible as it exhibits a very slow time evolution compared to the achievable simulation times. Also the sorption/desorption process requires information on the polymer surface which most of the times is not available. The solubility of a gas-penetrator in a polymer depends on the nature and intensity of the polymer-penetrator interactions relative to the corresponding polymer-polymer and penetrator-penetrator as well as the number, size and distribution of the accesible cavities that are formed along the chains in which the gas molecules may remain. The dual-mode sorption model is one that gives a satisfactory description of the solubility dependence of concentration or pressure on a glassy polymer. According to this model, there are two distinct molecular populations that make up the gas within the polymer: (a) molecules dissolved in the polymer by the usual Henry procedure and their C_D concentration is linearly proportional to pressure, and (b) C_H gas concentration molecules which are dissolved in a limited number of given pre-existing cavities within the polymeric matrix. The concentration of C_D depends on the pressure p through the relationship:

$$C_D = Hp \tag{1.2}$$

where H is the Henry constant. The C_H concentration is given by:

$$C_H = C_\infty \frac{bp}{1+bp} \tag{1.3}$$

that is, the Langmuir-type relation where C_∞ is the saturation constant and b is the affinity constant. The total concentration C of dissolved gas at a given pressure p is given by the sum of Equations 1.2 and 1.3

$$C = C_D + C_H = Hp + C_\infty \frac{bp}{1 + bp} \tag{1.4}$$

The dual sorption model applies to a large number of gases and polymers, but in the case of large molecules at high concentrations structural and dynamic changes in the polymer matrix due to the presence of gas are introduced and different models should be used. For the adsorption of gases on elastic polymers it has been experimentally shown that the Langmuir part of the equation (1.4) can be removed and Henry's law applies even to pressures of hundreds of atmospheres [17]. Solubility S is related to the excess free energy of a gas dissolved in the polymer by the following relation:

$$S = \exp\left(\frac{-\mathit{\Delta} G}{k_B \cdot T}\right) \tag{1.5}$$

where $\mathit{\Delta} G$ is the potential difference, k_B is the Boltzmann constant and T is the temperature.

The diffusion of a gas penetrator into the amorphous polymeric matrix is governed by the molecular size of the penetrator and its interactions with the polymer as well as by the shape, size, distribution and connectivity of the dispersed portions of the accessible volume of the system. At high temperatures (well above the glass transition temperature Tg (below Tg the polymer behaves like glass e.g. it is tough and stiff) the polymeric matrix performs local thermal motions which redistribute its accessible volume and connectivity by creating and/or removing free cavities. In these thermal movements of the polymer chains the intracellular molecule is entrapped and often (relatively) moves to new positions. Accordingly, diffusion consists of a large set of small, local, and random motions of the molecule. In the case of low temperatures the diffusion mechanism in glassy polymers is much more complex [18], [19]. In this case the polymer matrix is more or less clogged and the distribution of its free cavities is permanent. The main characteristic of diffusion in glassy polymers is that the gas molecule spends most of its time trapped in a free-volume cluster and rarely travels to a neighbouring cluster via a channel that is opened instantly due to thermal disturbances in low density or kinetic regions. The diffusivity in glassy polymers is orders of magnitude smaller than the corresponding melt and depends on the number, the connectivity of the free volume cavities as well as the distribution of constant rates that determine the transitions between them [14], [17].

1.5 Types of Diffusion

Diffusion is called the mechanism of transfer of molecules (identical or different) inside the mass of a material due to their thermal excitation. The effect of diffusion is to mix molecules of similar or different substances through their random thermal motion. Following is a brief description of the diffusion types [20].

Self-diffusion: According to the IUAPAC definition, the self-diffusion coefficient is the diffusion coefficient (D_i^*) of the i-th (i) number of species when the chemical potential equals zero. It is related to the diffusion coefficient (D_i) by the relation:

$$D_I^* = D_i \frac{\partial(lnC_i)}{\partial(ln\alpha_i)} \tag{1.6}$$

where α_i the activity of the species in solution and C_i the concentration of species (i).

Substitution diffusion: It refers to the crystalline solids and is the transfer of foreign atoms or voids (holes) to the matrix positions of the crystalline matrix. In this case, the size of foreign and maternal atoms is approximately the same, and the mechanism is greatly facilitated by the existence of gaps in the original mesh. In general, atoms and voids flow as the diffusion progresses.

Interstitial diffusion: It is the transfer of aliens to the extracellular positions of the crystalline matrix. Typical examples of the various types of diffusion are shown in Figure 1.10.

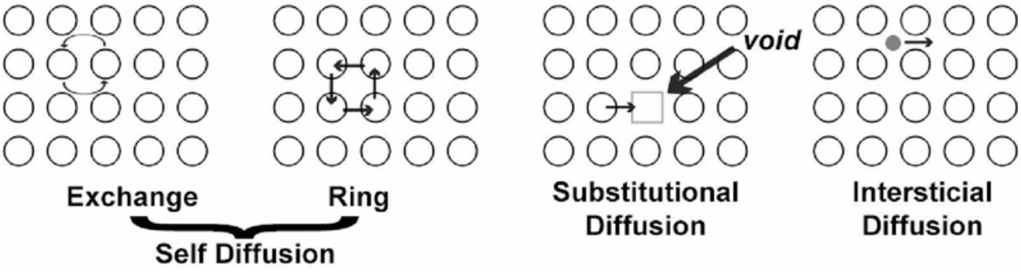

Figure 1.10: Diffusion type in crystalline solids.

1.5.1 Diffusion mechanisms

In substitutional diffusion and self-diffusion, individuals can move from one position to another if the energy derived from their thermal action exceeds their activation energy q (Figure 1.11). The existence of voids or defects in the grid while increasing the temperature facilitates this movement. The activation energy in the self-diffusion and substitutional diffusion is equal to the sum of the energy required to create a void and the energy to move it. On the other hand, in the diffusion of substitution, smaller atoms move from the parent atoms to one of the extracellular sites without any permanent movement of the matrix atoms [22]. Consequently, the required activation energy in the substitution diffusion is less than that of the diffusion or filling in grid gaps.

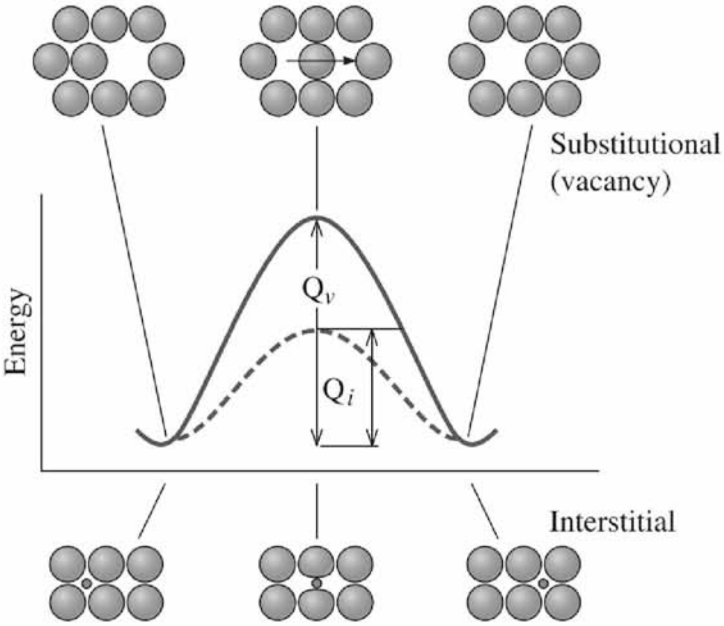

Figure 1.11: Changes in the oscillating energy of atoms [21].

1.6 Fick's Laws of Diffusion

This kind of diffusion phenomenon is mathematically described by Fick's laws and for this to occur the concentration of the diffuse element in the direction of mass transfer must have a gradient, as shown in Figure 1.12. A general definition of Fick's laws could be that the first law refers to diffusion under time-constant conditions, while the second law describes the diffusion under time-varying concentration conditions.

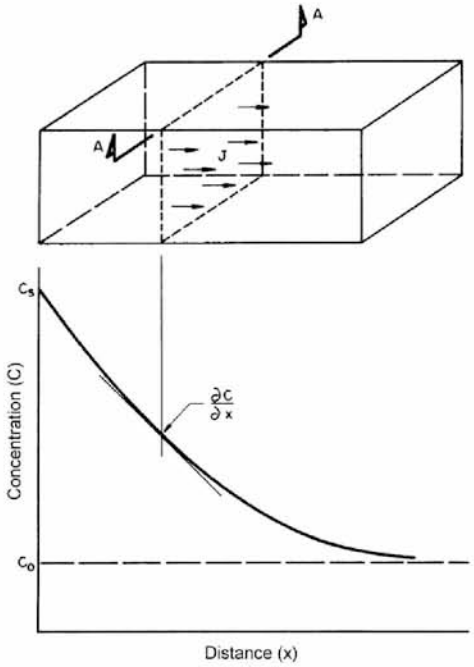

Figure 1.12: Diffusion and diffuse element concentration gradient

1.6.1 Fick's First Law

Adolf Fick proposed that, in a one-dimensional system, the flux is proportional to the concentration gradient and it can be described by the following relation [23], [24]:

$$J = -D \cdot \frac{\partial C}{\partial x} \tag{1.7}$$

where:

1. J is the flux (mol/m^2s).
2. D is the diffusion coefficient or diffusivity (m^2/s).
3. C (for ideal mixtures) is the concentration (mol/m^3).
4. x is position (m).

The flux J is defined as the number of atoms passing through a plane of unit area per unit time and the negative sign indicates that the diffusion is opposed to the concentration gradient, i.e. from high to low concentration areas of the diffusing species, as shown in Figure 1.13.

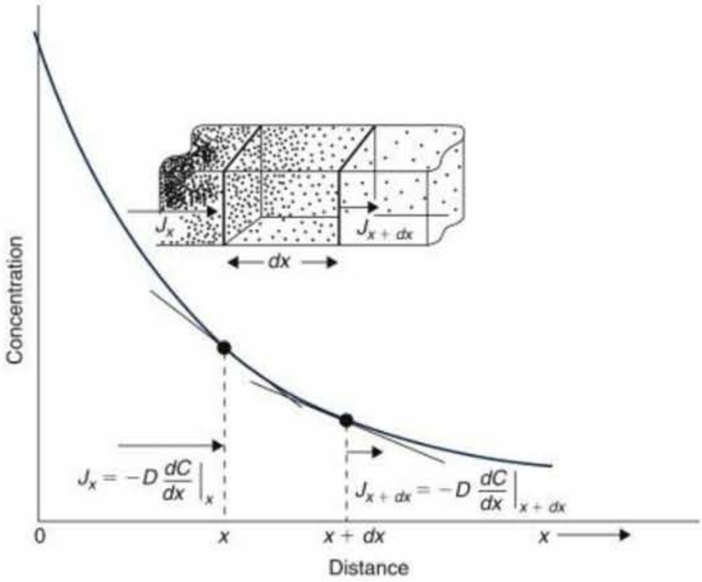

Figure 1.13: Fick's First Law - Diffusion of atoms from a surface into the bulk of a material [25].

1.6.2 Fick's Second Law

The time variation of the concentration, at each point of the solution, is proportional to the spatial variation of the flux (J) and is given, under constant diffusion coefficient, by the following equation:

$$\frac{\partial C}{\partial t} = D \cdot \frac{\partial^2 C}{\partial x^2} \tag{1.8}$$

where:

1. C is the concentration (mol/m^3).
2. t is time (t).
3. D is the diffusion coefficient (m^2/s).
4. x is the length (m).

In steady state the Equation 1.8 can be written as:

$$\frac{d^2C}{dx^2} = 0 \quad \rightarrow \quad \frac{dC}{dx} = const. \tag{1.9}$$

By combining Equation 1.7 and 1.9 we get:

$$J = -D \cdot \frac{dC}{dx} = -D \cdot \frac{\Delta C}{\Delta x} = -D \cdot \frac{C_{out} - C_{in}}{l} \tag{1.10}$$

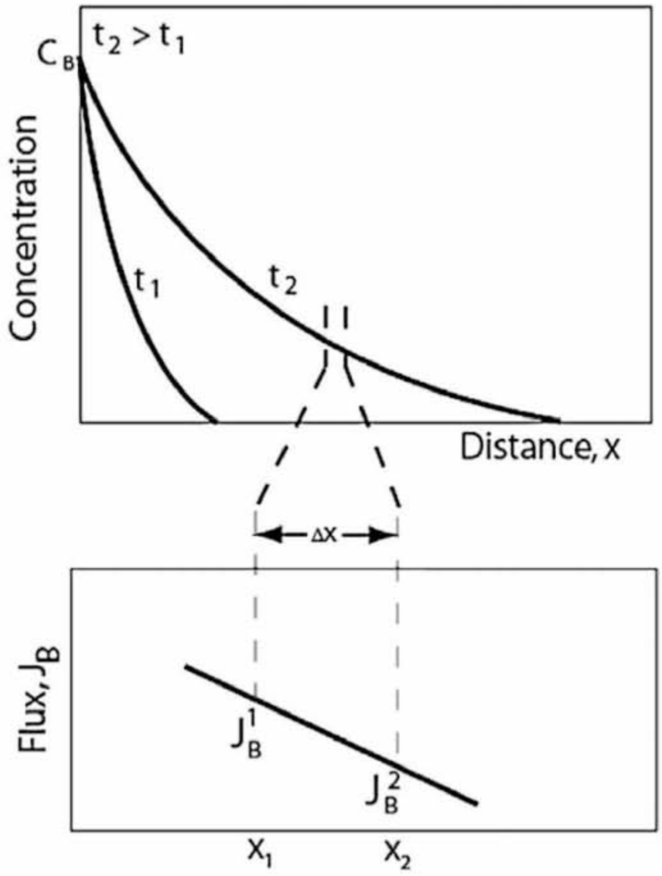

Figure 1.14: Non-steady-state diffusion profile and explanation of the derivation of Fick's second law [23].

Considering that from Equation 1.4 we can maintain as a good approximation (for low concentrations and small molecules) only the linear term (according to Henry) of the right, we have:

$$C_{out} = Sp_{out} \quad \text{and} \quad C_{in} = Sp_{in} \tag{1.11}$$

By combining Equations 1.10 and 1.11 we get:

$$J = D \cdot S \cdot \frac{p_{in} - p_{out}}{l} \tag{1.12}$$

In Equation 1.12 the product of the Diffusivity (D) to the solubility (S) defines the permeability (P) and we get:

$$J = P \cdot \frac{\Delta p}{l} \tag{1.13}$$

In fact the permeability is controlled by the dissolution and diffusion steps. The diffusion coefficient D, is a measure of the movement speed of the diffusible molecules in the polymer while the diffusion coefficient S, is an indication of the number of penetrated molecules diffused. The two coefficients together describe the coefficient of penetration, commonly called permeability P.

$$P = D \cdot S \tag{1.14}$$

In conclusion, a direct calculation of the permeability from Equation 1.1 can be avoided and the permeability can be described by the “sorption-diffusion” mechanism using the Equation 1.14. A basic understanding of the diffusion phenomenon can help distinguish the insulation characteristics of polymers. A diffusible molecule moves to a barrier surface by a multi-step process where the molecule first contacts the polymer surface. In the polymer, the molecule that penetrates diffuses randomly as its own thermal kinetic energy keeps it in motion from vacuum to vacuum, between the macromolecular chains of the polymer. This random diffusion results in the (macroscopic) movement of the diffuser toward the polymer side in contact with a high concentration of the diffuser in the contact side with a low concentration of diffuser.

1.7 Description of diffusion models

1.7.1 Solution-Diffusion model

The solution diffusion model is widely accepted as the primary model for describing transport phenomena in relation to chemical potential differentiation and relates to processes such as dissolution, reverse osmosis, gas permeability and more. These different modes of diffusion can be transformed into other more practical ones by changing the chemical potentials with measurable forces. This is achieved by using basic thermodynamic principles that relate the differentiation of chemical potentials to pressure, temperature, concentration and electrokinetic forces. Therefore, in the case of gas permeability, the differentiation of the chemical potential may be related to the differentiation of the gas concentration within the membrane. This model assumes that the pressure within the membrane is uniform and that the variation of chemical potential along the membrane can only be expressed as a function of concentration. When these conditions are met then the Solution-Diffusion Model can be used to calculate the mass flow rate of a gas through a dense membrane [17].

The mass flow rate can be defined as the amount of material passing through a section of the membrane over a specified period of time. When using the chemical potentials and Fick’s first law to describe gas permeability, it is easily understood that the system is in equilibrium. The permeability of gases can be simplified by considering one-dimensional flow. The one-dimensional assumption holds because differences in diffusion and concentration in the other directions are negligible [26].

Due to the uniformity of the surface concentration, there is no differentiation in the other directions. When all these assumptions are used, then the description of the gas transport effect can be described by the following equation:

$$J_i = -L\nabla\mu_i \cong -L_i\frac{\partial\mu_i}{\partial x} \tag{1.15}$$

1.7.2 Time-Lag method

The time lag is the time required for a gas to penetrate a membrane. It can be calculated using differential or integral techniques based on permeability or absorption rate data. According to the integral technique, the accumulation of gas in a space that has previously been evacuated over time is measured. This space is separated from the gas source by a membrane which has previously undergone degassing (removal of the gases inside it). A typical example of an experimental measurement for a gas permeability is shown in the following Figure 1.15.

Time Lag is defined as the point where the pressure is equal to zero, that is, where the extension of the straight line of the graph meets the x-axis of time (point i in the diagram). The reference curve is divided into two regions, the former referring to steady-state diffusion and the linear part being its reference curve. The second region is the unsteady-state diffusion region and refers to the initial pressure increase [18]-[26].

1.8 Barrier Improvement Factor - BIF

Concerning the very important part of the composite membranes, which we study in the present work, we can say that as a result of the dispersion of the flakes in the polymeric matrix, materials with improved insulating properties are produced since the existence of the flakes causes an increase in the distance traveled by the diffuse species through the membrane. This degree of difficulty depends on the loading rate of the reinforcing agents as well as on some characteristics, such as their size and orientation within the matrix and the overall effect is described by the

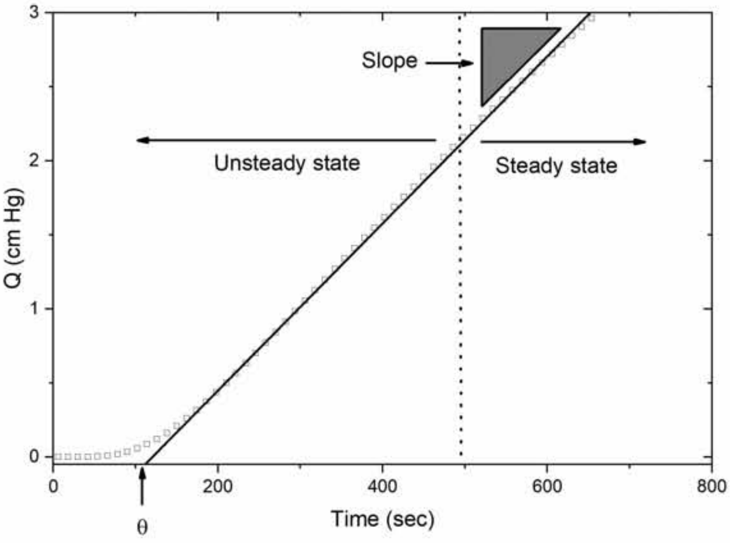

Figure 1.15: Schematic representation of the gas permeation process using the integral technique

Barrier Improvement Factor (BIF). Therefore this coefficient is used to quantify the effect of the flakes on the membrane barrier properties. Figure 1.16 schematically illustrates the increase in the distance travelled by the dispersed molecules through the composite polymer when flakes are present. It is not possible for any molecule to pass through the flakes as the flakes are impermeable. The Barrier Improvement Factor (BIF) has been used in a number of literature

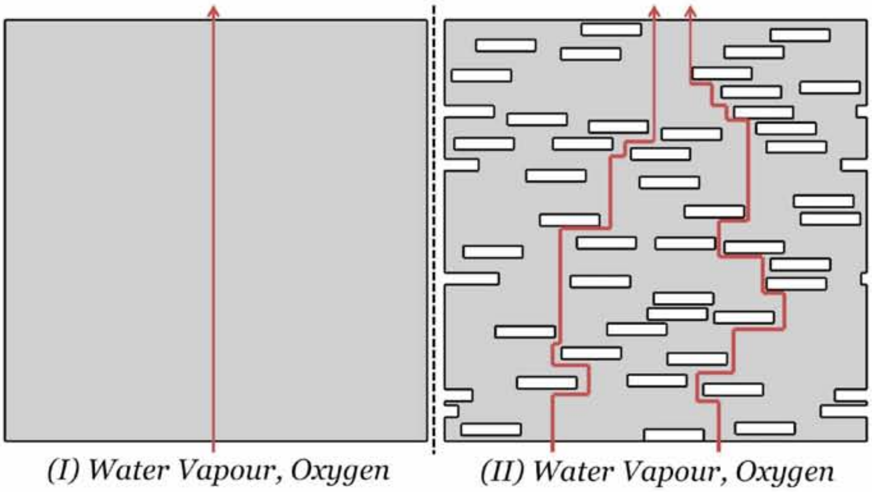

Figure 1.16: Path comparison between a membrane with no flakes and a membrane that includes flakes. The difference is obvious between the two materials.

references to study the permeability of gases through composite or simple polymeric materials and to describe their barrier properties. The final measurement which shows us the effectiveness of reducing the permeability of a polymeric membrane equals the permeability of the original polymer to the permeability of the composite polymer. So the Barrier Improvement Factor (BIF) can be defined as P_0/P_f and it turns out to be expressed also from the fractions D_0/D_f and J_0/J_f given that solubility S does not change and the conditions remain the same during diffusion both in the pure polymer and in the composite membrane.

To differentiate the starting state (pure polymer) from the composite membrane (polymer in the presence of flakes) we use the index *(0)* and *(f)*, respectively, for each membrane and the definition of BIF that we use in the present work is

$$BIF = \frac{D_0}{D_f}, \quad D_0 > D_f, \quad (BarrierImprovementFactor > 1) \tag{1.16}$$

Finally, we can say that an additional utility of (BIF) is that it allows the comparison of the results of the barrier properties of composite polymeric membranes with random and aligned distributions of flakes as we will see later in this work.

1.9 Flake characteristics that affect the BIF

1.9.1 The effect of flake length

The degree of difficulty of arranging the flakes inside the polymer increases with increasing length, as we will see in the geometry generation because the space available is limited and is further reduced when large flakes get random orientations. This problem is typical and is presented in the next chapter where some of the examples of geometries we have studied in this work are presented in detail. Composite membranes are distinguished in those in which the size (length) of the flakes is not different, and in those in which their size varies. In Figure 1.17 we can see pictures depicting the two aforementioned categories of composite membranes.

1.9.2 The effect of flake orientation

The orientation of the flakes in a polymeric matrix, their concentration, and their distribution play a key role in the properties of the composite. In terms of orientation there are two extreme arrangements: (1) parallel alignment of the flakes with one axis, and (2) completely random arrangement. For high loading rates ($\phi > 20\%$) some problems arise in the construction of the composite, since the flake cannot be fully covered by the matrix material for geometrical

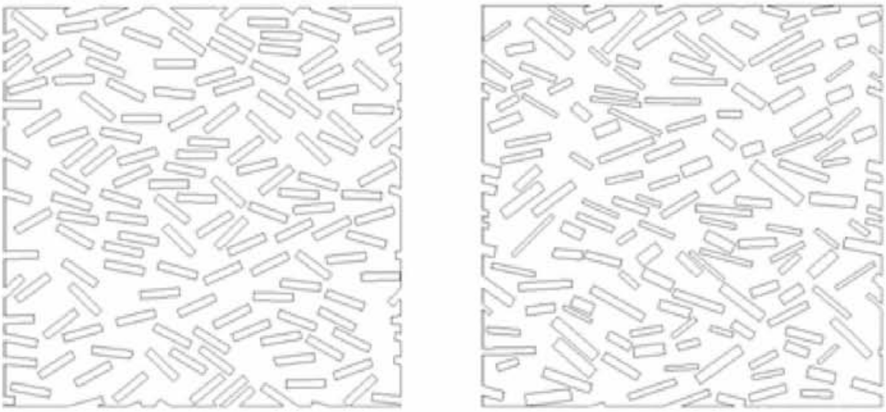

Figure 1.17: Membrane classes by size of (a) fixed length, (b) variable length and thickness

reasons. Many times, not only one type of flake is used to enhance the matrix but a mixture of two or more types. These are called hybrid composites [1].

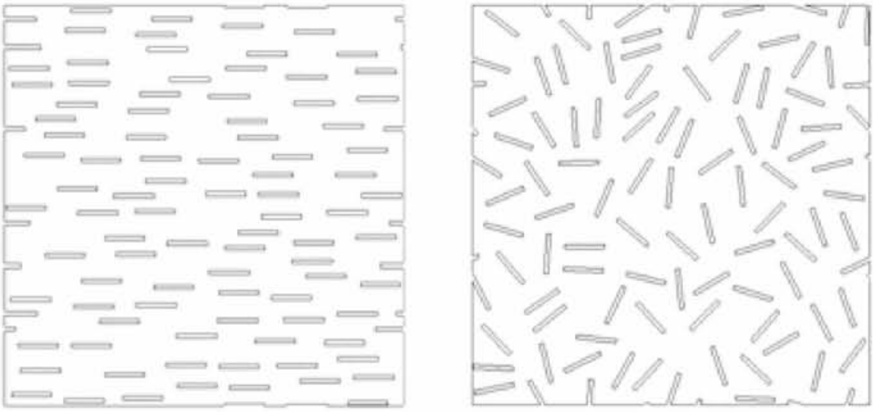

Figure 1.18: Flake distribution of flakes in polymeric matrix composites: (left) continuous and aligned flakes, (right) discontinuous and randomly oriented flakes.

1.10 References

1. Xiaoming Chen and T.D. Papathanasiou, Barrier Properties of Flake-Filled Membranes: Review and Numerical Evaluation, Journal of Plastic Film & Sheeting, Volume 23, `https://doi.org/10.1177/8756087907088437`
2. Jane Kucera (2015). Reverse Osmosis: Industrial Processes and Applications, 2nd Edition, John Wiley & Sons, Inc
3. Callister, W. D., & Rethwisch, D. G. Fundamentals of materials science and engineering: An integrated approach. Hoboken, NJ: John Wiley & Sons (2008).
4. Petra Pötschke, T.D. Fornes, D.R. Paul, Rheological behavior of multiwalled carbon nanotube/polycarbonate composites, Polymer, Volume 43, Issue 11, 2002, `https://doi.org/10.1016/S0032-3861(02)00151-9.`
5. N. G. McCrum, C. P. Buckley and C. B. Bucknall, Principles of polymer engineering, Oxford University Press, New York, (1989)
6. G. Papanikolaou, D. Mouzakis, Composite Materials, Kledarithmos Publications , (2007).
7. K. Panagiotou, Polymer Science and Technology, CRC Press (2000).
8. Flinn Richard A. and Trojan Paul K., Engineering Materials and Their Applications", 4th edition, John Wiley & Sons, Inc (1990),
9. Giles F. Carter and Donald E. Paul, editors, Materials Science and Engineering, A S M International (1991).
10. Müller-Plathe, F. Diffusion of water in swollen poly(vinyl alcohol) membranes studied by molecular dynamics simulation (1998) Journal of Membrane Science, 141 (2), pp. 147-154, DOI: 10.1016/S0376-7388(97)00289-5
11. J. G. A. Bitter. Transport Mechanisms in Membrane Separation Processes. Plenum press, New York (1991)
12. Fredrickson, G.H., Bicerano, J. Barrier properties of oriented disk composites (1999) Journal of Chemical Physics, 110 (4), pp. 2181-2188
13. Jaime Wisniak, Thomas Graham. II. Contributions to diffusion of gases and liquids, colloids, dialysis, and osmosis, Educación Química, Volume 24, Supplement 2, Pages 506-515 `https://doi.org/10.1016/S0187-893X(13)72521-7`
14. Bharadwaj, R.K. Modeling the barrier properties of polymer-layered silicate nanocomposites (2001) Macromolecules, 34 (26), pp. 9189-9192.

15. D.R. Paul, L.M. Robeson, Polymer nanotechnology: Nanocomposites, Polymer, Volume 49, Issue 15, 2008, Pages 3187-3204, ISSN 0032-3861, `https://doi.org/10.1016/j.polymer.2008.04.017`
16. Perez, E.V.; Karunaweera, C.; Musselman, I.H.; Balkus, K.J.; Ferraris, J.P. Origins and Evolution of Inorganic-Based and MOF-Based Mixed-Matrix Membranes for Gas Separations. Processes 2016, 4, 32.
17. Hofmann, D., Fritz, L., Ulbrich, J., Schepers, C., Bhning, M. (2000), Detailed-atomistic molecular modeling of small molecule diffusion and solution processes in polymeric membrane materials Macromolecular Theory and Simulations, 9 (6), pp. 293-327.
18. J. G. Wijmans, R. W. Baker, The solution-diffusion model: a review, Journal of Membrane Science 107 (1995) 1-21.
19. Hanika, M., Langowski, H.-C., Moosheimer, U., Peukert, W. Inorganic layers on polymer films - Influence of defects and morphology on barrier properties (2003) Chemical Engineering and Technology, 26 (5), pp. 605-614.
20. W.F. Smith, Foundations of Materials Science and Engineering 3rd ed., McGraw-Hill (2004).
21. Askeland D.R., Wendelin J. Wright. The Science and Engineering of Materials. Springer, Boston, MA (2016)
22. Jean Philibert, One and a Half Century of Diffusion: Fick, Einstein, before and beyond, Diffusion Fundamentals 2, (2005).
23. Aloke Paul, Sergiy Divinski (editors). Handbook of Solid State Diffusion: Volume 1, 1st Edition, Elsevier (2017)
24. A. Fick, Annalen der Physik 170 (1855) 59
25. Traugott Fischer. Materials Science for Engineering Students, Elsevier Inc (2009)
26. C. J. Cornelius, PhD. Thesis, Virginia (2000), Physical and gas permeation properties of a series of novel hybrid inorganicorganic composites based on a synthesized fluorinated polyimide.

Chapter 2

Geometry generation in 2D. A novel FastRSA algorithm: Statistical properties and evolution of microstructure[1]

Summary

In this chapter we deal with the creation of 2D geometries that were used in this work. Specifically we describe the RSA (Random Sequential Adsorption) algorithm which is used extensively for the creation of geometries not only for these types of problems but in numerous other applications as well. We also deal with the problem of the asymptotic nature of the algorithm which becomes a problem especially as $\alpha = l/t$ (the aspect ratio of a flake) is increased. We developed an algorithm (FastRSA) which can create high packing geometrical configurations in a much shorter time compared with traditional RSA algorithms especially when used with particles of large α. We also examine, with the use of this algorithm and its ability to create such configurations, the way the statistical properties evolve during the process and we use that calculation for determining an accurate estimation of the maximum packing that can be achieved. Also we shed light to the mechanisms of the formation of nematic structures as they appear in high

---

[1] As published in Physica A: A. Tsiantis, T.D. Papathanasiou, A novel FastRSA algorithm: Statistical properties and evolution of microstructure, Physica A: Statistical Mechanics and its Applications, Volume 534, 2019, 122083, ISSN 0378-4371, `https://doi.org/10.1016/j.physa.2019.122083`

packing configurations and we also introduce and use the concept of the probability field that is created around each particle.

In the beginning of the chapter we introduce the mathematical background behind the RSA process and we describe the key areas that are formed around a particle and their interactions. Then we describe the RSA and FastRSA algorithms (Figure 2.1). Their difference lies in the introduction of an extra step that calculates and uses the space properties around each particle. By using this information we are able to overcome the slow convergence of the algorithm to a high count configuration. After that we use the FastRSA algorithm for determining the space properties and their interactions. We show how space is polarized by the presence of particles and we reveal the mechanisms behind their interactions. We show that these interactions determine the creation of RSA configurations and their statistical properties mainly the formation of nematic structures and the degree of packing.

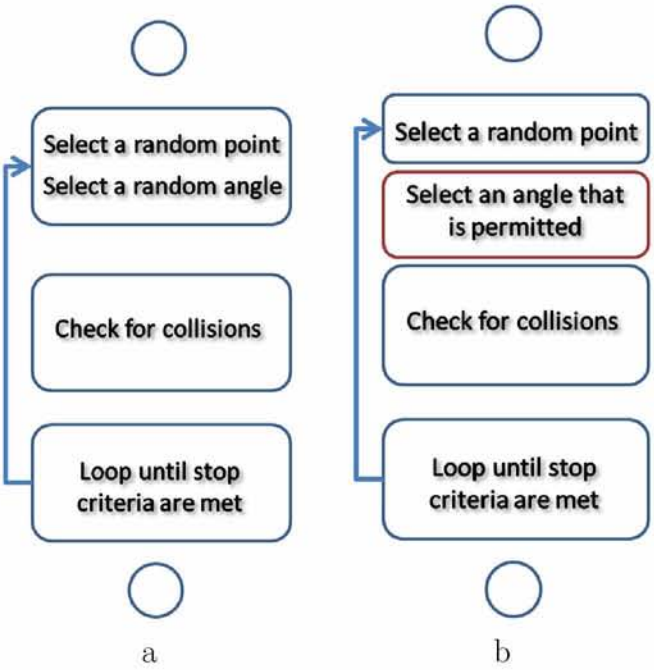

Figure 2.1: (a) RSA algorithm, (b) FastRSA algorithm. The difference between the two algorithms is the extra step in FastRSA which can calculate the probability of placing a particle.

The use of FastRSA has enabled us to create high density packings in reasonable cpu time and also it can give us the ability to examine the statistical properties of such configurations since we can calculate precisely all the corresponding probabilities that define them. Also we describe the mathematical background that governs the RSA process by looking in to the geometrical details and interactions between particles in such geometries. The ability of

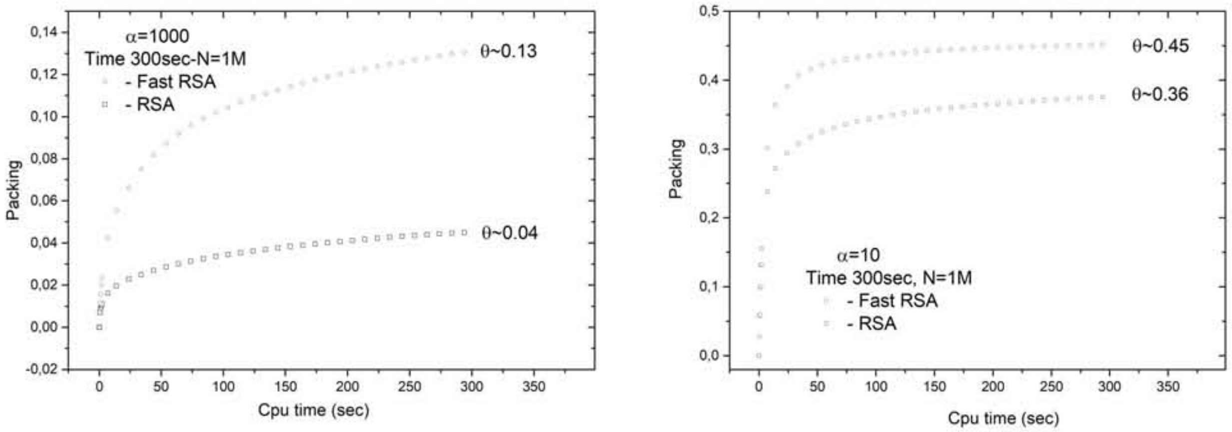

a

b

Figure 2.2: Achieved packing at various α using the two algorithms. (a) $\alpha = 1000$ (b) $\alpha = 10$. In (a) the packing achieved with RSA (0.04) at 300sec is achieved in the first 10 seconds with FastRSA (x30 speed-up). Similarly in (b) the speed-up is x15.

FastRSA to examine the space properties has enabled us to describe accurately and discuss the evolution of microstructure, especially the creation of nematic structures. We provide estimates of the maximum packing which we compare with published results. Finally besides an accurate estimation of maximum packing for various α also we show the difference in speed between the two algorithms as it can be seen in Figure 2.2.

2.1 Abstract

While the Random Sequential Adsorption (RSA) process for the generation of 2D geometries containing discrete entities has been extensively studied, both in terms of numerical simulations and in terms of its statistical properties, all the mechanisms involved are not fully understood, especially in dense configurations of elongated particles. This is mainly due to the very slow asymptotic approach to high packing configurations, especially when highly elongated particles are involved, which makes the creation of such configurations a time consuming task. For the estimation of the statistical properties of such configurations we therefore have to resort to extrapolations that do not always give accurate results. In this work we reveal the interaction of the mechanisms that come into play in the RSA process. We specifically show that the overall result of an RSA process is the summary outcome of these interwoven mechanisms, namely those involving the formation and destruction of Particle Area, Overlap Area and Influence Area – terms which we introduce and define in this work – resulting in a behavior that often appears counter-intuitive. We also show the shift of their importance as the particle aspect ratio α varies and explain how nematic structures are created when high aspect ratio particles are involved as well as the mechanisms behind their appearance. Following this, we propose a new algorithm for the process of random sequential adsorption (named FastRSA) which is capable of creating very high count configurations through all the range of particle aspect ratios and which follows Feder's law with a $\theta \sim \tau^{-1/2}$ behavior instead of the $\theta \sim \tau^{-1/3}$ of the classic approach, where τ is the number of attempts to place a particle and θ is the degree of packing. We show how the new algorithm can be coupled with the classic RSA approach and point out the benefits of such a coupling. Use of the FastRSA algorithm has enabled us to study the evolution of the extent of packing using actual geometries, without the need to resolve to extrapolations and assumptions. For the case of highly elongated particles, this is the first time in our knowledge that estimations of maximum packing from actual configurations near the jamming limit have been obtained.

2.2 Introduction

Random Sequential Adsorption (RSA) is a process by which geometrical entities (particles) are randomly and sequentially added on a substrate of surface A, with the requirements that

(i) no repositioning of an entity occurs after it has been placed and (ii) no overlap between entities occurs. The RSA process has been adequately described in the literature [1], [2], [3], [4] for various cases and geometries in 1D, 2D and 3D geometries, and is extensively used for the modelling of chemical reactions [5], in biology [6], [7] and in a variety of problems involving packing and packing estimations. Also much work has been done studying various aspects both in special case of geometries [8] or in an attempt to shed light to the statistical background [9] or special spatial properties [10] of RSA configurations. Recently new methods for more precise estimations of maximum packing have been introduced [11], [12]. In brief, the process of creating such a particle configuration involves the selection of one random point C_P with coordinates (C_X and C_Y) and a random angle ω and the subsequent placement of a particle at that point with the selected orientation angle. If the thus placed particle overlaps with any of the previously deposited particles, this attempt (C_X, C_Y, ω) is rejected, the newly added particle is removed and the process starts again with a different set of random coordinates and angle. The process stops when no more particles can be added, at which point the configuration is considered to have reached the 'jamming limit - θ_J' which is defined as the area occupied by particles divided by the total available area, at the end of the RSA process. In practice, the RSA process stops after a predefined number of placement attempts (or elapsed CPU time) is reached. A result of the statistical nature of the RSA process and especially of the fact that it follows Feder's law [4], namely that the achieved packing scales with a (negative) power of the number of placement attempts, is that the difficulty of placing additional particles increases dramatically as the RSA process evolves. As a result it is practically impossible to achieve high density and high count configurations, especially when elongated particles are used such as, for example, in fibrous composites [13]. One consequence of this is that multi-particle, direct simulations (such as transport phenomena or elasticity) in heterogeneous materials at very high packing densities have to-date been impossible to carry out, even though there are numerical schemes which could make such simulations possible [14]. An additional consequence of this state of affairs is that existing estimates of the ultimate packing densities achieved by an RSA process are not the result of actual simulations that have actually reached the jamming limit, but are instead extrapolations and therefore uncertain. This is especially true for elongated particles, such as rod-like macromolecules, viruses, fibers etc. Earlier computations have shown [15], [16], [17] that, using the classic RSA approach the evolution of packing scales with a power of (τ), typically $\theta_J \sim \tau^{-1/3}$ where τ is the number of (successful or not) placement attempts.

Swedsen [2] has proposed that the exponent in the above relationship between packing and placement attempts is (-1/d), where (d) is the dimensionality of the problem. In this work we will try to clarify these results and to provide some insight into observed discrepancies.

We deal with square and elongated rectangular particles of length=l and width=t and various aspect ratios $\alpha = l/t$ ranging from 1 (randomly oriented squares) to more than 10^3 (fiber-like elongated rectangles) and develop a new algorithm for the sequential adsorption process (named FastRSA in the rest of the manuscript). This algorithm is shown to offer a significant improvement in speed over the traditional RSA, by operating on the full scale of probabilities at any given candidate point of an area A. It belongs to the family of algorithms that are used to find the visibility polygon from a point, a significant problem in computer graphics [18], where such algorithms are used for faster rendering of 3D scenes. We show that the proposed FastRSA algorithm achieves significantly higher packing densities at realistic execution times and also that it follows Feder's law with $\theta_J \sim \tau^{-1/2}$.

2.3 Geometrical definitions and formulation

Consider one particle (as part of a multi-particle assembly) placed at point C with its elongated axis at an angle ω_e and a candidate particle at point C_P with its elongated axis forming an angle ω_n with the horizontal, as shown in Figure 2.3. Any attempt to place a new particle in such an assembly will be unsuccessful if the new particle overlaps with pre-existing ones. Existence of such overlaps is not random, but for a given set of C and C_P and angles ω_e and ω_n, depends on the relative position and the relative angle $\omega = \omega_e - \omega_n$ between the new particle (subscript n) and the pre-existing one (subscript e). If we plot the space comprised of all points where a new particle cannot be placed with respect to a pre-existing particle, at all levels of the relative angle $\omega = \omega_e - \omega_n$, we form the highlighted polygonal areas shown in Figure 2.3. These polygons are the result of the Minkowski Sum [19] between the pre-existing particle P and the new particle $B\omega_n$. The Minkowski Sum is defined as the locus of points satisfying

$$P + B := p + b : p \in P, \quad b \in B \tag{2.1}$$

and can be described briefly as the polygon that is created if we define as P the already placed particle and B the newly arrived particle with its center at a random point C_P. For every pre-existing particle P we can define the corresponding set of polygons M for $\omega \in [0, \pi]$ (due to symmetry, the polygons at angle ω are equal to $-\omega$), as:

$$M = \sum_{\omega=0}^{\omega=\pi} [P + B_\omega := p + b : p \in P, \quad b \in B_\omega] \tag{2.2}$$

where P is an already placed particle and B_ω is a new particle at point C_P and relative angle ω. By using the above definitions we can now define the probability of successfully placing a new particle at point C_P with a relative angle ω as

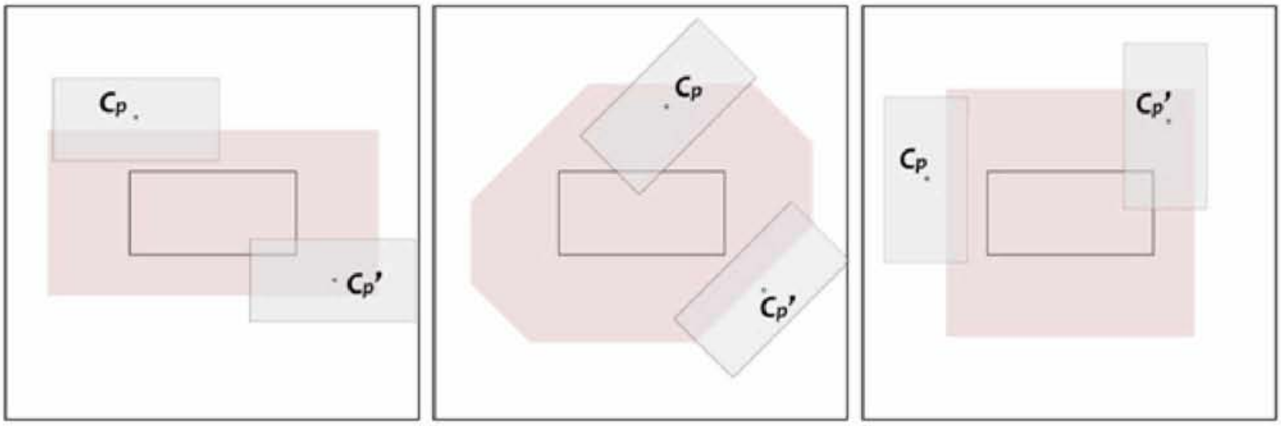

Figure 2.3: Placement of new particles of relative angle ω and their relation with the corresponding Minkowski polygon. Particles with center point inside the Minkowski polygon intersect with the pre-existing particle while new particles with their center point outside do not intersect. (left) $\omega = 0^o$, (middle) $\omega = 45^o$, (right) $\omega = 90^o$

$$p = 1 - \frac{| M' |}{| M |} \tag{2.3}$$

where M is the set calculated from Equation 2.2 and M' is the subset of Minkowski polygons that C_P resides in. Using the above result, we can define the following three areas that are formed around a particle as

1. The Overlap Area (A_O) as the area of points outside of a particle where $p = 0$,
2. The Influence Area (A_I) as the area where $0 < p < 1$ and
3. The Particle Area (A_P) as the area inside the particle for which also $p = 0$.

We can define geometrically the above areas by saying that the Overlap Area (A_O) is the area that extends from the boundaries of the particle to a distance $t/2$ and the Area of Influence (A_I) extends from the boundary of the overlap area up to a distance $R = 1/2\sqrt{l^2 + t^2}$ from the particle's boundaries (Figure 2.4a). We see that every point in the Overlap Area belongs to every polygon that is created as the result of the Minkowski sum, that is $\forall B_\omega, C_P \in B_\omega$ as seen in Figure 2.4b. This is also easily derived from geometry since every point C_P that has a distance smaller than $t/2$ from a pre-existing particle will inevitably collide with it. Similarly, the points in the Influence Area belong to some but not all the polygons of set M.

From the above definitions it becomes easy to draw a conclusion for the acceptance or rejection of a candidate point for the placement of a new particle; if the point C_P lies within the Minkowski polygon that is constructed from a pre-existing particle (P) and a candidate particle at point C_P and angle ω (B_ω), then this candidate point is rejected for particle placement using this angle. In the case however that the point resides in the Influence Area, successful particle placement may be possible at this point, using a different angle ω'.

Such a calculation, even though it seems intuitively easy, is of no practical use due to the sheer amount of geometrical calculations that need to be performed for every $\omega \in [0, \pi]$. We can however speed it up if we notice that we do not have to test against all the combinations of angles and polygons but instead we can check only for specific key angles that are formed between the new center point and an existing particle. We describe this procedure in the following section and we see that by calculating a visibility polygon from point C_P we can calculate the available arcs that allow for the placement of a newly arrived particle.

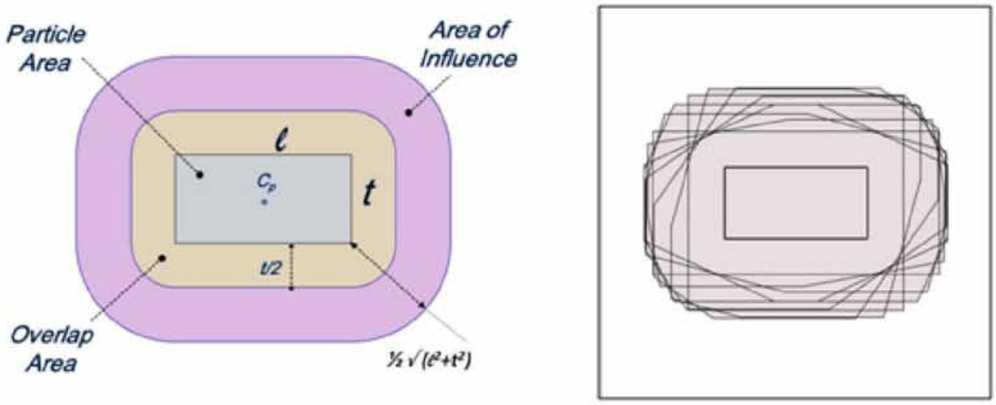

Figure 2.4: (left) Geometrical characteristics of area around a particle with length l, width t and $\alpha = l/t = 2$. (right) Minkowski polygons of set M as defined in Equation 2.2. The outline of Overlap Area and Interaction Area is easily seen. The number of drawn polygons in the right image is small for visual clarity

2.4 Computational

Visibility polygon algorithms consist of two phases - a broad phase and a narrow phase [18]. The broad phase is used to massively filter out elements -in our case particles- which are away from the neighborhood of the point of interest C_P; this is a first elementary step in speeding up calculations. During the narrow phase, we only deal with the elements that are near the area of interest. In the context of the FastRSA algorithm, we use a variation of such a procedure for the precise estimation of a visibility circle or radius R and the arc segments over which an attempt to place a particle at C_P will be successful with a probability $p = 1$. In its implementation, the algorithm computes and returns a pair of elements; the first element is the probability of placement (p^*) which is 1 if a particle can be placed and 0 if a particle cannot be placed. The second element is a list containing the boundaries of the available arc segments over which the placement of this particle is possible; each element of the list consists of two angle values $(\omega 1, \omega 2)$ defining the edges of these arc segments. In the case where a particle cannot be placed this list is empty. This is the main difference between FastRSA and the classic approach (named ClassicRSA in the text)– the latter will use brute force to find an acceptable angle for the placement of a particle at each randomly chosen C_P.

2.4.1 Fast RSA calculation steps

FastRSA consists of the following steps which are explained in detail:

1. Preprocessing steps
    1.1 A uniform grid is constructed which partitions the available area in grid cells. This way the majority of particles is excluded from consideration since they belong in cells that are away from our point of interest
    1.2 Pre-calculate numerical values that are to be used extensively during the course of the algorithm

Following preprocessing, the main loop of the algorithm is executed, in which we aim to place a particle in a randomly selected point C_P. The loop runs as long as the desired packing is achieved or a user specific number of tries has been reached. The following steps are followed for every placement trial.

2. Broad phase

   Executed for every particle that is in the grid cells surrounding the point C_P

   2.1 Check against the AABB (Axis Aligned Bounding Boxes) and a square AABB of size $\sqrt{l^2+t^2}$ where (l) is the length and (t) the thickness of the particle, centered at C_P. If they overlap then we continue with this particle to the next step. Otherwise the next particle in the grid cells is selected and we return to step 2.1.

   2.2 Check against the distance of the nearest point of the previously selected rectangle and point C_P. If the distance is smaller than $1/2 \cdot \sqrt{l^2+t^2}$ then we add this particle to the list of particles that have to be considered in the narrow phase, otherwise we continue with the next particle from step 2.1.

3. Narrow Phase

   If the list of particles for consideration is empty then the combination of point C_P and angle θ can be used without further calculations. If the list is not empty then for every particle in the list we execute the following:

   3.1 Find the intersection points of a circle located at C_P and having diameter $R = \sqrt{l^2+t^2}$ and the segments that make the particle from the previous step (Figure 2.5a).

   3.2 Create the circles that are centered in the intersection points (C_{P1}, C_{P2}) with radius $t/2$ (Figure 2.5b). This is to avoid overlap and the reasoning for this is obvious from Figure 2.5c

   3.3 Find the tangent points T_1, T_2 of the segments originating from point C_P to the previously formed circles (Figure 3c).

   3.4 Exclude the arc that is formed from the points T_1, C_P, T_2 from the available arc spaces that we can use (Figure 2.5d).

4. End Phase

   4.1 If after the above subtraction the available arc space is not empty then a) an angle ω that falls within the available arc space is selected randomly, b) a new particle is placed after a final collision check is made and c) we return to step 1

   4.2 If the resulting available arc space is empty we reject the point P, select a different point and we return to step 2.1.

The geometrical calculations involved in the above algorithm may appear tedious, however they offer two significant advantages. The first is that they work for every α and they are not limited to square or near square particles. The second is that they do not require the creation and handling of large arrays that would limit their usage to small numbers of particles. In fact the algorithm works extremely well and produces configurations within 2% of jamming limit with numbers of particles in the range of tenths of millions in reasonable CPU times with today's standards (less than an hour for $\sim$20 million particles of α =1000 on an i7 Desktop PC with 8Gb of RAM).

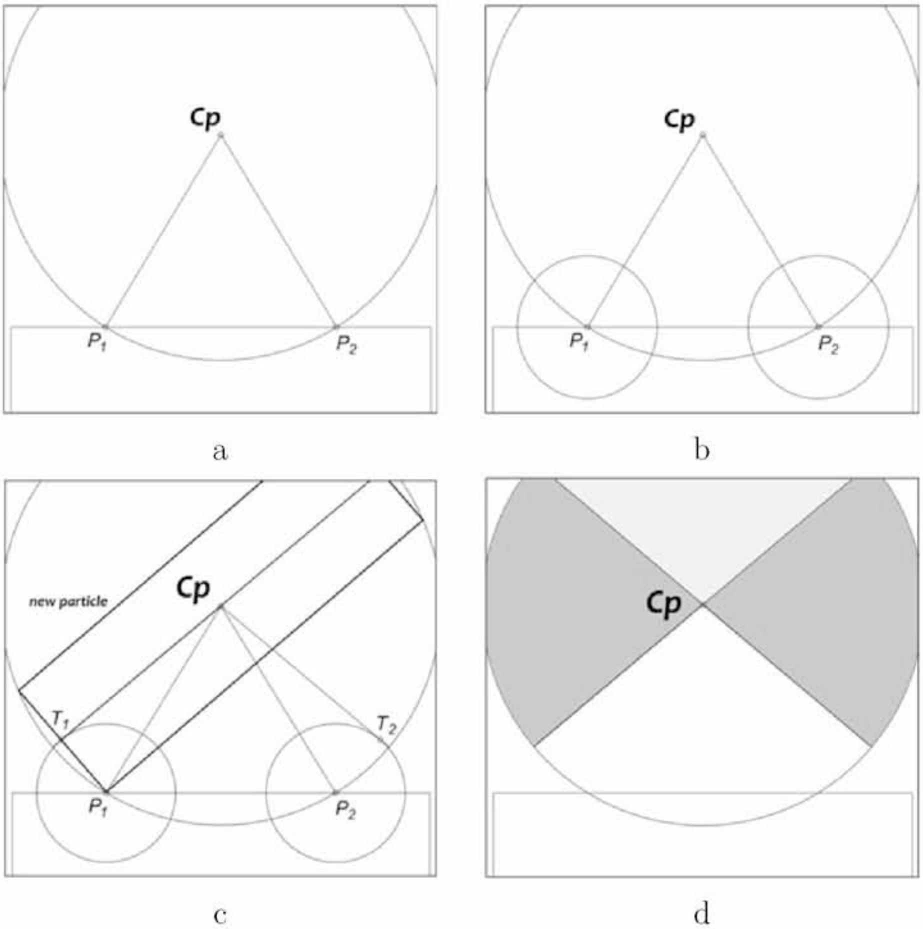

Figure 2.5: FastRSA algorithm steps. (a) Calculation of points P_1, P_2, (b) Calculation of circles of radius $t/2$, (c) Calculation of points T_1, T_2, (d) Calculation of the resulting arc. In this particular case, the arc corresponding to the grey part of the circle corresponds to admissible angles for the placement of a particle at point C_P. Due to symmetry the mirror arc is also excluded.

From the above we can see that the probability p of placing a particle defined earlier in Equation

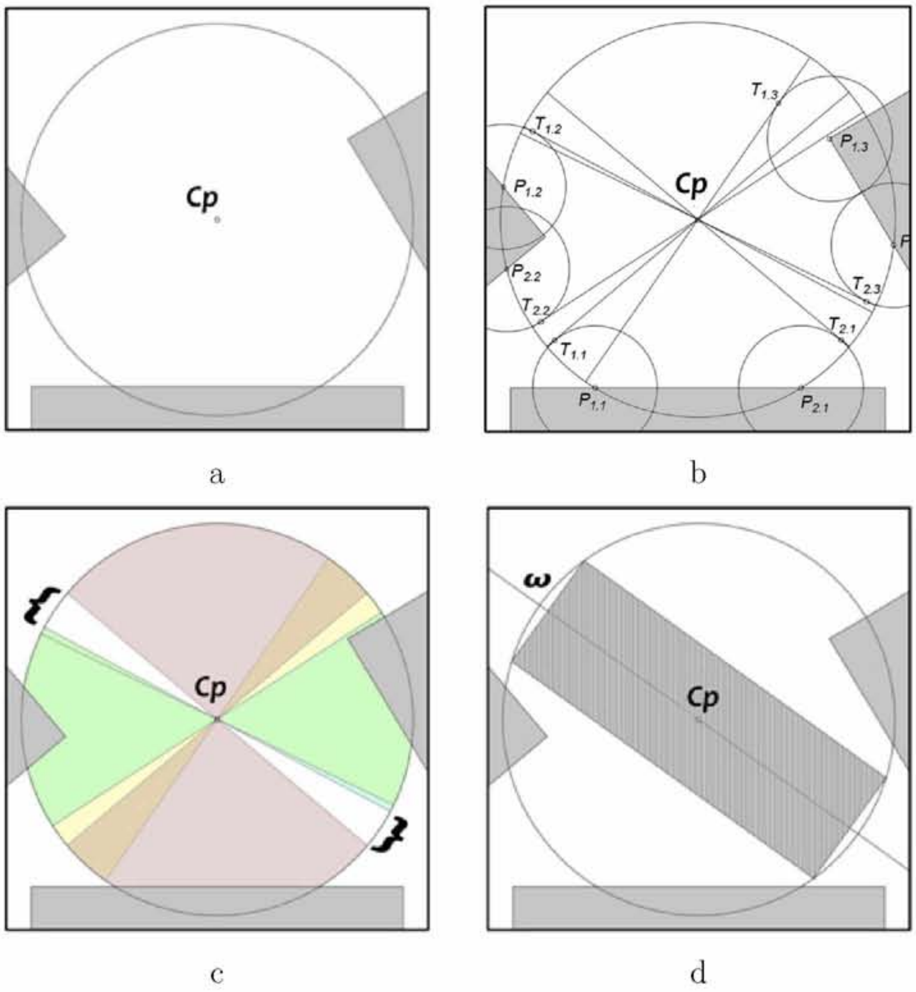

Figure 2.6: FastRSA steps for multiple pre-existing particles. (a) Initial configuration involving three pre-existing particles and the candidate point (C_P), (b) Calculation of intersection and tangent points, (c) Calculation of available arcs. The resulting available arcs are shown in white and the rejected arcs are shown in color- each color corresponding to exclusion due to one of the pre-existing particles(d) placement of a new particle after randomly picking an angle θ inside the available arc space (shown in white in Figure 2.6c).

2.3 can be also expressed as:

$$p_p = \frac{Avaiable\ Arc\ Space}{2\pi} = \frac{[\omega_1, \omega_2]_1 \cup \ldots \cup [\omega_1, \omega_2]_\nu}{2\pi} \tag{2.4}$$

where $[\omega_1, \omega_2]$ is the arc space that is returned from the FastRSA algorithm for every point C_P. We can also introduce the following definition for $p*$ at point C_P as

$$p_p^* = \begin{cases} 1, & p_{C_P} > 0 \\ 0, & p_{C_P} = 0 \end{cases} \tag{2.5}$$

2.5 Results and discussion

2.5.1 Statistical and geometrical properties

We see from the previous definitions that each particle creates a probability field around it which forbids other particles to be placed, at certain angles, within the surrounding space. The value of this probability field at every point C_P around a particle can be calculated using Equation 2.4 and Equation 2.5. Examples of this probability field, as computed by FastRSA, around particles of various aspect ratios (α), is shown in Figure 2.7. At points inside the particle and inside the Overlap Area the probability value is 0 and at points outside the Influence Area is always 1. In Figure 2.8 we can see the computed probability field in multi-particle configurations of various aspect ratios (α). It is interesting to note the unpredictable nature of the evolution of the Interaction Area A_I. As a increases the areas that are rendered un-usable for particle placement due to interactions of each particle's Influence Area become progressively more important and constitute the limiting factor in achieving a high packing. We can define the following two quantities over the entire area A as:

$$Totalp_A = \int^A pdA, \quad Totalp^*_A = \int^A p^* dA \tag{2.6}$$

Obviously, each of these quantities changes as the RSA process evolves and each can be calculated for any (α) of interest. This is illustrated in Figure 2.9, which shows the evolution of the total probability, as function of the (evolving) packing density at various particle aspect ratios (α). Evidently, this probability drops sharply as the RSA process evolves and maximum packing is approached. We also observe that $p*$ is orders of magnitude larger than p, especially when particles of high aspect ratio are involved. From Figure 2.9 it becomes clearer why FastRSA is much faster that ClassicRSA, especially in the case of elongated particles; since FastRSA utilizes $p*$, which is several orders of magnitude larger than p, for a given area A, it can successfully place particles at a much faster rate. In summary, the efficacy of a particle placement process depends on the available area. We show that, in turn, the evolution of this area depends on three mechanisms. These mechanisms remove available space from the total area A, and as a result, as new particles are added the total available space decreases. The interaction of these mechanisms gives valuable insights about the manner in which Random Sequential Adsorption works and is described in the following.

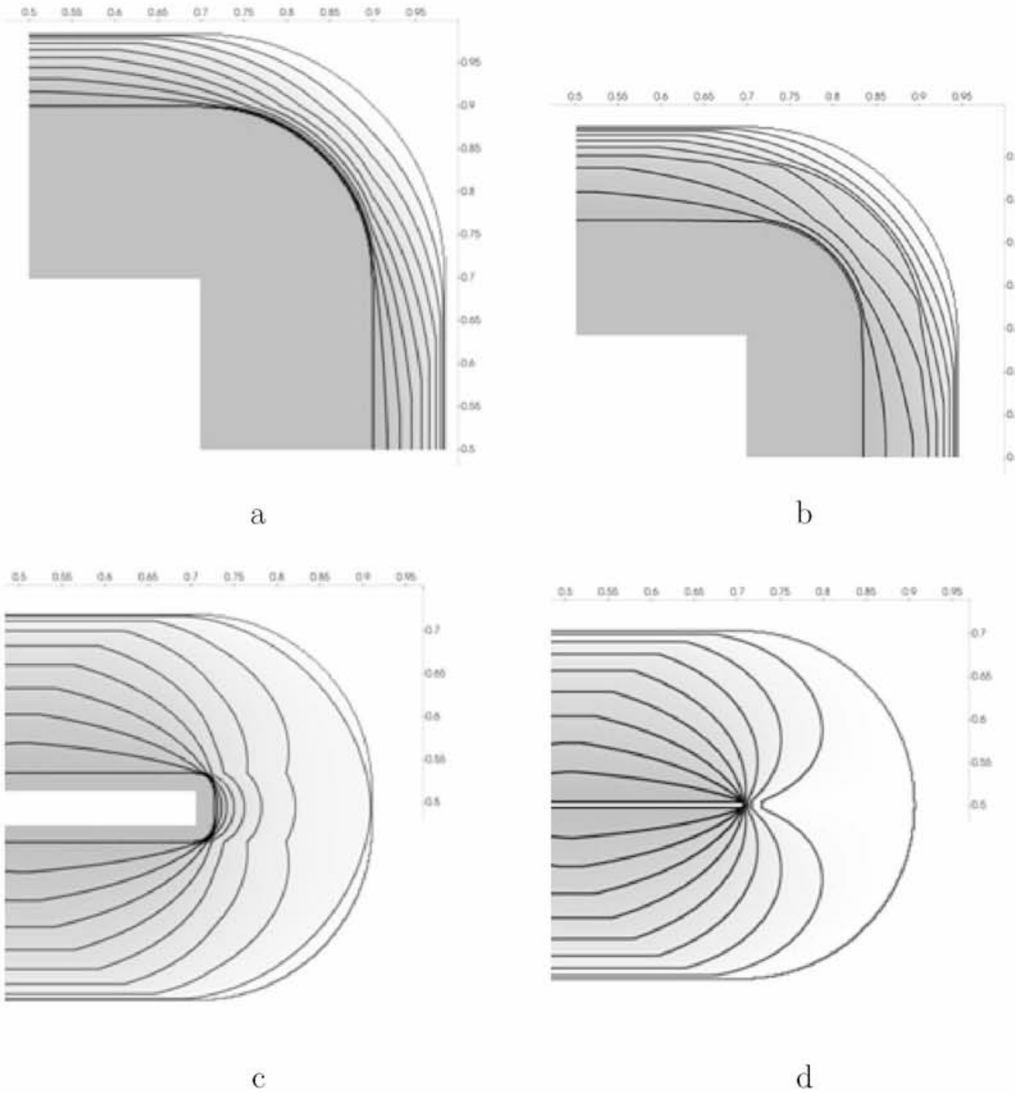

a b

c d

Figure 2.7: Contour plot of probability for placing a particle p for various particle aspect ratios α, at 0.1 intervals, from 0 at the Overlap Area around the particle (innermost contour) to 1 at a distance $R = 1/2 \cdot \sqrt{l^2 + t^2}$ from the particle. a) α =1, b) α =2, c) α =10, d) α =100. Due to symmetry only half or quarter of each particle is shown.

Particle Area (A_P)

The first and obvious mechanism is the placement of the particles themselves. As each particle is added, an area equal to the area of a particle $(l \cdot t)$ is removed from A. This area obviously evolves linearly with the addition of particles as $A_P = N_\tau \cdot l \cdot t$ where N_τ is the number of added particles at attempt τ.

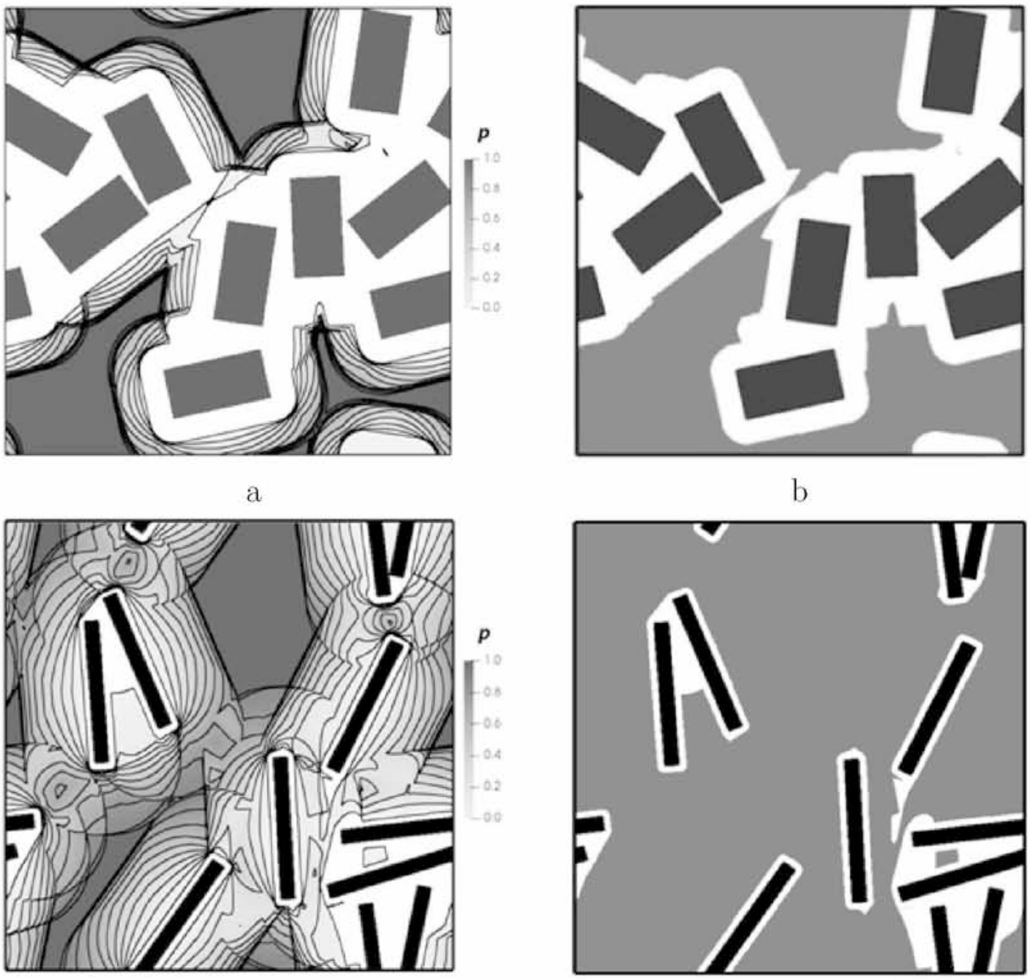

a b

c d

Figure 2.8: Contour plot of probability p and p^* for placing a particle in a pre-existing configuration at two values of the particle aspect ratio α. (a) p plot for $\alpha = 2$. (b) p^* plot for $\alpha = 2$.(c) p plot for $\alpha = 10$. (d) p^* plot for $\alpha = 10$. It is easily seen that p^* creates a binary probability field where values are either 1 (grey areas in Figure 2.8b and Figure 2.8d) or 0 (white areas) while p creates a field that varies from 0 to 1 as the distance from a particle increases

Overlap Area (A_O)

The second mechanism depends on the way the Overlap Area that surrounds the particles evolves as additional particles are placed. As discussed earlier in section 2 as new particles are added the area surrounding each particle at a distance up to $t/2$ from the particle sides is rendered unusable because any particle with a center point inside this area will overlap with the previously placed particle, irrespective of its orientation. However this area can overlap with similar areas of surrounding particles as it can be seen in Figure 2.10. As the process evolves, the extent of these overlaps increases and with the addition of new particles the Overlap Area surrounding an existing set of particles is reduced by being occupied by newly-added particles

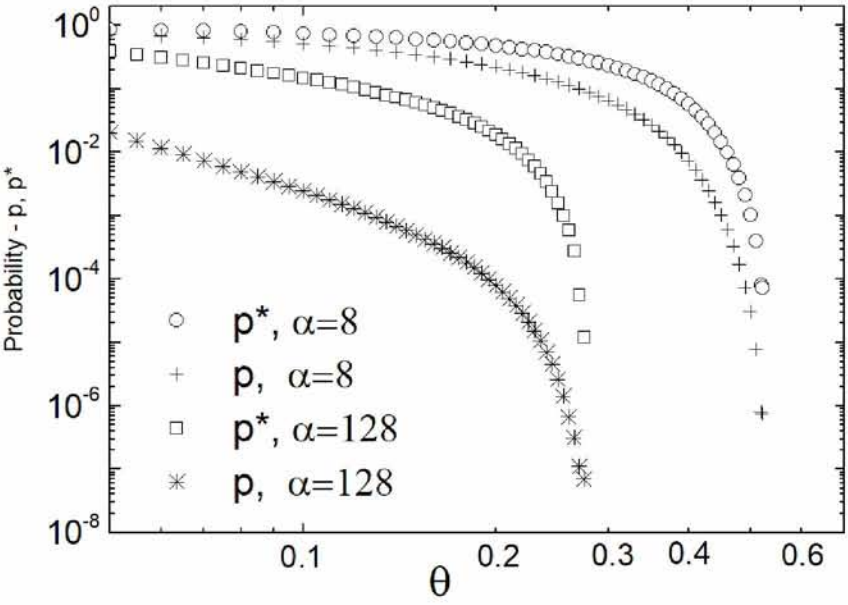

Figure 2.9: Plot of p and p^* onto an area A as particles are added. We can see that p^* is orders of magnitude larger at the same packing θ especially as α increases.

while also new Overlap Area is generated with the addition of each new particle. The process is illustrated in Figures 2.10 and 2.11.

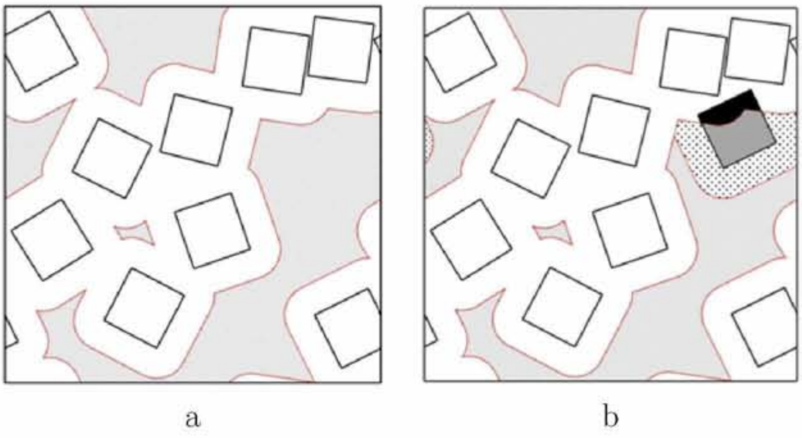
a
b

Figure 2.10: Detail view of the evolution of Overlapping Areas between two steps. Overlap area is shown in white. With the addition of a new particle (solid grey in image (b)), area that was characterized as overlap area (white) switches to particle area (black). Also the particle removes area from A and transforms it into Overlap Area (dotted area) and Particle Area (colored gray).

Interaction Area and Influence Area

The third mechanism that comes into play is the evolution of Interaction Area and Influence Area. Interaction Area consists of the points that cannot be used for placement of particle

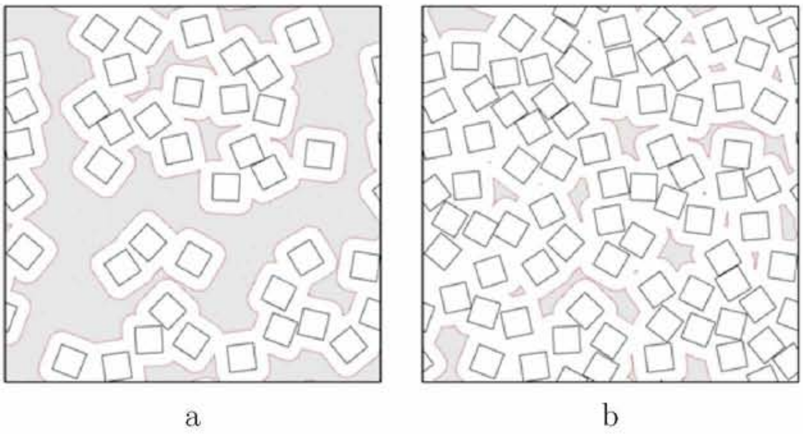

Figure 2.11: Evolution of Overlap Areas (shown as white) during the particle addition process.

centers because no particle can be added due to geometrical constraints. As particles are placed onto a surface, new particles can't be added in various points around them because they cannot fit at any orientation. These areas are formed outside the Overlap Area of pre-existing particles but from the interaction of their Influence Areas (A_I). For example, a particle might allow the placement of a new particle at a point C_P that falls in its Influence Area, with an angle θ, but the same point might belong to the Influence Area of nearby particles which might not allow the placement of a new particle at this specific angle. As a result no particles can be placed in this point at any angle $0^o < \omega < 180^o$. From the above we define the Interaction Area as the area that no particles can be added due to constraints that are imposed from the Influence Areas of surrounding particles. The evolution of Interaction Areas can be seen in Figure 2.12. For elongated particles these areas tend to become extremely large and occupy a big part of the total area A even if the area of individual particles is small.

Total available surface area

From the previous discussion, it is evident that placement of a particle at a point C_P depends on where this point resides in respect to the other, pre-existing particles. If the point C_P falls within a particle or in its Overlap Area it cannot be selected for placement of a new particle. If a point falls outside the Areas of Influence of the existing particles then a new particle can be placed in this point at any angle (ω). However if it falls within the Areas of Influence of nearby particles, the algorithm described above will screen potential candidate points. From

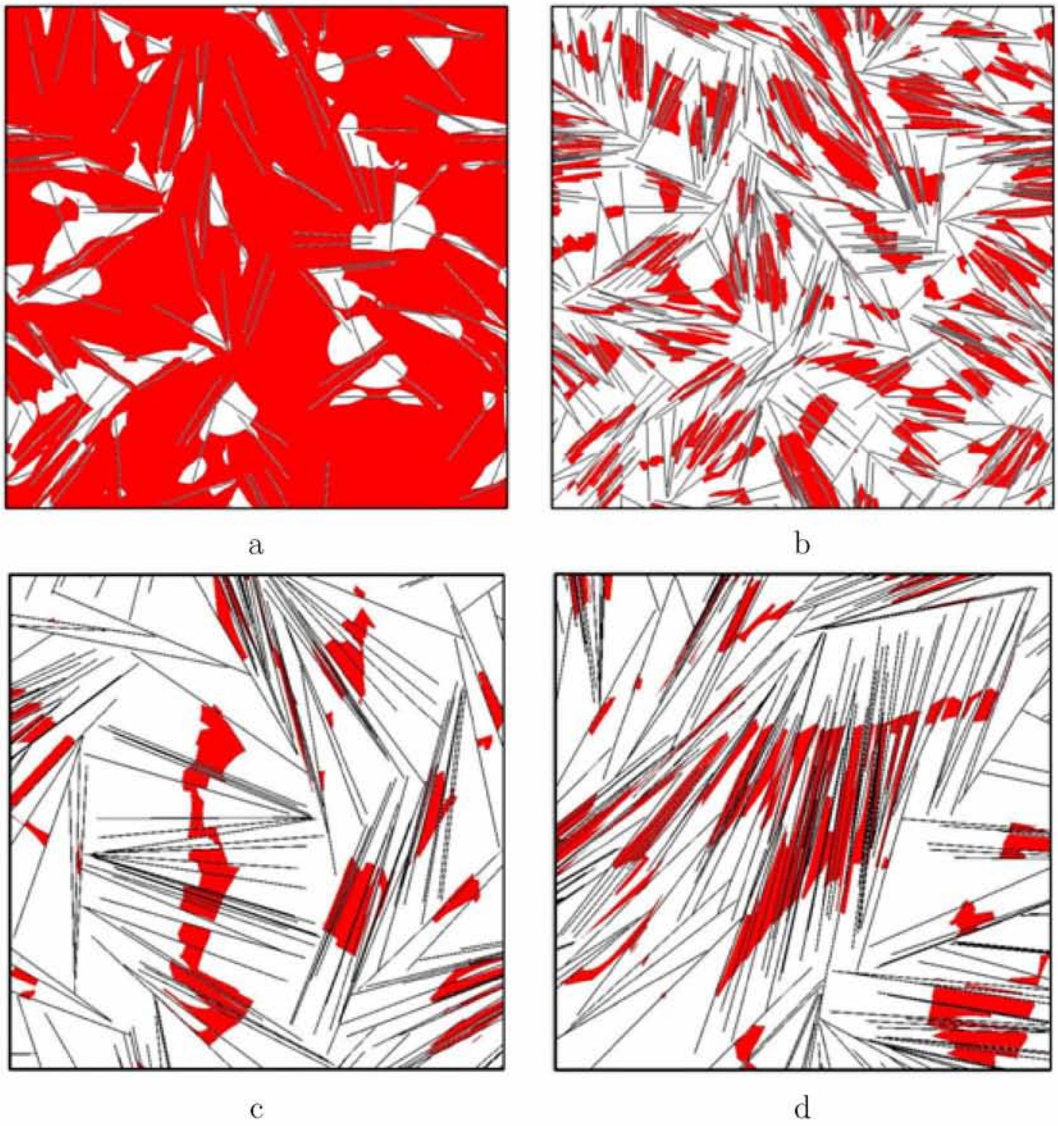

Figure 2.12: (a), (b). Evolution of Interaction Areas (shown as white) between time steps. The probability of placing a particle (p^*) is zero in these areas. Areas where p^*=1 are shown as red. The potential for the formation of nematic structures, with locally aligned particles is clearly visible at latter stages of the process. (c), (d) detail of areas between particles where p^*=0 (in white color) at α =512

the above we can define the Available Space (A_S) for the addition of a new particle as

$$A_S = A - A_P - A_O - A_I \tag{2.7}$$

The total Available Space (A_S) for particle placement is the result of the interaction of the above three mechanisms, which are not evolving monotonically as the RSA process unfolds, as it can be seen in Figure 2.13. We see that for small α the mechanism that subtracts large areas from A is the evolution of Overlap Areas while for large α the limiting mechanism becomes the evolution of Interaction Area. This observation is at the heart of the well-known differences in performance in terms of achieved packing of RSA algorithms when particles of small or large (α) are used.

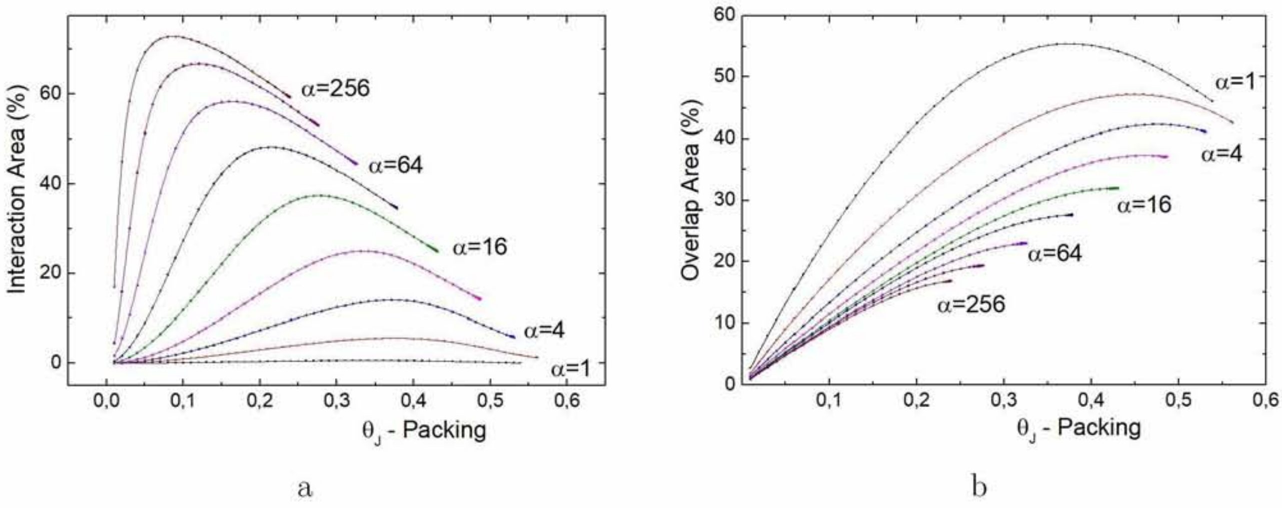

Figure 2.13: Evolution of area coverage mechanisms for various α. In the Y axis we can see the area fraction that is characterized as Interaction Area (a) and Overlap Area (b).

2.5.2 Particles of high aspect ratio and the formation of nematic structures

From the definitions of Overlap Area and Influence Area we see that as α increases the Overlap Area around each particles decreases since it is proportional to $t/2$. On the contrary, the Influence Area is proportional to l and therefore increases. In the case of elongated particles $(l \gg t, \alpha \gg 1)$ we see (Figure 2.13) that the main mechanism that influences A_S is the evolution of the Interaction Area. Since Interaction Areas occupy a big part of the total area A, new particles can be added only in close alignment with pre-existing ones. This can be easily seen in Figure 2.12 where it becomes obvious that the only possible way for new particles to be placed is in close correlation with their angles and thus, the only mechanism that could allow the addition of new particles in dense configurations is the formation of nematic structures. It appears therefore that for elongated particles the creation of nematic structures is a fundamental consequence of the RSA process and it emerges as packing increases. It also shows us the importance of the initial steps of the adsorption process, since the particles that arrive first create the scaffold which guides the addition of new ones as it can be easily seen in Figure 2.14. We can also note that, since the areas between existing particles become smaller, the available angles that can be used are limited to a very narrow range. Obviously, the ClassicRSA, by trying to randomly select, from the entire space $0 < \omega < \pi$, an angle ω that has to fall within a very limited range, needs many attempts for the same point C_P before successfully picking one that would allow the placement of a particle.

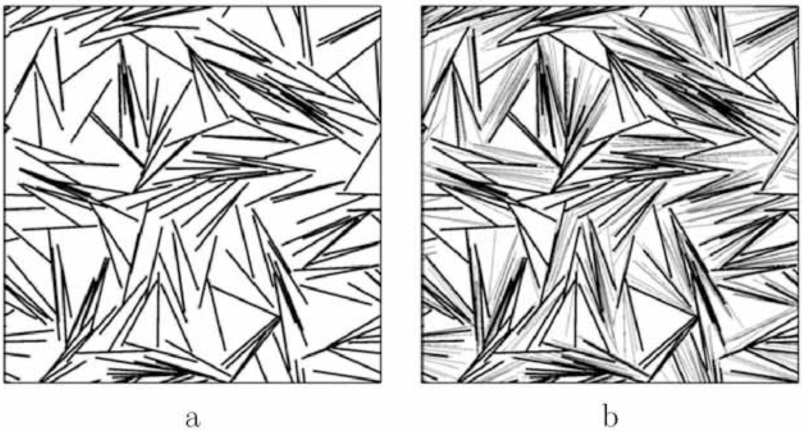

Figure 2.14: (a), (b). Evolution of alignment of particles between time steps as packing increases. By comparing the two Figures it is easy to see that the newly arrived particles in (b) (thin lines) are forced to align parallel to the pre-existing particles (bold lines).

2.5.3 Hybrid mode

We have shown that as particles get deposited within an area (A) they change the properties of the surrounding space by creating a probability field around them. We define as 'polarized space' in terms of an angle (ω) the set of points at which the probability (p) is $p < 1$. If we plot this field not in terms of p and p^* as in Figure 2.8 but in terms of relative angles ω we can see how the total area gets polarized in these specific angles during the RSA process (Figure 2.15). As new particles are deposited to a configuration their corresponding Minkowski Polygons at various angles ω ($B\omega$) occupy a progressively larger area of A. As we explained earlier in section 2, if a point lies within a Minkowski polygon $B\omega$ of a particle, it cannot be used for the placement of a new particle with this specific angle ω. Therefore as particles are added, the area A has less space left for specific angles ω and eventually there is no more area left within A for these specific angles.

Plotting the evolution of the area that remains un-polarized for various angles ω during the adsorption process we get the following results:

Using the above charts (and the underlining calculations) we can define the 'Freezing Point'

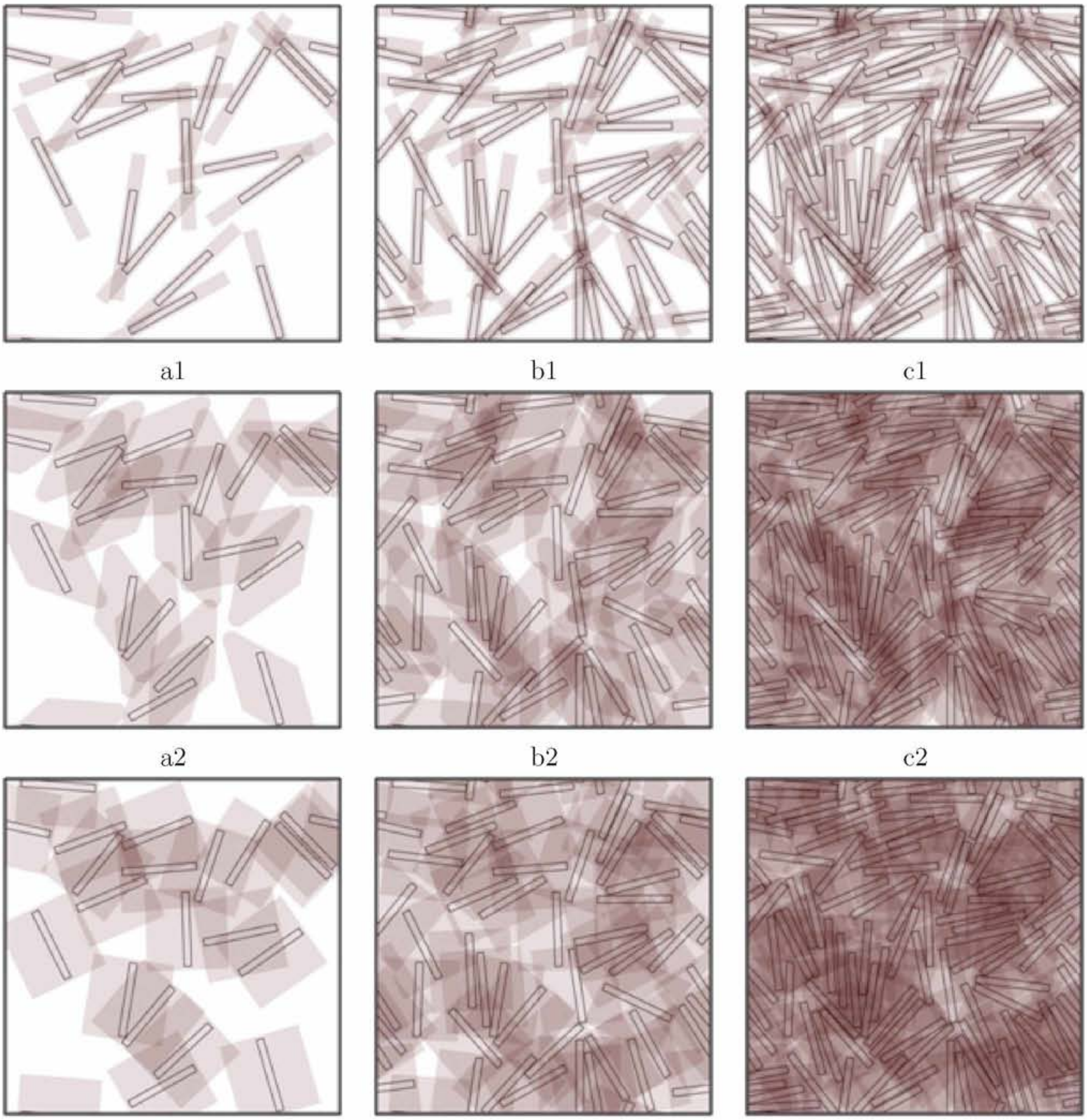

Figure 2.15: Polarization of space around deposited particles. $a_1 \ldots a_3$, $\theta = 0^o$, $b_1 \ldots b^3$, $\theta = 45^o$, $c_1 \ldots c_3$, $\theta = 90^o$. In images $a_1 \ldots a_3$ we see the space occupied by the Minkowski Polygons of $\omega = 0^o$. In images $b_1 \ldots b_3$ the Minkowski polygons at $\omega = 45^o$ are shown and in $c_1 \ldots c_3$ the corresponding polygons at $\omega = 90^o$. The space occupied by the corresponding Minkowski polygons is easily seen.

at a relative angle ω (FP_ω) as the packing fraction (θ_ω) at which a specific relative angle ω cannot be used anymore for placement of particles. This means that no new particles can be entered at any point C_P within the Area A at angle ω; the already existing particles won't allow this, since all area A is occupied by the Minkowski polygons B_ω of the pre-existing particles.

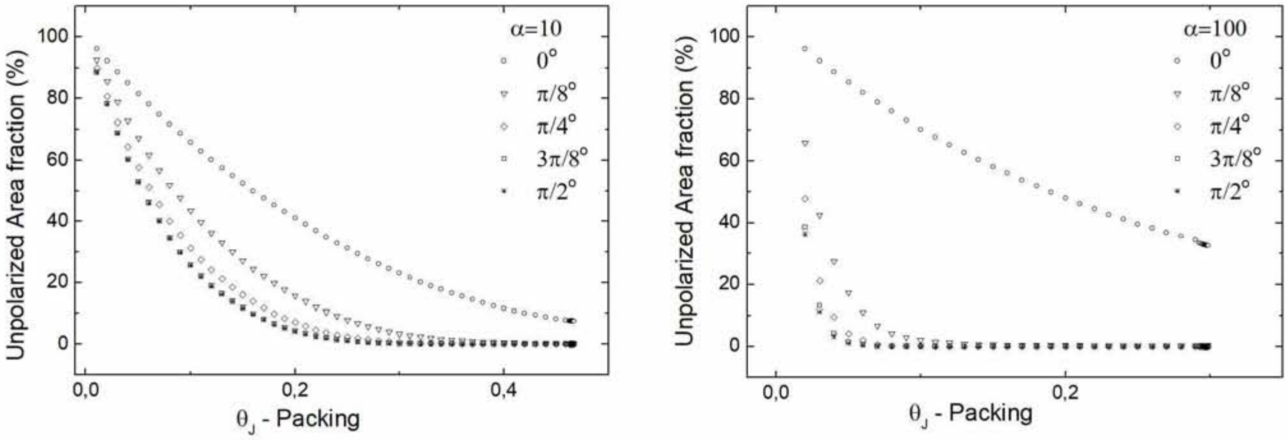

a

b

Figure 2.16: (a), (b). Evolution of polarization areas. (a) α =10, (b) α =100. We can see that as packing increases space (A) becomes completely polarized at various relative angles meaning that these angles cannot be used anymore.

For example in regards to Figure 2.16a, no more particles can be placed at $\omega = \pi/2$ after the packing has exceeded the value of $\theta \cong 0.3$ - the corresponding polarized area fraction has dropped to zero, while at the same packing (~30%) there is a 20% of the total area available for the placement of particles parallel to pre-existing ones (zero relative angle ω). In Figure 2.16b, which corresponds to more slender particles (α =100), the FP_{45} is around $\theta \cong 0.08$, at which packing there is an over 80% probability of placing particles aligned with pre-existing ones. Obviously, the formation of nematic structures is statistically favored at a much lower packing in the case of slender particles.

We can use the above observation and introduce a Hybrid Mode in the operation of the FastRSA algorithm that essentially begins the adsorption process with the ClassicRSA and after a point it switches to the FastRSA algorithm. This way we can have a configuration that has the statistical properties of ClassicRSA up to a user-defined point and the speed of FastRSA afterwards, along with the nematic structures that follow. For example, in the configurations of Figure 2.17, switching to the FastRSA after $\theta = 0.5$ and $\theta = 0.2$ (for α =10 and α =100 respectively) will produce configurations that are equivalent to Classic RSA up to a certain point. With the selection of such a switching point near the jamming limit we could produce configurations with very small statistical differences between the classic RSA approach and FastRSA since the configuration near jamming limit is essentially frozen in all but a small range of relative angles near ω=0 which would lead to the formation of nematic structures using both algorithms. We can see in Figure 2.17 the behaviour of the hybrid mode in terms of speed and packing achieved.

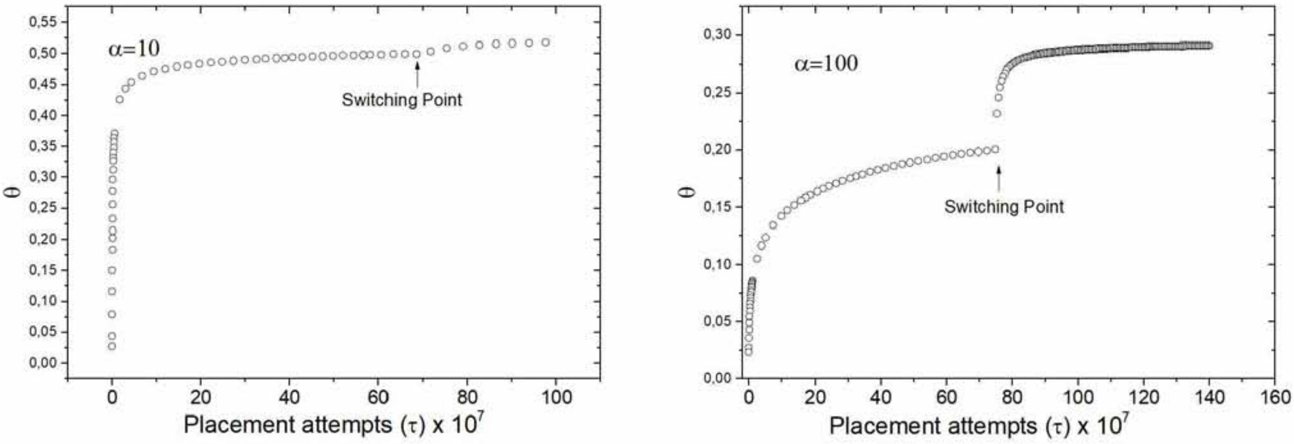

a

b

Figure 2.17: Packing evolution during hybrid mode. (a) α =10, (b) α =100. We see the difference in speed, especially as α increases. In this case simulation ended when a specific CPU time was reached

2.5.4 Estimation of maximum packing

As a geometrical configuration evolves with the addition of new particles, the FastRSA algorithm, through its ability to calculate p and p^* at every point, allows the measurement of various spatial properties such as the amount of Overlap Area and Interaction Area and thus leading to the accurate calculation of the total Available Space for particle placement (A_S). Using a Monte Carlo sampling procedure to calculate A_O and A_I, Available Space (A_S) can be estimated using Equation 2.7. Obviously, the jamming limit (θ_J) of a configuration can thus be found as the point at which A_S becomes zero. Extensive simulations (Figure 2.18) have shown that the Available Space (A_S) can be described by a function of the following form

$$A_S = M \cdot (\theta_\tau - \theta_j)^k \tag{2.8}$$

where θ_J is the maximum packing (jamming limit) at the point where the Available Space becomes zero and where θ_τ is the packing after (τ) attempts, at which point N_τ particles have been placed. The fit of Equation 2.8 to computational results for various values of the particle aspect ratio α can also be seen in Figure 2.18.

We also calculate the maximum packing using the assumption that it follows Feder's Law with

$\theta_J \sim \tau^{-1/2}$. Results of more than 50 calculations in various α with an accuracy at the 4th decimal digit are shown in Table 1 where we list and compare:

i. The estimation of maximum packing using FastRSA results based on Feder's Law using an expression of the form $\theta_\tau \sim \tau^{-1/3}$.
ii. The estimation of maximum packing using FastRSA results based on Feder's Law using an expression of the form $\theta_\tau \sim \tau^{-1/2}$.
iii. The coefficients M and K determined from fitting the computational results to Equation 2.8.
iv. The maximum packing as estimated from the extinction of Available Space at Equation 2.7
v. The actual achieved maximum packing from our simulations with FastRSA algorithm
vi. Literature estimation of maximum packing based on ClassicRSA [12]; only available for $\alpha < 2$.

We can see that using the results from FastRSA with an estimation of the form based on $\tau^{-1/3}$ systematically overestimates the maximum packing and that a behavior of $\tau^{-1/2}$ is closer to our actual packing results with FastRSA.

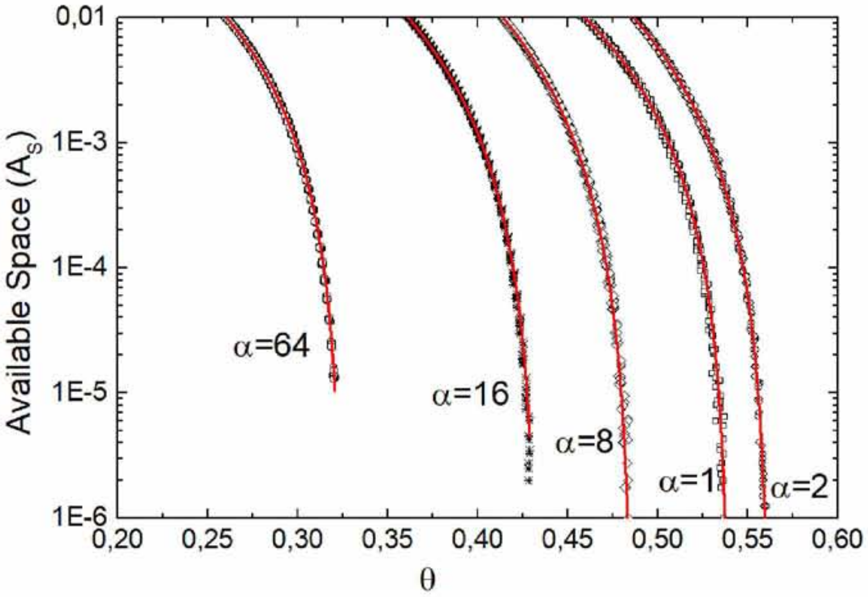

Figure 2.18: Evolution of the Available Space (A_S, as calculated from Equation 2.7) along with best fit curves of Equation 2.8 calculated for various α.

Table 2.1: Values of maximum packing (θ_J) as calculated with various methods. (M) and (k) refer to Equation 2.8.

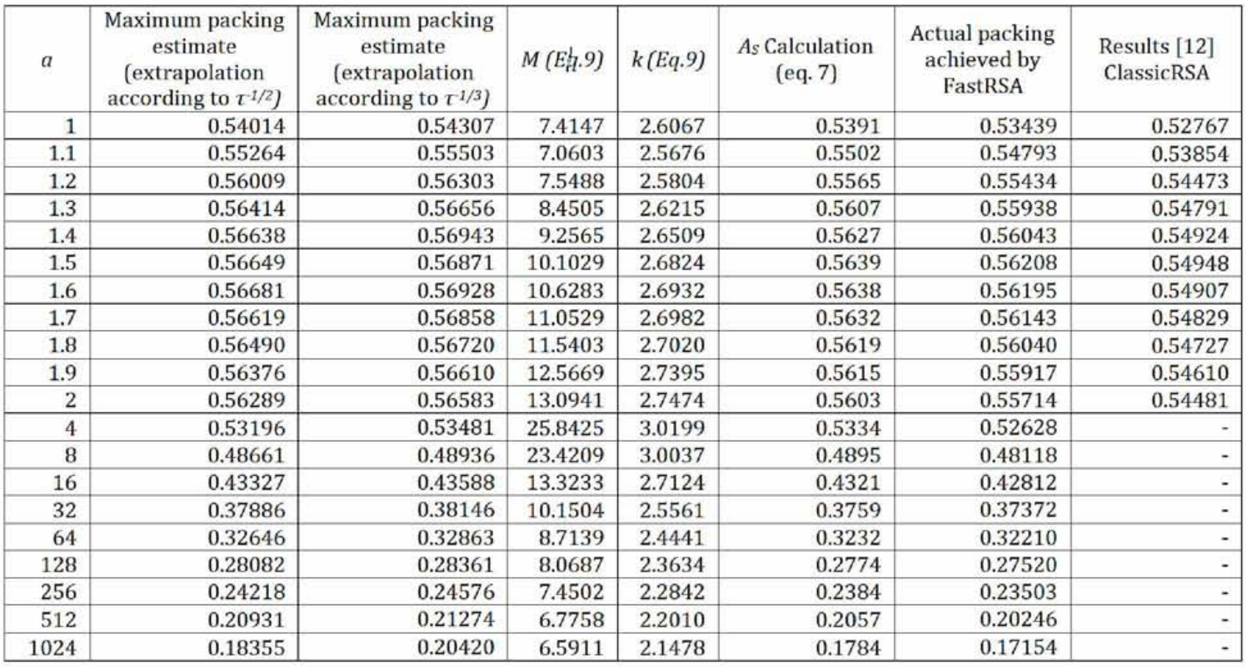

α	Maximum packing estimate (extrapolation according to $\tau^{-1/2}$)	Maximum packing estimate (extrapolation according to $\tau^{-1/3}$)	M (Eq.9)	k (Eq.9)	A_S Calculation (eq. 7)	Actual packing achieved by FastRSA	Results [12] ClassicRSA
1	0.54014	0.54307	7.4147	2.6067	0.5391	0.53439	0.52767
1.1	0.55264	0.55503	7.0603	2.5676	0.5502	0.54793	0.53854
1.2	0.56009	0.56303	7.5488	2.5804	0.5565	0.55434	0.54473
1.3	0.56414	0.56656	8.4505	2.6215	0.5607	0.55938	0.54791
1.4	0.56638	0.56943	9.2565	2.6509	0.5627	0.56043	0.54924
1.5	0.56649	0.56871	10.1029	2.6824	0.5639	0.56208	0.54948
1.6	0.56681	0.56928	10.6283	2.6932	0.5638	0.56195	0.54907
1.7	0.56619	0.56858	11.0529	2.6982	0.5632	0.56143	0.54829
1.8	0.56490	0.56720	11.5403	2.7020	0.5619	0.56040	0.54727
1.9	0.56376	0.56610	12.5669	2.7395	0.5615	0.55917	0.54610
2	0.56289	0.56583	13.0941	2.7474	0.5603	0.55714	0.54481
4	0.53196	0.53481	25.8425	3.0199	0.5334	0.52628	-
8	0.48661	0.48936	23.4209	3.0037	0.4895	0.48118	-
16	0.43327	0.43588	13.3233	2.7124	0.4321	0.42812	-
32	0.37886	0.38146	10.1504	2.5561	0.3759	0.37372	-
64	0.32646	0.32863	8.7139	2.4441	0.3232	0.32210	-
128	0.28082	0.28361	8.0687	2.3634	0.2774	0.27520	-
256	0.24218	0.24576	7.4502	2.2842	0.2384	0.23503	-
512	0.20931	0.21274	6.7758	2.2010	0.2057	0.20246	-
1024	0.18355	0.20420	6.5911	2.1478	0.1784	0.17154	-

2.5.5 Algorithm performance and results

In the following we present some results on the performance of the FastRSA algorithm. Configurations were created with particles of aspect ratio from 1 to 1024 and involving N particles placed in a periodic square unit cell. For each α, N was selected to be high enough in order to achieve a uniform orientation distribution of the particles; it typically was $N > 10^7$ for small ($\alpha < 10$) and it was increasing as α was increasing so that the length l of each particle would be less than 10^3 of the total area length (typically $N > 10^8$ for $\alpha \geq 100$). Periodic conditions were used to avoid wall effects due to particle alignment and/or particle exclusion at the borders of the unit cell.

In Figures 2.19 and 2.20 we show the maximum packing achieved with FastRSA at various particle aspect ratios. Our algorithm consistently achieves a maximum packing that is almost 2 percentage points higher (depending on α) than the values reported in the literature so far. It should be noted that such literature estimates are not actually achieved packings but rather extrapolations based on a power exponent of (-1/3). Besides the difference in the estimated packing values, FastRSA can achieve configurations that are by a margin of less than 1% from the theoretical jamming limit even for large α. This can be explained if we consider that the FastRSA works by calculating p^* which can either take the value of 1 or 0. So if a point is selected for particle placement a particle will either be placed, at the first attempt, or not placed, depending on whether p^* is one or zero, and no further iterations are required. Classic RSA works not only by trying to find an acceptable point C_P but by also finding, randomly, an acceptable angle over the entire arc space from 0^o to 180^o. This as we explained in section 4 becomes extremely difficult especially in large α because the formation of nematic structures can allow only for a very limited range of angles at every point of A. So, in the ClassicRSA algorithm, even if the same point is selected many times, successful particle placement is not certain, while, in contrast, the FastRSA algorithm will place (or not place) a particle at the first attempt. Therefore FastRSA fulfils one the basic assumptions of Swenden's analysis in which every point has to have an equal probability to be selected for the placement of a particle. By using Classic RSA two points C_{P1} and C_{P2} that could be used for particle placement $(p_1^* = p_2^* = 1)$ don't have the same probability p because they also have to pass the random process of selecting an acceptable angle θ and thus

$$p_1 = p_1^* \cdot Available\ Arc\ Space_{p1} \neq p_2^* \cdot Available\ Arc\ Space_{p2} \tag{2.9}$$

In addition, ClassicRSA will always produce a lower packing because of the nature of the probability field on which it operates. Specifically, as the field is created as a result of the placement of pre-existing particles, points that are nearby the particles have a probability p that becomes smaller as we move closer to the particles. It is as if the pre-existing particles repel the new ones since the field that has been created around them gives a smaller p and

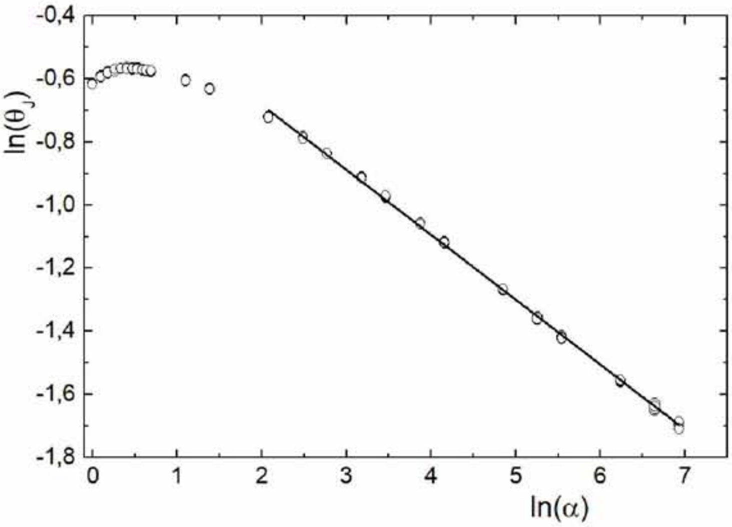

Figure 2.19: Log-log plot of θ_J vs α. The slope of the line is -0.20582

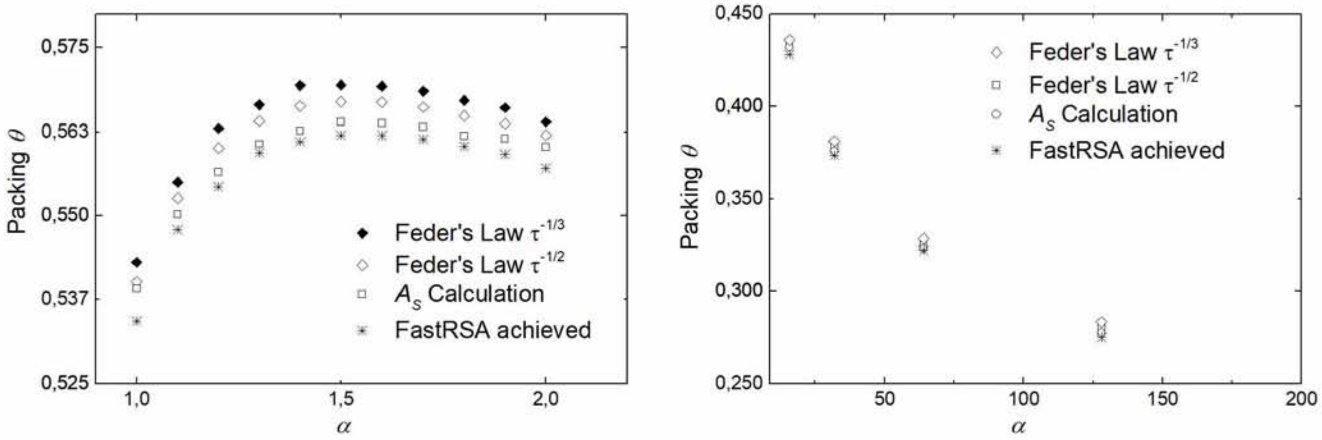

a b

Figure 2.20: Packing achieved by FastRSA for various α as given in Table 1.

so it becomes harder for ClassicRSA to use the points nearby existing particles. As a result ClassicRSA will fill the empty spaces first, where p is larger and as a consequence bigger interaction and overlapping areas will be created at the initial stages of a RSA configuration which will lead inevitably to a less efficient use of space and a smaller maximum packing.

2.6 Conclusions

A new RSA algorithm (FastRSA) with the ability to achieve very dense 2D geometrical configurations, with high particle count and using particles of aspect ratio from 1 to 1024, is introduced and studied. Using this algorithm we throw light to the inner mechanisms of an RSA process and explain its behaviour, in statistical terms, as we approach the jamming limit. We show that the total packing achieved is affected by the sum of the interaction of the spatial properties of the area A. Specifically we see how the Interaction Area, the Overlap Area and the Particle Area evolve throughout the RSA process and how they interact to produce the final configuration. We can also see the shift of their importance as α varies. We explain how nematic structures are created in dense packings of high aspect ratio particles in an RSA process and we show the main mechanisms behind their appearance. Our results further show that this approach can achieve packings that are $\sim$2 percentage points higher through all the range of aspect ratios α and we have shown how these high packings can be obtained in much faster computational times. Out algorithm follows Feder's Law and Swensen's conjecture, generating very dense geometrical configurations exhibiting a behavior of $\theta_\tau \sim \tau^{-1/2}$.

2.7 References

1. Y. Pomeau, “Some asymptotic estimates in the random parking problem”, J. Phys. A. Math. Gen 13 L193, 1980
2. Robert H. Swendsen, ‘Dynamics of random sequential adsorption’, Physical Review A, Volume 24, Number 1, July 1981.
3. K. E. Evans and A. G. Gibson, “Prediction of the maximum packing fraction achievable in randomly oriented short fibre composites”, Composites Science and Technology, 25 149-162, 1986
4. Jens Feder, “Random sequential Adsorption”, J. Theor. Biol. 87,237-254, 1980
5. J. J. Gonzalez, P. C. Hemmer and J. S. Hoye, Chem. Phys. 3.228 (1974)
6. J. Feder and Ivar Giaever, “Adsoprtion of Ferritin”, Journal of Colloid and Interface Science, Vol 87, N. 1, 1980
7. L. Finegold and J. T. Donnell, Nature 278:443 (1979)
8. Michal Ciesla, “Random packing of regular polygons and starpolygons on a flat two-dimensional surface”, Physical Review E 90, 022402, 2014
9. G. Tarjus, P. Schaaf and J. Talbot, “Random sequential addition: A distribution function approach”, Journal of Statistical Physics, Vol. 63, No 1 /2, 1991
10. R. M. Ziff and R. D. Vigil, “Kinetics and fractal properties of the random sequential adsorption of line segments”, 1990 J. Phys. A: Math. Gen. 23 5103
11. G. Zhang, “Precise algorithm to generate random sequential adsorption of hard polygons at saturation”, Physical Review E 97, 043311 (2018)
12. Wojciech Kasperek, Piotr Kubala and Michal Ciesla “Random sequential adsorption of unoriented rectangles at saturation”, Physical Review E 98, 063310 (2018)
13. M.S. Ingber and T.D. Papathanasiou, ”A Parallel-Supercomputing Investigation of the Stiffness of Aligned, Short-Fiber-Reinforced Composites using the Boundary Element Method”, International Journal for Numerical Methods in Engineering, 30, 3477-3491, 1997
14. Y.J. Liu, Fast Multipole Boundary Element Method - Theory and Applications in Engineering, Cambridge University Press, Cambridge, 2009.
15. R. Dennis Vigil and Robert M. Ziff, “Random sequential adsorption of unoriented rectangles onto a plane”, The Journal of Chemical Physics 91, 2599 (1989)

16. P. Viot, G. Tarjus, S. M. Ricci and J. Talbot, “Saturation coverage in random sequential adsorption of very elongated particles”, Physica A 191 (1992) 248-252
17. P. Viot and G. Tarjus, “Random sequential addition of unoriented squares: A breakdown of Swendsen’s Conjecture”, 1990 EPL 13 295
18. H. El Gindy, D. Avis, ≪A linear algorithm for computing the visibility polygon from a point≫, Journal of Algorithms, Volume 2, Issue 2, June 1981, Pages 186-197, `https://doi.org/0.1016/0196-6774(81)90019-5`
19. Minkowski Sum Construction and other Applications of Arrangements: and the Importance of Being Exact, LAP LAMBERT Academic Publishing (December 1, 2010), ISBN-13: 978-3843380942

Chapter 3

Orientational randomness and its influence on the barrier properties of flake-filled composite films[1]

Summary

In this chapter we study the role that flake orientational randomness plays in the barrier properties of composite materials. For doing this we solve an elliptic equation for the concentration field (for steady state systems) at a unit cell containing up to 500 flakes that assume random positions and their orientation angle takes uniform values at the interval $[-\epsilon, \epsilon], \epsilon \in [-90^o, 90^o]$ (Figure 3.1). The flakes are considered to be elongated, that is their aspect ratio α is greater that 1 ($\alpha = 50, 100, 1000$) and the product $\alpha\phi$ ranges from 0.01 (dilute regime) to 15 (concentrated regime). We use periodic boundary conditions at the sides of the unit cell ($C_{left} = C_{right}$) and periodic geometrical conditions (the unit cell effectively creates a tile) as shown in Figure 3.2. Numerous simulations (> 2500 cases) are solved at the full range of the above parameters.

Solving for the concentration field enables us to calculate the effective diffusion coefficient D_{eff} and with this we calculate the Barrier Improvement Factor ($BIF = 1/D_{eff}$). We see how the BIF depends on the flake aspect ratio $\alpha = l/t$, the volume fraction (ϕ) and flake orientation as expressed by the misalignment angle (ϵ).

---

[1] As published in Journal of Plastic Film & Sheeting: Papathanasiou, T., & Tsiantis, A. (2017). Orientational randomness and its influence on the barrier properties of flake-filled composite films. Journal of Plastic Film & Sheeting, 33(4), 438–456. `https://doi.org/10.1177/8756087916682793`

The results show us that there is a significant difference between dilute ($\alpha\phi < 1$) and concentrated systems ($\alpha\phi > 1$) in the behaviour of the BIF. In the dilute regime the BIF evolves linearly with ϵ and in concentrated systems it deviates from this behaviour as ϵ increases.

Using these results we propose a scaling that includes the effects of both ϵ and $\alpha\phi$ and we come to the conclusion that the bigger the misalignment angle the bigger the deviation from the anticipated barrier improvement especially as $\alpha\phi$ increases.

Finally at the end of this chapter we investigate the ratio $BIF_{random}/BIF_{aligned}$ and we confirm earlier results.

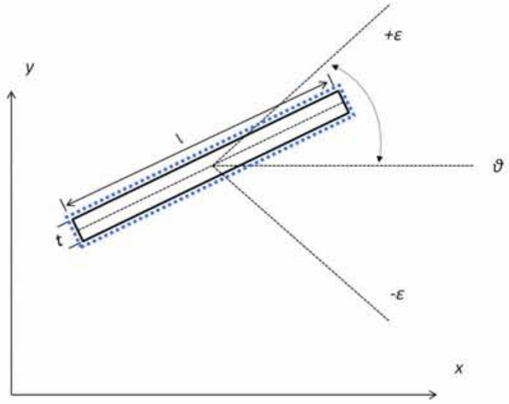

Figure 3.1: Typical 2D flake geometry. l is the flake length and t is the flake width. The flake axis assumes a random orientation inside $[-\epsilon, +\epsilon]$. θ is assumed to be 0 in the geometries used in this chapter. The diffusion direction is along the Y-axis.

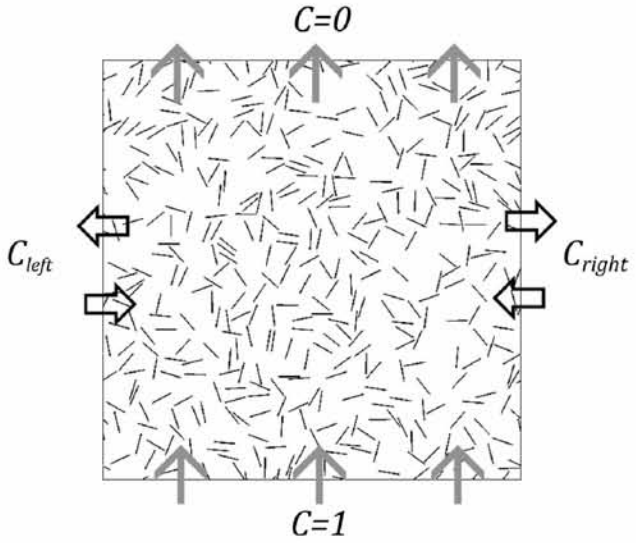

Figure 3.2: Typical concentration boundary conditions used in this study. The concentration (C) is 0 at the top and 1 at the bottom. In the left and right of the RVE periodic boundary conditions are used.

3.1 Abstract

This direct numerical study investigated the effect of orientational randomness on the barrier properties of flake-filled composites. Over 2500 simulations have been conducted in two-dimensional, doubly periodic unit cells, each containing 500 individual flake cross-sections which, besides being spatially random, assume random orientations within an interval $[-\epsilon, +\epsilon]$, $(0 \leq \epsilon \leq \pi/2)$. We consider long flake systems (aspect ratio $\alpha = 50, 100$, and 1000) from the dilute ($\alpha\phi = 0.01$) to the concentrated ($\alpha\phi = 15$) regime, where (ϕ) is the flake volume fraction. At each (ϵ) and ($\alpha\phi$), several realizations are generated. At each of those, the steady-state diffusion equation is solved, the mass flux across a boundary normal to the diffusion direction is computed and an effective diffusivity D_{eff} calculated from Fick's Law. The computational results for D_{eff} are analyzed and the effects of (ϵ) and ($\alpha\phi$) are quantified. These differ in the dilute ($\alpha\phi < 1$) and in the concentrated regimes ($1 < \alpha\phi < 15$). In the dilute regime, the barrier improvement factor is a linear function of (ϵ and a power function of ($\alpha\phi$), with the exponent (~ 1.07) independent of orientation. In concentrated systems, we find that for aligned flakes or flakes showing small deviations from perfect alignment, the barrier improvement factor approaches the quadratic dependence on ($\alpha\phi$) predicted by theory. However, the power exponent is found to decrease as (ϵ) increases, from 1.71 in the aligned system ($\epsilon = 0$) to ~ 0.9 in the fully random system ($\epsilon = \pi/2$). We propose a scaling which incorporates the effects of both ($\alpha\phi$) and (ϵ) on the barrier improvement factor, resulting in a master curve for all ($\alpha\phi$) and (ϵ). Our results suggest that the anticipated barrier property improvement may not be realized if the flake orientations exhibit a significant scatter around the desired direction.

3.2 Introduction

Flake-filled polymeric composites, incorporating mica, glass, or metallic flakes, offer significant processing and property advantages, such as high dimensional stability and low warpage in molding, uniform in-plane mechanical properties and superior mechanical performance for two-dimensional loading, corrosion protection, sound insulation as well as appearance and color control [1]–[4] Flake-filled polymeric composites also find uses as barrier materials in food packaging, where the objective is to hinder the oxygen, CO_2, or other vapor diffusion to and from a container [5], [6], while maintaining all the formability and design advantages afforded by plastic materials. One additional advantage is that the geometries in which such barrier property improvement is to be realized are very similar to those in which the mechanical superiority of flake-filled systems is also evident, such as in plates, shells, cylinders, pipes, etc.; therefore, barrier improvement can be combined with good mechanical performance. Besides micron-sized flakes of inorganic materials such as mica, nano-scale platelets of clay minerals such as hectorite, saponite, and montmorillonite and more recently graphene-oxide platelets of aspect ratios well over 1000 have been used for this purpose [7]. It has been demonstrated that incorporating such fillers aligned perpendicular to the macroscopic diffusion direction can be very effective in increasing barrier properties by providing a tortuous diffusion path for the diffusing species. When the flakes are randomly placed and well aligned, the predicted barrier efficiency improvement ranges from being ($\sim \alpha\phi$) in dilute systems, where (α) is the aspect ratio and (ϕ) the flake volume fraction, to being $\sim (\alpha\phi)^2$ in more concentrated dispersions [6], [8], [9]. Considering the usually large flake aspect ratio, significant barrier property improvement can be achieved by adding a small amount of filler. Computational and experimental studies are in agreement with these predictions [10]–[18].

While earlier works quantified the difference in barrier properties between aligned and random systems, there is limited understanding on how intermediate orientation states as well as random deviations from a predominant orientation might affect barrier properties. This is a significant shortcoming, especially for flake composites manufactured from the melt state through polymer processing operations [19], [20]. In such operations (extrusion, compression or injection molding, thermoforming and others) flake orientation is achieved as flakes tend to orient along the prevailing flow field – either in the main flow direction with shear flow or transverse to it with extensional flow. Special care is therefore needed in designing polymer processing equipment for a desired flake orientation [21] and even then, it is possible that, when it comes to 'on-site' use, not all flakes will be oriented perpendicular to the macroscopic diffusion direction [19], [20]. Even when the final average orientation is the desired one, not all flakes end up oriented in the desired direction, but instead have a distribution of orientations. The way this misalignment affects barrier properties is not well understood. This work's objective is to address this issue.

3.3 Computational

We carry out steady-state diffusion computations in doubly periodic representative volume elements (RVEs) containing up to 500 individual flake cross-sections. These are added in the domain sequentially, using a random sequential addition (RSA) procedure. Specifically, at each flake placement attempt, three random numbers are used to assign the flake center coordinates and its orientation angle (ϵ). The latter is allowed to be uniformly distributed in the interval $[\epsilon, -\epsilon]$. If $\epsilon = 0$, all flakes are oriented normal to the macroscopic diffusion direction. If $\epsilon = \pi/2$ flakes are allowed to assume completely random orientations. Intermediate states are formed for $0 < \epsilon < \pi/2$. If, after placement, no overlap with other flakes is detected, the process continues with the next flake, until the desired number of flakes has been placed, or, until no flake has been placed after 5M attempts; the latter number signals an abortive case.

High aspect ratio flakes were considered with aspect ratio (α) equal to 50, 100, and 1000. While flakes with (α) in excess of 1000 can be associated with nanocomposites [4], [5], [7], it is known that melt processing severely degrades flake size in traditional as well as nano-flake composites [22]. In that case, our predictions concerning the BIF can be viewed as an upper bound, and composites with substantially lower flake aspect ratios would exhibit lower BIFs.

In order to enable subsequent computational domain meshing, a minimum allowable flake separation (δ) is imposed; we used δ=2t where (t) is the flake thickness. In a rectangular unit cell with dimensions (H) (in the bulk diffusion direction) and (L) containing (N) flakes of dimensions (t, l) with $\alpha = l/t$, the flake area fraction is $\phi = N\alpha t^2/LH$ and each flake length is $l = \sqrt{LH\alpha\phi/N}$. In multi-particle simulations, using doubly periodic RVEs is essential when dealing with elongated particles in order to eliminate artefacts of oriented (or, depleted) layers which appear adjacent to cell boundaries. Figure 3.3 shows unit cells obtained for various values of (ϵ) with flakes extended outside the RVE limits to highlight the doubly periodic geometry. The boundary conditions are cyclic on the right and left boundaries, namely $C_{left}(0, y)$ and $C_{right}(L, y)$. On the top and bottom boundaries, fixed concentration values are prescribed. On each flake surface, we impose $\partial C/\partial n = 0$, indicating that the flakes are impermeable. It is known that in practical flake filled composite applications, surfactants or surface modifiers are often used to facilitate flake dispersion in the polymer matrix and this could create irregular interfaces between the flakes and the matrix. We would expect our results to be valid for such systems also, as long as the flakes remain impermeable and as long as the matrix/flake

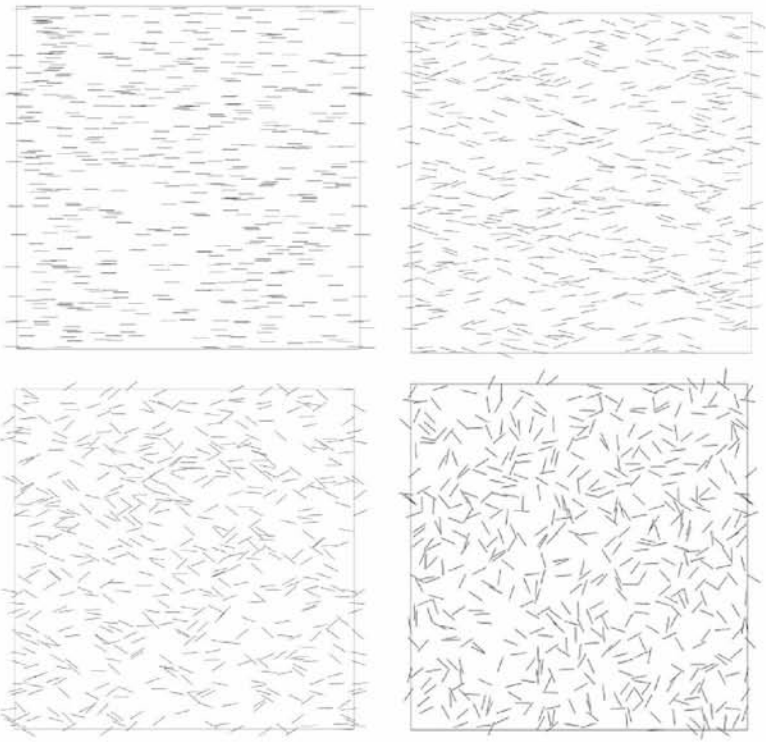

Figure 3.3: Example doubly periodic unit cells containing 500 randomly placed flake cross-sections. From top left to bottom right: $\epsilon = 0, \pi/8, \pi/4$ and $\pi/2$, $\alpha\phi = 1$. Flakes assume random orientations in the interval $[-\epsilon, +\epsilon]$, (α) is the flake aspect ratio and (ϕ) the flake volume fraction.

proportions are not affected, that is, as long as no substantial inter-phase regions are formed [17] At each (ϵ) and $(\alpha\phi)$, we generate 10 different realizations. The computational meshes are created by the mesh generating program Salome through an automated procedure developed in-house and each contain $\sim 10^6$ triangular elements. Figure 3.4 shows examples. These meshes are used by OpenFoam^{TM} to solve the steady-state diffusion equation $\nabla^2 C = 0$, C being the solute concentration, and obtain the distribution of C in the domain of interest. An isotropic matrix material assumption is also made. Figures 3.5 and 3.6 show typical concentration distributions, in which flake distributions corresponding to large $(\alpha\phi)$ can also be seen. It is clear that, in the presence of orientational randomness, the macroscopically one-dimensional distribution of (C) typical of dilute systems becomes progressively two dimensional as $(\alpha\phi)$ increases. This is at the heart of the observed variation in D_{eff}, as will be discussed in the following section. The solution also supplies the value of $(\partial C/\partial n)$ at each point on the upper (or lower) boundary. Thus, the mass flux along this boundary can be calculated as

$$J = -D_0 \int_0^L \frac{\partial C}{\partial n} dx \tag{3.1}$$

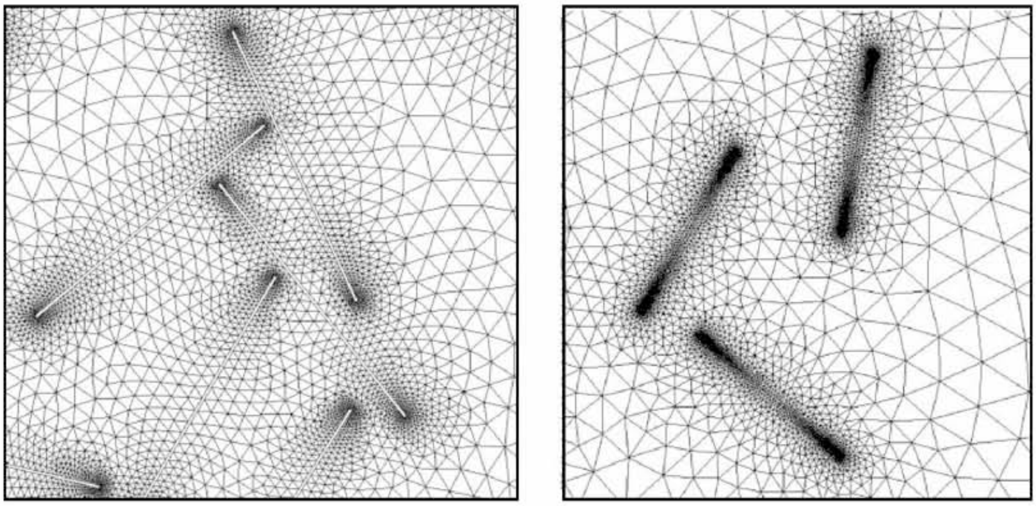

Figure 3.4: Computational mesh details. (α) is the flake aspect ratio and (ϕ) the flake volume fraction. (Left) α =100 and $\alpha\phi$ =1, (Right) α =1000 and $\alpha\phi$ =0.1

where $\boldsymbol{n}$ is the outward unit vector and L is the width of the unit cell.

Because of impermeable flakes crossing boundaries, which results in sudden local changes of the flux, care must be taken in performing this integration. In this work, we used adaptive intervals and only accepted values of the integral when these were convergent with refinement. Equating this flux with the one obtained from Fick's law in a macroscopic equivalent cell (whose diffusivity is D_{eff}), we obtain

$$D_{eff} = \frac{H \cdot D_0}{\triangle C \cdot L} \int_0^L \frac{\partial C}{\partial N} dx \tag{3.2}$$

where C is the macroscopically imposed concentration difference and D_0 the diffusivity of the matrix material. These effective diffusivities will be presented and discussed for various values of (ϵ), (α), and (ϕ) in the following sections.

We examined how the number of flakes included in the RVE affected the computed D_{eff}. Due to the doubly periodic nature of our RVEs, a convergent value is achieved with a relatively small (100) number of flakes; however, we chose to work with N=500 to allow the systems to form inter-flake arrangements closer to what might be encountered in reality (e.g. Figures 3.5 and 3.6) and whose existence will be reflected in the computed effective diffusivities. In addition, and since the flake length to the characteristic length ratio of the unit cell is $l = \sqrt{LH} = \sqrt{\alpha\phi/N}$, it is evident that a larger (N) will help keep that ratio at acceptable levels; for $\alpha\phi$ and N=500 that ratio is 0.17, which we deem acceptable, given that our unit cells are doubly periodic.

One note on the actual orientation statistics of the generated geometries is in order. While at

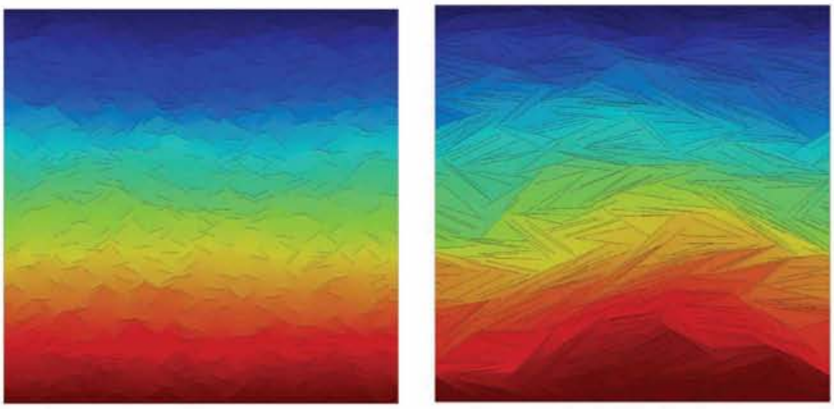

Figure 3.5: Concentration distribution in samples with $\epsilon = \pi/4$. The number of flakes is N=500. Flakes assume random orientations in the interval $[-\epsilon, +\epsilon]$,(α) is the flake aspect ratio and (ϕ) the flake volume fraction.

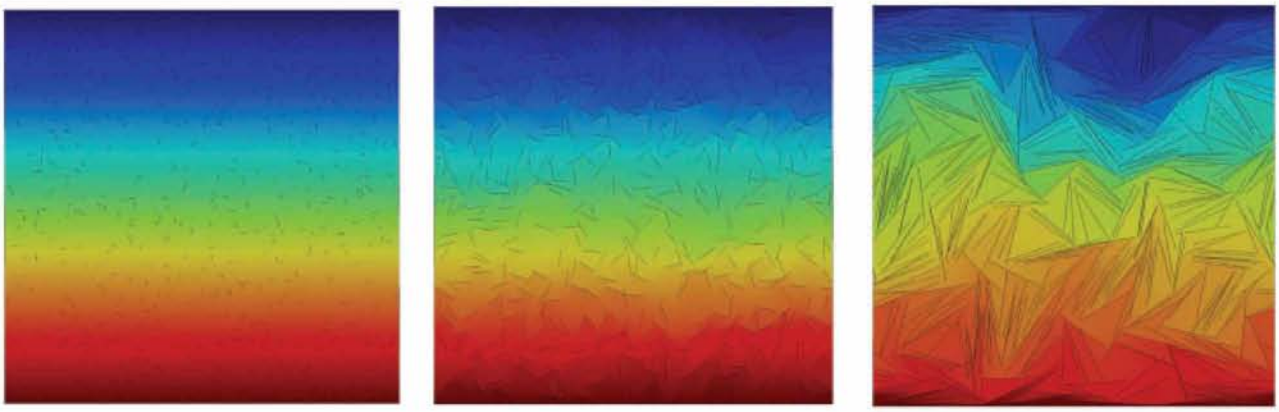

Figure 3.6: Concentration distribution in randomly oriented samples $\epsilon = \pi/2$. The number of flakes is N=500. Flakes assume random orientations in the interval $[-\epsilon, +\epsilon]$,(α) is the flake aspect ratio and (ϕ) the flake volume fraction.

lower concentrations, the target random distribution of orientation angles is readily achieved, this is not a given at high $\alpha\phi$, as seen in Figures 3.5 and 3.6. Besides checking the orientation angle frequency distribution (the cumulative distribution would be a straight line for uniformly distributed orientation angles), we also evaluated a more formal orientation metric, namely the flow orientation strength (f) defined as $f = 1 - 4det(\mathbf{A})$ where ($\mathbf{A}$) is the orientation tensor whose components are defined as $A_{ij} = \langle p_i p_j \rangle$. The brackets indicate ensemble averaging over the entire flake population and p is the the orientation vector of each flake cross-section [21].

For a random orientation, we expect that f=0. For the two-dimensional cross-sections considered in this study, $p_1 = \sin\theta, p_2 = \cos\theta$, and the tensor $\mathbf{A}$ is

$$\boldsymbol{A} = \begin{vmatrix} \langle \sin^2\theta \rangle & \langle \sin\theta\cos\theta \rangle \\ \langle \sin^2\theta\cos\theta \rangle & \langle \cos^2\theta \rangle \end{vmatrix} \tag{3.3}$$

It is straightforward to compute the orientation parameter in our computational samples (f), since the orientation vectors $\boldsymbol{p}$ of all flakes are directly available. For $\alpha\phi$ =10, in a set of 10 realizations, we find that the average orientation parameter is $f_{av}(\alpha\phi = 10) = 0.00961 \pm 0.0051$ (at the 95% confidence level). At the more extreme value of $\alpha\phi$ =20 (at which we have not reported results for $\pi/2$), we find that $f_{av}(\alpha\phi = 20) = 0.028 \pm 0.02$. For $f_{av}(\alpha\phi = 1) =$ 0.00907±0.0037. For comparison, a calculation of (f) in which 500 angles (θ_i) were simply picked using a random number generator (without eliminating overlaps and thus without creating the structures of Figure 3.6 gave $f \sim 0.00202$. In conclusion, for randomly oriented systems ($\epsilon = \pi/2$), there is a gradual deviation of the orientation parameter (f) from zero, as well as an increase of the corresponding standard deviation with increasing ($\alpha\phi$) but only at very high ($\alpha\phi$). For ($\alpha\phi$) at which we report results, the related statistics confirm that we are still safe in what would be considered "random" regime.

One final computational issue arising in fully aligned high ($\alpha\phi$) systems is the fact that flakes may end up placed very close to the upper/lower RVE boundary and due to their large length and parallel orientation effectively "screen" a large portion of it. This can result in high scatter in the predicted D_{eff} values, something that is not expected from the physics of the problem. The generated meshes can also be severely distorted in that region and this is significant, since subsequent flux calculation requires differentiating the concentration profile across that line. This was resolved by setting, for aligned systems only, a minimum flake separation from the upper/lower boundaries equal to 20 times the flake thickness and by finely meshing these regions.

3.4 Results and discussion

In the following, we present the results of a comprehensive computational study of diffusion across doubly periodic unit cells, each containing 500 randomly placed impermeable flakes of rectangular cross-section. Complete randomness corresponds to $\epsilon = \pi/2$, while more narrow distributions are obtained for $\epsilon < \pi/2$. This is a situation of relevance to flake composites manufactured from the melt state (or through other liquid-based processing routes), where a flow-induced average orientation is typically accompanied by random variations around that average orientation.

Figure 3.7 plots the barrier improvement factor (BIF=D_0/D_{eff}) versus the maximum misalignment angle (ϵ) for all computational results. It is evident that, for the (ϵ) and ($\alpha\phi$) studied, the computed BIF's vary over five orders of magnitude; this indicates that further data analysis is justified. Figure 3.8 presents D_0/D_{eff} versus ($\alpha\phi$). One observes that the flake aspect ratio appears to have very little effect on D_{eff} for the (α) studied. Earlier studies [15] show that, in the dilute limit, aspect ratios higher than 50 at constant ($\alpha\phi$) do not noticeably change the diffusion coefficient, which approaches a plateau value. Our data suggests that this conclusion can be extended at least into the semi-concentrated regime. Obviously, the key observation concerning the data in Figure 3.8 is that the effective diffusivity at each (ϵ) appears to be a power function of ($\alpha\phi$), namely

$$D_{eff} = \frac{D_0}{1 + m(\alpha\phi)^n} \tag{3.4}$$

in which the power exponent (n) seems to not remain constant at the higher ($\alpha\phi$). For this reason, the following data analysis will be carried out separately for the dilute regime ($\alpha\phi \leq 1$) and the more concentrated systems – ($\alpha\phi$) up to 15.

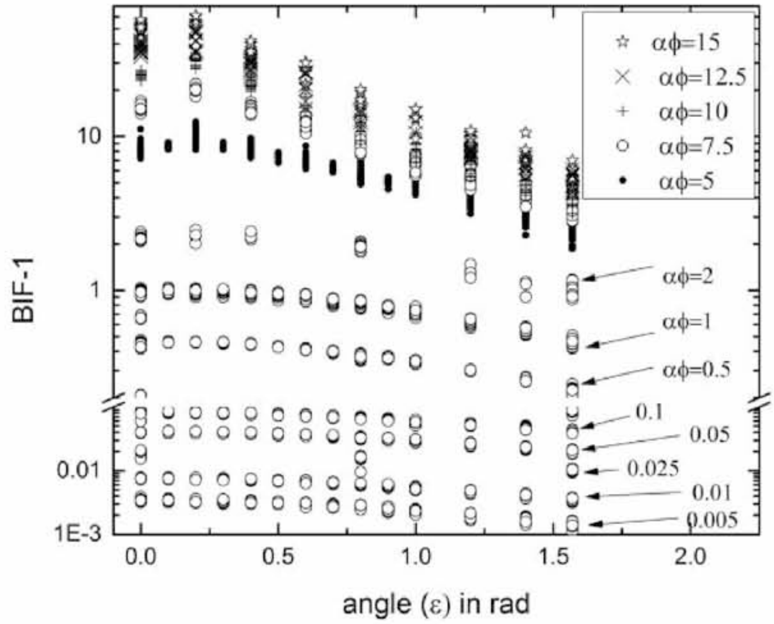

Figure 3.7: Computed barrier improvement factor (BIF) versus angle. All results (2552 data points) corresponding to $\alpha = 50, 100, 1000$, misalignment angles ($0 < \epsilon < \pi/2$) and $\alpha\phi$ as indicated. Flakes assume random orientations in the interval $[-\epsilon, +\epsilon]$, (α) is the flake aspect ratio and (ϕ) the flake volume fraction

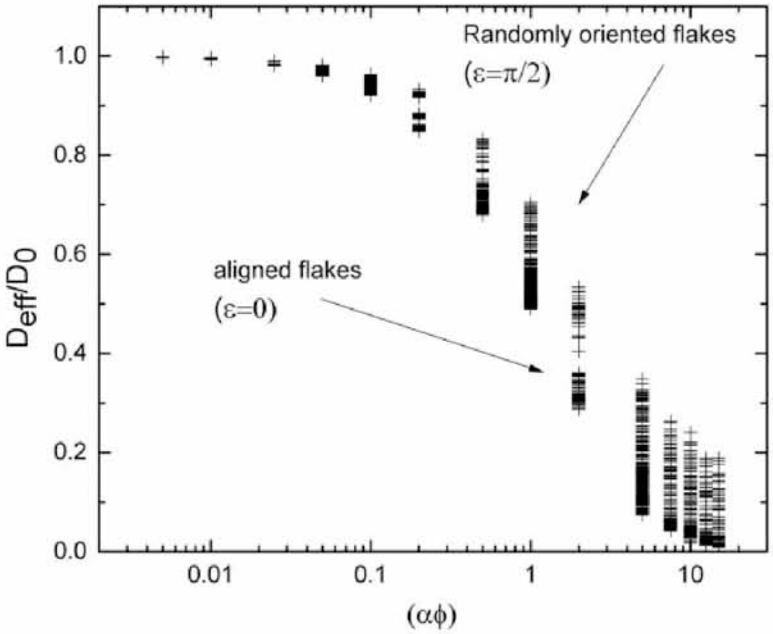

Figure 3.8: D_{eff}/D_0 versus $\alpha\phi$. All computational results (2552 data points) corresponding to α =50, 100, 1000, all misalignment angles ($0 < \epsilon < \pi/2$) and $0.005 < \alpha\phi < 15$. Aligned flakes form the lower edge of the data envelope, while randomly oriented systems with $\epsilon = \pi/2$ the upper edge. Flakes assume random orientations in the interval $[-\epsilon, +\epsilon]$, (α) is the flake aspect ratio and (ϕ) the flake volume fraction

3.4.1 Dilute systems ($0.005 \leq \alpha\phi \leq 1$)

Figure 3.9 plots ln(BIF-1) versus ln($\alpha\phi$) for $\alpha\phi \leq 1$ and selected (ϵ) along with the best-fit lines. All lines are parallel to one another suggesting that the exponent (n) in Equation 3.4 is not a function of (ϵ). The mean for (n) is 1.07, its standard deviation 0.00923 and the 95% confidence interval is $\pm 4 \cdot 10^{-4}$.

Equation 3.4 is an excellent fit to the computational data at all (ϵ), with a correlation coefficient greater than 99% in all cases. Further data analysis suggests that both parameters (m) and (n) are very weakly dependent on (α). We find that (m) varies linearly with (ϵ) between 0 and $\pi/2$ (99.5% correlation), with slope 0.317 and intercept 1.021, while (n) is practically constant and averaging 1.07 – as evidenced by the lines in Figure 3.9 being parallel to each other. If these are taken into account, Equation 3.4 can be written in terms of the BIF as

$$\frac{BIF-1}{1.021-0.317\epsilon} = (\alpha\phi)^{1.07} \tag{3.5}$$

Equation 3.5 suggests a scaling of the computational data in the dilute regime for all states of misalignment. Statistical analysis of the results in light of equation 3.5 shows that at the 95%

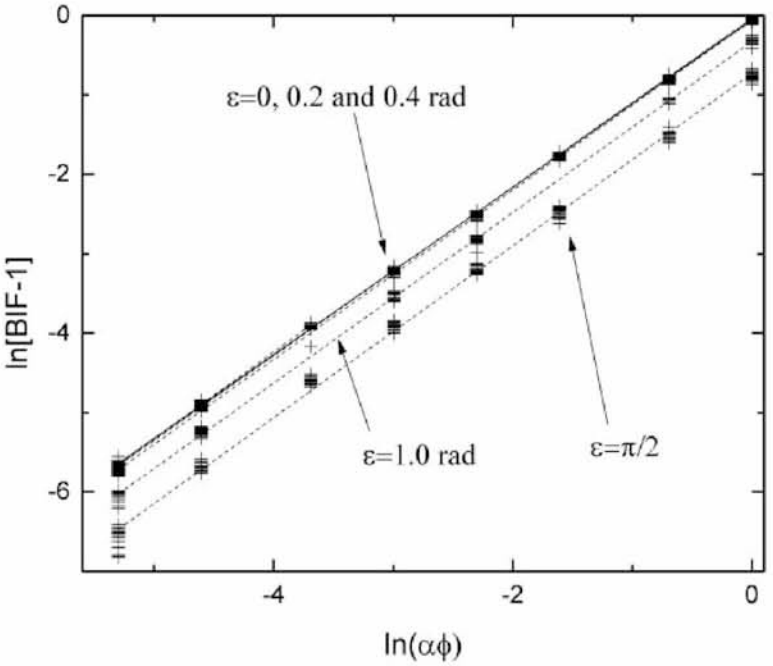

Figure 3.9: Computational results for the barrier improvement factor (BIF) versus $\ln(\alpha\phi)$ in the dilute regime at selected misalignment angles (ϵ). Flakes assume random orientations in the interval $[-\epsilon, +\epsilon]$, (α) is the flake aspect ratio and (ϕ) the flake volume fraction

confidence level, it is

$$\frac{BIF-1}{(1.021-0.317\epsilon)\cdot(\alpha\phi)^{1.07}} = 1.004 \pm 0.0034 \tag{3.6}$$

Figure 3.10 plots the computational results as suggested by Equation 3.5. The scatter observed at all ($\alpha\phi$) and for all orientation states ($0 \leq \epsilon \leq \pi/2$) is substantially reduced. Figure 3.10 also shows the model predictions of Lape et al. [8] according to which the BIF is given by

$$BIF = \frac{D_0}{D_{eff}} = \frac{(1+\alpha\phi/3)^2}{1-\phi} \tag{3.7}$$

In this case, for (α) and ($\alpha\phi$) comparable to those used in our computations, we can safely set $1-\phi \sim 1$ in which case the model of Lape et al. [8] is a quadratic polynomial in ($\alpha\phi$) and in the dilute regime, the linear term dominates.

The linear relationship $F(\epsilon) = 1.021 - 0.317\epsilon$ was derived from analyzing the computational data. In addition, we have examined the use and performance of functions of the form $S(\epsilon) = A\cos^2(\epsilon) + B\sin^2(\epsilon)$ to describe the misalignment effect on diffusivity. This functional form can be inferred by closely inspecting Figure 3.7 in the dilute regime, and this inference also appears in the orientation distribution function of Yang et al. [23] used to describe flake orientation in composite coatings. We fitted our data with a function of the form $S(\epsilon)$ and found the best-fit parameters to be $A = 1.01$ and $B = 0.53$. The original data can therefore also be reduced to a master expression of the form

$$\frac{BIF - 1}{[1.01\cos^2\epsilon + 0.53\sin^2\epsilon] \cdot (\alpha\phi)^{1.07}} = 0.9984 \pm 0.0033 \tag{3.8}$$

The two expressions, Equations 3.6 and 3.8 are practically equivalent and this can be understood by observing that the scaling function $F(\epsilon)$ is essentially a linear approximation of $S(\epsilon)$. Equation 3.8 allows us to compare our computations and model predictions to experimental evidence [23] namely that for small misalignment angles (θ), it is $D_{eff}(\theta = 0)/D_{eff}(\theta) \approx \cos^2\theta$, in which $\theta = 0$ corresponds to a composite with flakes fully aligned normal to the diffusion direction. The above statement implies that $BIF \approx \cos^2\theta/D_{aligned}$ and, since in the dilute regime $1/D_{aligned} \sim \alpha\phi$, we deduce that per experimental evidence $BIF \sim (\alpha\phi)^{1.07}\cos^2(\epsilon)$ for small (θ). From Equation 3.8, one easily sees that for small angles ($\sin(\epsilon) \sim 0$) our computations and model predict that $BIF \sim (\alpha\phi)^{1.07}\cos^2(\epsilon)$, which agrees with the above experimental observation – if the "misalignment" angle θ in the previous expression is directly related to (ϵ) of our work. Without additional information, it is logical to consider that to be the case; however, for that reason, we treat this agreement as "qualitative".

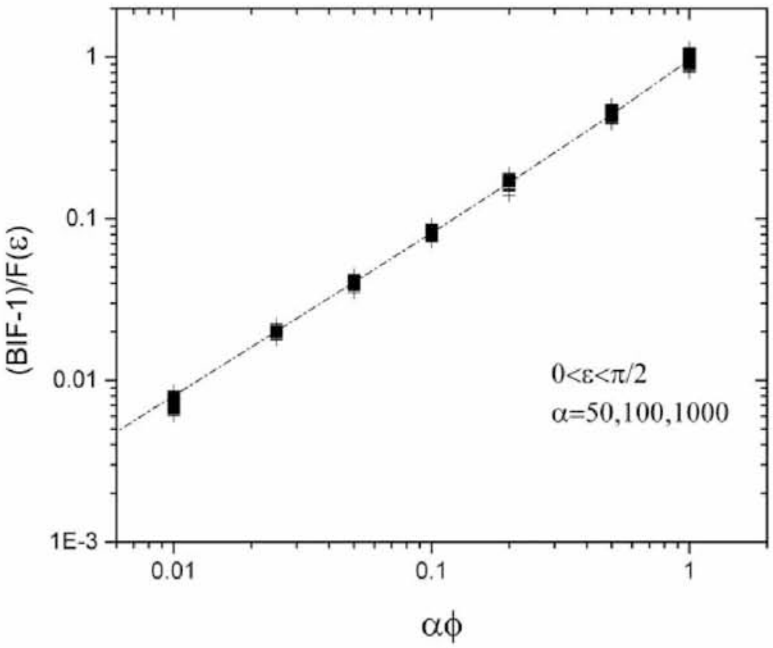

Figure 3.10: Computed barrier improvement factor (BIF) versus $\alpha\phi$ in the dilute regime, plotted as suggested by Equation 3.5, where $F(\epsilon) = 1.021 - 0.317\epsilon$, with ($\epsilon$) in rad. The broken line are the predictions of Lape et al. [8] for the quantity (BIF-1); these correspond to a fully aligned composite ($\epsilon = 0$). Flakes assume random orientations in the interval $[-\epsilon, +\epsilon]$, (α) is the flake aspect ratio and (ϕ) the flake volume fraction

3.4.2 Concentrated systems ($2 \leq \alpha\phi \leq 15$)

Similar to Figure 3.9, Figure 3.11 plots the computed BIF versus $\ln(\alpha\phi)$ in the concentrated regime. It is evident from these as well as from additional results at all other (ϵ) values that the exponent of the power law Equation 3.4 is now a strong function of the misalignment angle (ϵ). We find that it can be approximated as $n(\epsilon) = 1.632 - 0.575(\epsilon)$, with the angle ($\epsilon$) expressed in rad. The correlation coefficient of that fit is 0.972. On the other side, (ϵ) and (m) were not correlated (correlation coefficient 0.07) and (m) is therefore approximated by its average value m=0.793±0.006 (95% confidence level).

A correlation between BIF and ($\alpha\phi$) in the concentrated regime could therefore be

$$\frac{1}{1.632 - 0.575\epsilon} ln\left(\frac{BIF - 1}{0.793}\right) = ln(\alpha\phi) \qquad (3.9)$$

If this were to hold, the BIF data plotted versus ($\alpha\phi$) in the manner suggested by Equation

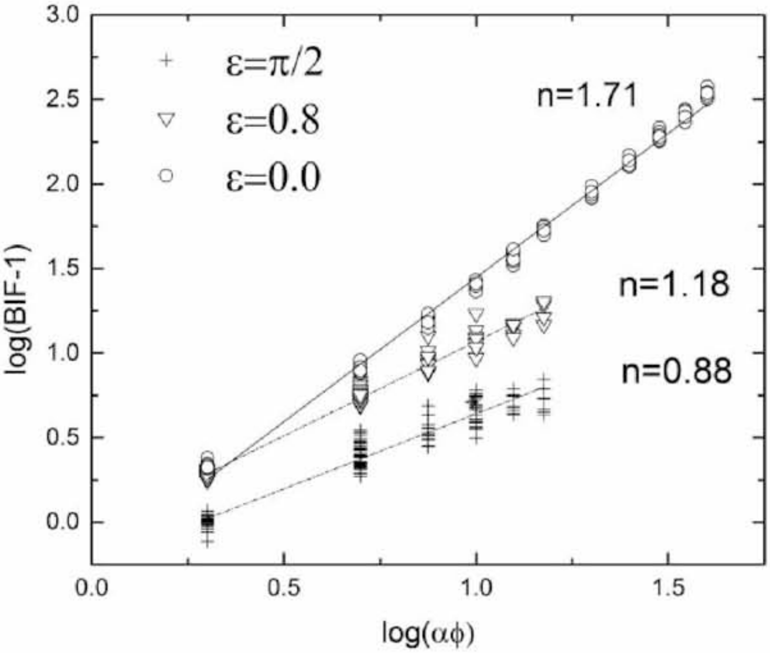

Figure 3.11: Computed barrier improvement factor (BIF) versus $\ln(\alpha\phi)$ in the concentrated regime ($\alpha\phi > 1$). For clarity, only data corresponding to ϵ=0, 0.8, and $\pi/2$ are shown (294, 83, and 294 data points, respectively). The best-fit lines and their slopes (n) are also shown. α=50, 100, and 1000. Flakes assume random orientations in the interval $[-\epsilon, +\epsilon]$, (α) is the flake aspect ratio and (ϕ) the flake volume fraction

3.9 would fall on a straight line with unit slope. Figure 3.12 shows that this is indeed the case, with the slope of the best-fit line being 1.046. The correlation coefficient of $\frac{1}{1.632-0.575\epsilon} ln\frac{BIF-1}{0.793}$ versus $\ln(\alpha\phi)$ is 0.973. There is still scatter around that line; however, this is anticipated for such dense systems and we note the significant reduction in scatter as compared to the raw data; in that case, the correlation between ln(BIF-1) and $\ln(\alpha\phi)$ is 0.743.

Statistical analysis of the results in light of Equation 3.9 above shows that at the 95% confidence level, it is

$$\frac{ln(\alpha\phi)\cdot(1.632-0.575\epsilon)}{ln\left(\frac{BIF-1}{0.793}\right)} = 1.0464 \pm 0.0197 \tag{3.10}$$

It is interesting to see the complete picture, over all (ϵ) and $(\alpha\phi)$ studied (Figure 3.13). In the vertical axis, the raw data, presented as ln(BIF-1), are shifted upwards by five units so as to be clearly discernible from the scaled data, which are presented as

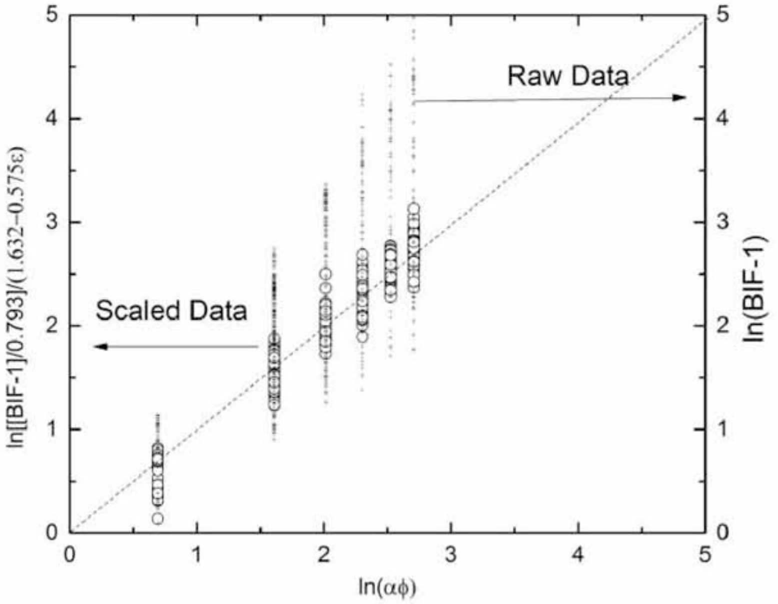

Figure 3.12: Summary of computed barrier improvement factor (BIF) versus $\ln(\alpha\phi)$ at high concentration ($\alpha\phi$= 2, 5, 7.5, 10, 12.5, 15) for $\alpha\phi$ =50, 100, 1000 and (ϵ) from 0 to $\pi/2$. The data transformed as suggested by Equation 3.9 are shown as circles (left axis). The raw data are shown as (+) are plotted as ln(BIF-1) (right axis). There is a total of 985 data points. Flakes assume random orientations in the interval $[-\epsilon, +\epsilon]$, (α) is the flake aspect ratio and (ϕ) the flake volume fraction

$$DATA = ln[(BIF-1)/F(\epsilon)] \quad for \quad \alpha\phi \leq 1 \tag{3.11}$$

and

$$DATA = \frac{ln(BIF-1)/0.793}{1.632-0.575\epsilon} \quad for \quad \alpha\phi > 1 \tag{3.12}$$

The scaled data, for all $(\alpha\phi)$, can be described as a linear function of $\ln(\alpha\phi)$ with slope 1.05 and intercept 0.07 (correlation 0.999) One final note on how the data behaves for perfect alignment ($\epsilon = 0$) and complete randomness ($\epsilon = \pi/2$). Figure 3.14 shows the BIF predictions from

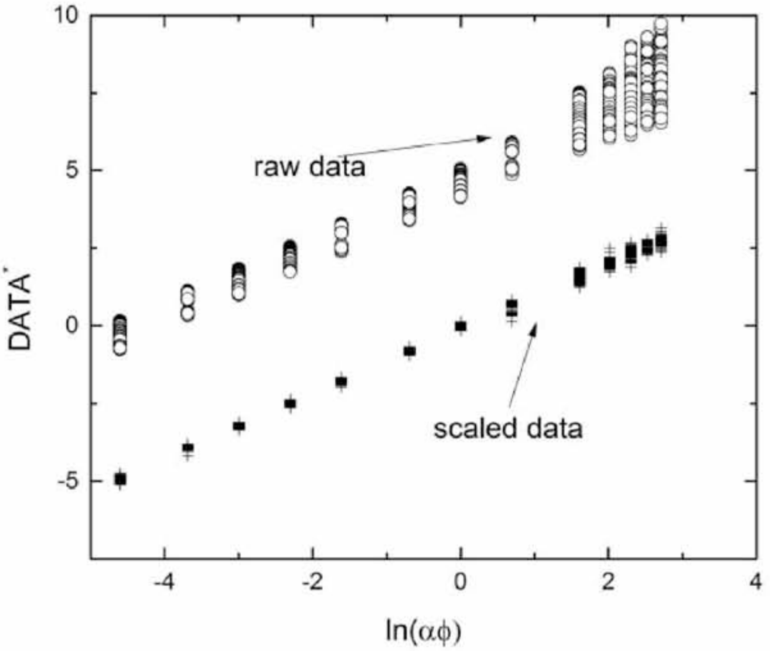

Figure 3.13: Summary of all computed results (over 2500 data points) plotted as suggested by equations 3.11 and 3.12. The raw data have been shifted up by five units, so as not to overlap with the scaled results. The scatter reduction offered by the proposed scaling, both in the dilute and concentrated regime, is evident. (α) is the flake aspect ratio and (ϕ) the flake volume fraction

the data-derived models in this study, namely Equation 3.5 for $\alpha\phi \leq 1$ and Equation 3.9 for $\alpha\phi > 1$. Also, shown in Figure 3.14 are the model predictions of Lape et al. [8] for aligned flakes and Liu et al. [24] in which $BIF \approx (1 + 2\alpha\phi/3\pi)^2$ for randomly oriented flakes. For the aligned systems, it is clear that the Lape et al. [8] model agrees with our data very well and into the concentrated regime, approaching a quadratic rise with ($\alpha\phi$). However, the randomly oriented composite is very different. While up to $\alpha\phi \sim 2$, its BIF follows the same trend with the oriented data, namely BIF-1 $\sim (\alpha\phi)^{1.07}$, and is in good agreement with the Liu et al. [24] model up to $\alpha\phi \sim 2$. In the concentrated regime, the BIF rate of rise with ($\alpha\phi$) drops and the BIF appears to be trending towards a plateau value.

The implication of these results is significant. While the BIF of the aligned flake composite shows a near-parabolic increase with ($\alpha\phi$), as would be expected from theory [8], [9] randomly oriented composites deviate from that behaviour and, instead, achieve BIF values which seem to plateau for increasing ($\alpha\phi$) at a fraction of the BIF of the corresponding aligned composite. A similar result is implicit in the work of Lusti et al.[15] While these authors did not elaborate on the matter, they presented computational results for 3D randomly placed and oriented systems of disks, in the dilute and semi-dilute regimes, in terms of the parameter

$\chi = (D_0 - D_{random})/(D_0/D_{aligned})$, and proposed a polynomial form for (χ) which best described their data, namely $\chi = \chi(\alpha\phi) = 0.0082(\alpha\phi)^2 + 0.0879(\alpha\phi) + 0.4157$. While that polynomial is strictly limited to the $(\alpha\phi)$ in which data were obtained $(\alpha\phi < 7)$, it shows that the BIF of a randomly oriented flake system will grow slower with $(\alpha\phi)$ in the semi-dilute regime than the BIF of a fully aligned system. Figure 3.15 plots our computational results for the $(BIF)_{random}/(BIF)_{aligned}$ ratio. We also plot the same ratio, when the BIF_{random} is computed from the polynomial $\chi(\alpha\phi)$ proposed in Lusti et al. [15] and the $BIF_{aligned}$ is the same as the one computed in our study. Also, we plot the same ratio as $(1 + 2\alpha\phi/3\pi)^2/(1 + \alpha\phi/\lambda)^2$ in which the nominator corresponds to Liu et al. [24] for randomly oriented flakes and the denominator corresponds to Lape et al. [8] for an aligned composite. There is a qualitative agreement between the latter and our computational results up to intermediate $(\alpha\phi)$ (ratio dropping with increasing $\alpha\phi$) and also a quantitative agreement up to $\alpha\phi \sim 2$. At higher $(\alpha\phi)$ values, however, the ratio $(1 + 2\alpha\phi/3\pi)^2/(1 + \alpha\phi/\lambda)^2$ is predicted to approach a plateau, indicating the same (terminal) rate of increase for the BIF_{random} as for the $BIF_{aligned}$ – for very concentrated, or very long flake systems. In this respect, these predictions differ from our results as well as from Lusti et al. [15] This point certainly merits further investigation; however, our work in this direction is complicated by the ordering that naturally occurs in high

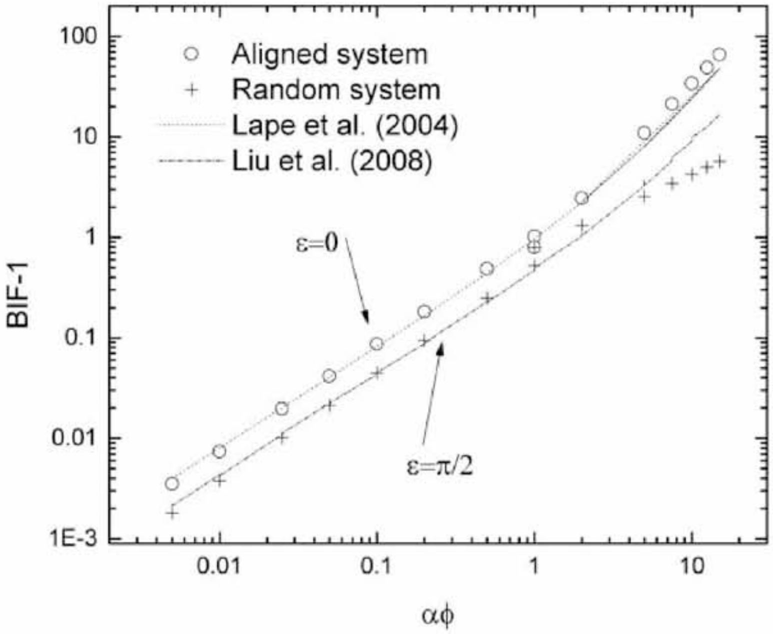

Figure 3.14: Predictions of equations 3.5 and 3.9 for the barrier improvement factor (BIF) of a flake composite in two cases; aligned flakes (o) and randomly oriented flakes (+). The predictions of Lape et al. [8] corresponding to an aligned and those of Liu et al. [24] corresponding to a randomly oriented composite are also shown. (α) is the flake aspect ratio and (ϕ) the flake volume fraction

$(\alpha\phi)$ systems of long flakes and the resulting progressive loss in orientational randomness. It is quite possible that randomly oriented systems at extreme $(\alpha\phi)$ simply do not exist. We are currently researching this topic.

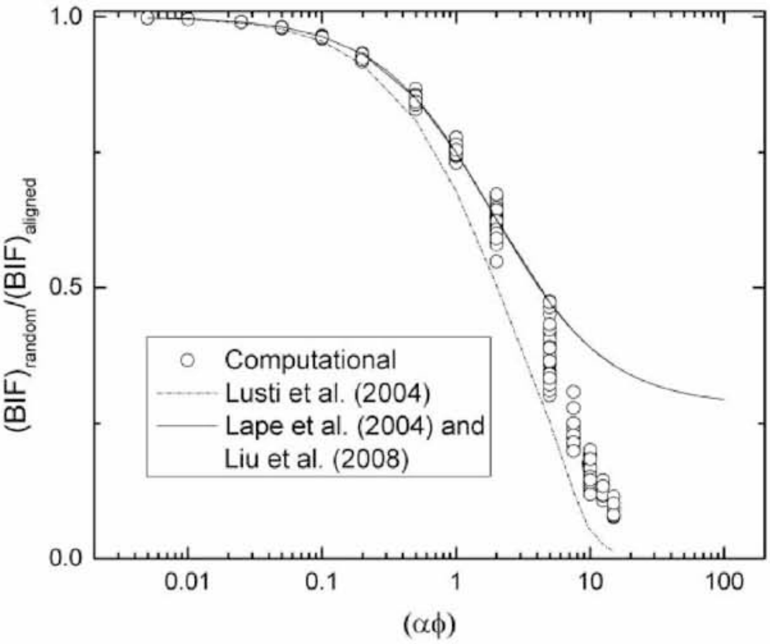

Figure 3.15: Ratio of the barrier improvement factor (BIF) of a randomly oriented composite divided by the BIF of an aligned flake composite as a function of $(\alpha\phi)$, where (α) is the aspect ratio of the flake and (ϕ) its volume fraction. Computational results are shown as points (o). Also, shown are the ratio predictions based on earlier studies [15], [8], [24]

3.5 Conclusions

We have presented the results of a computational study in flake-filled composites aimed at elucidating the effect of deviations from perfect alignment on their barrier properties. These deviations take the form of uniformly distributed random variations in orientation angle (θ) within the envelope $[-\epsilon, +\epsilon]$ in systems in which the average orientation is always perpendicular to the diffusion direction. The computed results for D_{eff} are analyzed and the effect of (ϵ) is decoupled from $(\alpha\phi)$ to a satisfactory degree. These dependencies differ in the dilute $(\alpha\phi \leq 1)$ and in the concentrated regimes $(15 \leq \alpha\phi \leq 15)$. In the dilute regime, the BIF is a power function of $(\alpha\phi)$, with the exponent (~ 1.07) being independent of the extent of orientational randomness, a finding that is in line with existing theories. The effect of misalignment is found to be described by a linear function of the maximum misalignment angle (ϵ). A scaling is proposed by which we derive a simple explicit BIF model which incorporates both, $(\alpha\phi)$ and

(ϵ). Through the proposed scaling, the data collapse on a line and the correlation coefficient is 0.996. We note that the proposed scaling is in agreement with experimental evidence. In the concentrated case ($\alpha\phi > 1$), we find that the power exponent is a function of the maximum misalignment angle (ϵ). For aligned systems ($\epsilon = 0$) or systems showing small deviations from perfect alignment, we find that the BIF approaches the quadratic dependence on ($\alpha\phi$) predicted by theory. However, the power exponent is reduced progressively as the deviation from perfect alignment increases, from 1.71 in the aligned system to ∼0.9 in the fully random one. A scaling is also proposed here by which all data fall on a line of slope 1.04 with a correlation coefficient 0.973. This suggests that the theoretically anticipated improvement in barrier properties may not be realized if the flake orientations exhibit a significant scatter around the desired direction, regardless of the average fiber orientation, which may well be perpendicular to the bulk diffusion direction. Finally, we investigated the $BIF_{random}/BIF_{aligned}$ ratio; our computational results show this ratio decreases as ($\alpha\phi$) increases into the semi-concentrated regime, in line with earlier findings [15].

3.6 References

1. Seubert CM, Nickols ME, Frey J, et al. The characterization and effects of microstructure on the appearance of platelet-polymer composite coatings. J Mater Sci,2016; 51: 2259–2273.
2. Pavlidou S and Papaspyrides CD. A review on polymer-layered silicate nano-composites. Prog Polym Sci 2008; 33: 1119-1198.
3. Pajarito B and Kubuchi M. Flake-filled polymers for corrosion protection. J Chem Eng Jpn 2013; 46: 18–26.
4. Kalendova A, Merinska D, Gerard JF, et al. Polymer/clay nanocomposites and their gas barrier properties. Polym Compos 2013; 34: 1418–1424.
5. Bhunia K, Dhawan S and Sablani SS. Modeling the oxygen diffusion of nanocomposite-based food packaging films. J Food Sci 2012; 77: N29–N38.
6. Lagaron JM and Nunez E. Nanocomposites of moisture-sensitive polymers and biopolymers with enhanced performance for flexible packaging applications. J Plast Film Sheet 2011; 28: 79–89.
7. Lee K-H, Hong J, Kwak SJ, et al. Spin self- assembly of highly ordered multilayers of graphene-oxide sheets for improving oxygen barrier performance in polyolefins. Carbon 2015; 83: 40–47.
8. Lape NK, Nuxoll EE and Cussler EL. Polydisperse flakes in barrier films. J Memb Sci 2004; 236: 29–37.
9. Lebovka N, Khrapatiy S and Vygornitskyi PN. Barrier properties of k-mer packings. Physica A 2014; 408: 19–27.
10. Chen X and Papathanasiou TD. Barrier properties of flake-filled membranes: Review and numerical evaluation. J Plast Film Sheet 2007; 23: 319–346.
11. Guseva O and Gusev AA. Finite element assessment of the potential of plateletfilled polymers for membrane gas separations. J Memb Sci 2008; 325: 125–129.
12. Greco A and Maffezzoli A. Two-dimensional and three-dimensional simulation of diffusion in nanocomposite with arbitrarily oriented lamellae. J Membr Sci 2013; 442: 238–244.
13. Minelli M, Baschetti MG and Doghierri F. Analysis of modeling results for barrier properties in ordered nanocomposite systems. J Memb Sci 2009; 327: 208–215.
14. DeRocher JP, Gettelfinger BT, Wang J, et al. Barrier membranes with different sizes of aligned flakes. J Memb Sci 2005; 254: 21–30.

15. Lusti HR, Gusev AA and Guseva O. The influence of platelet disorientation on the barrier properties of composites: A numerical study. Modell Simul Mater Sci Eng 2004; 12: 1201–1207.
16. Gusev AA and Lusti HR. Rational design of nanocomposites for barrier applications. Adv Mater 2001; 21: 1641–1643.
17. Pajarito BB, Kubuchi M, Sakai T, et al. Effective diffusion in flake-polymer composites with accelerated interphase transport. J Soc Mater Sci Jpn 2012; 61: 860–866.
18. Goodyer CE and Bunge A. Comparison of numerical simulations of barrier membranes with impermeable flakes. J Memb Sci 2009; 329: 209–218.
19. Nawani P, Burger C, Rong L, et al. Characterization of nanoclay orientation in polymer nanocomposite film by small-angle X-ray scattering. Polymer 2010; 51: 5255–5266.
20. Dykes LMC, Torkelson JM, Burghardt WR, et al. Shear-induced orientation in polymer-clay dispersions via in-situ X-ray scattering. Polymer 2010; 51: 4916–4927.
21. Mohamadi M, Garmabi H and Keshavarzi F. An investigation on the effects of organo-modified fluoromica on mechanical and barrier properties of compatibilized HDPE nanocomposite films. J Plast Film Sheet 2016; 32: 10–33.
22. Papathanasiou TD and Guell DC. Flow induced alignment in composite materials. Cambridge, UK: Woodhead Publishing, 1997.
23. Yang C, Smyrl WH and Cussler EL. Flake alignment in composite coatings. J Memb Sci 2004; 231: 1–12.
24. Liu W, Hoa SV and Pugh M. Water uptake of epoxy-clay nanocomposites: Model development. Compos Sci Technol 2008; 68: 156–163.

Chapter 4

The Barrier Properties of Flake-Filled Composites with Precise Control of Flake Orientation[1]

Summary

In this chapter we deal with the properties of flake filled composites in cases where all the flakes assume the same orientation. In this cases all the flakes are parallel to each other and all have the same angle θ with the X axis (Figure 4.1).

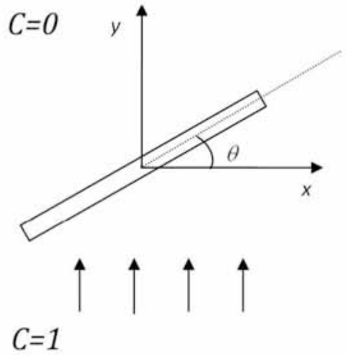

Figure 4.1: Flake geometry used in this chapter. All flakes assume an angle θ with the horizontal (X) axis. The direction of diffusion is also shown (from C=1 to C=0).

---

[1] As published in Materials Sciences and Applications: Tsiantis, A. & Papathanasiou, Thanasis. (2017). The Barrier Properties of Flake-Filled Composites with Precise Control of Flake Orientation. Materials Sciences and Applications. 08. 234-246. 10.4236/msa.2017.83016.

We solve an elliptic equation for the concentration field of diffusion (steady state) in numerous simulations with unit cells filled within a range of N=500 to 3000 flakes and at various orientations (θ). We use very elongated particles (α=100 & 1000) and $\alpha\phi$ ranging from 0.01 to 40. Especially for extremely dense systems ($\alpha\phi > 15$) this work is the first in the literature to introduce results for the BIF (Barrier Improvement Factor).

By combining the models of Nielsen and Lape for the principal diffusivity components (normal and parallel to the flake axis) we define a new theoretical model for the BIF and it is clearly seen how our model exhibits an excellent agreement with the numerical results at the full range of all the studied parameters, in more than 4 orders of magnitude of $\alpha\phi$ (from 0.01 to 40) and for $\theta = 0^o$ to 90^o. Finally the change in the behaviour of BIF at dense systems is demonstrated and specifically our model and the results clearly indicate that at these high density systems the quadratic dependence of BIF with $\alpha\phi$ is lost as θ increases. This shows the importance of flake alignment and is discussed in detail in the final section of this chapter especially in the case of dense systems.

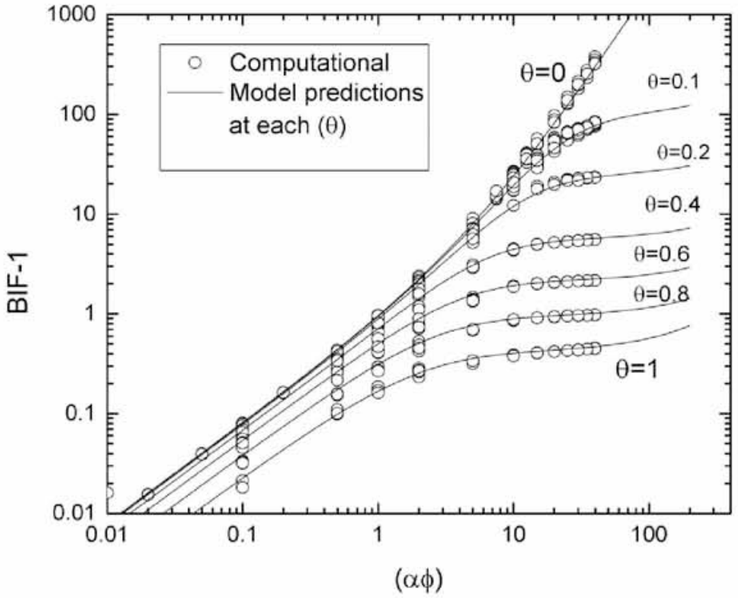

Figure 4.2: Summary of computational results (circles) for α =1000 and θ =0, 0.1, 0.2, 0.4, 0.6, 0.8, and 1.0, all in rad. We observe the anticipated quadratic rise of the BIF with ($\alpha\phi$) for higher values of ($\alpha\phi$) at θ=0 and also a progressively lower plateau reached at increasing values of the misalignment angle (θ). The predictions of Equation 4.11 are also shown as solid lines. Total of 1295 data points.

4.1 Abstract

Additive manufacturing, especially in the form of 3D printing, offers the exciting possibility of generating heterogeneous articles with precisely controlled internal microstructure. One area in which this feature can be of significant advantage is in diffusion control, specifically in the design and fabrication of microstructures which minimize the rate of transport of a solute to and from a contained fluid. In this work we focus on the use of flake-filled composites and study computationally and theoretically the effect of misalignment on their barrier properties. We conducted over 1500 simulations in two-dimensional, doubly-periodic unit cells each containing up to 3000 individual flake cross-sections which are randomly placed and with their axes forming an angle $(\pi/2 - \theta)$ with the direction of macroscopic diffusion. We consider long-flake systems of aspect ratio (α) 100 and 1000, from the dilute $(\alpha\phi{=}0.01)$ and into the concentrated $(\alpha\phi{=}40)$ regime. Based on the rotation properties of the diffusivity tensor, we derive a model which is capable of accurately reproducing all computational results $(0.01 < \alpha\phi < 40$ and $0 < \theta < \pi/2)$. The model requires as inputs the two principal diffusivities of the composite, normal and parallel to the flake axis. In this respect, we find that the models of Lape et al. [1] and Nielsen [2] form an excellent combination. Both our model and our computational data predict that at $\mid \theta \mid > 0$ the quadratic dependence of the Barrier Improvement Factor (BIF) on $(\alpha\phi)$ is lost, with the BIF approaching a plateau at higher values of $(\alpha\phi)$. This plateau is lower as (θ) increases. We derive analytical estimates of this maximum achievable BIF at each level of misalignment; these are also shown to be in excellent agreement with the computational results. Finally we show that our computational results and model are in agreement with experimental evidence at small values of (θ).

4.2 Introduction

Additive manufacturing, especially in the form of 3D printing, offers the exciting possipossibility of generating articles with precisely controlled internal microstructure. One area in which this feature can be of significant advantage is in diffusion control, specifically in the design and fabrication of microstructures which allow for minimization of the transport of a solute to/from a contained fluid. Flake-filled polymeric composites, incorporating mica, glass or metallic flakes have found many uses in this direction, as they offer significant processing and property advantages, namely high dimensional stability and low warpage in molding, uniform in-plane mechanical properties, corrosion protection, sound insulation as well as appearance and color control [3]-[7]. Micron-sized flakes of inorganic materials such as mica, nano-scale platelets of clay minerals such as hectrite, saponite and montmorillonite and more recently graphene-oxide platelets of aspect ratios well over 1000, have been used for this purpose [6]. It has been demonstrated that incorporation of such fillers aligned perpendicular to the direction of macroscopic diffusion can be very effective in increasing the tortuosity of the diffusion path of the diffusing species. When the flakes are in general randomly placed, as would be the case in a flake composite manufactured from the melt, the predicted improvement in barrier efficiency ranges from being $\sim (\alpha\phi)$ in dilute systems, where (α) is the aspect ratio and (ϕ) the volume fraction of the flakes, to being $(\alpha\phi)^2$ in more concentrated dispersions [1], [9]-[16].

One notable disadvantage of traditional processing methods vis-à-vis flake-filled composites is the fact that flake orientation cannot be precisely controlled. In such operations (extrusion, compression or injection molding, thermoforming and others) flake orientation is achieved due to the propensity of the flakes to orient in accordance to the prevailing flow field – either in the main direction of flow when the flow is shear or transverse to it when the flow is extensional [17]. An additional shortcoming of traditional flow-processing routes is the inability to utilize high flake loadings since, in that case, the viscosity of the resulting melt becomes prohibitively high. Given the capability afforded by 3D printing to fully control flake orientation as well as generate articles with flake loadings approaching those at maximum packing, it is desirable to predict the effective diffusion coefficient (or its inverse, the barrier improvement factor, *BIF*) as an explicit function of the flake orientation angle and for very high, previously untenable, concentrations.

The two main approaches which have been used in the literature to-date for this purpose are (i) an ad-hoc incorporation of orientation metrics in existing models for the *BIF* [8], [18] and (ii) derivation of *BIF* models from diffusion path calculations [19]-[21]. In both cases, the proposed models have been derived for low or very-low flake concentrations and have not been extensively tested in the moderate to high-concentration regime, which will be of importance in any 3D printing application. In addition, by not respecting the rotational properties of the diffusivity tensor, these models are not grounded on a sound theoretical footing. This paper addresses the above issues both computationally and theoretically, by proposing a model based on the two principal diffusivities of a flake composite. We also show that the implications of our theoretical model are fully supported by extensive computational results.

4.3 Computational

We carry out steady-state diffusion computations in doubly-periodic unit cells containing up to 3000 individual flake cross-sections. These are added in the domain sequentially, using a Random Sequential Addition (RSA) procedure. Specifically, at each flake placement attempt, two random numbers are used to assign the coordinates of the flake center while its orientation angle (θ) is fixed and the same for all flakes. If, after placement, no overlap with other flakes is detected, the process continues with the next flake, until the desired number of flakes has been placed, or, until no flake can be placed after 50,000 attempts; in this case no geometry is generated. In order to enable subsequent meshing of the computational domain, a minimum allowable distance between flakes is imposed; this is ($2t$) where (t) is the thickness of the flake. Since in this work we have dealt with flakes of high aspect ratio ($\alpha = 100$ and $\alpha = 1000$), this minimum distance requirement is deemed reasonable so as to not result in excessive local mesh refinement. In a rectangular unit cell of dimensions (H) and (L) containing (N) flakes of dimensions (t, α), the flake area fraction (ϕ) is $\phi = N\alpha t^2/LH$ and (l) is the length of each flake $l = \sqrt{LH(\alpha\phi)/N}$. We have looked at systems in which $0.01 \leq 40 \leq \alpha\phi$. At higher values of ($\alpha\phi$) it becomes impossible to fill the space with non-overlapping flake crossections. This not-withstanding, the present study is to our knowledge the first to investigate systems of such large concentration.

In multi-particle simulations, use of doubly-periodic cells is essential when dealing with elongated particles so as to eliminate artefacts of oriented (or, depleted) layers which would otherwise appear adjacent to cell boundaries [10], [15]. The effect of the RVE dimensions on the computed effective diffusivity is also eliminated when using periodic unit cells. A sample unit cell, showing flakes oriented at an angle $\theta = 0.8$ rad with respect to the horizontal (x) axis (extended slightly outside the limits of the unit cell to show the doubly-periodic geometry) is shown in Figure 4.3.

The boundary conditions are cyclic on the right and left boundaries, namely $C_{left}(0, y) = C_{right}(L, y)$. On the top and bottom boundaries, fixed values of concentration are prescribed. On the surface of each flake we impose, indicating that the flakes are impermeable. At each level of (α) and (ϕ) we generate $\sim$ 10 different realizations, each containing up to 3000 randomly

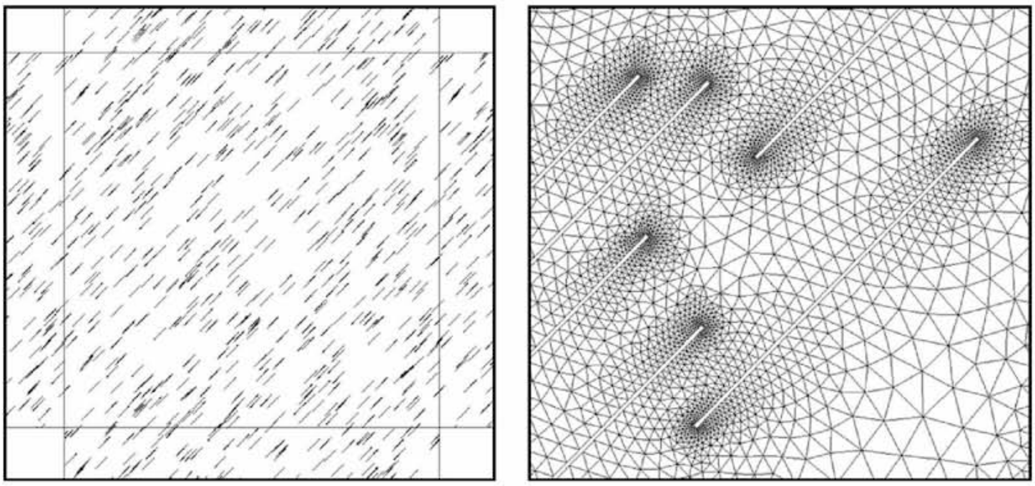

Figure 4.3: Sample unit cell – doubly-periodic – containing 500 flake crossections, all oriented at an angle θ =0.8 rad to the horizontal (x) axis. $\alpha = 100$, $\alpha\phi = 1$. On the right is shown a detail of the computational mesh.

placed flakes. The computational meshes are created by the mesh generating program Salome through an in-house automated procedure and contain between $\sim 10^6$ triangular elements.

These meshes are then used by OpenFoam to solve the steady-state diffusion equation $\nabla^2 C = 0$, (C) being the solute concentration, and provide its distribution in the domain of interest. The assumption of an isotropic matrix material is also made. The solution also supplies the value of $\partial C/\partial \mathbf{n}$ at each point on the upper (or lower) boundary. As a result, the mass flux along this boundary can be calculated as

$$J_n = -D_o \int_0^L \frac{\partial C}{\partial \mathbf{n}} \mathrm{d}x \tag{4.1}$$

where the subscript (n) indicates numerically computed value, $\boldsymbol{n}$ is the outward unit vector and (L) is the width of the unit cell. Because of impermeable flakes crossing boundaries, which results in sudden local changes of the flux, care must be taken in performing this integration. In this work, we used adaptive intervals and only accepted values of the integral when these were convergent with refinement. Equating this flux with the one obtained from Fick's law in a macroscopic equivalent cell (whose diffusivity is D_{eff}) we obtain

$$D_{eff} = \frac{H \cdot D_0}{\Delta C \cdot L} \int_0^L \frac{\partial C}{\partial n} \mathrm{d}x \tag{4.2}$$

where ΔC is the macroscopically imposed concentration difference and H the height of the unit cell. These effective diffusivities will be presented and discussed for various values of (θ), (α) and (ϕ) in the following sections.

4.4 Results and Discussion

In the following we present the results of a comprehensive computational study of diffusion across doubly-periodic unit cells, each containing up to N=3000 randomly placed impermeable flakes of rectangular cross-section. In such a system, the orientation of each flake is defined by the orientation angle (θ) formed between the vertical axis (y), which is taken to be the direction of macroscopic diffusion, and the outward normal vector on the flake surface. The horizontal axis is indicated as (x). Parametric studies have shown that for N≥200 the obtained D_{eff} were practically indistinguishable; this conclusion extended for ($\alpha\phi$) as large as 40; therefore most of our computations have been carried out in RVEs containing 500 flake cross sections. We look at systems ranging from dilute to concentrated and in which the fiber orientation (θ) changes between zero (flake orientation perpendicular to the direction of diffusion) to $\pi/2$ (fibers oriented along the direction of macroscopic diffusion). We have carried out computations in unit cells similar to those of Figure 4.3 for α =100 and $\alpha = 0.01, 0.1, 1.0$ and $\alpha\phi = 10$, as well as for α =1000 and $0.01 \leq \alpha\phi \leq 40$.

4.4.1 Effect of flake misalignment on effective diffusivity

Representative results of the distribution of (C), also showing the corresponding flake distributions, are shown in Figures 4.4 and 4.5. We define as D_{11} the diffusivity of such a system when $\theta = 0^o$ (all flakes oriented perpendicular to the direction of macroscopic diffusion) and D_{22} the diffusivity when $\theta = 90^o$ (all flakes oriented parallel to the direction of diffusion). D_{11} and D_{22}

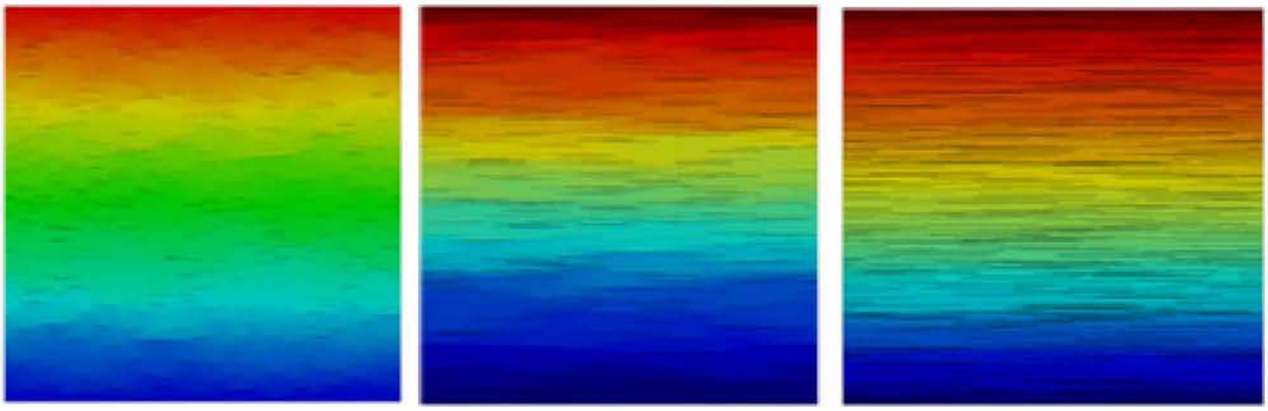

Figure 4.4: Distribution of concentration in geometries with θ =0 and $\alpha\phi$ = 1, 10, 40. The distribution of flakes is also visible. The number of flakes is N=500.

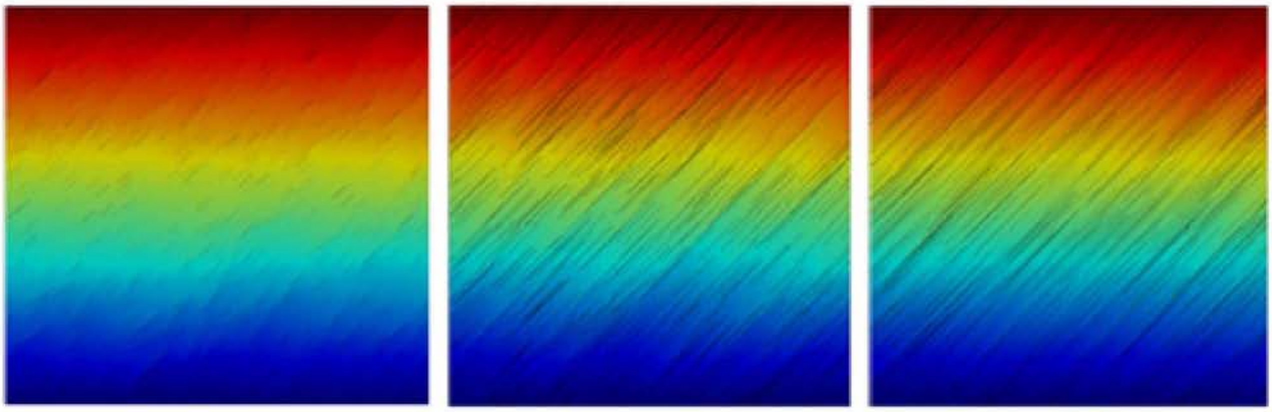

Figure 4.5: Distribution of concentration in geometries with $\theta = \pi/4$ and $\alpha\phi = 1, 10, 40$. The distribution of flakes is also visible. The number of flakes is N=500.

are the principal values of the two-dimensional diffusivity tensor, $\boldsymbol{D}$. The diffusivity tensor **D'** corresponding to a system in which the flakes assume an orientation angle θ (counter-clockwise with respect to the x-axis) can be determined according to the relation $\boldsymbol{D'} = \boldsymbol{Q}\boldsymbol{D}\boldsymbol{Q}^{\boldsymbol{T}}$, where $\boldsymbol{Q}$ is the rotation tensor.

$$Q = \begin{bmatrix} \cos\theta & -\sin\theta \\ \sin\theta & \cos\theta \end{bmatrix} \tag{4.3}$$

Hence

$$D' = \begin{bmatrix} D_{11}\cos^2\theta + D_{22}\sin^2\theta & -D_{11}\sin\theta\cos\theta + D_{22}\sin\theta\cos\theta \\ -D_{11}\sin\theta\cos\theta + D_{22}\sin\theta\cos\theta & D_{11}\sin^2\theta + D_{22}\cos^2\theta \end{bmatrix} \tag{4.4}$$

Therefore, the effective diffusivity of this system in the direction (y) forming an angle $(\pi/2 - \theta)$ with the axis of the flakes will be

$$D_{eff}(\theta) = D_{11}\cos^2\theta + D_{22}\sin^2\theta \tag{4.5}$$

We will investigate the use of Equation 4.5 to determine $D_{eff}(\theta)$, provided the principal permeabilities D_{11} and D_{22} are known. By comparing its predictions to our computational results we will identify which models for D_{11} and D_{22} give the best agreement with computation.

In the first instance we have compared the computational results for dilute cases ($\alpha\phi = 0.01$ and $\alpha\phi = 0.1$) with the predictions of Equation 4.5, in which Nielsen's [2], model has been used for D_{11} and D_{22}, namely

$$D_{22} = D_0 \frac{1-\phi}{1+\phi/2\alpha} \quad \text{and} \quad D_{11} = D_0 \frac{1-\phi}{1+\alpha\phi/2} \tag{4.6}$$

Extensive comparisons have shown that predictions of Equation 4.5 based on Nielsen's model for D_{11} and D_{22} are close to the computational results only for the very dilute regime ($\alpha\phi \sim 0.01$). For progressively higher of ($\alpha\phi$) there is a growing discrepancy.

It is of course possible to use diffusivity models for D_{11} and D_{22} more suitable for concentrated suspensions. A review and evaluation of available models has been carried out by Chen and Papathanasiou [11]. Of the models discussed there, we single out those of Cussler and co-workers [1], [9] mainly because of their relevance to the systems modeled here (randomly placed flakes) as well as due to the small number of adjustable parameters needed in their implementation and their extensive use in the literature. Lape et al. [1] proposed that for diffusion across arrays of unidirectional randomly placed flakes it is

$$\frac{D_0}{D_{eff}} = \frac{(1+\alpha\phi/3)^2}{1-\phi} \tag{4.7}$$

In deriving this model, the tortuosity factor was taken to be $1+\alpha\phi/3$ and it was further assumed that the ratio of the areas available for diffusion is

$$A_0/A_f = (1+\alpha\phi/3)/(1-\phi). \tag{4.8}$$

Implicit in the above derivation is the assumption that the diffusion paths around a flake form straight lines; therefore it is not unreasonable to treat the factor '3' in the expression above as a geometrical parameter that may be adjusted if so suggested by the data. Since that was found to be the case in analyzing our data, we use the model of Lape et al. [1] in the form:

$$\frac{D_0}{D_{eff}} = \frac{(1+\alpha\phi/\lambda)^2}{1-\phi} \tag{4.9}$$

in which (λ) is an adjustable geometrical parameter. Another model suitable for concentrated aligned flake systems [9] reads

$$\frac{D_0}{D_{eff}} = \frac{1+\alpha^2\phi^2}{\beta(1-\phi)} \tag{4.10}$$

where (β) is also an adjustable geometric factor. The following Figure 4.6 gives a comparison between the computational results, for flakes with $\alpha = 100$ and for $\alpha\phi = 1$ and $\alpha\phi = 10$, in unit cells similar to those of Figure 4.5 and the predictions of Equation 4.5, in which D_{11} is taken from [1], [9] and D_{22} from [2]. It is evident that use of models for D_{11} more suitable for concentrated systems results in significantly improved predictions of D_{eff} for all (θ). The model of Lape et al. [1] gives an excellent agreement with the computational results for λ=2.5 even for $(\alpha\phi)$ as low as 0.01 (especially away from $\theta \sim \pi/2$) with a slight adjustment of λ to 2.7 at $\alpha\phi$=0.01, while the model of Cussler et al. [9], gave a very good fit with β=1.15 at $\alpha\phi \geq 1$. The latter model (Equation 4.10) can also be used at lower $(\alpha\phi)$ values with proper adjustment of the parameter (β); at $\alpha\phi = 0.1$ best agreement was obtained for β=0.117 and at $\alpha\phi = 0.01$ best agreement was obtained for β=0.014. Finally, it is noteworthy that near $\theta = \pi/2$ (flakes oriented almost parallel to the direction of diffusion) the numerical results are in very close agreement with Equation 4.5 for all concentrations. Since at $\theta \sim \pi/2$ the term containing D_{22} dominates, this shows that Nielsen's model for diffusion parallel to the flakes is a reliable one, even for $(\alpha\phi)$ as high as 10.

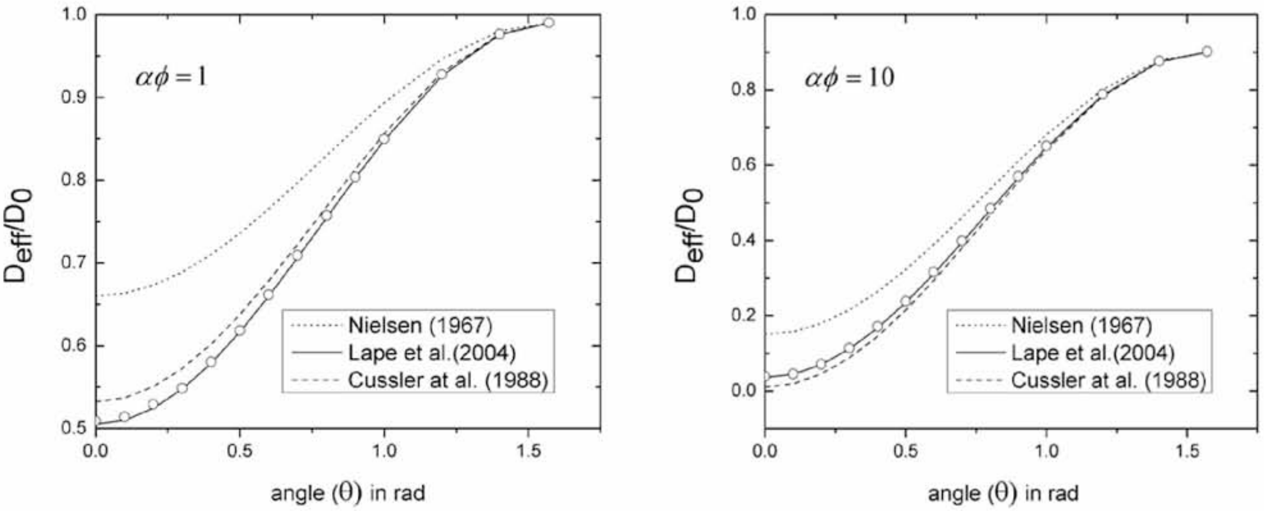

Figure 4.6: Comparison of computational results (points) with predictions of Equation 4.5 for $\alpha\phi = 1$ and $\alpha\phi = 10$. The legend refers to the model used in place of D_{11}. For D_{22} Nielsen's model [8] was used. In all cases $\alpha = 100$, $\beta = 1.15$ in Equation 4.10 and λ=2.5 in Equation 4.9.

Additional comparisons for $\alpha = 1000$ and higher values of $(\alpha\phi)$ are shown in Figure 4.7, in terms of the *BIF*. There are 50 computational data-points at each value of $(\alpha\phi)$ and those at the same (θ) almost completely overlap. This has been shown before [11], namely that spatial randomness has a very small effect on the diffusivity of such systems.

In summary, our computational results and the comparisons presented above have shown that

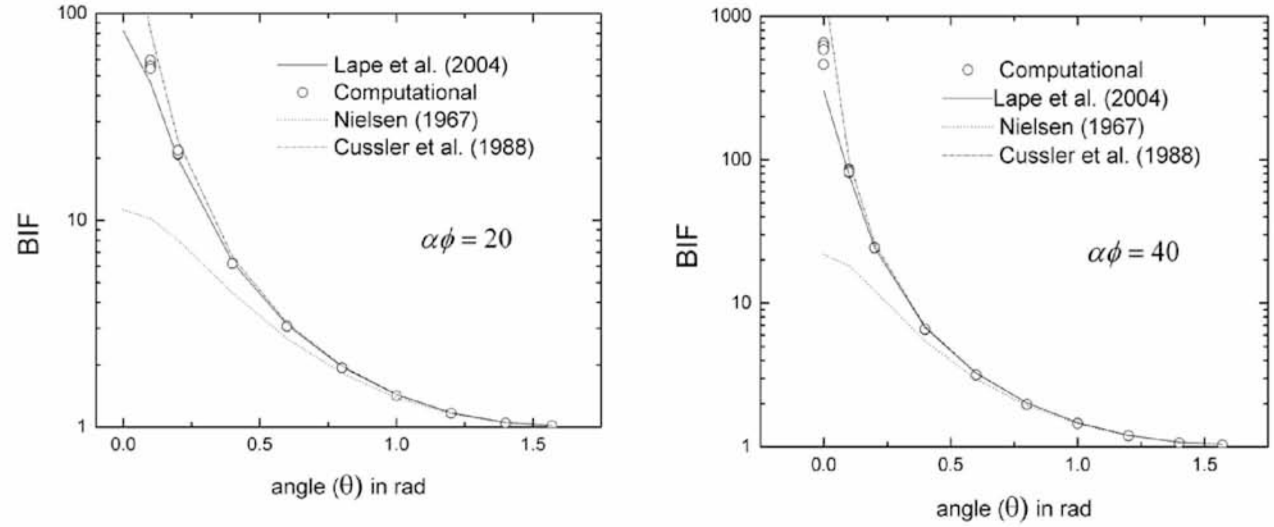

Figure 4.7: Comparison of computational results (points) with predictions of Equation 4.5 for $\alpha\phi$=20 and $\alpha\phi$=40. The legend refers to the model used in place of D_{11}. For D_{22} Nielsen's model [8] was used. In all cases α=1000, β=1.15 in Equation 4.9 and λ=2.5 in Equation 4.10.

the effective diffusivity D_{eff} of a system of randomly placed flakes oriented at an angle $(\pi/2-\theta)$ with the direction of macroscopic diffusion can be predicted by

$$\frac{D_{eff}(\theta)}{D_0} = \frac{1-\phi}{(1+\alpha\phi/\lambda)^2}\cos^2\theta + \frac{1-\phi}{1+\phi/2\alpha}\sin^2\theta \tag{4.11}$$

where λ=2.5. As explained above, this model is in excellent agreement with the computational data for the entire range of $(\alpha\phi)$ and (θ) studied. In addition, we compare the predictions of our model to a well-known experimental result [22], [23], namely that for small values of the misalignment angle (θ) it is

$$\frac{D_{eff}(\theta=0)}{D_{eff}(\theta)} = \cos^2\theta \tag{4.12}$$

in which θ=0 corresponds to a composite fully aligned normal to the direction of diffusion. If D_{11} is the diffusivity of the fully-aligned system, the BIF implied by the above statement will be

$$BIF_1 = \frac{\cos^2\theta}{D_{11}} \approx \alpha\phi\cos^2\theta \tag{4.13}$$

From Equation 4.5 it can be seen that the BIF implied by our model, (setting, without loss of generality or relevance, $D_{22} \sim D_0 \sim 1$) is

$$BIF_2 = \frac{1}{1+(D_{11}-1)\cos^2\theta} \tag{4.14}$$

As shown in Figure 4.8, at each value of (θ) the predictions of Equation 4.14 approach asymptotically those of Equation 4.13 albeit at progressively higher values of D_{11} (that is, for more dilute systems) as (θ) increases. However, the limiting behavior of Equation 4.14 in the concentrated regime (small D_{11}) suggests a qualitatively different behavior for the *BIF*. Our computational results support this prediction, as will be elaborated upon in the following section. With reference to Figure 4.8, if the model of Lape et al. [1] is adopted for D_{11}, a value of D_{11}=0.1 corresponds to $\alpha\phi = 6.5$ while a value D_{11}=0.01 will give $\alpha\phi = 27$. Therefore, our model is consistent with Equation 4.13 well into the semi-concentrated regime, for small misalignment angles.

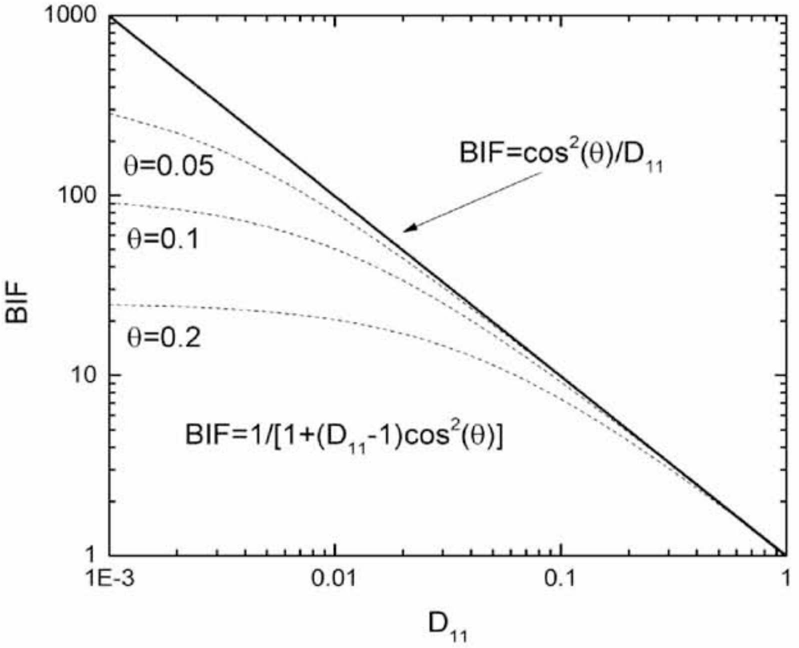

Figure 4.8: Predictions of Equation 4.14 (broken lines) showing its asymptotic approach to the experimental result represented by Equation 4.13 (solid line). Larger values of D_{11} correspond to more dilute systems.

4.4.2 The effect of flake concentration

In aligned systems, it is known [1], [9], [10] that the *BIF* scales with $(\alpha\phi)^2$ at higher concentrations, and linearly with ($\alpha\phi$) in the dilute regime. No such definitive information is available when deviations from perfect alignment occur. Figure 4.9 shows all our computational results for $\alpha = 1000$. It is clear that while the quadratic rise with ($\alpha\phi$) is indeed observed in aligned systems ($\theta = 0$), this asymptotic behaviour is lost as (θ) increase and the *BIF* approaches a plateau value; this plateau is lower the larger the misalignment angle (θ) is. The implication of this result is that for the full potential of large - α flake systems as diffusion barriers to be realized, good alignment is essential. Also shown in Figure 4.9 are the predictions of Equation 4.11; as in Figures 4.7 and 4.8 the agreement between the two is excellent.

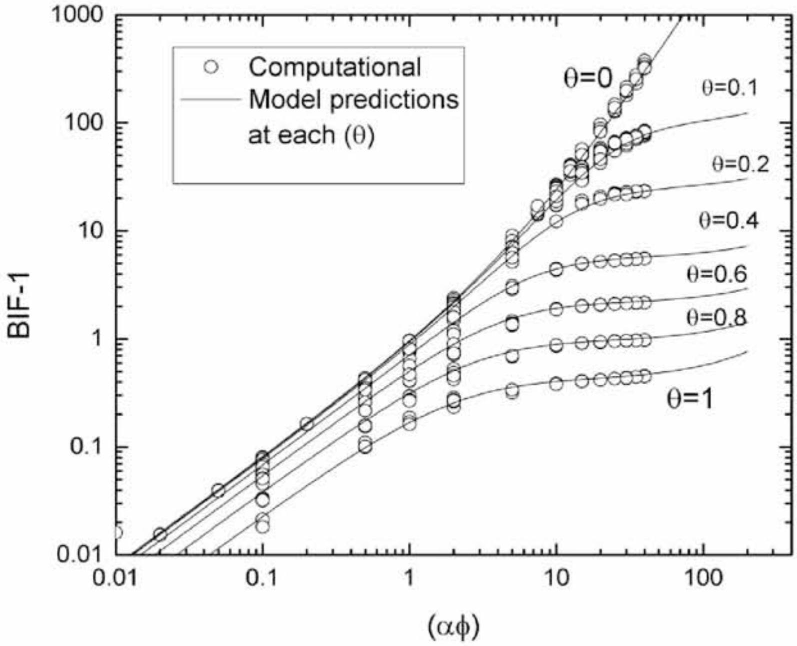

Figure 4.9: Summary of computational results (circles) for $\alpha = 1000$ and $\theta = 0$, 0.1, 0.2, 0.4, 0.6, 0.8, and 1.0, all in rad. We observe the anticipated quadratic rise of the *BIF* with $(\alpha\phi)$ for higher values of $(\alpha\phi)$ at $\theta{=}0$ and also a progressively lower plateau reached at increasing values of the misalignment angle (θ). The predictions of Equation 4.11 are also shown as solid lines. Total of 1295 data points.

4.4.3 Limiting behaviour of the *BIF* at very high $(\alpha\phi)$

In light of the excellent agreement between computational results and Equation 4.11 it is possible to use the latter to obtain analytical estimates of the leveling-off values of the *BIF* (lim(*BIF*)) at each (θ), by observing that the first term of Equation 4.11 becomes negligible at high $(\alpha\phi)$, leaving

$$\lim(BIF)_{\alpha\phi\to\infty} = \left[\frac{1-\phi}{1+\phi/2\alpha}\sin^2\theta\right]^{-1} \tag{4.15}$$

Figure 4.10 compares our computational results to the predictions of Equation 4.15 as well as the approach to that limit based on Equation 4.11. A conclusion is obvious – the quadratic rise of the *BIF* with $(\alpha\phi)$ is lost when $\theta > 0$. For a misalignment as small as 5.7^o (0.1 rad) the upper limit on the achievable *BIF* from Equation 4.9 is 104 – a three-fold decrease from the theoretical *BIF* of a perfectly aligned composite with $\alpha\phi = 40$ and a multi-fold decrease from an aligned composite of even higher ($(\alpha\phi)$). In fact, for such concentrated systems the departure from the theoretical *BIF* can be very rapid at small misalignment angles, as can be inferred from Equation 4.15. This we show in Figure 4.11 in which we plot the predictions of Equation 4.15 along with our computational results for $\alpha = 1000$ and $\alpha\phi = 40$.

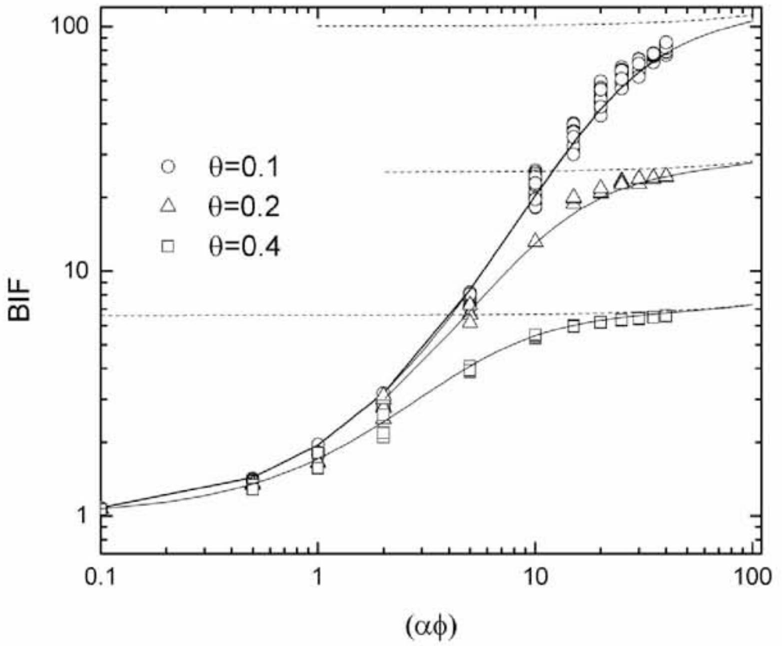

Figure 4.10: The approach to the *BIF* limit (as predicted by Equation 4.15, dotted lines) for $\theta = 0.1, 0.2$ and 0.4 (in rad) as well as the predictions of Equation4.11 (solid lines). Points are computational results. $\alpha = 1000$

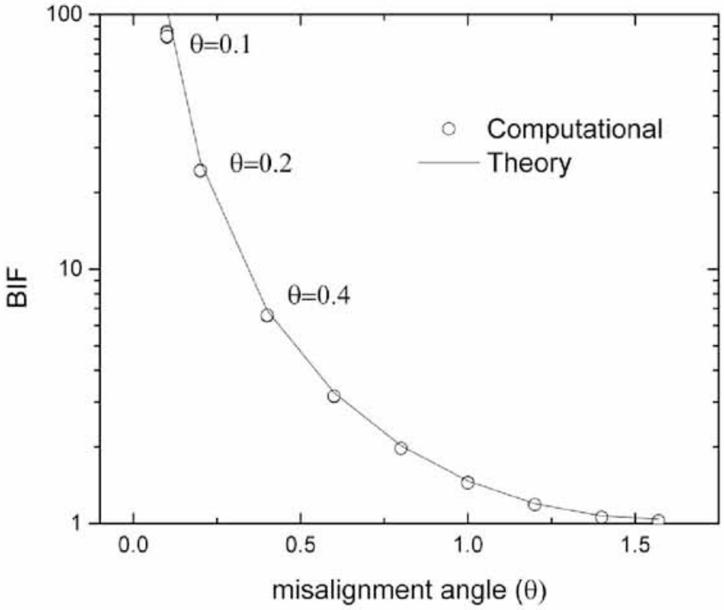

Figure 4.11: Computed *BIF* at $\alpha\phi = 40$ ($\alpha = 1000$) as a function of the misalignment angle (θ). With a solid line are shown the predictions of Equation 4.15. The rate of decline in barrier performance with even a slight misalignment is very significant at small (θ), when ($\alpha\phi$) is large

The above comments and results are particularly pertinent to high aspect ratio flakes, such as found in exfoliated nanoclay or graphene composites, for which even at low (ϕ) a high ($\alpha\phi$) value can be achieved; in our simulations in which $\alpha = 1000$, the maximum $\alpha\phi$ of 40 translates into $\phi = 4\%$. Evidently, Equation 4.15 in that case says that the limiting *BIF* is only a function of the misalignment angle – and our computations are in complete agreement with this prediction. At higher loadings, Equation 4.15 predicts that the limiting *BIF* will increase for larger values of ($\alpha\phi$).

4.5 Conclusions

In this study we proposed a model for the Barrier Improvement Factor (*BIF*) of misaligned flake composites which is valid up to very high flake concentrations, as could be found in composites fabricated by 3D printing. The model requires as inputs the two principal diffusivities of the composite, normal and parallel to the flake axis. In this respect, we find that the models of Lape et al. [1] and Nielsen [2] form an excellent combination.

This model was tested exhaustively by comparing to predictions of 2D computer simulations which included up to 3000 randomly placed but uniformly oriented flake cross-sections in each RVE. Each cross-section forms an angle ($\pi/2 - \theta$) with the direction of macroscopic diffusion. Over 1500 simulations were carried out and upon comparison the model was found in agreement with computational results for all misalignment angles and for values of ($\alpha\phi$) up to 40.

Both our model and our computational data predict that at $\mid \theta \mid > 0$ the quadratic dependence of the *BIF* on ($\alpha\phi$) is lost, with the *BIF* approaching a plateau at higher values of ($\alpha\phi$). This plateau is lower as (θ) increases. We derive analytical estimates of this maximum achievable *BIF* at each level of misalignment; these are also shown to be in excellent agreement with the computational results. Finally we show that our computational results and model are in agreement with experimental evidence at small values of (θ).

4.6 References

1. Lape, N.K., Nuxoll, E.E. and Cussler, E.L. (2004) Polydisperse Flakes in Barrier Films. Journal of Membrane Science, 236, 29-37. `https://doi.org/10.1016/j.memsci.2003.12.026`
2. Nielsen, L.E. (1967) Models for the Permeability of Filled Polymer Systems. Journal of Macromolecular Science Part A: Chemistry, 5, 929-942. `https://doi.org/10.1080/10601326708053745`
3. Panwar, A., Choudhary, V. and Sharma, D.K. (2013) Role of Compatibilizer and Processing Method on the Mechanical, Thermal and Barrier Properties of PS/Organoclay Nanocomposites. Journal of Reinforced Plastics and Composites, 32, 998-1002. `https://doi.org/10.1177/0731684413477770`
4. Pavlidou, S. and Papaspyrides, C.D. (2008) A Review on Polymer-Layered Silicate Nano-Composites. Progress in Polymer Science, 33, 1119-1198. `https://doi.org/10.1016/j.progpolymsci.2008.07.008`
5. Pajarito, B. and Kubuchi, M. (2013) Flake-Filled Polymers for Corrosion Protection. Journal of Chemical Engineering of Japan, 46, 18-26.`https://doi.org/10.1252/jcej.12we133`
6. Mohamadi, M., Garmabi, H. and Keshavarzi, F. (2016) An Investigation on the Effects of Organo-Modified Fluoromica on Mechanical and Barrier Properties of Compatibilized HDPE Nanocomposite Films. Journal of Plastic Film and Sheeting, 32, 10-33. `https://doi.org/10.1177/8756087915569097`
7. Lagaron, J.M. and Nunez, E. (2011) Nanocomposites of Moisture-Sensitive Polymers and Biopolymers with Enhanced Performance for Flexible Packaging Applications. Journal of Plastic Film and Sheeting, 28, 79-89. `https://doi.org/10.1177/8756087911427756`
8. Lee, K.-H., Hong, J., Kwak, S.J., Park, M. and Son, J.G. (2015) Spin Self-Assembly of Highly Ordered Multilayers of Graphene-Oxide Sheets for Improving Oxygen Barrier Performance in Polyolefins. Carbon, 83, 40-47. `https://doi.org/10.1016/j.carbon.2014.11.025`
9. Cussler, E.L., Hughes, S.E., Ward, W.J. and Aris, R. (1988) Barrier Membranes. Journal of Membrane Science, 38, 161-74. `https://doi.org/10.1016/S0376-7388(00)80877-7`
10. Lebovka, N., Khrapatiy, S., Vygornitskyi. and Pivovarova, N. (2014) Barrier Properties of K-Mer Packings. Physica A, 408, 19-27. `https://doi.org/10.1016/j.physa.2014.`

04.019

11. Chen, X. and Papathanasiou, T.D. (2007) Barrier Properties of Flake-Filled Membranes: Review and Numerical Evaluation. Journal of Plastic Film and Sheeting, 23, 319-346. `https://doi.org/10.1177/8756087907088437`
12. Dondero, M., Cisilino, A.P. and Tomba, J.P. (2013) Experimental Validation of Computational Models for Mass Transport through Micro Heterogeneous Membranes. Journal of Membrane Science, 437, 25-32. `https://doi.org/10.1016/j.memsci.2013.02.039`
13. Minelli, M., Baschetti, M.G. and Doghierri, F. (2011) A Comprehensive Model for Mass Transport Properties in Nanocomposites. Journal of Membrane Science, 381, 10-20. `https://doi.org/10.1016/j.memsci.2011.06.036`
14. Tan, B. and Thomas, N.L. (2016) A Review of the Water Barrier Properties of Polymer/Clay and Polymer/Grapheme Nanocomposites. Journal of Membrane Science, 514, 595-612. `https://doi.org/10.1016/j.memsci.2016.05.026`
15. DeRocher, J.P., Gettelfinger, B.T., Wang, J., Nuxoll, E.E. and Cussler, E.L. (2005) Barrier Membranes with Different Sizes of Aligned Flakes. Journal of Membrane Science, 254, 21-30. `https://doi.org/10.1016/j.memsci.2004.12.025`
16. Papathanasiou, T.D. and Tsiantis, A. (2016) Orientational Randomness and Its Influence on the Barrier Properties of Flake-Filled Composite Films. Journal of Plastic Film and Sheeting, On Line.
17. Papathanasiou, T.D. and Guell, D.C. (1997) Flow Induced Alignment in Composite Materials. Woodhead Publishing, Cambridge. `https://doi.org/10.1201/9781439822739`
18. Bharadwaj, R.K. (2001) Modeling the Barrier Properties of Polymer-Layered Silicate Nanocomposites. Macromolecules, 34, 9189-9192. `https://doi.org/10.1021/ma010780b`
19. Greco, A. (2014) Simulation and Modeling of Diffusion in Oriented Lamellar Nanocomposites. Computational Materials Science, 83, 164-170. `https://doi.org/10.1016/j.commatsci.2013.11.019`
20. Greco, A. and Maffezzoli, A. (2013) Two-Dimensional and Three-Dimensional Simulation of Diffusion in Nanocomposite with Arbitrarily Oriented Lamellae. Journal of Membrane Science, 442, 238-244. `https://doi.org/10.1016/j.memsci.2013.04.038`
21. Sorrentino, A., Tortora, M. and Vittoria, V. (2006) Diffusion Behavior in Polymer-Clay Nanocomposites. Journal of Polymer Science Part B: Polymer Physics, 44, 265-274. `https://doi.org/10.1002/polb.20684`

22. Yang, C., Smyrl, W.H. and Cussler, E.L. (2004) Flake Alignment in Composite Coatings. Journal of Membrane Science, 231, 1-12. `https://doi.org/10.1016/j.memsci.2003.09.022`
23. Eitzman, D.M., Melkote, R.R. and Cussler, E.L. (1996) Barrier Membranes with Tipped Impermeable Flakes. AIChE Journal, 42, 2-9. `https://doi.org/10.1002/aic.690420103`

Chapter 5

An evaluation of models and computational approaches for the barrier properties of coatings containing flakes of high aspect ratio[1]

Summary

In this chapter we compare existing models with our results as described in the previous chapters. We show the shortcomings of such models and their discrepancies with numerical results. For this we use an extensive dataset of numerical simulations that solve Fick's First Law for steady state problems and extend in to 4 orders of magnitude in terms of $(\alpha\phi)$ and in the full range of misalignment angles (θ). Also we show the problems that arise when poorly defined numerical studies in terms of boundary conditions and geometry construction of unit cells are used.

The geometries of the unit cells we used in this study exhibit both periodic boundary conditions and periodic geometrical conditions (Figure 5.1). We also solve the same problems by using combinations of adiabatic boundary conditions and non periodic geometrical boundary conditions. This has allowed us to examine not only possible problems that arise when inap-

---

[1] As published in Journal of Coatings Technology and Research: Tsiantis, A., Papathanasiou, T.D. An evaluation of models and computational approaches for the barrier properties of coatings containing flakes of high aspect ratio. J Coat Technol Res 16, 521–530 (2019). `https://doi.org/10.1007/s11998-018-0130-z`

propriate boundary conditions are used but also to examine the effect of the periodic geometry in the numerical solutions as well. We can clearly see from our study that the wrong boundary conditions introduce such an error in the numerical results that they are rendered effectively useless even in the limits of the range of semi-dilute systems ($\alpha\phi \geq 1$). At the same time the superiority of the periodic boundary and geometrical conditions is shown where we can see that with their use, even in extremely distorted unit cells, the obtained results remain the same (Figure 5.3). Using the above results we are able to pinpoint the cause of problems in the formulation of some models especially in the concentrated region.

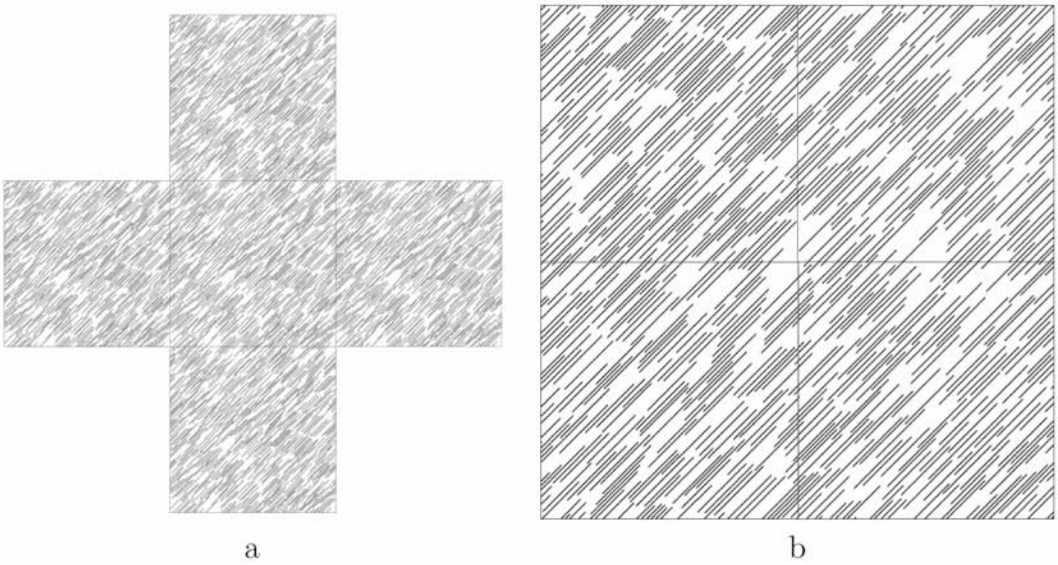

Figure 5.1: Periodic geometry used in this study. (a) Unit cell in periodic arrangement. Each tile is an identical copy of the center tile. (b) Detail at the tile borders. Only 500 flakes are shown for clarity.

At the second part of this chapter we discuss in detail the differences between our model and models that have been proposed in the literature so far. It is clearly seen that many proposed solutions have shortcomings not only due to wrong assumptions that reduces their use in a limited scope of ($\alpha\phi$) but they were suffering from numerical problems as well because of poor simulation definitions.

We have checked our numerical results for spatial convergence by using the Richardson extrapolation method. This way we estimated the simulation accuracy and we were able to determine the best settings in both number of flakes (N) to use and also the number of mesh elements in the numerical solution for obtaining as accurate as possible simulation results.

5.1 Abstract

We report on the results of a comprehensive two-dimensional computational study of diffusion across disordered, two-phase flake composites. Our objective is (1) the evaluation of existing literature models for the effect of flake orientation and (2) the evaluation of the influence of boundary conditions and unit-cell types on the predicted barrier properties. Flake orientation is an important parameter affecting barrier properties in flake-filled composites, as the barrier efficacy of such systems depends significantly on the extent to which the flakes have been oriented as close as possible to being perpendicular to the direction of macroscopic diffusion. Our comparisons rely on an extensive set of computational results in two-dimensional, doubly-periodic unit cells, each containing up to 3000 individual unidirectional flake cross-sections which are randomly placed and with their axes forming an angle $(\pi/2 - \theta)$ with the direction of macroscopic diffusion. A unique feature of our study is the consideration of high aspect ratio (α) systems with $\alpha = 100$ and $\alpha = 1000$, from the dilute ($\alpha\phi = 0.01$) and into the very concentrated ($\alpha\phi = 40$) regime. The effective diffusivity of the corresponding unit cells is computed from the imposed concentration difference and the computed mass flux, using Fick's Law. We show that use of cyclic boundary conditions and doubly-periodic unit cells results in effective diffusivities which are in agreement with theory and invariant of the shape of the unit cell. In addition, we show that the use of adiabatic boundary conditions produces erroneous results at high flake concentrations. Comparison of our results with existing theoretical models revealed several shortcomings of the latter concerning both, the effect of flake concentration ($\alpha\phi$) and the effect of the orientation angle (θ). The principal reason for the latter shortcomings is the fact that said models do not respect the rotational invariance of the diffusivity tensor.

5.2 Introduction

Flake-filled polymeric composites find uses as barrier materials, among others in food packaging, where the objective is to hinder the diffusion of Oxygen, H_2O vapors and/or CO_2 to and from a container while maintaining all the advantages of formability and design afforded by plastic materials. Flakes of inorganic materials such as mica, nano-scale platelets of clay minerals such as hectorite, saponite and montmorillonite as well as graphene-oxide platelets of aspect ratios well over 1000, have been used for this purpose [1], [2]. It is known that incorporation of such fillers aligned perpendicular to the direction of macroscopic diffusion is very effective in increasing the barrier properties by increasing the tortuosity of the diffusion path of the diffusing species. Theory and computation agree that, for flakes aligned perpendicular to the direction of macroscopic diffusion, the improvement in barrier efficiency ranges from being $\sim (\alpha\phi)$ in dilute systems, where (α) is the aspect ratio and (ϕ) the volume fraction of the flakes, to being $\sim (\alpha\phi)^2$ in more concentrated dispersions [3]-[6]. When deviations from such perfect alignment occur, our understanding is not as clear, even though the topic of flake misalignment and its effect on the Barrier Improvement Factor ($BIF = D_0/D_{eff}$, where D_0 is the diffusion coefficient of the neat matrix material and D_{eff} the diffusion coefficient of the composite) is definitely of great practical interest - actual melt-processed composites are never characterized by perfect flake alignment in the desired direction [7]. The two main approaches used to derive analytical models for the barrier efficiency of misaligned systems have been either an ad-hoc incorporation of orientation metrics in existing models [2], [8], [9] or derivation of models from diffusion path calculations [10]-[12].

In an extensively cited paper, Bharasdwaj [9] combined the Herman's orientation parameter (H) with Nielsen's model [13] which is suitable for dilute suspensions. The metric (H) has been used with success to describe orientation of axisymmetric entities such as fibers and macromolecules; however, with the flake-composites considered here this is not the case, since two angles are required to describe their orientational state. In that case Herman's function provides an incomplete characterization [14]. In a similar direction, Lee at al. [2] have proposed combining Cussler's model [3], [4], suitable for aligned-flake systems at higher concentrations, with the Herman's parameter to account for the effect of flake misalignment on diffusivity. Predictions were compared to experimental data and differences in the permeability of sheets produced by different methods were attributed by the authors to variations in orientation. Greco [10] and Greco and Maffezzoli [11] derived analytical models for the effective diffusivity, based on diffusion path length considerations; their models incorporated explicitly the flake orientation angle. They also studied computationally 2D systems containing up to 75 flakes oriented at an angle $(\pm\theta)$, defined as the angle formed between the outward normal vector to the flake surface and the direction of diffusion, and 3D systems containing up to 20 randomly placed and aligned disks, whose orientation varied between perpendicular and parallel to the direction of diffusion. Conditions up to $\alpha\phi$=3.5 were examined. Sorrentino et al. [12] similarly proposed models for the effective diffusivity of 2D and 3D misaligned flake systems based on diffusion path arguments. A recent review of the topic and an evaluation of existing models has been given by Dondero et al [8]. They concerned themselves with the case when the fibers assume orientations which are randomly distributed around a mean direction and with systems of dilute and semi-dilute systems of low aspect ratio ($\alpha < 50$ and $\alpha\phi < 5.0$). All previous studies have limited themselves to these or similar values of (α) and ($\alpha\phi$).

Nevertheless, very high aspect ratio flakes have appeared in recent years in the context of nanotechnology (montmorillonite, graphene) and they have offered the potential of generating very dense flake dispersions at relatively low levels of (ϕ). There is therefore a need to (1) investigate computationally the effect of high aspect ratio and high concentration on barrier properties and also to (2) examine critically the relevance of existing theoretical or empirical models to such systems.

In the present study we deal with flakes of $\alpha = 100$ and $\alpha = 1000$ and ($\alpha\phi$) up to 40. Such highly concentrated systems have not been considered to-date in the technical literature. We consider 2D systems systems in which all flakes are uniformly oriented forming a fixed angle with the direction of macroscopic transport. This feature obviously limits the applicability of some of our findings to unidirectional systems - at an angle with the direction of macroscopic diffusion. Such systems are of practical interest due to the simple fact that while flakes may show a uniform orientation in a finished composite part or film, the direction of orientation is not necessarily the same with the direction of macroscopic diffusion. Literature models such as those of references [11] and [12] have been developed addressing that need. Figure 5.2, an example of the types of microstructures addressed in this work, shows (almost) unidirectional montmorilonite platelets dispersed in a Nylon matrix. One additional and significant novelty of the present work is that, contrary to earlier studies [6], [8], in which the computational unit cells were characterized by adiabatic boundary conditions at their side faces, we consider fully periodic geometries and cyclic boundary conditions. We show that in highly concentrated systems, use of adiabatic boundary condition on the side walls will result in erroneous predictions of the Barrier Improvement Factor. At high values of ($\alpha\phi$), as those achieved in this study, it is important to compute and report values of the Barrier Improvement Factor (BIF) and not of the effective diffusivity, since the latter is close to zero and thus make it difficult to differentiate between the predictions of various models.

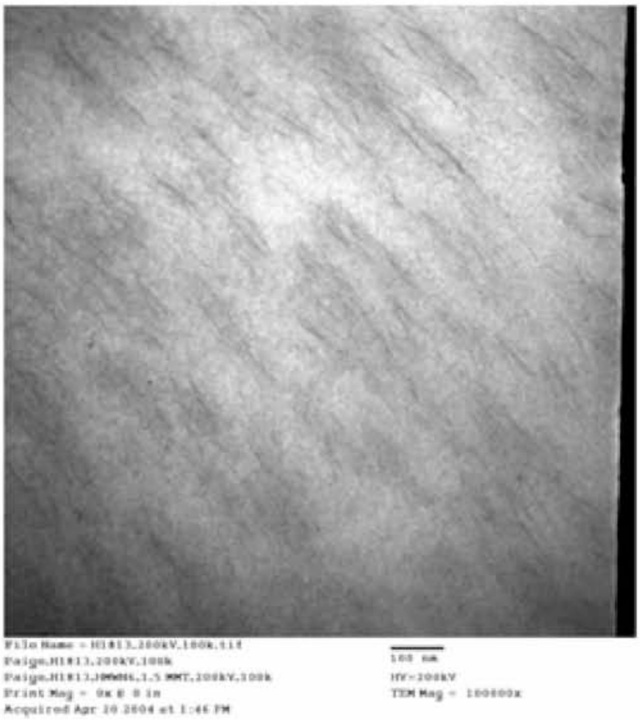

Figure 5.2: TEM picture of a Nylon/Organoclay composite film produced by melt extrusion, showing exfoliated and near-unidirectional platelets. The direction of this process-induced orientation is not necessarily normal to the direction of bulk diffusion, the latter determined chiefly by the geometry of the coating and of the substrate. Results obtained in the PI's laboratory at the University of South Carolina (2008).

5.3 Computational

The computations were carried out in 2D unit cells, generated by adding up to 3000 individual flake cross-sections to a containing geometry (H/L=1) using a Random Sequential Addition (RSA) algorithm. The planar coordinates of the center of each flake are determined using a random number generator, while the orientation angle (θ) is fixed and the same for all flakes. The algorithm checks for overlap of the last placed flake with existing ones in a sub-region surrounding the center of the last-placed flake, and, if no overlap is detected, the process continues with the addition of the next flake, until the desired number of flakes has been placed, or, until no flake can be placed after 10^5 attempts; in this case the algorithm exits without a result and a new attempt commences. A minimum allowable distance (2t) between flakes is imposed, where (t) is the thickness of the flake; this is necessary so that the resulting geometry can be subsequently meshed. If the dimensions of the unit cell are (H) and (L) and if it contains (N) flakes of dimensions (t, α), the flake area fraction (ϕ) is $\phi = N\alpha t^2/LH$ and the length (l) of each flake is $l = \sqrt{LH(\alpha\phi)/N}$. The effect of the number of flakes as well as the convergence of our results with mesh refinement was studied extensively and the results are presented in Appendix-1. In relation to the three-dimensional reality, our simulations are strictly valid for ribbon composites, that is, for composites with flakes extending infinitely in the out-of-plane direction. There are no published comparisons between 2D and 3D simulations in flake-filled systems; however, 2D simulations are expected to produce a conservative estimate of the BIF.

Cyclic boundary conditions are used on the right and left boundaries, specifically $C_{left}(0,y) = C_{right}(L,y)$, where (C) is the solute concentration. The concentration (C) is fixed on the top and bottom boundaries, so that a macroscopic concentration difference $(\mathit{\Delta} C)$ is established. Since the flakes are impermeable, it is $\partial C/\partial n = 0$ on their surfaces. At each pair of (α) and (ϕ) we generate ∼10 different geometries; these differ in flake placement. An in-house procedure is used to mesh the resulting domains using the mesh generating program Gmsh [17]; each case contains ∼4x10^6 triangular elements. These meshes are ported into OpenFoam to solve the steady-state diffusion equation $\nabla^2 C = 0$ and provide its distribution in the domain of interest. The solution also supplies the value of $(\partial C/\partial n)$ at each boundary point. As a result, the mass flux along the top (or bottom) boundary, on which (C) is constant, can be calculated using

$$J_n = -D_o \int_0^L \left(\frac{\partial C}{\partial n}\right) \mathrm{d}x \tag{5.1}$$

where $\mathbf{n}$ is the outward unit vector and (L) is the width of the unit cell. If D_{eff} is the effective diffusivity of an equivalent representative material, equating this flux with the one obtained from Fick's law we obtain

$$D_{eff} = \frac{H \cdot D_0}{\mathit{\Delta} C \cdot L} \int_0^L \left(\frac{\partial C}{\partial n}\right) \mathrm{d}x \tag{5.2}$$

In the following sections we will discuss the effect of geometry and boundary conditions on D_{eff} and also compare our predictions with available literature models.

Use of doubly periodic unit cells eliminates the effect of the dimensions and aspect ratio of the computational domain on the computed effective diffusivity and thus renters the studied geometries true RVEs. Alternative approaches [6], [8], result in artifacts, such as oriented or depleted layers adjacent to boundaries, and thus in predictions of D_{eff} which are not geometry-invariant. This is demonstrated in Figure 5.3, which shows computational results for the predicted effective diffusivity (D_{eff}) for $\alpha\phi = 5$ and $\theta = \pi/4$ and various shapes of unit cells. As expected, use of periodic unit cells coupled with cyclic boundary conditions results in geometry-invariant effective diffusivities.

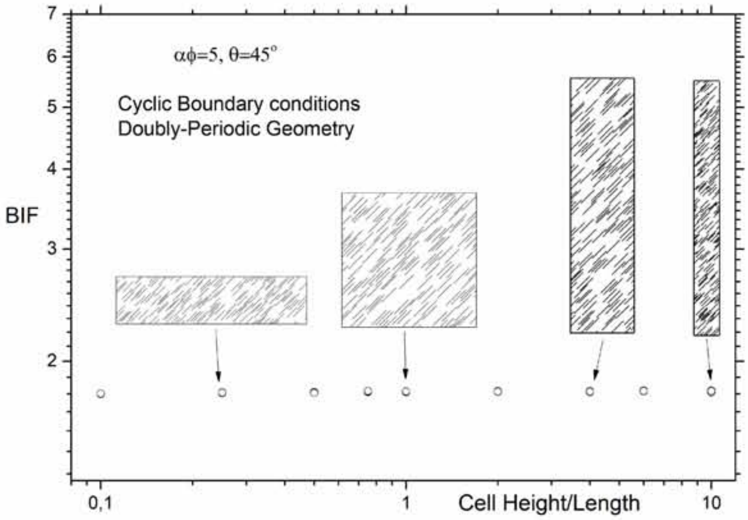

Figure 5.3: The predicted BIF ($\sim 1/D_{eff}$) as function of the aspect ratio (H/L) of the unit cell. The inserts also show typical flake distributions. The number of flakes shown has been reduced for clarity

5.4 Results and Discussion

In the following we present the computational results obtained in two-dimensional doubly-periodic unit cells, each containing up to N=3000 randomly placed impermeable flakes of rectangular cross-section. The horizontal axis is indicated as (x). We look at systems in which the fiber orientation (θ) changes between zero (flake orientation perpendicular to the direction of macroscopic diffusion) to $\pi/2$ (fibers oriented along the direction of macroscopic diffusion). We have carried out computations in unit cells similar to those of Figure 5.3 (H/W=1) for α =100, $\alpha = 1000$ and $0.01 \leq \alpha\phi \leq 40$.

5.4.1 Effect of boundary conditions

The effect of the boundary conditions on the predicted effective diffusivities in flake-filled composites has not been analyzed in previous studies. Chen and Papathanasiou [6] and Dondero and co-workers [8] used non-periodic unit cells and adiabatic conditions on the side boundaries of the unit cells. Being aware that this would have some impact on the predicted diffusivities, both, as a result of flake layers forming adjacent to unit-cell walls as well as a result of artificially restricting diffusion across these boundaries, they computed the effective diffusivity from a central region of their unit cells. While correct, this is certainly inefficient and does not offer a clear estimate of possible errors or any guidance on the required size of this internal region. In the following we summarize the results of an extensive comparison of BIFs predicted through the use of unit cells having

i. doubly-periodic geometry
ii. geometry in which flakes were excluded from crossing boundaries
iii. cyclic boundary conditions and
iv. adiabatic boundary conditions

Characteristics (iii) and (iv) refer to the boundary condition applied on the two vertical sides of the unit cell (the two horizontal sides being at constant concentration).

For such systems, by taking into account the rotational properties of the diffusivity tensor, which dictates that $D_{eff}(\theta) = D_{11}\cos^2\theta + D_{22}sin^2\theta = D_{11} + (D_{22} - D_{11})\sin^2\theta$ and by utilizing the models of Lape et al. [4] and Nielsen [13] for the principal diffusivities D_{11} and D_{22} respectively, Tsiantis and Papathanasiou [15] proposed the following model for D_{eff}:

$$\frac{D_{eff}(\theta)}{D_0} = \frac{1-\phi}{(1+\alpha\phi/\lambda)^2}\cos^2(\theta) + \frac{1-\phi}{1+\phi/2\alpha}\sin^2(\theta) \tag{5.3}$$

This model was found [15] to be in excellent agreement with computational predictions for $0 < \theta < \pi/2$ and $\alpha\phi \leq 40$. A key result of both, this model and of the computational results of reference [15] is the fact that at $\theta > 0$ the BIF ($\sim 1/D_{eff}$) does not grow monotonically with ($\alpha\phi$) but instead it reaches a plateau value; this plateau value is reduced as (θ) increases and as (θ) approaches $\pi/2$ the BIF approaches the (plateau) value implied by the Nielsen model [13].

Figure 5.4 shows predicted values of the BIF as function of ($\alpha\phi$) for various combinations of unit cell type and boundary conditions. It is interesting to observe that while the effect of unit cell type and/or boundary conditions is very small for dilute systems, thus validating in earlier studies [6] ,[8], major differences are observed for $\alpha\phi > 5$ – this is incidentally the concentration beyond which no results have been reported in the literature this far.

For all conditions, as long as the system remains in the dilute or semi-dilute regime ($\alpha\phi < 5$) the results appear to be little affected by the type of unit cell or by the boundary conditions used, the effect being more pronounced as (θ) increases. However, for concentrated systems the predicted BIF is affected dramatically by the choice of the unit cell type or of the boundary conditions, in a quantitative as well as in qualitative sense. In fully-aligned systems (θ =0) the

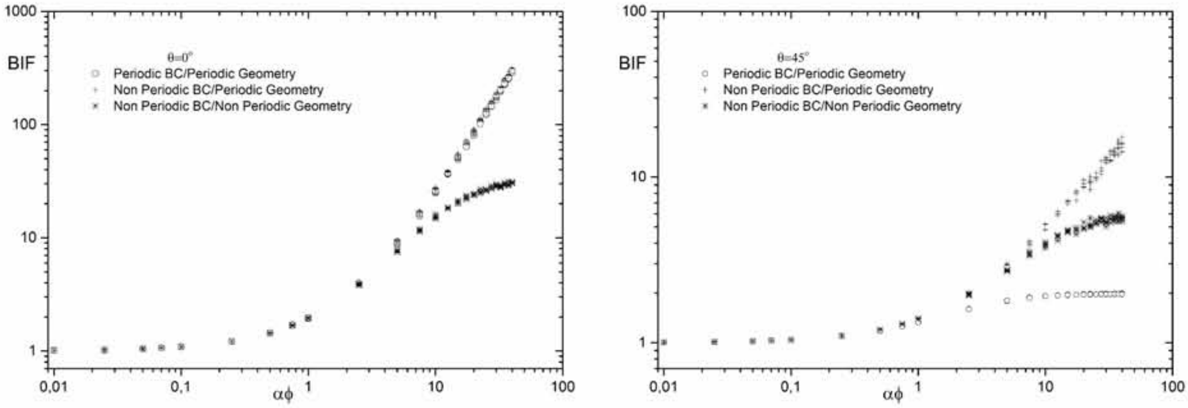

a

b

Figure 5.4: Predicted values of the BIF as function of flake concentration ($\alpha\phi$) for various combinations of geometry (periodic/non-periodic) and boundary conditions on the side walls (cyclic/adiabatic). Two values of the misalignment angle and H/W=1.

key factor appears to be the type of geometry used; as long as the geometry is periodic (that is, flakes are allowed to cross the vertical boundaries of the unit cell) the correct behavior is predicted, namely a quadratic dependence on ($\alpha\phi$) at high values of ($\alpha\phi$), in agreement with the model of Lape et al. [4] and earlier computational results of [6]. However, use of a non-periodic geometry results in the prediction of a totally wrong dependence of the BIF on ($\alpha\phi$) (Figure 5.4a), probably as a result of the formation of flake-exclusion zones adjacent to the vertical boundaries. The approach used in references [6] and [8] to deal with this problem will most probably reduce or even eliminate this error, but in the absence of direct evidence it can only be seen as empirical. For misaligned systems (Figure 5.4a) only a periodic unit cell and cyclic boundary conditions result in the anticipated behavior of the BIF, all other combinations yielding unacceptable predictions. The reasons for this can be inferred by examining the contour maps of concentration in selected cases, as shown in Figures 5.5 and 5.6. It is evident that the imposition of adiabatic conditions changes the nature and direction of the mass transfer in a way that renders the geometry a non-representative unit cell; therefore the computed diffusivity can no longer be considered an effective property but rather a “component property”, the result of the particular set of conditions and of the particular geometry.

The combined effect of the type of boundary conditions used and of the aspect ratio of the unit cell is shown in Figure 5.7. It is clear that use of adiabatic conditions on the vertical boundaries of the unit cell will only yield the correct effective diffusivity if the aspect ratio of the unit cell (L/H) is greater than 10. Otherwise, the predicted BIF will be overestimated several-fold and thus be completely unreliable.

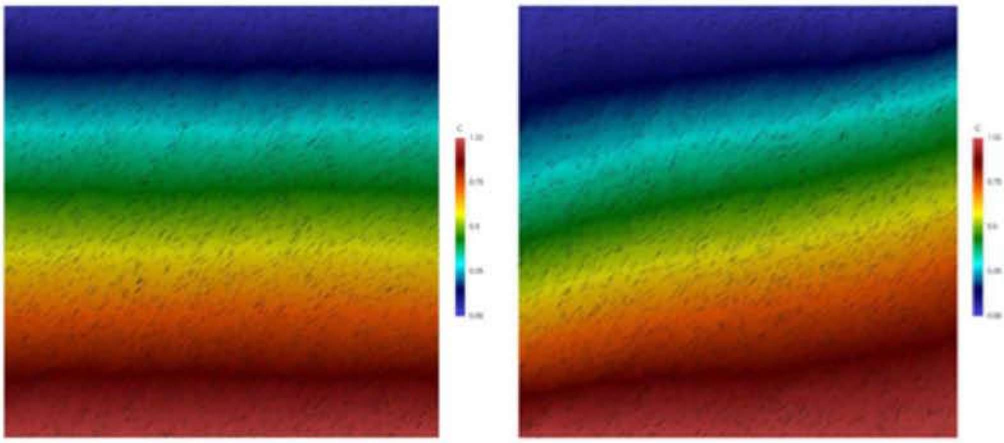

Figure 5.5: Concentration profiles in systems with $\alpha\phi = 1$, $\theta = 45^o$ and cyclic (left) and zero-gradient (right) boundary conditions on the vertical boundaries. The flakes are also visible. The number of flakes is N=3000

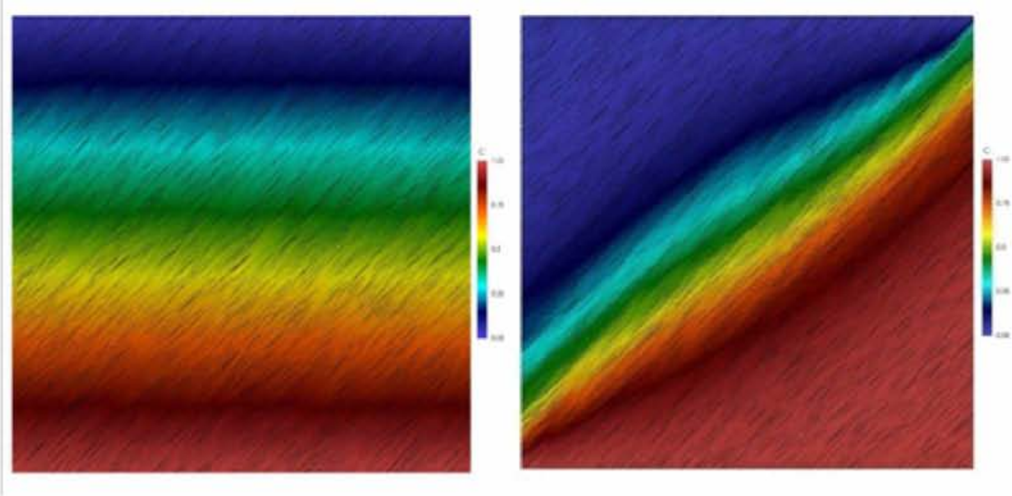

Figure 5.6: Concentration profiles in systems with $\alpha\phi = 10$, $\theta = 45^o$ and cyclic (left) and zero-gradient (right) boundary conditions on the vertical boundaries. The flakes are also visible. The number of flakes is N=3000

5.4.2 Comparison to other relevant models

In the following we compare the computational results and the predictions of the model of Equation 5.3 for D_{eff} to the predictions of other literature models. Among existing models, the model of Bharadwaj [9] was derived by combining Nielsen's model [13] with Herman's orientation parameter $H = \frac{1}{2}(3\langle\cos^2\theta\rangle - 1)$ where the brackets $\langle\rangle$ indicate ensemble averaging over the entire flake population. For general, three-dimensional orientation distributions, the parameter H is zero for a random system, takes the value 1 for flakes aligned perpendicular to the direction of diffusion) and -0.5 for flakes oriented along the direction of diffusion. For

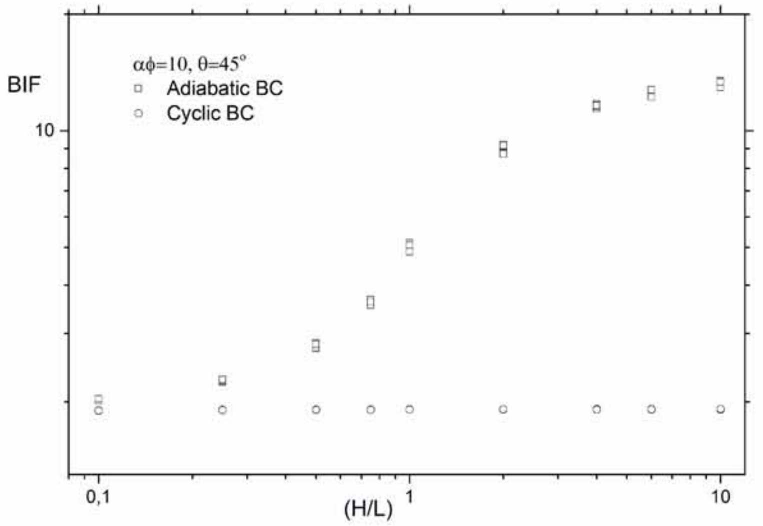

Figure 5.7: The combined effect of the shape of the unit cell (expressed by the ratio H/L) and of the type of boundary conditions used on the computed barrier factor (BIF). $\alpha\phi$ =10, θ =45^o and N=3000. (H) is the height and (L) the length of the unit cell

two-dimensional distributions of orientations, such as those dealt with in this study, this interpretation is no longer correct. The above limits in (H) are based on the fact that in a 3D randomly oriented distribution of flakes it is $\langle\cos^2\theta\rangle = 1/3$ while in a 2D random system it is $\langle\cos^2\theta\rangle = 1/2$. The Herman parameter should therefore be expressed as $H = 2\langle\cos^2\theta\rangle - 1$ so that it yields H=0 for a random and H=1 for a transverse system. For a system aligned along the direction of diffusion this definition will give H=-1. With this in mind the expression of reference [9] for D_{eff} takes the form

$$\frac{D_{eff}(\theta)}{D_0} = \frac{1-\phi}{1+0.25\alpha\phi(H+1)} = \frac{1-\phi}{1+0.5\alpha\phi\langle\cos^2\theta\rangle} \tag{5.4}$$

Equation 5.4 yields the Nielsen model for flakes aligned perpendicular to the direction of diffusion (θ =0) and to the dilute limit result ($D_{eff} \sim 1-\phi$) for flakes parallel to the direction ($\theta = \pi/2$). The term (H+1) in Equation 5.4 is the 22-diagonal component of the orientation tensor ($\boldsymbol{A}$), defined as $A_{ij} = \langle p_i p_j\rangle$. Since for the two-dimensional cross-sections considered in this study, $p_1 = \sin\theta, p_2 = \cos\theta$, it is

$$\boldsymbol{A} = \begin{vmatrix} \langle\sin^2(\theta)\rangle & \langle\sin(\theta)\cos(\theta)\rangle \\ \langle\sin^2(\theta)\cos(\theta)\rangle & \langle\cos^2(\theta)\rangle \end{vmatrix} \tag{5.5}$$

Lee et al. [2] proposed to use the Herman's orientation function in the context of Cussler's model [3], which is more suitable for dense systems; in 2D and using (H) in the form indicated earlier, the expression for Deff reads

$$\frac{D_{eff}(\theta)}{D_0} = \left[1 + \frac{\alpha^2\phi^2}{1-\phi}\langle\cos^2(\theta)\rangle\right]^{-1} \tag{5.6}$$

The above models [Equations 5.3 and 5.4] are meant to be used for a population of flakes with a distribution of orientation angles; we will nevertheless compare their predictions to our results.

In the case of flakes with precise orientation, Greco et. al. [10], [11], derived, using diffusion path arguments, closed form expressions for the diffusivity of unidirectional systems comprised of misaligned flakes in terms of the misalignment angle (θ). The expressions for D_{eff} are:

$$\frac{D_{eff}(\theta)}{D_0} = \frac{1-\phi}{\left[1 + \sqrt{2}(1-\sqrt{2}/2)\cdot\alpha\phi\cdot\cos^2(\theta)\right]^4} \tag{5.7}$$

and

$$\frac{D_{eff}(\theta)}{D_0} = \frac{1-\phi}{\left[1 + \frac{\pi}{3.62\sqrt{3}}\cdot\alpha\phi\cdot\cos(\theta)\cdot(1-\sin(\theta))\right]^4} \tag{5.8}$$

respectively.

Based also on diffusion path arguments, Sorrentino et al. [12] proposed a model for misaligned-flake composites which for unidirectional flakes reads

$$\frac{D_{eff}(\theta)}{D_0} = \frac{1-\phi}{(\alpha+2)^2}\cdot[\alpha\sin(\theta) + 2\cos(\theta)]^2 \tag{5.9}$$

In the case of large (α) Equation 5.9 will predict that for flakes oriented perpendicular to the direction of diffusion $D_{eff}(0) \sim 0$, (the formal limit as (θ) approaches zero is $4(1-\phi)/(\alpha+2)^2$ and thus, the predicted BIF will grow $\sim \alpha^2$).

The predictions of the above models will not revert to a rotation-independent diffusivity when $\alpha \sim 1$ and therefore should only be used for elongated particles. All above models (Equations 5.4 and 5.6-5.9) revert to the mixing rule result $D_{eff}(\theta = \pi/2) \sim D_0(1-\phi)$ when the flakes are aligned with the direction of diffusion. For $\theta = 0$, the model of reference [9] predicts that BIF$-1 = \alpha\phi/2$, in agreement with the assumption of a dilute system, while the model of reference [2] predicts BIF$-1 = (\alpha\phi)^2$ in agreement with the assumption of a concentrated system. The model of reference [10] predicts that for $\theta = 0$, $D_{eff} = (1-\phi)/(1+\sqrt{2}(1-\sqrt{2}/2)\cdot\alpha\phi)^4$ and this will not predict correctly the principal diffusivity D_{11}. It should be noted, that the exponent (4) in the denominator of Equation 5.7 was obtained by curve-fitting computational results for the effective diffusion path and it is conceivable that an exponent closer to 2 would result is a similar fit. Obviously the numerical predictions of the above models for aligned flake systems (θ =0) differ significantly from each other. More significantly, their predictions do not agree with the well-tested models for D_{11}.

Predictions of the above models vis-a-vis the concentration of flakes (expressed by ($\alpha\phi$) are shown in Figure 5.8 for two values of (θ), namely $\theta = 0$ and $\theta = 45^o$. Our computational results obtained for various types of unit cells and various boundary conditions are also shown.

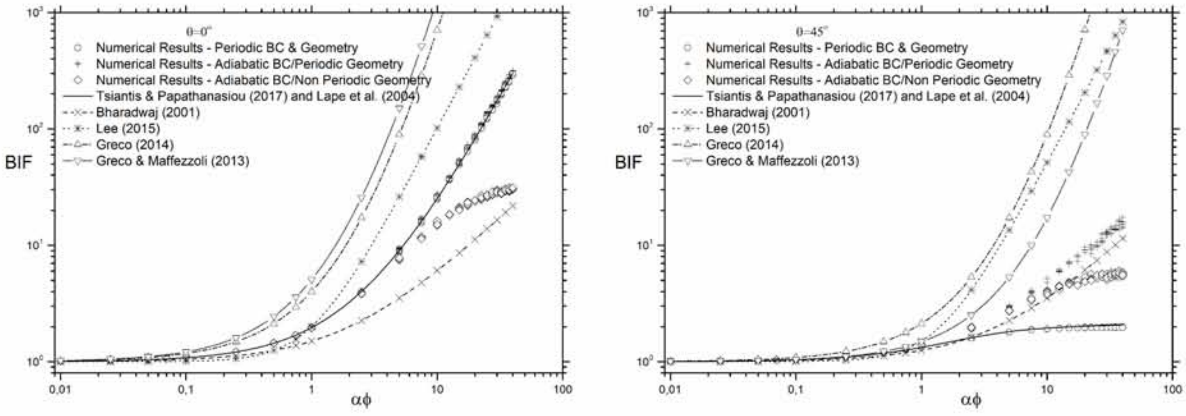

a b

Figure 5.8: Comparison of computational results with theoretical models for a range of ($\alpha\phi$).

In the following, we focus our comparisons on the predicted effect of (θ); these are shown in Figure 5.9 for various values of ($\alpha\phi$). Our computational results at each ($\alpha\phi$) are superimposed as well. In order to allow for a comparison that will focus on the effect of misalignment angle (θ) and will not be overwhelmed by different predictions at (θ=0), as shown in Figure 5.7, we compute and compare a normalized diffusivity

$$D_{norm} = \frac{D_{eff}(\theta) - D_{eff}(\theta = 0)}{D_{eff}(\theta = \pi/2) - D_{eff}(\theta = 0)} \tag{5.10}$$

which can be seen as a measure of the deviation from the diffusivity of a fully aligned system. The terms $D_{eff}(\theta = 0)$ and $D_{eff}(\theta = \pi/2)$ in each case are obtained from the corresponding model.

For dilute concentrations there is agreement between our computations and the models, with the exception of the model of Greco and Maffezzoli [11], which appears to be in better agreement with computational results only in the range of intermediate concentrations. The predictions

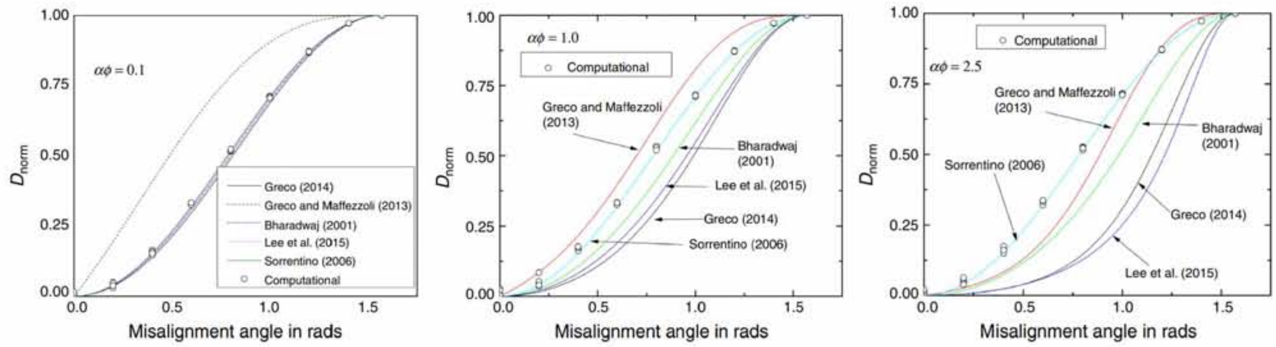

Figure 5.9: Comparison of the predictions of literature models with the computational results of this study. α =1000, $\alpha\phi$ =0.1, 1 and 2.5.

of references [2], [9] and [10] diverge, significantly, from computational results at $\alpha\phi > 5$. The model of Sorrentino et al. [12] is in very good agreement with both, our computations and the proposed model Equation 5.3 but only for large $(\alpha\phi)$. At lower $(\alpha\phi)$, it dictates that the predicted D_{eff} (from Equation 5.9) at θ =0 will always be $\sim$0, irrespective of the value of $(\alpha\phi)$, unless we deal with very low aspect ratio flakes.

5.5 Conclusions

We have presented the results of a computational evaluation of the effect of misalignment on the effective properties of composites filled with high aspect ratio flakes. We allow the flakes to assume orientations in an interval ranging from zero (aligned perpendicular to macroscopic diffusion) to $\pi/2$ (aligned parallel to macroscopic diffusion). We analyze the results and compare them to the predictions of existing theoretical models, including one which the barrier properties of the composite are related to the two principal diffusivity and thus to flake loading $(\alpha\phi)$ as well as (θ). After careful evaluation of the spatial convergence of our computations, we also examine the effect of boundary conditions on the predicted effective diffusivity. Our results show that at higher flake loading, use of adiabatic boundary conditions at the side walls of the unit cell will result in erroneous predictions for the effective diffusivity. We show that use of cyclic conditions will result in effective diffusivities which are, as expected, unaffected by the shape of the unit cell. We also show that most existing literature models do not respect the rotational invariance of the diffusivity tensor and for this reason their predictions diverge from computational results at moderate to high flake concentrations.

5.6 Appendix 1

Examination of the spatial convergence of a simulation is an essential step in determining simulation accuracy and eliminating mesh-dependence. The Richardson extrapolation method we use allows us to obtain the highest order estimate for the value of an unknown function (f) at the limit of zero grid spacing (infinitely dense mesh), from a range of lower order values, which are obtained using progressively finer meshes. The advantage of this approach is significant when large numbers of simulations are to be performed, since one does not need to use fine grids but instead, obtain the limiting value $f_h = 0$ from the results of simulations using coarser meshes.

The method involves performing simulations on two or more successively finer grids. As the grid is refined (grid cells become smaller and the number of cells in the domain increases), the spatial discretization errors decrease and should asymptotically approach the machine accuracy at the limit of zero grid spacing. The order of convergence n for three levels of grid spacing is defined as:

$$n = ln\left(\frac{f_3 - f_2}{f_2 - f_1}\right)/ln(r) \tag{5.11}$$

where r is the refinement factor $r = h_2/h_1$ and where f_1, f_2 and f_3 are values of the computed function (in our case, of the effective diffusion coefficient). By computing the rate of convergence from equation (5.11), one can get an estimate of the value of the unknown function (f) at zero grid spacing, using, for example,

$$f_{h=0} \cong f_1 + \frac{(f_1 - f_2)}{r^n - 1} \tag{5.12}$$

The quality of this estimate of $f_h = 0$ is based on the calculation of the Grid Convergence Index (GCI) [16]. The GCI based on the fine grid is defined as:

$$GCI_{fine} = \frac{F_s \mid e \mid}{r^n - 1} \tag{5.13}$$

where F_s is a safety factor equal to 3.0 or 1.25 for 2- or 3-grid comparison, respectively. The GCI on the coarser grid is computed as:

$$GCI_{coarse} = \frac{r^n F_s \mid e \mid}{r^n - 1} = r^n GCI_{1,2} \tag{5.14}$$

If the ratio of the grid convergence indices (GCI) based on the fine and the coarser meshes is close to one, the computations used to compute $f_h = 0$ have been performed in the region of the asymptotic range of convergence of our problem, and thus, the value of $f_h = 0$ computed from Equation (5.12) is reliable.

As an example, we use a case with $\theta = 45^o$, $\alpha\phi = 10$ and N = 3000, for which five 2D unstructured meshes with different cell numbers were created on the same geometry. We will use the three coarsest meshes (grid numbers 5, 4 and 3) to perform the analysis described above, and the results on the finer meshes (grids 1 and 2) will be compared with the asymptotic value at zero grid spacing obtaining from the Richardson extrapolation method. The results are shown in Figure 5.10.

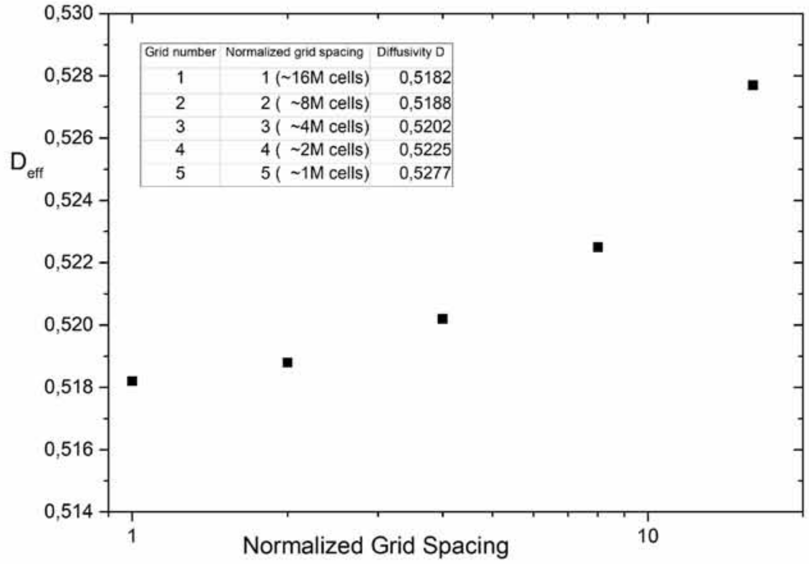

Grid number	Normalized grid spacing	Diffusivity D
1	1 (~16M cells)	0,5182
2	2 (~8M cells)	0,5188
3	3 (~4M cells)	0,5202
4	4 (~2M cells)	0,5225
5	5 (~1M cells)	0,5277

Figure 5.10: Numerical values for the effective diffusivity obtained using the same geometry but with variable grid spacing. As grid spacing decreases the cell count increases. Meshes are refined as we move from right to left.

The order of convergence is found (Equation 5.11) to be $n = log(\frac{0.5277-0.5225}{0.5225-0.5202})/log(2) = 1.176878$, and the effective diffusivity is computed form Equation (5.12) to be $D_{h=0} = 0.518376$. Since we used three levels of grid refinement, $F_S = 1.5$. The GCI computed for the grids 3 and 4, as well for grids 4 and 5, using Equations 5.13 and 5.14 is $\text{GCI}_{3,4} = 0.52368\%$ and $\text{GCI}_{4,5} = 1.17230\%$, and thus, the asymptotic range of convergence ratio is $\frac{1.17230}{2^{1.176878 \cdot 0.52368}} = 0.99015 \cong 1$, indicating that we are in the regime of asymptotic convergence range.

Figure 5.11 shows how the effective diffusion coefficient varies with the number of mesh elements and flake numbers.

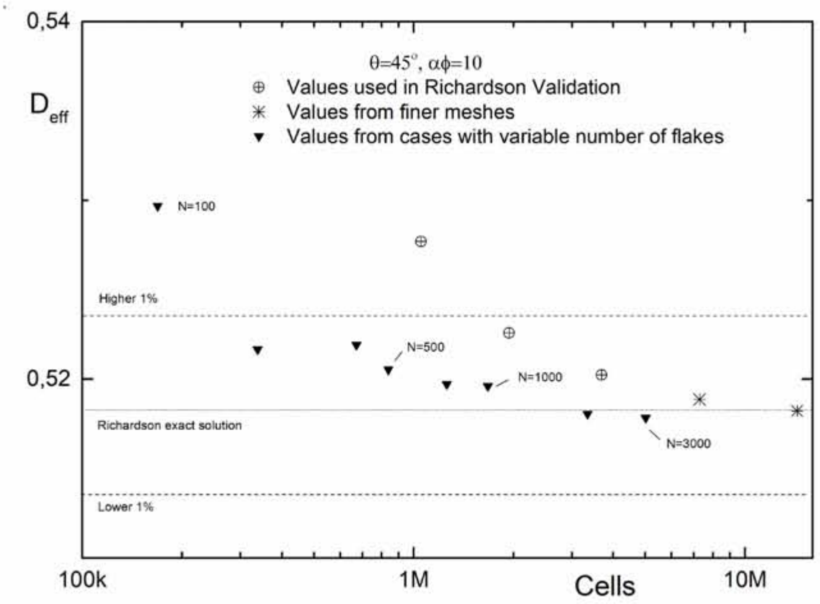

Figure 5.11: Representative convergence of numerical results in terms of the number of flakes considered and also in terms of the Richardson extrapolation method outlined above. We show the values used for the convergence study with constant flake number (N=3000) and the values from cases with variable flake numbers. The result obtained for use in the Richardson extrapolation method were obtained in one specific geometry having N=3000 (see Figure below) on which only the mesh size was varied

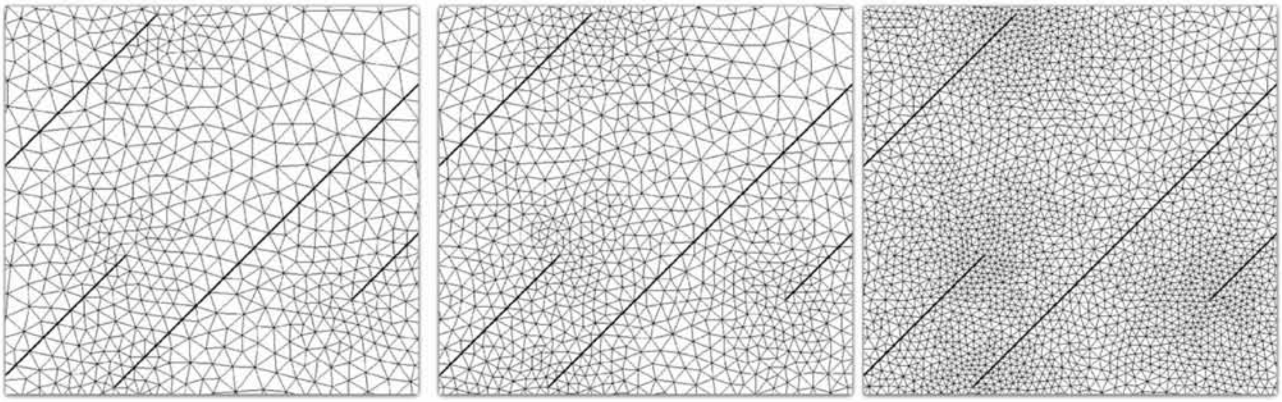

Figure 5.12: Detail of a region in a geometry of interest in which successively finer meshes are constructed.

5.7 References

1. Lagaron, JM, Nunez, E, “Nanocomposites of MoistureSensitive Polymers and Biopolymers with Enhanced Performance for Flexible Packaging Applications.” J. Plastic Film Sheet., 28 (1) 79–89 (2012)
2. Lee, K-H, Hong, J, Kwak, SJ, Park, M, Son, JG, “Spin Selfassembly of Highly Ordered Multilayers of Graphene-Oxide Sheets for Improving Oxygen Barrier Performance in Polyolefins.” Carbon, 83 40–47 (2015)
3. Cussler, EL, Hughes, SE, Ward, WJ, Aris, R, “Barrier Membranes.” J. Membr. Sci., 38 161–174 (1988)
4. Lape, NK, Nuxoll, EE, Cussler, EL, “Polydisperse Flakes in Barrier Films.” J. Membr. Sci., 236 29–37 (2004)
5. Nyflott, A, Mericer, C, Minelli, M, Moons, E, Jarnstrom, L, Lestelius, M, Baschetti, MG, “The Influence of Moisture Content on the Polymer Structure of PVOH in Dispersion Barrier Coatings and Its Effect on The Mass Transport of Oxygen.” J. Coatings Technol. Res., 14 (6) 1345–1355 (2017)
6. Chen, X, Papathanasiou, TD, “Barrier Properties of FlakeFilled Membranes: Review and Numerical Evaluation.” J. Plastic Film Sheet., 23 319–346 (2007)
7. Papathanasiou, TD, Tsiantis, A, “Orientational Randomness and Its Influence on the Barrier Properties of Flake-Filled Composite Films.” J. Plastic Film Sheet., 33 (4) 438–456 (2017)
8. Dondero, M, Tomba, JP, Cisilino, AP, “The Effect of Flake Orientational Order on the Permeability of Barrier Membranes: Numerical Simulations and Predictive Models.” J. Membr. Sci., 514 95–104 (2016)
9. Bharadwaj, RK, “Modeling the Barrier Properties of Polymer-Layered Silicate Nanocomposites.” Macromolecules, 34 9189–9192 (2001)
10. Greco, A, “Simulation and Modeling of Diffusion in Oriented Lamellar Nanocomposites.” Comput. Mater. Sci., 83 164–170 (2014)
11. Greco, A, Maffezzoli, A, “Two-dimensional and Threedimensional Simulation of Diffusion in Nanocomposite with Arbitrarily Oriented Lamellae.” J. Membr. Sci., 442 238–244 (2013)
12. Sorrentino, A, Tortora, M, Vittoria, V, “Diffusion Behavior in Polymer-Clay Nanocomposites.” J. Polym. Sci. Part B Polym. Phys., 44 265–274 (2006)

13. Nielsen, LE, "Models for the Permeability of Filled Polymer Systems." J. Macromol. Sci. Part A Chem., 5 (1) 929–942 (1967)
14. Papathanasiou, TD, Guell, D, (Eds.) Flow-Induced Alignment in Composite Materials. Woodhead Publishing (1997)
15. Tsiantis, A, Papathanasiou, TD, "The Barrier Properties of Flake-Filled Composites with Precise Control of Flake Orientation." Materials Sciences and Applications, 8 234–246 (2017)
16. Roache, PJ, Verification and Validation in Computational Science and Engineering. Hermosa Publishers, Albuquerque, NM (1998)
17. Geuzaine, C, Remacle, JF, "Gmsh: a Three-Dimensional Finite Element Mesh Generator with Built-in Pre- and PostProcessing Facilities." Int. J. Numer. Methods Eng., 79 (11) 1309–1331 (2009)

Chapter 6

A New Closed Form Solution for the Barrier Properties of Randomly Oriented and Highly Filled Nano-Flake Composites[1]

Summary

In this chapter we introduce a model for the BIF for composite materials with flakes that are randomly oriented so that $-\epsilon < \theta < +\epsilon$, with $0^o < \epsilon < 90^o$ (Figure 6.1). Such models have been introduced in the past but they suffer from either small validation range ($\alpha\phi < 5$) or they are based on various ad-hoc orientational metrics of unproven correctness.

In our case we treat the RVE as if it consists of resistances in series and/or in parallel, in the direction of diffusion, based on the model presented in Chapter 3. We perform an averaging that takes into account the orientational randomness and we compare the computational results with the Harmonic, Arithmetic and Geometric average. We found that computational results follow the Harmonic average with good agreement in the range of (ϵ) and (α) tested.

In the second part we compare our model with earlier published results. We found that these models can show big differences in their predictions and the numerical results, while our model

---

[1] As published in Journal of Composite Materials: Tsiantis, A., & Papathanasiou, T. (2019). A closed-form solution for the barrier properties of randomly oriented high aspect ratio flake composites. Journal of Composite Materials, 53(16), 2239–2247. `https://doi.org/10.1177/0021998318825295`

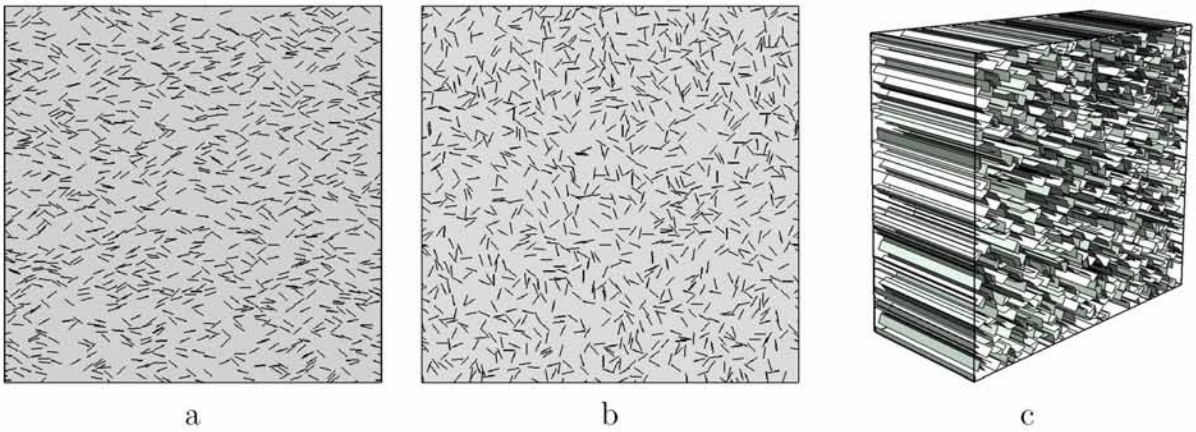

Figure 6.1: Various 2D RVEs. (a) $\theta = 0, \epsilon = 45^o$, (b) $\theta = 0, \epsilon = 90^o$, (c) 2D RVE with $\theta = 0, \epsilon = 90^o$ in perspective view. The flakes can be seen extending like ribbons in the Z-axis. 1000 flakes are shown for clarity.

exhibits a better overall behaviour.

There is still a degree of empiricism in our proposed solution, and this can be traced in the choice of the tortuosity parameter (λ) used in the context of the model of Lape et. al. for the principal diffusivity D_{11} (fully aligned system). Similar empirical coefficients can be found in the other models tested in this Chapter. However, because of the robust foundation of our model a good fit with computational results at all states of misalignment is achieved, once a value of (λ) is determined by fitting the unidirectional data. In other models, the corresponding geometrical factors will have to become functions of ($\alpha\phi$) and (ϵ) in order for their predictions to be reliable across the entire space of concentration and misalignment.

It is also to be noted that our model shows very good agreement with computational results in cases where $\alpha > 1000$ by using in the numerical simulations flakes that have zero width (t=0). This way we have effectively simulated materials with extremely big (α) such as flake nanocomposites. Our model shows consistently good agreement even in these extreme cases.

6.1 Abstract

We derive closed form solutions for the effective diffusion coefficient of flake-filled composites, in which the flakes are randomly placed and oriented, with the orientations uniformly distributed in an interval $[-\epsilon, +\epsilon]$, $0 < \epsilon < \pi/2$. Our solutions are based on the arithmetic and harmonic averaging of the diffusivity of unidirectional misaligned flake systems, the latter having the form , where D_{11} and D_{22} are the principal components of the diffusivity tensor and (θ) the misalignment angle. Using large-scale 2D simulations, some involving up to 50.000 individual flakes in one unit cell and spanning the regime from dilute to highly concentrated, the proposed solutions are tested against and confirmed by computational results. We use both, traditional 2D and also 1D representations of the flake cross-sections. The 1D representation is suitable for very high aspect ratio flakes, such as exfoliated nano-platelets of montmorillonite or graphene-oxide. This approach greatly simplifies the construction of the computational mesh. It is also the only feasible approach to model flake nano-composites $(\alpha > 1000)$, in which $(\alpha\phi)$ can reach levels in excess of 100. Such high levels of $(\alpha\phi)$ are obviously unrealistic in traditional flake composites and existing literature has reported results for values of $(\alpha\phi)$ only up to 10. Comparison of the derived closed form solutions to computational results reveals that both the harmonic and the arithmetic averages are adequate in dilute systems; however, at large values of $(\alpha\phi)$ and (ϵ) only the harmonic average is in good agreement with the computational results. The predictions of the proposed solution (harmonic averaging) are also compared to those of existing literature models for the effective diffusivity of flake composites. We find that discrepancies become very significant at large (ϵ) and also at large values of $(\alpha\phi)$, pointing further to the conclusion that the proposed solution is currently the only accurate one to predict the effective diffusivity of randomly oriented and highly concentrated nano-flake composites.

6.2 Introduction

Prediction of the barrier properties of flake-filled composites has been the subject of active research in recent years, due to their importance as barrier materials and in nano-technology. Original models for aligned-flake composites have been derived from analysis of simple unit-cells corresponding to idealized flake arrangements [1], [2]. These have been found to be in good agreement with computation, even in cases when the spatial arrangement of the flakes deviate drastically from regular packing [3]. The key and rather undisputed result concerning aligned systems is that the Barrier Improvement Factor ($BIF \sim 1/D_{eff}$), D_{eff} being the effective diffusivity of the composite, is a quadratic polynomial of ($\alpha\phi$), where (α) is the aspect ratio of the flakes and (ϕ) their volume fraction [4]. When the flake orientations deviate from perfect alignment, the picture is far less clear. When the flakes assume a fixed orientation with respect to the direction of bulk transport, [5] proposed a model capable of reproducing 2D computational results for ($\alpha\phi$) up to 40. When the flakes assume random orientations, either fully or within an interval $[-\epsilon, +\epsilon]$, numerical results along with an empirical model capable of representing them for ($\alpha\phi$) up to 15 have been presented in [6]. A review of the state of the art along with a new model for the barrier properties of flake systems in which the flakes orientations are normally distributed within an interval and for ($\alpha\phi$) up to 5, have been presented in [7]. This problem has also been reviewed in [8] where detailed reference to earlier work has been made. Three dimensional simulations using the Latice-Boltzman method have been presented in [9] and the conclusion was reached that for flakes of high aspect ratio (argued in [9] to be between 4.500 and 10.500 for graphene) existing models do not capture the variation of barrier properties. From a literature review, it is evident that, while the topic has received significant attention in the last 15 years, there does not exist a single predictive model capable of capturing both, the effect of concentration and the effect of orientational randomness on the barrier properties of flake composites. This is particularly true for high aspect ratio nano-composites, for which very high values of ($\alpha\phi$) can be achieved; the ($\alpha\phi$) implied in [9] for a graphene composite in LDPE can be as high as 100. Since earlier models have been validated with computational results for ($\alpha\phi$) only up to 7, their suitability for this class of materials is not proven [9]. It is also evident that existing models are based on the ad-hoc utilization of orientational metrics without a solid theoretical footing and, most importantly, without preserving the rotational invariance of the diffusivity tensor. With these in mind, the purpose of the present communication is to propose a model for the barrier properties of randomly oriented flake composites which will incorporate both, the effect of flake concentration and the effect of orientational randomness. The model is free of ad-hoc pronouncements and is solidly footed on averaging of the diffusivity tensor. The model is tested extensively with computational results and is found to be valid for all states of misalignment and for the entire range of ($\alpha\phi$) that is achievable computationally.

6.3 Theoretical

Consider a system of randomly placed and randomly oriented flakes. The orientation of each flake is defined by the angle (θ) formed between the vertical axis (y), which is taken to be the direction of macroscopic diffusion, and the outward normal vector on the flake surface. The horizontal axis is indicated as (x). D_{11} is the diffusivity of such a system of flakes when $\theta = 0^0$ (all flakes oriented perpendicular to the direction of macroscopic diffusion) and D_{22} the diffusivity when $\theta = 90^0$ (all flakes oriented parallel to the direction of diffusion) - D_{11} and D_{22} are the principal values of the two-dimensional diffusivity tensor, D. In this case, the effective diffusivity (D_{eff}) in the direction (y) of such a system of misaligned flakes can be expressed as a function of the misaligned angle (θ) as:

$$D_{eff}(\theta) = D_{11}\cos^2\theta + D_{22}\sin^2\theta \tag{6.1}$$

Equation 6.1 can be used to determine the diffusion coefficient of a system of misaligned flakes, provided ${}_{D}11$ and D_{11} are known. In previous work [5] we investigated computationally the performance of Equation 6.1 and determined that the best agreement with the computational results was obtained when the models of [12] and [4] were used for the principal diffusivities, namely

$$D_{22} = D_0\frac{1-\phi}{1+\phi/2\alpha} \quad \text{and} \quad D_{11} = D_0\frac{1-\phi}{(1+\alpha\phi/\lambda)^2} \tag{6.2}$$

respectively, where D_0 is the diffusivity of the matrix material. The parameter (λ) is meant to reflect the tortuous path of the solute around each flake and it was set to λ=3 in the original model of [4]; a value of λ=2.5 was found to give the best agreement between Equation 6.1 and our 2D computational results and this value has been used throughout this study. Once established, Equation 6.1 can be used as the basis of deriving estimates of the effective diffusivity in systems in which the flakes assume a range of orientations. For that purpose, some type of averaging must be performed.

The arithmetic mean is defined as $D_{eff} = \frac{1}{N}\sum_i^N D_i$ where D_i for $i = 1 \ldots N$ are the diffusivities of the N sub-cells which comprise the geometry of interest. Each sub-cell is characterized by a flake orientation angle (θ_i). The arithmetic mean corresponds to a system in which mass transport is envisaged to occur through resistances in parallel; this assumption is more consistent with a dilute system of flakes, in which, macroscopically, lines of constant concentration will tend to be equally spaced and parallel to one another. For a continuous distribution of flake orientations with it will be

$$\langle D^{\alpha}_{eff} \rangle = \frac{1}{2\epsilon}\int_{-\epsilon}^{\epsilon}(D_{11}\cos^2\theta + D_{22}\sin^2\theta)d\theta = \frac{1}{2}(D_{11}+D_{22}) + \frac{\sin(2\epsilon)}{4\epsilon}(D_{11}-D_{22}) \tag{6.3}$$

where brackets are used to indicate averaging and the superscript (α) indicates arithmetic mean. In Equation 6.3 the pre-factor $(1/2\epsilon)$ corresponds to flakes being oriented with equal probability at each orientation within the interval $[-\epsilon, +\epsilon]$. Other probability functions can also be included in Equation 6.3. In the special case when $\epsilon = \pi/2$, corresponding to a system in which the flakes assume all possible orientations with equal probability (random orientation), it is

$$\langle D^{\alpha}_{eff} \rangle = \frac{1}{2}(D_{11}+D_{22}) \tag{6.4}$$

In the dilute limit and using dilute-regime models for D_{11} and D_{22} [12], namely

$$D_{22} = D_0\frac{1-\phi}{1+\phi/2\alpha} \quad \text{and} \quad D_{11} = D_0\frac{1-\phi}{1+\alpha\phi/2} \tag{6.5}$$

we can derive an explicit expression for the arithmetic mean of a system with random $(\epsilon = \pi/2)$ distribution of orientations, in terms of (ϕ) and (α).

$$\langle D^{\alpha}_{eff} \rangle = \frac{(1-\phi)(4\alpha+\phi+\phi\alpha^2)}{(2\alpha+\phi)(2+\alpha\phi)} \cdot D_0 \tag{6.6}$$

If the model of [4] is used for D_{11}, the arithmetic mean $\langle D^{\alpha}_{yy} \rangle$ can also be obtained in closed form in terms of (ϕ), (α) and (λ) from Equation 6.3 as

$$\langle D^{\alpha}_{eff} \rangle = \frac{(1-\phi)(\lambda^2\phi + 4\lambda^2\alpha + 4\lambda\phi\alpha^2 + 2\phi^2\alpha^3}{2(2\alpha+\phi)(\lambda+\alpha\phi)^2} \tag{6.7}$$

Equation 6.7 is also suitable for concentrated systems.

If transport in a flake composite is better approximated by resistances in series, the Harmonic mean, defined as $1/D_{eff} = (1/N)\cdot\sum_1^N(1/D_i)$, is a more appropriate measure. As above, for a continuous distribution of orientations it will be

$$\langle D^{h}_{eff} \rangle^{-1} = \frac{1}{2\epsilon}\int_{-\epsilon}^{\epsilon}(D_{11}\cos^2\theta + D_{22}\sin^2\theta)^{-1}d\theta = \frac{1}{\epsilon\sqrt{D_{11}D_{22}}} \cdot \arctan\left[\sqrt{\frac{D_{22}}{D_{11}}}\tan(\epsilon)\right] \tag{6.8}$$

where the superscript (h) indicates the harmonic mean. When $\epsilon = \pi/2$ (randomly oriented system), Equation 6.8 gives

$$\langle D^h_{eff} \rangle = \sqrt{D_{11} D_{22}} \tag{6.9}$$

Closed form expressions in terms of (α), (λ) and (ϕ) can be obtained by substituting D_{11} and D_{22} in Equation 6.8 with the corresponding models, as was done in the case of the arithmetic mean (Equations 6.6 and 6.7 above).

According to the Harmonic averaging (Equation 6.9), the ratio between the effective diffusivity of a system comprised of aligned flakes over the diffusivity of a system comprised of randomly oriented flakes can be found to be

$$\frac{D_{aligned}}{D_{random}} = \sqrt{\frac{D_{11}}{D_{22}}} = \frac{\lambda\sqrt{\alpha^2 + \alpha\phi/2}}{\alpha(\alpha\phi + \lambda)} \tag{6.10}$$

in which the models of [4] and [12] were used for D_{11} and D_{22} respectively. Evidently, for very long flakes, Equation 6.10 predicts that the ratio is proportional to $(1/\alpha\varphi)$.

Finally, the geometric mean provides that

$$D_{eff} = \left(\prod_{1}^{N} D_i \right)^{1/N} \tag{6.11}$$

where $\prod$ indicates a product and (N) is again the number of sub-cells comprising the system. In that case, for a continuous distribution of (θ) it will be

$$\langle D^g_{eff} \rangle = \exp\left[\frac{1}{2\epsilon} \int_{-\epsilon}^{\epsilon} ln(D_{11} \cos^2\theta + D_{22} \sin^2\theta) d\theta \right] \tag{6.12}$$

where again a uniform distribution of orientations is assumed and the superscript (g) stands for the geometric mean.

In the following, we will validate the proposed model (Equations 6.3, 6.8 and 6.13) by comparing its predictions to computational results. Subsequently, we will compare its predictions to those of existing literature models. Comparison of model predictions to experimental data is a not-sostraightforward matter, since, in order for the comparison to be meaningful, the microstructure of the physical specimens (in terms of placement, dispersion and orientation of the platelets/flakes) should be comparable to those of the theoretical model (uniformly dispersed flakes, with their orientations uniformly distributed between [-ϵ, +ϵ]). In addition, several physico-chemical factors come into play in nano-composites and as a result the observed BIFs show a very significant scatter. Wolf and co-workers [10] have presented a comprehensive summary and analysis of all experimental data published on the topic of barrier properties of nano-composites (to O_2, CO_2 and H_2O) between 1995 and 2015. It is very instructive to see that almost half the experimental data show that inclusion of nano-fillers results in a decrease of the BIF of the composite. The authors of [10] clearly show that this is because it is very common, when preparing a nano-composite specimen, to have other factors present, such as formation of high-D interphases, chemical modification of the matrix, formation of agglomerates, particle attrition etc. Dontero and coworkers [11] validated the use of diffusion theory and theoretical diffusivity models for platelet filled composites systems. They conducted ODOL diffusion experiments in carefully constructed PDMS models which included carefully aligned slender obstacles and found a good agreement between measured and computed diffusion profiles.

6.4 Results and Discussion

6.4.1 Computational

We carry out a comprehensive computational evaluation of the above-proposed models, using earlier obtained data [6] as well as results of new computations. All our computations are two dimensional and as such, are strictly valid for ribbon-composites, which are materials in which the flakes have a very long length in the out-of-plane direction. Comparison between 2D and 3D computational results in randomly oriented flake systems are currently unavailable; however, the 2D results provide a low (conservative) estimate of the BIF of the composite. In all cases the open-source computational environment OpenFoam was used. Details of the computations have been presented in [5] and [6] and are omitted here for the sake of brevity. Each geometry contained usually 3,000 randomly placed impermeable flake cross-sections; however, unit cells containing 10.000 or 50.000 flake cross-sections were also considered. Such an example is shown in Figure 6.2. We look at systems ranging from dilute to concentrated and in which the fiber orientations (θ) assume random values in the interval $[-\epsilon, +\epsilon], 0 < \epsilon < \pi/2$. In addition to two-dimensional flake cross-sections, we also consider an alternative, one-dimensional flake representation, suitable for flakes of very high aspect ratio, as would be the case in platelet-reinforced

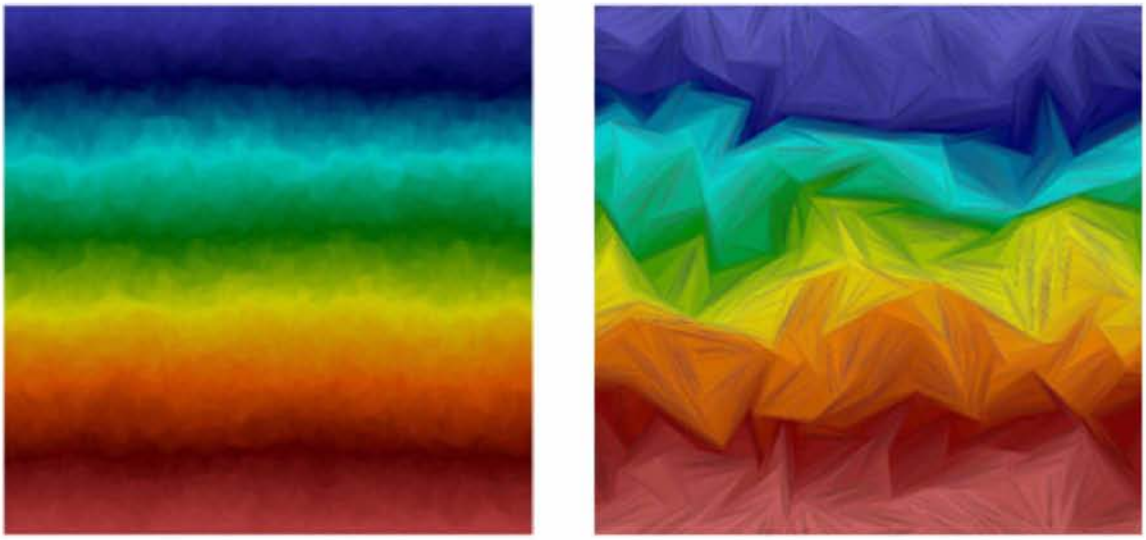

Figure 6.2: (Left) Example geometry and concentration profile in a system containing N=50.000 individual flake cross-sections with $\alpha\phi$ =10. Due to their small size, the outline of the flakes is only faintly visible and can be inferred by local variations in the concentration field. (Right) Example geometry with N=3,000 and $\alpha\phi = 20$. In both cases the flakes assume fully random orientations ($\epsilon = \pi/2$).

nano-composites. In this, each flake is represented by one line, on which the impermeability condition ($\partial C/\partial \mathbf{n} = 0$) is applied. Figure 6.3.b shows a detail of such a geometry containing 1D flake cross-sections, along with the computational mesh. For comparison, a 2D representation is shown in Figure 6.3.a. Obviously, when impermeable lines are used, instead of rectangles, to represent flake cross-sections, the use of the volume fraction (ϕ) becomes irrelevant. Recognizing that in a 2D representation it is $\alpha\phi = (Nl^2)/HL$, where (l) is the length of each flake and H, L, the dimensions of the containing unit cell, we choose to form "lines" by connecting the two mid-points of the short sides of the corresponding rectangle (Figure 6.3). In this case, a measure of the concentration of the corresponding 1D-flake system is the ratio (Nl^2/HL). Figure 6.4 shows a comparison between the predictions of the two approaches for D_{eff}. It can be seen that the use of impermeable lines to represent flakes is an acceptable simplification when large aspect ratio flakes are considered. Because of the simplicity a 1D representation affords to meshing, the range of computationally achievable flake concentrations is expanded in this manner. However, since in the 1D representation the excluded volume is always zero, irrespective of the number and size of the flakes, this approach is expected to break down at high values of (ϕ). This is not a serious short-coming however; when high aspect ratio flakes are involved, very large ($\alpha\phi$) values can be achieved at very low values of (ϕ); with reference to Figure 6.4, the maximum achieved value of $\alpha\phi$ =30 corresponds to ϕ =0.003 (0.3%). The

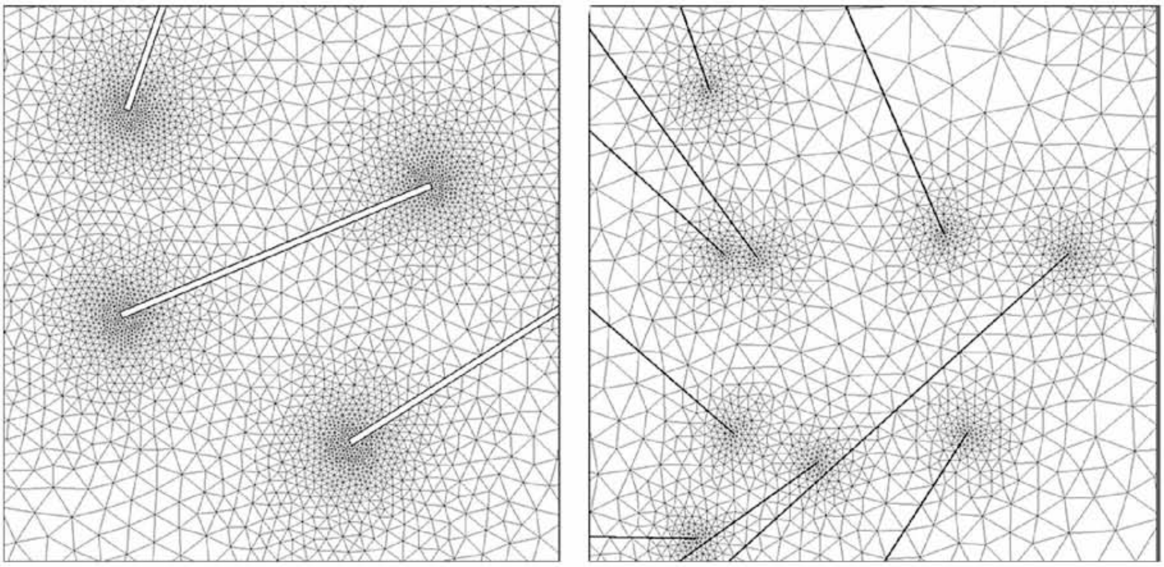

Figure 6.3: (Left) Detail of a geometry and the corresponding computational mesh, when the flake cross-sections are represented by 2D rectangles of aspect ratio $\alpha = l/t$. (Right) Corresponding detail and mesh when the flakes are represented by one-dimensional lines. (l) and (t) are the length and thickness of the flake respectively

good agreement in Figure 6.4 suggests that, for the loadings and (α) considered, the observed barrier property improvement is due to the increase in the tortuosity caused by the presence of the flakes and not the result of any excluded volume. This conclusion was also reached in [9] and appears to suggest that in flake nano-composites the improvement in barrier performance is entirely due to the increase of the tortuosity of the medium.

6.4.2 Comparison of theoretical predictions to computational results

Figure 6.5 shows a comparison between the Arithmetic, Harmonic and Geometric averages, defined by Equations 6.3, 6.8 and 6.13 above, to the computational results for D_{eff}. As outlined previously, in computing an average one needs to decide on an appropriate model for the principal diffusivities D_{11} and D_{22}. For D_{22}, Nielsen's model [11] has been shown to be reliable in the case when the flakes are aligned parallel to the direction of diffusion even for ($\alpha\phi$) as high as 50. In the following we use the model of [4] for D_{11} as it gave the best fit to earlier computational results [5] ,[6], with a value of λ=2.5.

As expected, it is $\langle D^{\alpha}_{yy} \rangle \geq \langle D^{g}_{yy} \rangle \geq \langle D^{h}_{yy} \rangle$. When the two terms D_{11} and D_{22} in the integral kernel of Equations 6.3, 6.8 and 6.13 are approximately equal (as would be the case in a dilute

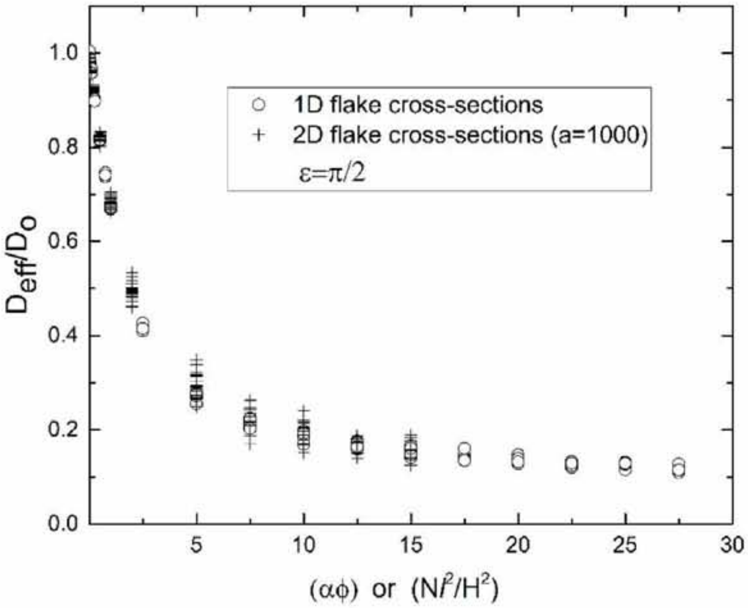

Figure 6.4: Comparison of the predicted effective diffusivity of a system with randomly oriented flake cross-sections ($\epsilon = \pi/2$) which are considered to be either 2D rectangles of aspect ratio α $=$1000 or 1D lines, for a range of values of $(\alpha\phi)$ (in the 2D representation) and $(Nl^2)/HL)$ (in the 1D representation). In the case of 2D representation, the data of [6] were used (+). In the case of 1D representations, results shown (o) correspond to N=3000

suspension of flakes, $\alpha\phi < 0.1$) the results of the three averages are practically indistinguishable. However, significant differences appear in the concentrated regime. These differences are more pronounced at higher values of (ϵ). When these differences become significant (large values of (ϵ) and $(\alpha\phi)$, choice of the correct averaging becomes important. It is evident that the arithmetic average is definitely an inappropriate model for computing the effective diffusivity of randomly oriented and concentrated flake systems – irrespective of the models used for D_{11} and D_{22}. In conjunction with the model of [4], the harmonic average is found to give a very good fit to the computational results for the entire range of $(\alpha\phi)$ studied.

As the spread in flake orientations narrows, the three averages come closer, with the harmonic mean remaining closer to the computational results, as shown in the following Figure 6.6 for ϵ=0.8 rad. The generation of computational meshes becomes easier as the flake orientation range decreases; as a result the computationally achievable range of $(\alpha\phi)$ increases as (ϵ) decreases.

Comparisons for a case of lower aspect ratio ($\alpha = 50$), in which flake cross-sections are necessarily represented as 2D rectangles, are shown in Figure 6.7.

Large values of $(\alpha\phi)$ are not achievable when the flake aspect ratio is low. In the case of Figure

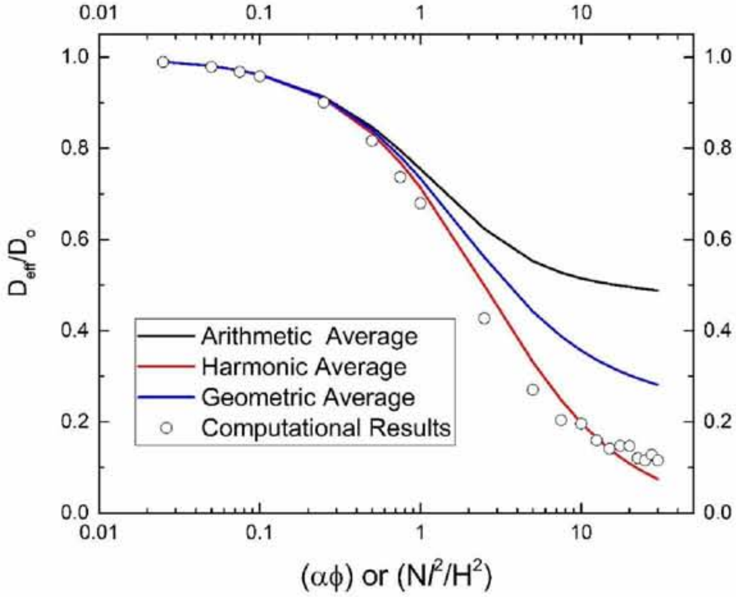

Figure 6.5: Comparison of computational results (points) and the predictions of the arithmetic, harmonic and geometric averages (Equations 6.3, 6.8 and 6.13) based on the model of [4] for D_{11} and [11] for D_{22}. Random flake orientations ($\epsilon = \pi/2$). The computational results shown correspond to the use of 1D flake cross-sections, therefore, instead of $(\alpha\phi)$ the corresponding measure of concentration is $Nl^2)/HL$, where N=3000 and H=L are the dimensions of the unit cell.

6.7 with $\alpha = 50$, $\alpha\phi = 10$ implies a volume fraction of 20%; this level of packing is at the limit of what can be achieved in real composite fabrication as well as in the generation of a computational RVE. The analytical predictions for the ratio $D_{aligned}/D_{random}$, expressed by Equation 6.10, are compared to computational results in Figure 6.8. The implication of this chart as well as of Equation 6.10 is that the ratio of the Barrier Improvement Factors (BIF) of the aligned and random composite scales with $(\alpha\phi)$ and thus, the benefit to be gained by aligning the flakes is larger the more concentrated the system is. The effect of the flake aspect ratio, as predicted by the Harmonic average (Equation 6.8) is compared to computational results in Figure 6.10, for fully random flake orientations ($\epsilon = \pi/2$) and for $\epsilon = 0.8$ rad. The numerical data as well as the model predictions follow an asymptotic behavior at increasing (α), with a limiting value already reached at $\alpha = 100$. This is in agreement with earlier published studies [13] - [16] as well as in agreement with experimental studies in well disersed nano-composites [10].

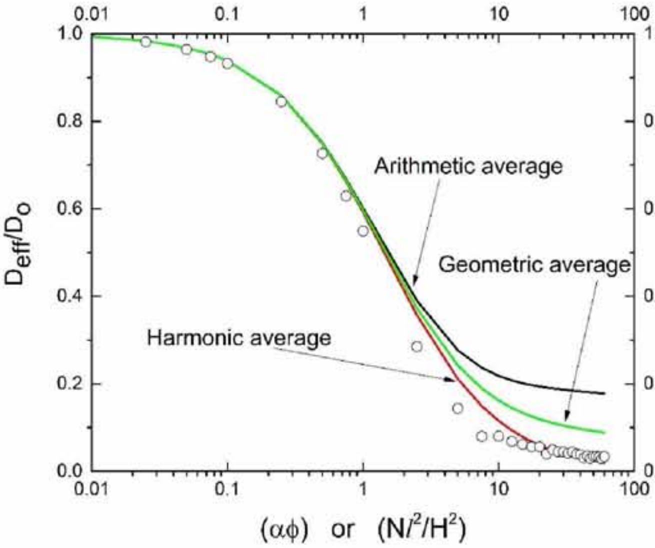

Figure 6.6: Comparison of computational data (points) and the predictions of the arithmetic, harmonic and geometric averages. Random fiber orientation between [$-\epsilon, +\epsilon$] (ϵ=0.8 rad or 45.8^o). The computational results shown correspond to the use of 1D flake cross-sections, therefore, instead of ($\alpha\phi$) the corresponding measure of concentration is Nl^2/HL, where N=3000, l is the flake length and H=L are the dimensions of the unit cell.

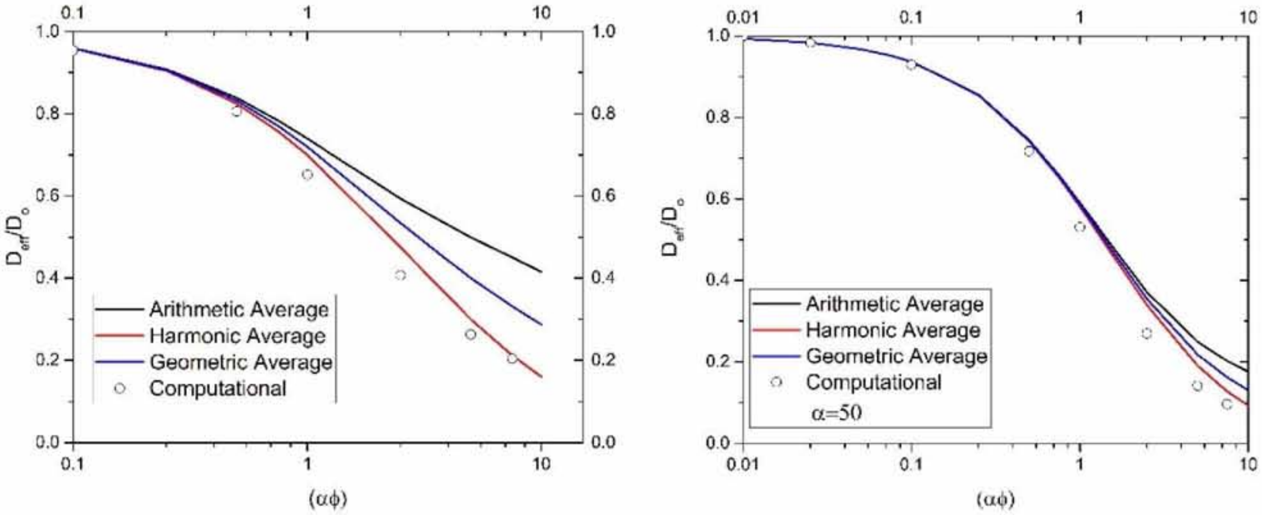

Figure 6.7: Comparison of computational data (points) corresponding to α =50 and the predictions of the arithmetic, harmonic and geometric averages. (Left) Random fiber orientation ($\epsilon = \pi/2$); (Right) $\epsilon = 45^o$. 2D representation of the flake cross-sections

6.4.3 Comparison with existing models

Among existing models which express the effect of misorientation on the barrier properties of flake composites, the model of Bharadwaj [17] was proposed by combining Nielsen's model [12] with Herman's orientation parameter $\frac{1}{2}(3\langle\cos^2\theta\rangle - 1)$ where the brackets $\langle\ldots\rangle$ indicate ensemble averaging over the flake population. For general, three-dimensional orientation distributions,

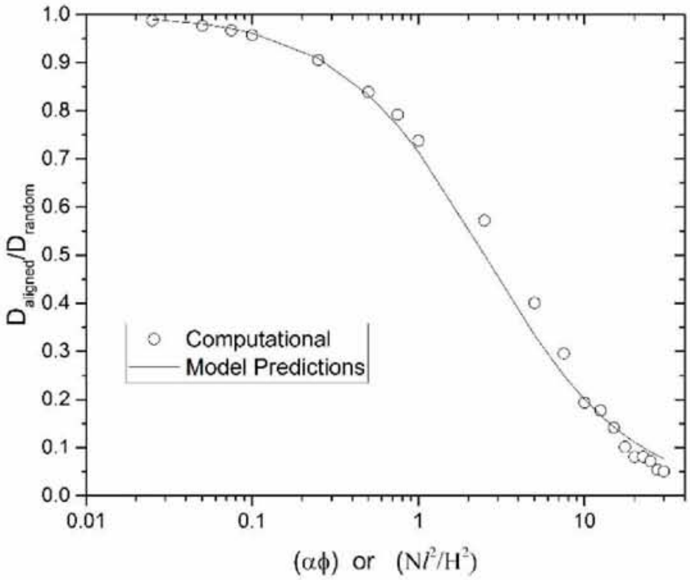

Figure 6.8: Comparison between analytical predictions based on the proposed model (Equation 6.10, line) and computational results (o). The latter were obtained using 1D representation of the flakes and the former correspond to $\alpha = 1000$. The concentration corresponding to the computational results is expressed by the ratio $Nl^2/H2$, as outlined in previous section.

the parameter (H) takes the value of zero for a random system, 1 for flakes aligned in the direction from which the angle (θ) is measured (that is, perpendicular to the direction of diffusion) and -0.5 for flakes oriented along the direction of diffusion. For two-dimensional distributions of orientations, such as those dealt with in this study, this interpretation is no longer correct. In a 3D randomly oriented distribution of flakes it is $\langle \cos^2\theta \rangle = 1/3$ while for a 2D random distribution of orientations it is $\langle \cos^2\theta \rangle = 1/2$. For this reason, we express the Herman parameter as $H = 1/2[2\langle \cos^2\theta \rangle - 1]$. In this form, for a randomly oriented system it is H=0; a system aligned perpendicular to the direction of diffusion will have H=1/2 and a system aligned along the direction of diffusion will have H=-1/2. With this in mind the expression for D_{eff} takes the form

$$\frac{D_{eff}}{D_0} = \frac{1-\phi}{1+(H+1/2)\cdot\alpha\phi/2} = \frac{1-\phi}{1+(\alpha\phi/2)\langle \cos^2\theta \rangle} \tag{6.13}$$

Equation 6.13 correctly reverts to the Nielsen model for flakes aligned normal to the direction of diffusion ($\theta = 0$) and to the dilute limit model ($D_{eff} \sim 1-\phi$) for flakes aligned parallel to the direction of diffusion ($\theta = \pi/2$). It should be noted that the term (H+1/2) in Equation 6.13 is no different than the 22-diagonal component of the orientation tensor (**A**) defined as $A_{ij} = \langle p_i p_j \rangle$.

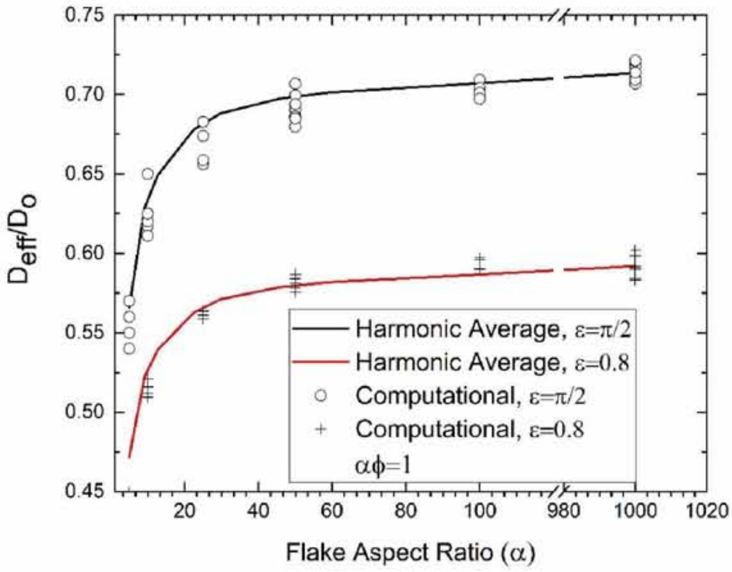

Figure 6.9: Effect of flake aspect ratio on the D_{eff} as predicted by Equation 6.8 (lines) for $\epsilon = \pi/2$ and ϵ=0.8 rad. In both cases, $\alpha\phi$ =1.0. Points are computational results obtained for N=500. 2D representation of flake cross-sections.

Since for the two-dimensional cross-sections considered in this study, $p_1 = \sin\theta, p_2 = \cos\theta$, it is

$$\boldsymbol{A} = \begin{vmatrix} \langle\sin^2\theta\rangle & \langle\sin\theta\cos\theta\rangle \\ \langle\sin^2\theta\cos\theta\rangle & \langle\cos^2\theta\rangle \end{vmatrix} \tag{6.14}$$

Using a similar reasoning, Lee et al. [18] proposed to use Herman's orientation function but in the context of Cussler's model [1], which is more suitable for dense systems; adapted to a 2D system and using (H) in the form indicated earlier, the resulting expression for D_{eff} reads

$$\frac{D_{eff}\theta}{D_0} = \left[1 + \frac{\alpha^2\phi^2}{1-\phi}\langle\cos^2\theta\rangle\right]^{-1} \tag{6.15}$$

Recently Dondero et al. [7] proposed a model which also makes use of the orientational metric (H). Keeping in mind our previous discussion on the application of the Herman's orientation function in 2D and 3D systems, we write the model of [7] as

$$\frac{D_{eff}\theta}{D_0} = \frac{1-\phi}{\left[1 + \left(H + \frac{1}{2}\right)\frac{5\alpha\phi}{9}\right]^2} = \frac{1-\phi}{\left[1 + \frac{5\alpha\phi}{9}\langle\cos^2\theta\rangle\right]^2} \tag{6.16}$$

The ensemble average directional cosine term $\langle\cos^2\theta\rangle$ assumes a simple and easier to understand form, when the flakes assume equi-probable random orientations in the interval $[-\epsilon, +\epsilon]$. It can be shown that

$$H + \frac{1}{2} = \langle \cos^2 \theta \rangle = \left(\frac{1}{2} + \frac{\sin(2\epsilon)}{4\epsilon} \right) \tag{6.17}$$

and thus, in case of a uniform distribution of flake orientations, the model of [7] can be written as

$$\frac{D_{eff}}{D_0} = \frac{1-\phi}{\left[1 + \left(1 + \frac{\sin(2\epsilon)}{2\epsilon}\right) \frac{5\alpha\phi}{18}\right]^2} \tag{6.18}$$

Similarly, expressions involving the misalignment range (ϵ) can be obtained for the models of [12] and [13]. The predictions of Equations 6.9, 6.16 and 6.18 are compared to the models derived in this study and to computational results in the following figures. Figure 6.10 shows comparisons corresponding to $\alpha = 1000$ and $\epsilon = \pi/2$. The computational results shown correspond to 2D flake representation and N = 5000 and also to 1D flakes and N = 3000. It is evident that the model proposed in this study follows the computational results much more closely, up to very large values of the concentration parameter ($\alpha\phi$). When the misalignment angle decreases, the predictions of the various models come closer together and also closer to the computational results. This is shown in Figure 6.11. In the case of small misalignment angles, the predictions of the models based on the harmonic, arithmetic and geometric averages are also close to each other (e.g Figure 6.7 above).

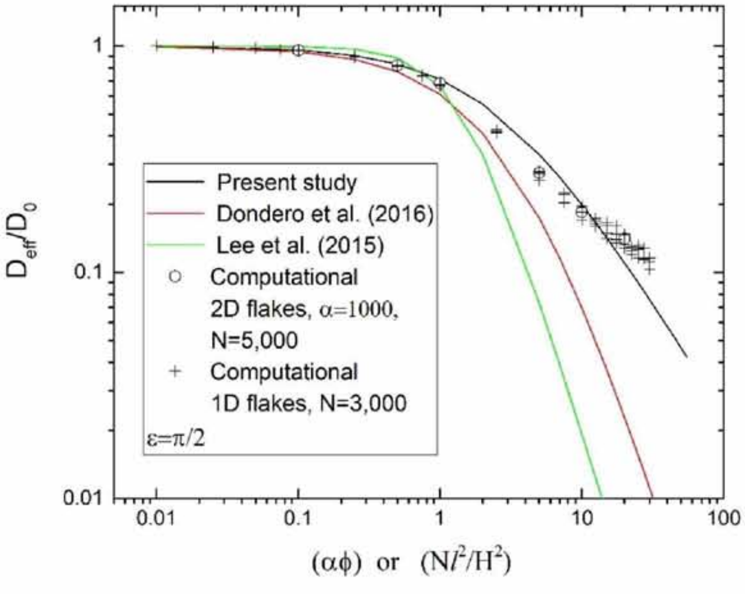

Figure 6.10: Comparison between computational results for 2D and 1D flakes (o, +) and the predictions of various theoretical models. The results of the current study correspond to the use of the harmonic average, Equation 6.8

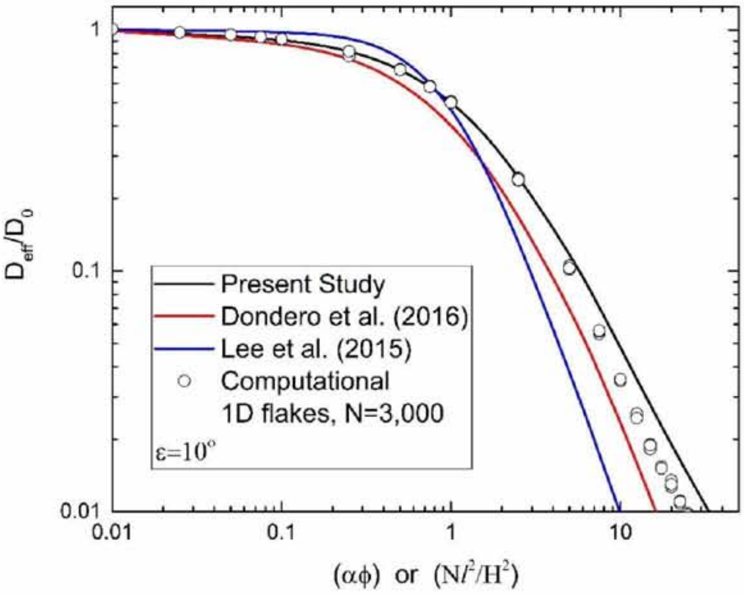

Figure 6.11: Comparison between computational results for 1D flakes (o) and the predictions of various theoretical models, when flakes assume random orientations in the interval [-10^o, +10^o]. The results of the current study shown correspond to the use of the harmonic average, Equation 6.8

6.5 Conclusions

We have presented a closed form solution for the effective diffusion coefficient of flake-filled composites, in which the flakes are randomly placed and oriented, with the orientations uniformly distributed in an interval $[+\epsilon, -\epsilon]$, $0 < \epsilon < \pi/2$. Our solution is based on the harmonic averaging of the diffusivity of unidirectional misaligned flake systems, and has been extensively validated using large-scale 2D simulations. In these simulations we have used both, traditional 2D (rectangles of finite aspect ratio) and also 1D (lines) representations of the flake cross-sections. The 1D representation is suitable for very high aspect ratio flakes, such as exfoliated nano-platelets of montmorillonite or graphene-oxide. This approach greatly simplifies the construction of the computational mesh. It is also the only feasible approach to model flake nano-composites (α >1000), in which $(\alpha\phi)$ can reach levels in excess of 100. The actual aspect ratio (α) of nano-platelets is not easy to measure [15] and its value is sometimes unclear. In certain cases, values of (α) were reported based on fitting simple, and in light of the present study, inadequate, permeability models to experimental data. For example, in [9] it was clear that a perfect fit between model and experiment could only be achieved if a value of (α) that was about 1/3 of the correct value was used. Our proposed solution for D_{eff} offers a better alternative in case such an indirect estimation of (α) is to be attempted. Our solution is found to be in very good agreement with computational results for all stages of misalignment (from unidirectional to random) and for $(\alpha\phi)$ up to 30 for a randomly oriented composite and higher for lower (ϵ). The predictions of the proposed solution were also compared to those of existing literature models. We find that discrepancies become very significant at large (ϵ) and also at large values of $(\alpha\phi)$, pointing further to the conclusion that the proposed solution is currently the only accurate one to predict the effective diffusivity of randomly oriented and highly concentrated nano-flake composites.

There is still a degree of empiricism in our proposed solution, and this can be traced in the choice of the tortuosity parameter (λ) used in the context of the model of [4] for the principal diffusivity D_{11} (fully aligned system). Similar empirical coefficients can be found in the other models tested in this study, such as in Equations 6.14-6.18. However, because of the robust foundation of our model on the properties of the diffusivity tensor and on formal averaging (e.g. Equation 6.8), a good fit with computational results at all states of misalignment is achieved, once a value of (λ) is determined by fitting the unidirectional data. In other models, the corresponding geometrical factors will have to become functions of $(\alpha\phi)$ and (ϵ) in order for their predictions to be reliable across the entire space of concentration and misalignment.

6.6 References

1. Cussler EL, Hughes SE, Ward WJ. Aris R. Barrier Membranes. Journal of Membrane Science, 1988; 38:161-74.
2. Aris, R. On a problem in hindered diffusion, Arch. Rat. Mech. Anal., 1986; 95:83-91.
3. Chen X, Papathanasiou TD. Barrier properties of flake-filled membranes: Review and numerical evaluation. Journal of Plastic Film and Sheeting, 2007;23:319-346.
4. Lape NK., Nuxoll EE., Cussler EL. Polydisperse Flakes in Barrier Films, J Membrane Science, 2004; 236:29-37.
5. Tsiantis A, Papathanasiou TD. The Barrier Properties of Flake-Filled Composites with Precise Control of Flake Orientation. Materials Sciences and Applications: Special Issue on Additive Manufacturing, 2017; 8:234-246.
6. Papathanasiou TD, Tsiantis A. Orientational Randomness and its Influence on the Barrier Properties of Flake-Filled Composite Films, Journal of Plastic Film and Sheeting, 2017; 33(4):438-456.
7. Dondero M, Tomba JP, Cisilino AP. The effect of flake orientational order on the permeability of barrier membranes: numerical simulations and predictive models, J. Membrane Science 2016;514:95–104.
8. Zid S, Zinet M, Espuche E. Modeling Diffusion Mass Transport in Multiphase Polymer Systems for Gas Barrier Applications: A Review, JH. Polymer Science Part B Polymer Physics, DOI: 10.1002/polb.24574, 2018
9. Roding M, Gaska K, Kadar R, Loren N. Computational Screening of Diffusive Transport in Nanoplatelet-Filled Composites: Use of Graphene To Enhance Polymer Barrier Properties, ACS Appl. Nano Mater. 2018; 160-167.
10. Wolf C, Angelier-Coussy H, Contard N, Doghieri F, Guillard V. How the shape of fillers affects the barrier properties of polymer/non-porous particles nanocomposites: A review. J. Membr. Sci. 2018; 556: 393-418
11. Dontero M, Cisilino AP, Tomba JP. Experimental validation of computational models for mass transport through micro heterogeneous membranes. J. Membr. Sci. 2013; 437: 25-32
12. Nielsen LE. Models for the permeability of filled polymer systems, Journal of Macromolecular Science Part A- Chemistry 1967;5(1):929-942.
13. Minelli M, Baschetti MG, Doghierri F. A comprehensive model for mass transport prop-

erties in nanocomposites. J. Membr. Sci. 2011; 381:10-20.

14. Lusti HR, Gusev AA, Guseva O. The influence of platelet disorientation on the barrier properties of composites: A numerical study. Modelling Simul. Mater. Sci. Eng. 2004;12:1201-1207.
15. Tan B, Thomas NL. A review of the water barrier properties of polymer/clay and polymer/graphene nanocomposites: J. Membr. Sci. 2016; 514: 595-612
16. Chen X, Papathanasiou TD. Barrier properties of flake-filled membranes: Review and numerical evaluation. Journal of Plastic Film and Sheeting, 2007;23:319-346.
17. Bharadwaj RK. Modeling the barrier properties of polymer-layered silicate nanocomposites. Macromolecules 2001;34:9189–9192.
18. Lee K-H, Hong J, Kwak SJ, Park M, Son JG. Spin self-assembly of highly ordered multilayers of graphene-oxide sheets for improving oxygen barrier performance in polyolefins. Carbon 2015;83:40-47.

Chapter 7

A general scaling for the barrier factor of composites containing thin layered flakes of rectangular, circular and hexagonal shape[1]

7.1 Abstract

We propose a general scaling which allows for the results of 3D mass transfer computations in layered flake composites containing square, circular or hexagonal flakes to collapse on a single master curve. We show that the Barrier Improvement Factor ($BIF \sim 1/D_{eff}$) of such composites is well represented by a power function of that scale (M) namely $BIF = (1+M)^2$. Our simulations are carried out in three-dimensional multi-particle RVEs each containing up to 4000 randomly placed individual flakes. The flakes are represented as two-dimensional squares, disks or hexagons; this representation is suitable for very thin flakes, such as exfoliated nanoplatelets. Around 3000 simulations are carried out, and the effective *BIF* is computed for different values of flake orientation, shape, dimensions and number density. We show that our scaling is consistent with the traditional representation of the BIF as a power function of ($\alpha\phi$), (α) and (ϕ) being the aspect ratio and the volume fraction of the flakes, while at the same time offering a generalized approach that is valid for all flake shapes. When the flakes are

---

[1] Part of this chapter was submitted in: Journal of Membrane Science, `https://www.journals.elsevier.com/journal-of-membrane-science`

layered at an angle (θ) to the direction of macroscopic diffusion, we propose a model for the *BIF* in terms of the principal diffusivity and (θ); this is found to be in very good agreement with computational results, which show that while the *BIF* increases with increasing (M), this increase is no longer monotonic but, instead, *BIF* approaches an asymptotic plateau value which is determined by (θ).

7.2 Introduction

Flake-filled composites are of interest in applications in which the transport of a species is to be hindered without resorting to the use of expensive and possibly environmentally hazardous additives [1]-[3]. Notable examples of such "passive" barrier materials can be found in packaging applications [4], [5], sound insulation [6], anti-corrosion coatings [7] as well as in fire-retarding polymers [8]. In all cases, the impetus for the use of (essentially) two-dimensional flakes lies in the tortuous internal structure of the corresponding composites, which allows for a substantial improvement ($\sim (\alpha\phi)^2$) in barrier properties at very modest flake concentrations. In addition, the fluid mechanics of the manufacturing (injection molding, blow molding) or application (coating) processes lead to orientation of the flakes that is largely parallel to the surface of the part and thus perpendicular to the direction of diffusion. In fire-retarding plastic parts manufactured by injection molding, the fountain flow and the shear gap-wise flow [9] result in highly oriented surface and subsurface regions, thus maximizing the barrier effect. The effect of flake concentration on the barrier properties have been studied, mainly in 2D [10]-[14] and models have been proposed, some of which [10], [11], have been found to be in excellent agreement with computational results in two-dimensional RVEs [15]-[20]. However, all these results are strictly valid for ribbon composites and their relevance to three-dimensional reality is yet to be proven.

There have been some notable attempts to simulate transport across fully three-dimensional flake-filled composites. Nagy and Duxbury [21] carried out random walk computations in large-scale 2D and 3D geometries containing randomly placed unidirectional square-shaped platelets (sticks in 2D) of finite volume. They concluded that a quadratic polynomial of ($\alpha\phi$), where (α) is the flake aspect ratio and (ϕ) the total flake volume fraction, can represent the *BIF* of such a composite over a wide range of concentrations, up to $\alpha\phi = 30$ in 3D configurations. The coefficients of this polynomial were determined by fitting computational results. Lusti et al.

[22] presented a small number (40 geometries) of finite element simulation results in systems containing $\sim$ 50 disks (aspect ratio 3, 10 and 100) dispersed randomly in a cubic RVE. They presented the first quantitative comparison between randomly oriented and aligned composites, expressing the difference in terms of a dimensionless parameter. Greco et al. [23], [24], considered composites containing stacks of unidirectional disks; a total of 85 simulations were run, in which orientation angle, the number of disks in a stack and the volume fraction varied. Greco (2014) [25], carried out 3D simulations also in disk-containing systems, in which the volume fraction, the aspect ratio (from 10 to 50) and the orientation angle were varied. Recently, Roding at al. [26] presented results of a large-scale study in systems each containing 1000 disks of circular or elliptical shape. They carried out $\sim$ 1000 transient diffusion simulations, using a dynamic “random walk particle tracking” scheme. After [21] these were the first dynamic simulations for transport across flake filled systems and also the first attempt to model large-scale 3D systems. The influence of several morphological factors, such as flake misorientation, flake shape, flake thickness and flake polydispercity, was discussed. The works of [26] and [21] not-withstanding, it is fair to say that there has been no detailed study of three-dimensional diffusion in flake composites that covers a comprehensive range of the pertinent parameters. Beyond disks or squares, the effect of the flake shape on effective diffusivity remains largely unknown, even though hexagonal flakes are known to occur, (eg. in Graphene, MgO_2, hBN) - with the exception of the work of [27] who suggested a heuristic modification of the model of Cussler et al [11] to be used in the case of hexagonal flakes. In addition, the effect of misorientation has only received spotty attention and remains to be quantified. Finally, the relevance of existing and well-studied models for fully-aligned systems [10]-[12] to three-dimensional reality is not proven. In fact, the study of Roding [26] has raised significant questions on the validity of existing 2D models. In this study we carry out a comprehensive ($\sim$ 3000 simulations) computational study of steady state diffusion in three-dimensional, multi-particle (up to 4000 flakes in each RVE) and periodic RVEs with the objective of giving answers to some of these questions.

7.3 Computational

Steady-state diffusion computations in three-dimensional Representative Volume Elements (RVEs) were carried out using the open source package OpenFoam. Each RVE is a parallepiped of dimensions L, H, D (along the X, Y and Z axes respectively) and contains a number (N) of flakes placed in random positions. We consider flakes of square, circular and hexagonal shape, as shown in Figure 7.1. For the purpose of geometry generation, the circular flakes are inscribed in the corresponding rectangular shaped flake and the hexagonal flake is inscribed in the corresponding circular geometry. The thickness dimension of the flakes was taken to be zero; this is not far from reality since in flake systems of practical importance flake thickness is very small comparing to the planar dimensions. We define the planes that are formed from the X-Y axis, X-Z axis and Y-Z axis as PXY, PXZ and PYZ respectively (Figure 7.2). The plane PXZ is perpendicular to the direction of diffusion (Y); PXY is perpendicular to the Z-axis where the flake rotation is taking place and PYZ is normal to the X-axis. The diffusion direction is taken to be along the Y-axis with $C = 0$ at $y = 0$ and $C = 1$ at $y = H$. The equation solved is the steady-state diffusion equation :

$$\nabla^2 C = 0 \tag{7.1}$$

The above equation was solved on RVEs generated using an in-house software solution that can create any variety of 2D and 3D RVEs with any combination of boundary and geometrical periodic conditions, including a user-specified number of flakes with any combination of sizes, shapes, spatial distributions and orientations. Subsequently the geometry files were imported to the mesh generator GMSH [28] and a triangular mesh was created with element count in the order of 100M. Finally the simulations were solved using the OpenFOAM toolkit [29].

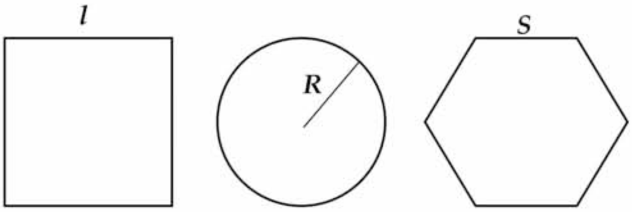

Figure 7.1: Flake shapes considered in this study with their geometrical characteristics. l is the side of the square flake, R is the radius of the disk and S the side of the hexagon.

The boundary conditions on the top and bottom surfaces of the unit cell are:

$$C_{(XYplane),Y=0} = 0 \quad and \quad C_{(ZXplane),Y=1} = 1 \tag{7.2}$$

Periodic conditions are applied at the sides of the RVE, namely

$$C_{(XYplane),X=0} = C_{(XYplane),X=1} \quad and \quad C_{(ZXplane),Y=0} = C_{(ZXplane),Y=1} \tag{7.3}$$

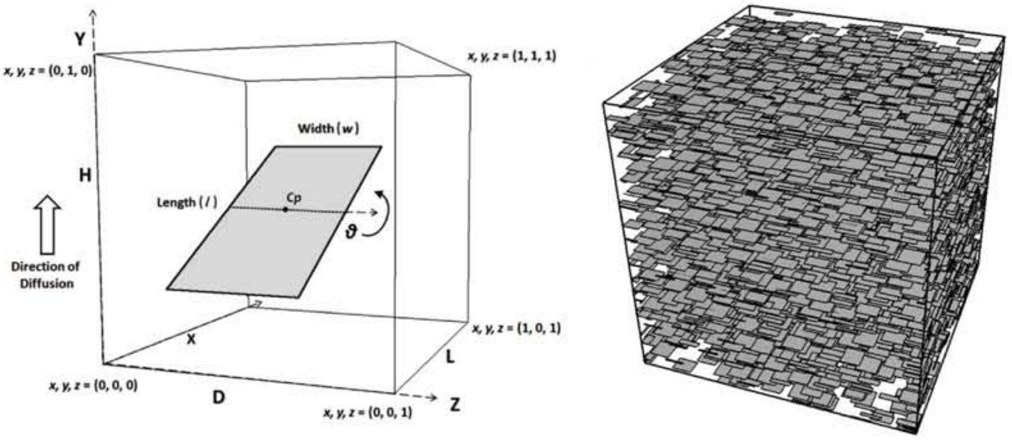

Figure 7.2: (left) Schematic of the RVE and the geometrical characteristics of rectangular flakes. (right) a sample geometry containing $N = 4000$ square flakes at $\theta = 0^o$.

In 2D models, use of periodic conditions has been shown [15] to eliminate artifacts due to the shape of the unit cell and we see, from the results shown in Figure 7.3, that this is also true in 3D models as well.

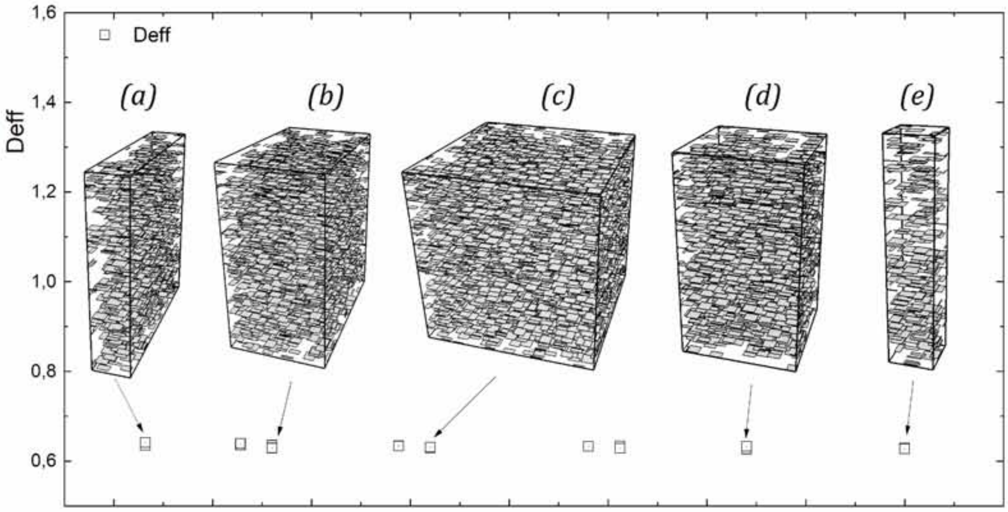

Figure 7.3: Invariance of computational results for D_{eff} with size/shape of the RVE. Shown are values of D_{eff} calculated for various sizes of RVE's at $\theta = 0$ and having $M = 0.25$. In all cases the height of the RVE was kept constant. In (a) and (b) the height and depth were kept constant ($H = D = 1$) and the length was changed ($L < H$). In the middle case (c) the RVE is a cube of unit length ($L = H = D = 1$). In (d) and (e) the depth and the length changed while being kept equal ($L = D < H$). The middle case (c) has $N = 4000$ flakes. In the other cases the number of flakes (N) was changed accordingly in order to keep the flake number-density, $N/\Delta V$, and thus the scale M, constant.

The flakes are placed within the RVE using a random sequential addition procedure, in which random numbers assign the centroid coordinates of the flake. For a flake to be placed in the chosen position a triangle-triangle collision detection algorithm [30] was used since each flake is represented as a combination of triangles. If any triangle of the candidate flake overlaps with any triangle of the pre-existing flakes the position is rejected and a new combination of coordinates and appropriate angle is chosen until the RVE is filled with the desired number of flakes or a predetermined number of tries (10^7) is reached. During the collision detection stage a small safety distance between flakes was considered in order to avoid the creation of degenerate cells at the later stage of meshing. In randomly oriented configurations, the orientation vectors are assigned random values and the flakes are rotated at the X axis then the Y axis and finally at the Z axis. In the cases where the flakes are unidirectional, the rotation is applied only to the Z axis thus rotating the flakes perpendicular to the direction of diffusion, as illustrated in Figure 7.2a. In Figure 7.4 we can see additional example geometries of various shapes.

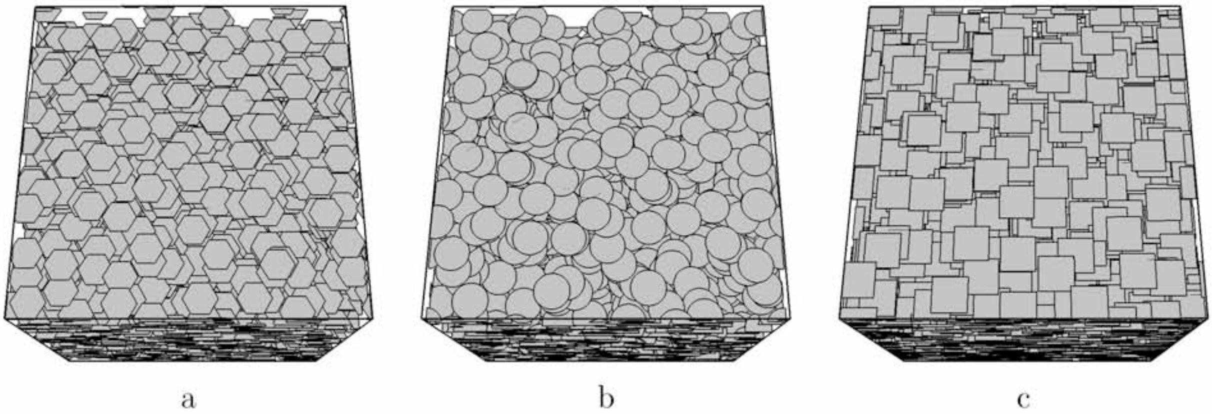

Figure 7.4: Example geometries containing oriented flakes at $\theta = 0$. (a) hexagonal, (b) circular and (c) rectangular. In all cases N=4000.

Solution of Equation 7.1 supplies the concentration (C) and the concentration gradient ($\partial C/\partial n$) at each position of the domain. Figure 7.5 shows a representative concentration field as well as a representative distribution of the corresponding flux field on the top surface of the RVE. Once the flux (Q) on the top surface is computed, an effective diffusivity (D_{eff}) of the unit cell can be calculated from Fick's law as:

$$D_{eff} = \frac{H \cdot D_0}{\Delta C \cdot D \cdot L} \int_0^D \int_0^L \frac{\partial C}{\partial n} dx dz \tag{7.4}$$

The so computed D_{eff} is the D_{yy} principal diffusivity that will be used in later section of this paper. In the following we will investigate the effect of flake size, shape, orientation and number density on the computed effective diffusivities. In the process we will propose a novel scaling that allows for a generalization of the observed behavior.

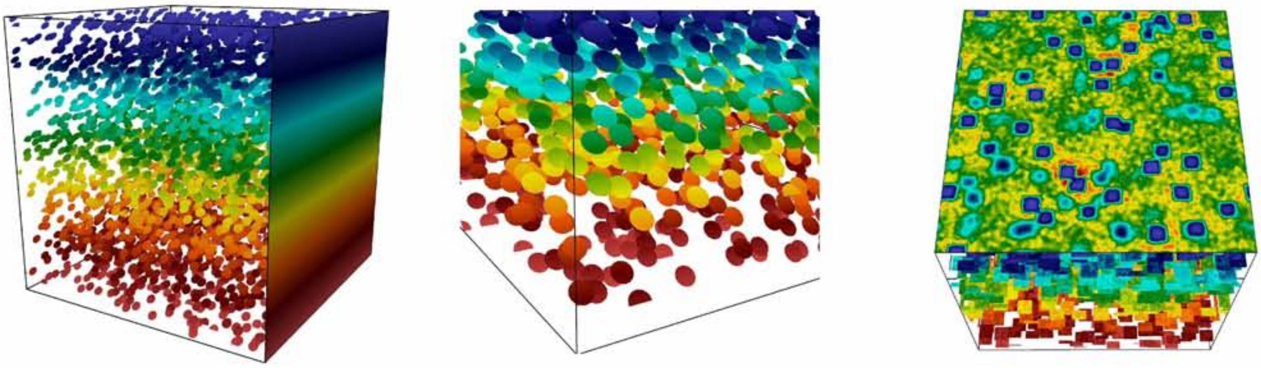

Figure 7.5: Concentration fields in a 3D flake system containing randomly placed circular and rectangular flakes. (a) & (b) show circular flakes oriented at 45^o to the direction of diffusion. (a) shows the concentration distribution, along a clipping plane at Z=1, from the bottom of the unit cell where C=1 (coloured red) to the top where C=0 (coloured blue) in the periodic surface of the unit cell and on the flakes. (b) shows a close-up view is shown near the bottom of the unit cell (the colors in the image are out of scale for illustration purposes). (c) Shows a typical flux distribution on the top surface of a unit cell with rectangular flakes. The underlying placement of flakes can be inferred from variations in the flux field.

7.4 Results and Discussion

7.4.1 Scaling of the results

At first we will focus our attention on the analysis and scaling of computational results. A suitable scale should be based on observations [26] that, among various parameters, the flake area and flake shape (elongated vs. square) affect the effective diffusivity. We have therefore chosen to represent our results in terms of a dimensionless parameter (M) defined as:

$$M = \frac{N \cdot (A)^2}{\Delta V \cdot (P)} \tag{7.5}$$

where (A) is the flake area, (P) its perimeter, ΔV is the volume of the RVE and the ratio (A/P) can be taken as a characteristic length of the flake, expressing also the flake shape. In the case of flakes of square shape, $A = l^2$ and $P = 4l$, resulting in

$$M^{sq} = \frac{N \cdot l^3}{4 \cdot \Delta V} \tag{7.6}$$

This result is consistent with earlier work in 2D flake systems [10], [18], where it was shown that for flakes of zero thickness (in 2D these are represented by straight lines) a suitable scale is $N(l/H)^2$. The expressions for (M) in the case of disk-shaped and hexagonal flakes can be shown to be

$$M^c = \frac{1}{2}\frac{N}{\Delta V}\pi R^3 \quad (circular), \quad M^h = \frac{27}{24}\frac{N}{\Delta V}S^3 \quad (hexagonal) \tag{7.7}$$

Our results for all flake shapes and concentrations, scaled in terms of the parameter (M), are summarized in Figure 7.6. It is observed that use of the scale (M) collapses all data, irrespective of flake shape, on a single master curve. The form of the scaled data suggests that the effective diffusivity (D_{eff}) of a three-dimensional flake composite can be expressed as a power function in terms of (M). The simplest possible such function which follows our results very closely, is

$$D_{eff} = \frac{1}{(1+M)^2} \tag{7.8}$$

in which the scale (M) is based on the general definition of Equation 7.5 and is expressed by Equations 7.6 – 7.7 for the case of square, disk and hexagonal shaped flakes. The form of the power function of Equation 7.8 is in line with earlier studies in 2D systems [10], [18], and it essentially confirms, also in 3D, that in systems with flakes aligned perpendicular to the direction of macroscopic transport, the *BIF* will asymptotically grow with the square of the appropriate scale, in our case (M).

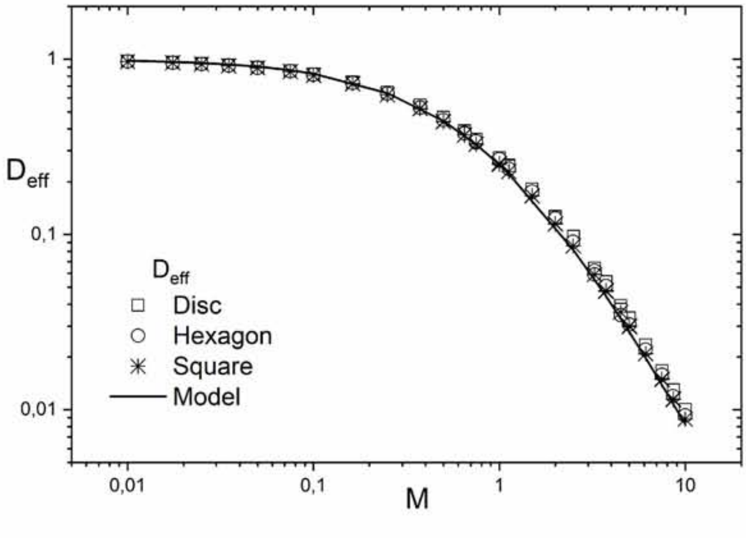

Figure 7.6: Computational results obtained for different geometries and their comparison to Equation 7.8. The formula used in the computation of (M) is different at each geometry, depending on flake shape (Equations 7.6 and 7.7 for flakes of square, disk and hexagon shape respectively).

We can easily notice from Equations 7.6 and 7.7 that the flake dimensions scale with a power of (3) of the corresponding flake characteristic length. This leads to inclusions whose size grows fast with (l), as can be seen in Figure 7.7 where comparisons between geometries corresponding to various M for square geometries are shown. While at large values of (M) (Figure 7.7c) the flake dimensions seem large compared to the RVE, we have shown that the use of periodic geometries and periodic boundary conditions eliminates the edge effects even in extremely elongated RVEs (Figure 7.3).

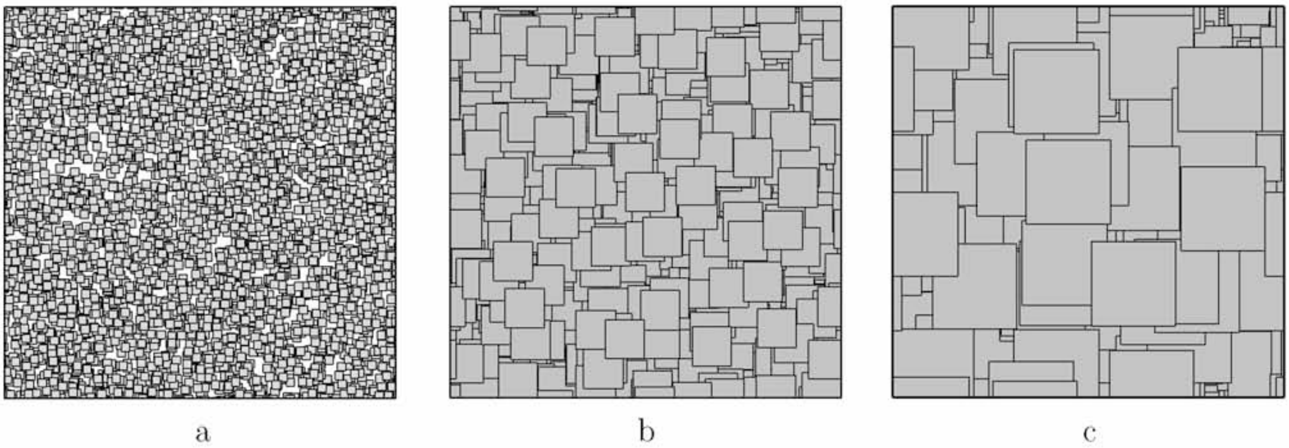

Figure 7.7: Scaling of geometries according to different M. The top view of the RVE is shown with square geometries at $\theta = 0$. $M = 0.01$ (left), $M = 1.0$ (center) and $M = 10$ (right). In all cases the dimensions of the unit cell remain the same therefore the relative size of the flakes is clearly seen.

7.4.2 Relation with previous work

As elaborated in the Introduction, all previous studies were concerned with disk-shaped or square flakes. These are geometries in which a definition of the flake aspect ratio (α) can be given without much ambiguity. It is natural therefore that the product ($\alpha\phi$), (ϕ) being the flake volume fraction, was the scale of choice. For the case of 3D flakes of square shape ($\phi = N \cdot l^2 \cdot t/\Delta V$), the BIF was found in [21] to be represented by

$$BIF = 1 + C_1(\alpha\phi) + C_2(\alpha\phi)^2 \tag{7.9}$$

In Equation 7.9, t is the flake thickness and $\alpha = l/t$ is a definition of the flake aspect ratio. The constants C_1 and C_2 were determined in [21] by fitting computational results of $(BIF-1)/(\alpha\phi)$ vs. ($\alpha\phi$) and were found to be $C_1 = 0.44 \pm 0.03$ and $C_2 = 0.05 \pm 0.005$. It is instructive to compare the results of the proposed model (Equation 7.8) to those of [21], and Equation 7.9.

According to Equation 7.8, $BIF = (1 + M)^2 = 1 + 2M + M^2$. For the case of square flakes Equation 7.6 can be rearranged by dividing and multiplying with flake thickness (t) so that

$$M^{sq} = \frac{1}{4} \cdot \frac{N \cdot l^2 t}{\Delta V} \cdot \frac{l}{t} = \frac{\alpha\phi}{4} \tag{7.10}$$

Therefore, for the case of square flakes, our proposed model for the BIF gives

$$BIF_{sq} = (1 + M_{sq})^2 = 1 + \frac{1}{2}\alpha\phi + \frac{1}{16}(\alpha\phi)^2 \tag{7.11}$$

resulting in $C_1 = 0.5$ and $C_2 = 0.0625$. A comparison between our results and Equation 7.9 is shown in Figure 7.8 in which we plot $(BIF - 1)/\alpha\phi$ vs $\alpha\phi$.

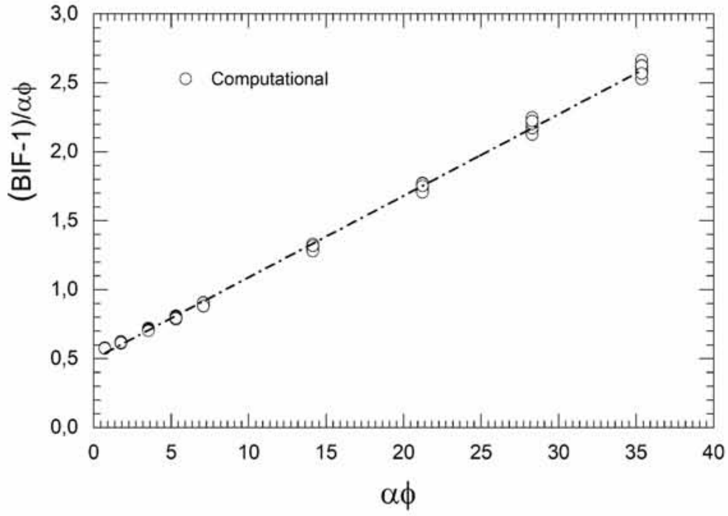

Figure 7.8: Computational results for square flakes at $\theta = 0$ plotted as suggested by Eq. 7.9. The intercept gives $C_1 = 0.4987$ and this compares favourably with the value of 0.5 anticipated from Eq. 7.11. The slope gives $C_2 = 0.0591$; and this is very close to the result $C_2 = 0.05$ of [21] and also compares to 0.0625=1/16 anticipated from Eq. 7.11.

The values for C_1 and C_2 obtained from our computational results are very close to those of [21], the differences probably originating from the different numerical method used and also from the fact that in our study the flake thickness has been neglected, flakes being in our case essentially 2D entities. In the case of circular and hexagonal flakes, it can be shown that the concentration metric ($\alpha\phi$) is related to the scaling parameters M^h and M^c as $\alpha\phi = 4M^c$ for the case of circular and $alpha\phi = M^h$ for the case of hexagonal flakes. In obtaining these, the aspect ratio of the disk is defined as $\alpha = 2R/t$, while for the hexagon, $\alpha = Lc/t$, where Lc is a

Table 7.1: Values of the polynomial coefficients C_1 and C_2 obtained from our computational results (Figs. 7.8 & 7.9) for various flake shapes.

	Squares	Squares [21]	Disks	Hexagons	
				($\alpha = L_C/t$)	($\alpha = 2S/t$)
C_1	0.4987	0.44	0.4715	1.91	0.4015
C_2	0.0591	0.05	0.0498	0.876	0.0413
Implied from Eq. 7.8					
C_1	0.5		0.5	2.0	0.4325
C_2	0.0625		0.0625	1.0	0.04687

characteristic length defined as $(Area)/(Perimeter)$ ($Lc = \sqrt{3} \cdot S/4$). It is therefore,

$$BIF^c = 1 + \frac{1}{2} \cdot \alpha\phi + \left(\frac{1}{4}\right)^2 \cdot (\alpha\phi)^2 \tag{7.12}$$

yielding $C_1 = 1/2$ and $C_2 = 1/16$ for disks and

$$BIF^h = 1 + 2\alpha\phi + (\alpha\phi)^2 \tag{7.13}$$

yielding $C_1 = 2$ and $C_2 = 1$ for hexagons. If, alternatively, the aspect ratio of the hexagon is based on its longest diagonal, which is $2S$, then it can be shown that

$$\alpha\phi = \frac{8}{\sqrt{3}} M^h \tag{7.14}$$

In that case,

$$BIF^h = 1 + \frac{\sqrt{3}}{4}\alpha\phi + \frac{3}{64}(\alpha\phi)^2 \tag{7.15}$$

yielding $C_1 = \sqrt{3}/4$ and $C_2 = 3/64$.

The computational results for disk-shaped and hexagonal flakes are plotted as suggested by Equations 7.12, 7.13 & 7.15 in Figure 7.9. As in the case of square flakes, we find that the computational results follow closely the behaviour suggested by Equation 7.9, with suitably defined coefficients. Our results are summarized in Table 7.1.

7.4.3 Comparison to predictions of existing models

In the following we compare the results of our 3D computations and the proposed model (Equation 7.8) with the predictions of frequently used models for the *BIF* of flake composites,

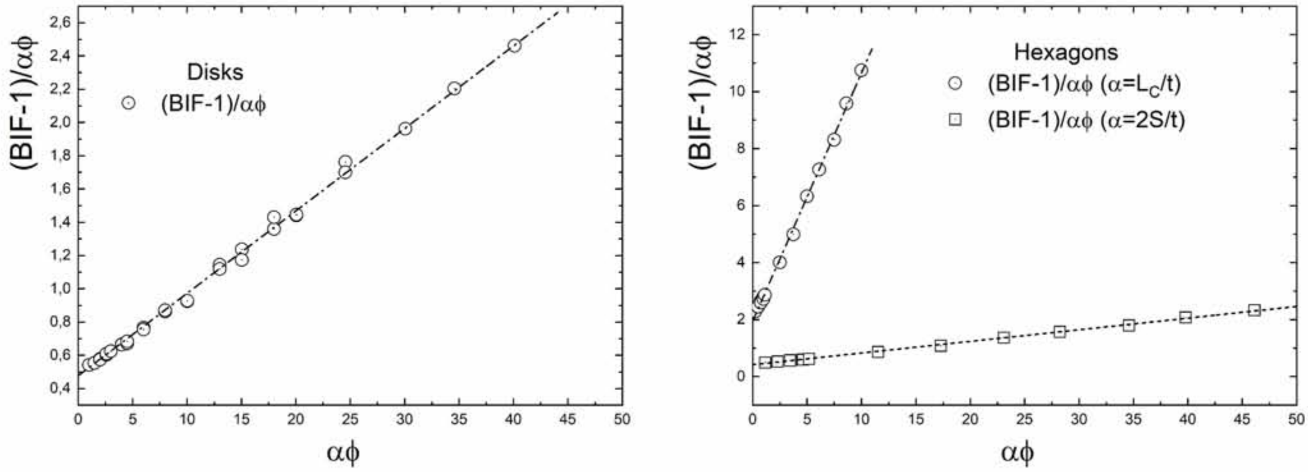

a

b

Figure 7.9: Computational results for circular and hexagonal flakes at $\theta = 0$ plotted as suggested by Eq. 7.9. The intercepts give $C_1 = 0.4715$ for disks and $C_1 = 1.91$ for hexagons, in which case aspect ratio is based on L_C. These compare with the values of 1/2 and 2 suggested by Eqs. 7.12 & 7.13. The slopes give $C_2 = 0.0498$ and $C_2 = 0.876$ and these compare to 1/16 (for disks) and 1.0 (for hexagons) suggested by Eqs. 7.12 & 7.13. In Fig. 7.9b the linear fit corresponding to the alternative definition of the aspect ratio (based on the long diagonal of the hexagon, Eq. 7.23) is also shown. The corresponding best-fit values are $C_1 = 0.4015$ and $C_2 = 0.0413$.

namely those of [10], [11]. The relevant equations are:

$$\frac{D_o}{D_{eff}} = \frac{(1 + \alpha\phi/\lambda)^2}{1 - \phi} \tag{7.16}$$

and

$$\frac{D_o}{D_{eff}} = 1 + \frac{\alpha^2\phi^2}{\beta(1 - \phi)} \tag{7.17}$$

Where (λ) and (β) are geometrical factors, reflecting the tortuous path the diffusing species follows as it travels around individual flakes. It is understood that these geometrical factors will depend on flake shape. In the original work of [11] it was suggested that $\lambda = 3$. Computational results of [17] in 2D geometries (in which flake cross sections are represented as lines or rectangles) have given a best fit for $\lambda = 2.5$. In the present study the flakes are infinitely thin and thus $1 - \phi \sim 1$, yielding

$$BIF = (1 + \alpha\phi/\lambda)^2 = 1 + \frac{2}{\lambda}\alpha\phi + \frac{1}{\lambda^2}(\alpha\phi)^2 \tag{7.18}$$

Comparing this expression to the previously derived expressions for the BIF of composites containing square, circular and hexagonal flakes, we are able to obtain estimates of the geometrical parameter (λ) for each flake shape.

1. For squares $\lambda = 4$, ($2/\lambda = 0.5$ and $1/\lambda^2 = 1/16$)
2. For disks $\lambda = 4$, ($2/\lambda = 1/2$ and $1/\lambda^2 = 1/16$), when aspect ratio is defined as $\alpha = 2R/t$.
3. For hexagons
   (a) $\lambda = 1$, ($2/\lambda = 2$ and $1/\lambda^2 = 1$), if aspect ratio is based on characteristic length $L_C = \sqrt{3} \cdot S/4$.
   (b) $\lambda = 8\sqrt{3}/3$, ($2/\lambda = \sqrt{3}/4$ and $1/\lambda^2 = 3/64$) if the longest flake diagonal is used in the calculation of the aspect ratio of the flake ($\alpha = 2S/t$)

For the particular case of hexagonal flakes, [27] have proposed an expression for the *BIF*, based on a generic model of the form of Equation 7.17 and using heuristic diffusion path arguments. The expression offered is

$$BIF = 1 + \frac{2}{27}(\alpha\phi)^2 \tag{7.19}$$

While omission of the linear term is bound to affect the predictions of this model, especially in the dilute and semi-dilute regimes, the coefficient of the quadratic term will determine the asymptotic growth of *BIF* vs. ($\alpha\phi$) in the concentrated regime. This coefficient, $2/27 = 0.074$, compares with the coefficient 0.0413 (Table 7.1) obtained from our computational data for hexagonal flakes (Fig. 7.9b) when the aspect ratio is based on the flake longest diagonal and to the value $3/64 = 0.0469$ inferred from Eq. 7.23. Note that this value would be very different if the flake aspect ratio were to be determined by using a different flake length in calculating the flake aspect ratio.

7.4.4 The effect of flake orientation

Having proposed Equation 7.8, we further investigate the effect of flake misalignment, by considering unidirectional systems in which the flakes form an angle (θ) with the direction of diffusion, as shown in Figure 7.10. We carry out simulations for $\theta = 15^o$, 30^o and 45^o, for various flake shapes and dimensions. In all simulations $N = 4000$.

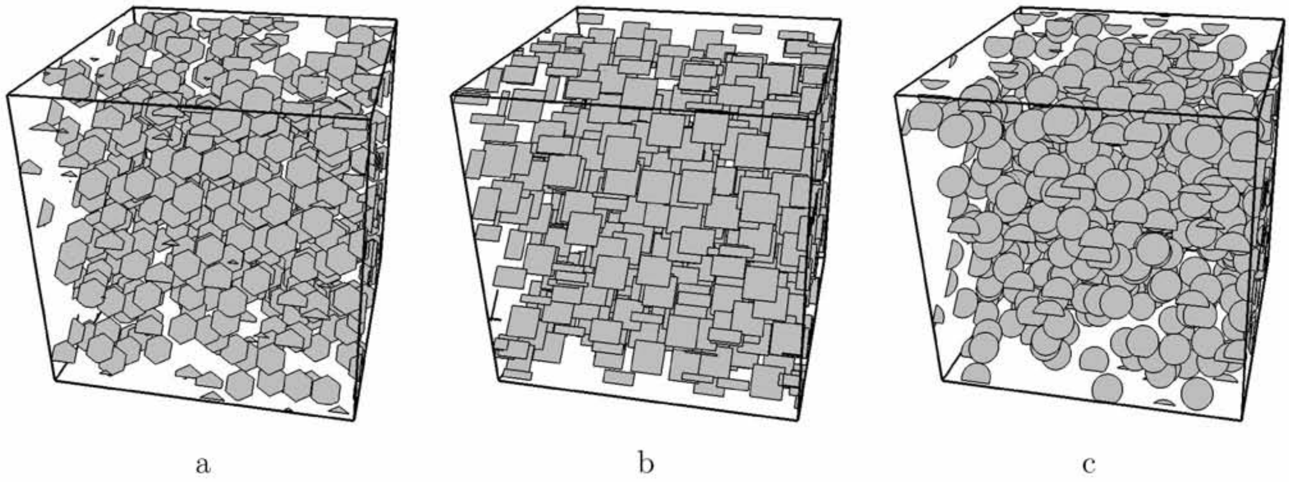

Figure 7.10: 3D oriented flake configurations at $\theta = 45^o$. Number of flakes has been reduced to 500 for visual clarity.

In line with similar work in 2D [17], in order to capture the effect of misalignment we investigate the use of expressions of the form:

$$\frac{D_{eff}(\theta)}{D_0} = \frac{1}{(1+M)^2}\cos^2\theta + \sin^2\theta \tag{7.20}$$

Since in our study the flake thickness is neglected, the flake volume fraction is zero and the second principal diffusivity D_{22} is the same as that of the matrix material ($D_0 = D_{22}$). Figure 7.11 summarizes the results of our computations as well as the predictions of Equation 7.20. It is clear that misalignment reduces the barrier factor. In a manner similar to what has been

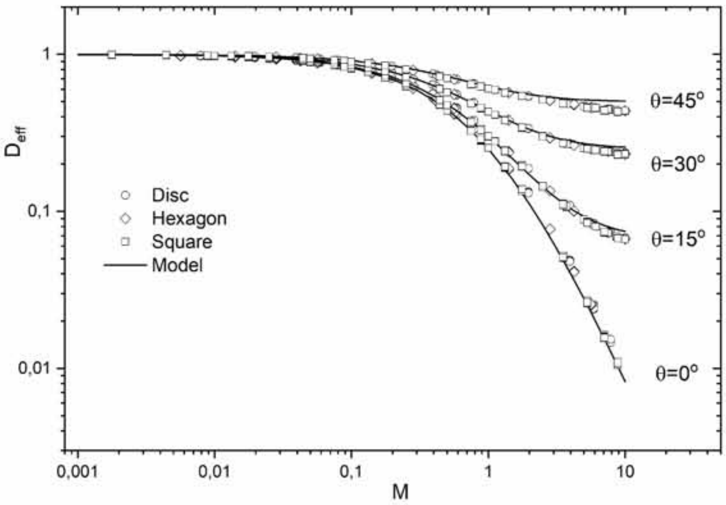

Figure 7.11: Computational results (points) and model predictions (lines) for various flake shapes and orientations. Model predictions based on Equation 7.20.

observed in 2D systems, our results also show that when $\theta > 0$ the BIF does no longer grow with the square of (M), but that it approaches a plateau value as (M) increases. From Equation 7.20 it is clear that this plateau value is a function of the misalignment angle (θ).

7.4.5 The effect of flake aspect ratio

One obvious result of Equations 7.5-7.7 is that D_{eff} will decrease as the flake area, $A_f = l \cdot w$ increases. At each level of flake area, Equation 7.6 can also predict the effect of flake aspect ratio on D_{eff}. In the case of rectangular flakes we have defined r as $r = l/w$ and $A_f = l \cdot w = l^2 r$. Therefore, the scale parameter (M) of Equation 7.5 for constant A_f (indicated as M_A) becomes

$$M_A = \frac{N}{\Delta V}(A_f)^{1.5}\frac{\sqrt{r}}{2(1+r)} \tag{7.21}$$

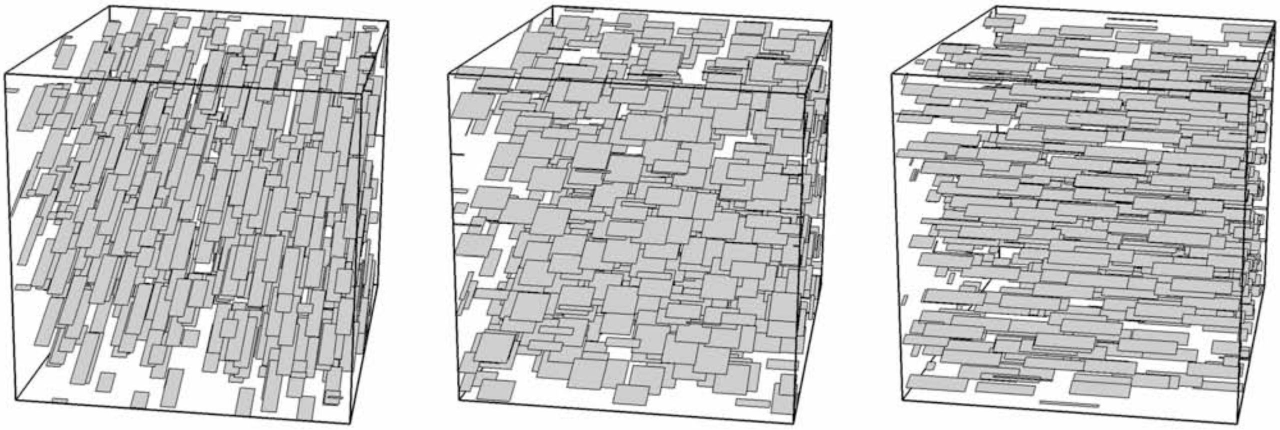

a b c

Figure 7.12: Sample geometries at various r. (a) $r = 4$, (b) $r = 1$ and (c) $r = 1/4$ and in all cases $\theta = 45^o$.

In Figure 7.12 we can see characteristic geometries at various r and in Figure 7.13 we can see the comparison between numerical results and analytical results from Equation 7.13. Along with Equation 7.6, Equation 7.13 provides an expression for D_{eff} in terms of (r). Evidently, $\partial M_A/\partial r < 0$, therefore as r increases, D_{eff} is predicted to increase.

Results of simulations for various r are also summarized in Figure 7.14, which illustrates the effect of flake shape on the effective diffusivity (D_{eff}), for the case when the flake diagonal is kept constant. It is clear from Figures 7.13 and 7.14 that maximum barrier effect is achieved by using square flakes (r=1). This effect is more pronounced when the flakes are aligned normal to the direction of diffusion (θ=0). This result is in agreement with Roding et al. 2018 in which

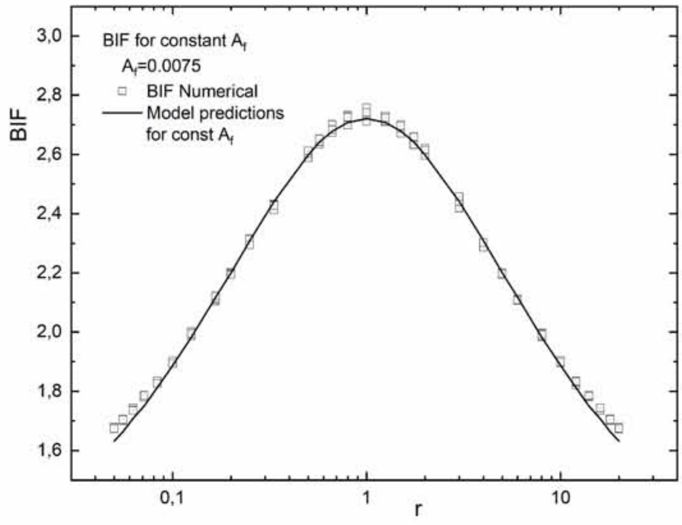

Figure 7.13: Computational results and model predictions for rectangular flakes at constant area ($A_f = 0.0075$), $1/20 \leq r \leq 20$ and $\theta = 0$.

it was found that elongated ellipsoidal disks are less effective, for barrier purposes, than disks of circular profile. Elongated particles are less effective as barrier materials, since they provide shorter alternative diffusion paths around their small axis, than would rectangular or circular inclusions. Also as we deviate from the case of square flakes the effective diffusivities are the same if we interchange l and w and as a result $D_{eff}(r) = D_{eff}(1/r)$.

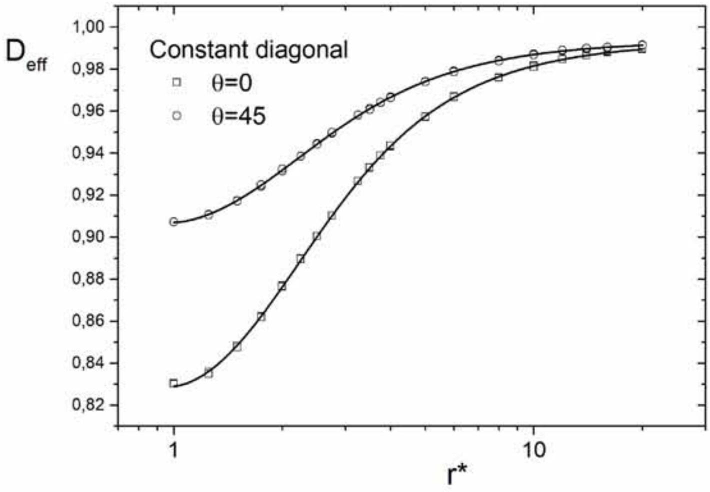

Figure 7.14: D_{eff} versus r^* as other geometrical characteristics, namely flake diagonal remains constant for two angles ($\theta = 0^o, 45^o$). The number of flakes is N=4000 at all simulations. The line is drawn for visual aid.

We can take this analysis one step further and express the BIF, as suggested by Equation 7.6, in terms of the flake aspect ratio. Equation 7.6 gives

$$BIF = 1 + 2M + M^2 \tag{7.22}$$

By using the flake (planar) aspect ratio $r = w/l > 1$, the scale (M) can be expressed as

$$M = \frac{N}{\Delta V} \cdot \frac{1}{2(1+r)} \cdot \frac{l}{t} = \frac{1}{2(1+r)} \cdot \alpha\phi \tag{7.23}$$

in which case we have assumed that the flake aspect ratio (such as used in [21] or [26]) is defined as $\alpha = w/t$, where (w) is the larger flake dimension. Therefore, the coefficients C_1 and C_2 from Equation 7.7 can be expressed in terms of the flake aspect ratio, as

$$C_1 = \frac{1}{1+r}, \quad \text{and} \quad C_2 = \frac{1}{4(1+r)^2} \tag{7.24}$$

The above results are plotted in Figure 7.15 where we can see the lines with intercept C_1 and slope C_2 as they are plotted from the computational results. We can also see in Figure 7.16 these coefficients and their comparison with model predictions (Equation 7.16).

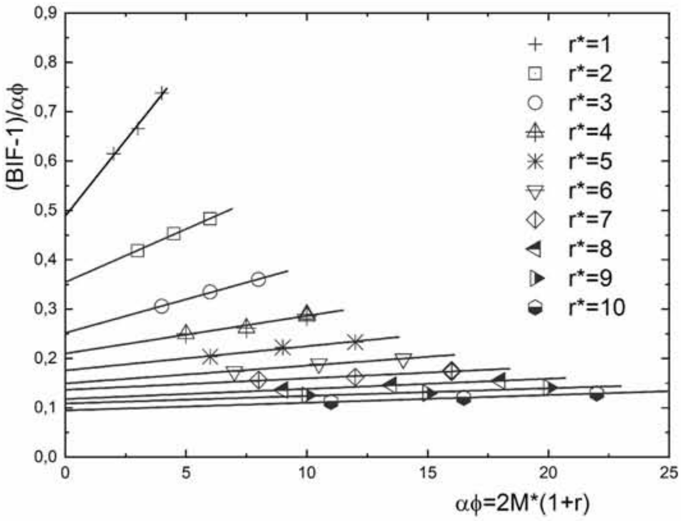

Figure 7.15: Lines with coefficients C_1 (intercept) and C_2 (slope) obtained from computational data.

From the above relations for r=1, we recover the result C_1=0.5, C_2=0.0625. When $r > 1$, it is clear that $C_1 < 0.5$ and $C_2 < 0.0625$, in agreement with the observation that the best barrier result is obtained for square flakes.

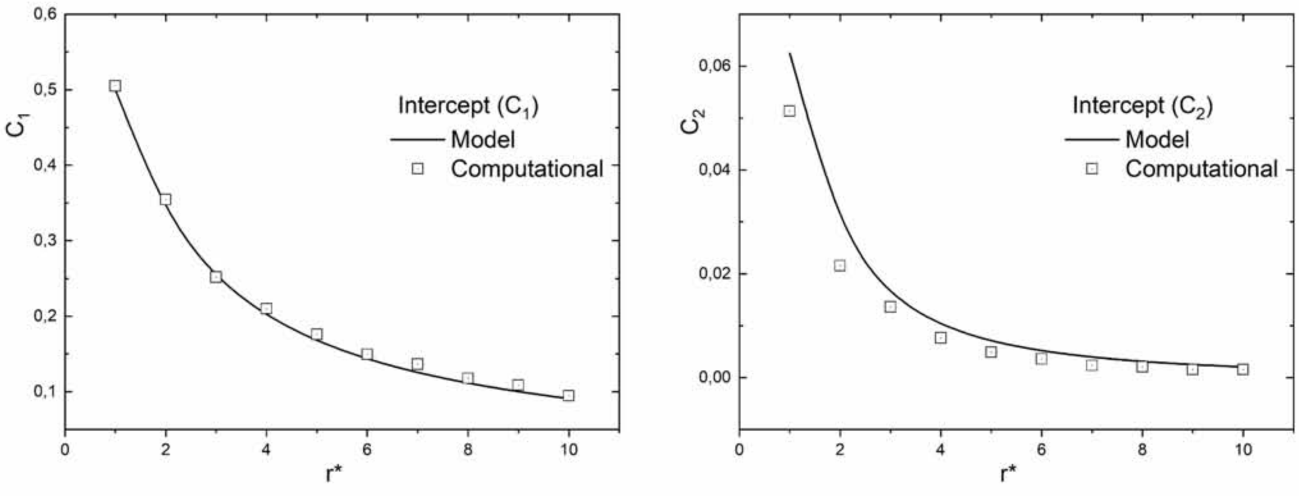

a

b

Figure 7.16: (a) Plot of coefficient C_1 and (b) of coefficient C_2 from Equation 7.7 compared with computational results.

7.5 Conclusions

We have investigated computationally three dimensional transport in composite systems consisting of randomly placed unidirectional flakes of square, circular and hexagonal shape. Analysis of the results reveals that use of a scale of the form $M = (N/\Delta V) \cdot (A) \cdot (A/P)$ is capable of reducing the BIF for composites containing flakes oriented perpendicular to the direction of macroscopic diffusion on one single master curve. This master curve is represented by a power function of the form $BIF = (1 + M)^2$. The proposed scale requires knowledge of the number density and dimensions (Area, Perimeter) of the flakes. We show how the common description of the BIF as a quadratic polynomial of $(\alpha\phi)$ can be deducted from our general model and find the appropriate polynomial coefficients for each flake shape. We show that beyond disks and squares, these coefficients are very sensitive to the length used in the calculation of the flake aspect ratio (α). Our model is also compared to established models which, being developed using heuristic diffusion path arguments, include an adjustable geometrical constant; we derive values for these geometrical constants at each flake shape. Additional simulations in systems in which the flakes form an angle with the direction of the macroscopic diffusion, have resulted in a model for the BIF in terms of the principal diffusivity and (θ); this is found to be in very good agreement with computational results, which show that while the BIF increases with increasing (M), this increase is no longer monotonic but, instead, BIF approaches an asymptotic plateau value which is determined by (θ).

7.6 References

1. Ophir, A. Dotan, I. Belinsky, and S. Kenig. Barrier and mechanical properties of nanocomposites based on polymer blends and organoclays. Journal of Applied Polymer Science , 116(1):72–83, 2010.
2. S. Pavlidou and C.D. Papaspyrides. A review on polymer–layered silicate nanocomposites. Progress in Polymer Science , 33(12):1119 – 1198, 2008.
3. Tan and N.L. Thomas. A review of the water barrier properties of polymer/clay and polymer/graphene nanocomposites. Journal of Membrane Science , 514:595 – 612, 2016.
4. Kanishka Bhunia, Sumeet Dhawan, and Shyam Sablani. Modeling the oxygen diffusion of nanocomposite-based food packaging films. Journal of food science , 77:N29–38, 07 2012.
5. Jose Maria Lagaron and Eugenia Nunez. Nanocomposites of moisture-sensitive polymers and biopolymers with enhanced performance for flexible packaging applications. Journal of Plastic Film and Sheeting , 28:79–89, 01 2011.
6. Lichao Xia, Hong Wu, Shaoyun Guo, Xiaojie Sun, and Wenbin Liang. Enhanced sound insulation and mechanical properties of ldpe/mica composites through multilayered distribution and orientation of the mica. Composites Part A: Applied Science and Manufacturing, 81:225 –233, 2016.
7. Bryan Pajarito and Masatoshi Kubouchi. Flake-filled polymers for corrosion protection. Journal of Chemical Engineering of Japan , 46:18–26, 01 2013.
8. Aravind Dasari, Zhong-Zhen Yu, Gui-Peng Cai, and Yiu-Wing Mai. Recent developments in the fire retardancy of polymeric materials. Progress in Polymer Science , 38(9):1357 – 1387, 2013.
9. T. D. Papathanasiou. 4 - flow-induced alignment in injection molding of fiber-reinforced polymer composites. In T D Papathanasiou and D C Guell, editors, Flow-Induced Alignment in Composite Materials , Woodhead Publishing Series in Composites Science and Engineering, pages 112 – 165. Woodhead Publishing, 1997.
10. Nancy K. Lape, Eric E. Nuxoll, and E.L. Cussler. Polydisperse flakes in barrier films. Journal of Membrane Science , 236(1):29 – 37, 2004.
11. E. L. Cussler, Stephanie E. Hughes, William J. Ward, and Rutherford Aris. Barrier membranes. Jornal of Membrane Science, 38(2):161–174, 8 1988.
12. Matteo Minelli, Marco Giacinti Baschetti, and Ferruccio Doghieri. A comprehensive model for mass transport properties in nanocomposites. Journal of Membrane Science,

381(1):10 – 20, 2011.

13. Matteo Minelli, Marco Giacinti Baschetti, and Ferruccio Doghieri. Analysis of modeling results for barrier properties in ordered nanocom-posite systems. Journal of Membrane Science, 327:208–215, 02 2009.
14. Marco Dondero, J. Pablo Tomba, and Adrián P. Cisilino. The effect of flake orientational order on the permeability of barrier membranes: numerical simulations and predictive models. Journal of Membrane Science, 514:95 – 104, 2016.
15. Tsiantis and T. D. Papathanasiou. An evaluation of models and computational approaches for the barrier properties of coatings containing flakes of high aspect ratio. Journal of Coatings Technology and Research, 16(2):521–530, Mar 2019.
16. Xiaoming Chen and T.D. Papathanasiou. Barrier properties of flake-filled membranes: Review and numerical evaluation. Journal of Plastic Film & Sheeting , 23(4):319–346, 2007.
17. Tsiantis and Thanasis Papathanasiou. The barrier properties of flake-filled composites with precise control of flake orientation. Materials Sciences and Applications, 08:234–246, 01 2017.
18. A. Tsiantis and T. D. Papathanasiou. A closed-form solution for the barrier properties of randomly oriented high aspect ratio flake composites. Journal of Composite Materials , 53(16):2239–2247, 2019.
19. T. D. Papathanasiou and A. Tsiantis. Orientational randomness and its influence on the barrier properties of flake-filled composite films. Journal of Plastic Film & Sheeting, 33(4):438–456, 2017.
20. Marco Dondero, J. Pablo Tomba, and Adrián P. Cisilino. The effect of flake orientational order on the permeability of barrier membranes: numerical simulations and predictive models. Journal of Membrane Science, 514:95 – 104, 2016.
21. F. Nagy and P. M. Duxbury. Permeability and conductivity of platelet-reinforced membranes and composites. Physical Review E, 66(2), Aug 2002.
22. Hans Lusti, Andrei Gusev, and Olga Guseva. The influence of platelet disorientation on the barrier properties of composites: A numerical study. Modelling and Simulation in Materials Science and Engineering, 12:1201, 10 2004.
23. Greco and A. Maffezzoli. Two-dimensional and three-dimensional simulation of diffusion in nanocomposite with arbitrarily oriented lamellae. Journal of Membrane Science,

442:238 – 244, 2013.

24. Greco, C. Esposito Corcione, and A. Maffezzoli. Diffusion in oriented lamellar nanocomposite: Numerical analysis of the effects of dispersion and intercalation. Computational Materials Science, 133:45 – 51, 2017.
25. Greco. Simulation and modeling of diffusion in oriented lamellar nanocomposites. Computational Materials Science , 83:164 – 170, 2014.
26. Magnus Röding, Karolina Gaska, Roland Kádár, and Niklas Lorén. Computational screening of diffusive transport in nanoplatelet-filled composites: Use of graphene to enhance polymer barrier properties. ACS Applied Nano Materials , 1(1):160–167, 2018.
27. G.D Moggridge, Nancy K Lape, Chuanfang Yang, and E.L Cussler. Barrier films using flakes and reactive additives. Progress in Organic Coatings , 46(4):231 – 240, 2003.
28. Christophe Geuzaine and Jean-François Remacle. Gmsh: A 3-d finite element mesh generator with built-in pre- and post-processing facilities. International Journal for Numerical Methods in Engineering, 79:1309 – 1331, 09 2009.
29. H.G. Weller, Gavin Tabor, Hrvoje Jasak, and Christer Fureby. A tensorial approach to computational continuum mechanics using object orientated techniques. Computers in Physics, 12:620–631, 11 1998.
30. Tomas Oller. A fast triangle-triangle intersection test. Journal of Graphic Tools, 2, 05 2004

Chapter 8

Conclusion

8.1 Summary of Thesis Achievements and Contributions to Knowledge

1. A new algorithm for creating high packing geometrical configurations in 2D space and more detailed results of maximum 2D packing for particles with aspect ratio (α) from 1 to 1000+.

2. Developed a phenomenological, data-based model for the BIF of 2D ribbon-filled composites, which accounts for the effect of both, concentration (expressed by $\alpha\phi$) and orientational randomness.

3. We have shown beyond doubt the importance of periodic geometrical and periodic boundary conditions in solving diffusion problems in unit RVE's and the erroneous results that can be produced from deviations from the correct modelling conditions.

4. Proposed and tested a novel, previously unavailable closed form model for the BIF of 2D ribbon-filled composites (Chapter 6 & Reference [7.18]). This model offers a rational way for the inclusion of the effect of orientational randomness, at all concentration regimes. It should be noted that prior to this work, the effect of orientational randomness was accounted for by an ad-hoc inclusion of terms of the form $\langle \cos^2(\theta) \rangle$ in existing models; we have shown that that approach produces mistaken predictions when the concentration (expressed by $\alpha\phi$) deviates from the dilute regime.

5. A new dimensionless metric for the description of BIF evolution in the full range of 3D geometries with various flake shapes, aspect ratios and orientations.

8.2 Recommendations for Future Work

The results from the present research could be extended in the future into the following research areas:

1. Further investigation of the evolution of 2D RSA created geometries. This could lead to an analytical solution for the 2D packing estimation. Also a new algorithm for accurate estimation of packing could be created.
2. Numerical studies that take into account the spatial variability in the distribution of flakes inside unit cells in both 2D and 3D geometries. This could lead to an accurate coupling between numerical, theoretical and experimental data.
3. Improvement of the 2D and 3D models by taking into account the deformation zones around flakes that are created by the interaction of the matrix material with the flake material.

Appendix A

Publications and Conferences

A.1 Publications

A.1.1 Publications related to this thesis

1. T. D. Papathanasiou and A. Tsiantis. Orientational randomness and its influence on the barrier properties of flake-filled composite films. Journal of Plastic Film & Sheeting, 33(4):438–456, 2017.
2. A. Tsiantis and T. D. Papathanasiou. The barrier properties of flake-filled composites with precise control of flake orientation. Materials Sciences and Applications, 08:234–246, 01 2017.
3. A. Tsiantis and T. D. Papathanasiou. A closed-form solution for the barrier properties of randomly oriented high aspect ratio flake composites. Journal of Composite Materials, 53(16):2239–2247, 2019.
4. A. Tsiantis and T. D. Papathanasiou. An evaluation of models and computational approaches for the barrier properties of coatings containing flakes of high aspect ratio. Journal of Coatings Technology and Research, 16(2):521–530, Mar 2019.
5. A. Tsiantis, T.D. Papathanasiou, A novel FastRSA algorithm: Statistical properties and evolution of microstructure, Physica A: Statistical Mechanics and its Applications, Volume 534, 2019, 122083, ISSN 0378-4371,`https://doi.org/10.1016/j.physa.2019.122083`.
6. A. Tsiantis, T.D. Papathanasiou, A general scaling for the barrier factor of composites containing thin layered flakes of rectangular, circular and hexagonal shape, Journal of

Membrane Science, (Under review)

A.1.2 Publications not directly related to this thesis

1. E.G. Karvelas, A. Tsiantis, T. D. Papathanasiou, Effect of micropolar fluid properties on the hydraulic permeability of fibrous biomaterials, Computer Methods and Programs in Biomedicine 185 (2020) 105135, `https://doi.org/10.1016/j.cmpb.2019.105135`
2. C. Eriskena, A. Tsiantis, T.D. Papathanasiou, E.G. Karvelas, Collagen Fibril Diameter Distribution Affects Permeability of Ligament Tissue: A Computational Study on Healthy and Injured Tissues, Journal of Biomechanics (Under review)

A.2 Conferences

1. A. Tsiantis and T.D. Papathanasiou, “The effect of misorientation on the barrier properties of flake-filled composites: A 3D approach”, SAMPE-2019, Charlotte, USA, `https://doi.org/10.33599/nasampe/s.19.1421.May2019.`
2. A. Tsiantis, S. Sumbekova and T.D. Papathanasiou, “Computational Analysis of transport across flake-filled composites of realistic microstructure”, 34^{th} Annual Meeting of the Polymer Processing Society (PPS-34), Taipei, Taiwan AIP Conference Proceedings 2065 (1), 030039, 5/2018.
3. A. Tsiantis and T.D. Papathanasiou, “A novel structure-permeability correlation in random and aggregated fiber arrays”, 35^{th} International Conference of the Polymer Processing Society, Cesme, Turkey, May 2019.
4. A. Tsiantis, T.D. Papathanasiou and I. Sarris, “Study of flows in cavities having fractal wall topology”, 10^{th} National Meeting on Flow Processes (FLOW2016), 12/2016, Patras, Greece.
5. A. Tsiantis, T.D. Papathanasiou, ”Microstructural clustering in composite materials and its influence on effective properties”, 11^{th} National Meeting on Flow Processes (FLOW2018), 11/2018, Kozani, Greece.
6. T.D. Papathanasiou, A. Tsiantis, ”Quantitative relationships between the aggregation state and the permeability of fibrous systems”, 9th International Meeting of the Hellenic Society of Rheology, Samos, Greece, 24-27 June, 2019